JAERI-M
8059

ANNUAL REPORT OF THE DIVISION OF THERMONUCLEAR FUSION RESEARCH AND THE DIVISION OF LARGE TOKAMAK DEVELOPMENT, FOR THE PERIOD OF APRIL 1, 1977 TO MARCH 31, 1978

February 1979

Division of Thermonuclear Fusion Research and
Division of Large Tokamak Development

日本原子力研究所
Japan Atomic Energy Research Institute

JAERI-M 8059

Annual Report of the Division of Thermonuclear Fusion Research and the Division of Large Tokamak Development for the period of April 1, 1977 to March 31, 1978

Division of Thermonuclear Fusion Research
and Division of Large Tokamak Development,
Tokai Research Establishment, JAERI

(Received December 26, 1978)

Research and development works in fiscal year 1977 of the Division of Thermonuclear Fusion Research and the Division of Large Tokamak Development are described; these two divisions are in association*.

1) Theoretical studies on tokamak confinement have continued with more emphasis on computations. A task was started of developing a computer code system for mhd behavior of tokamak plasmas.
2) Experimental studies of lower hybrid heating up to 140 kW were made in JFT-2. The ion temperature was increased by 50 % -- 60 % near the plasma center. Plasma-wall interactions (particle and thermal fluxes to the wall, and titanium gettering) were studied. In JFT-2a (DIVA) ion sputtering, arcing and evaporation were identified, and the impurity ion sputtering was found to be a dominant origin of metal impurities in the present tokamaks. A divertor was studied at high temperatures. And high-density plasma divertor actions were demonstrated; i.e. the divertor decreases the radiation power loss by a factor of 3 and increases the energy confinement time by a factor of 2.5. Various diagnostic instruments operated sufficiently to provide useful information for the research with JFT-2 and JFT-2a(DIVA).

---

* The preceding annual reports are JAERI-M 4654(FY 1970), 5029, 5564, 5888, 6359, 6926 and 7479(FY 1976).

3) JFT-2 and JFT-2a(DIVA) operated as scheduled with careful maintenance. Technological improvements were made such as titanium coating of the chamber wall, discharge cleaning and pre-ionization.

4) Detailed design of the prototype JT-60 neutral beam injector was made. Developments of ion source and beam line components have continued. A 200 kW, 650 MHz radiofrequency heating system for JFT-2 was completd; a lower hybrid heating experiment in JFT-2 was successful.

5) In particle-surface interactions, the sputtering and surface erosion were studied successfully using two ion accelerators. Studies on vacuum pumping and wall cleaning were started.

6) Improvement designs of a superconducting cluster test facility and a test module coil were made in development of the toroidal coil development. A large current superconductor test facility was installed in the laboratory. The large Coil Task, as an IEA cooperation for the development of superconducting toroidal coils was studied.

7) Second preliminary design of the tokamak experimental fusion reactor JXFR started in April 1977. Safety analyses were made of the main components and system of JXFR on the basis of the first preliminary design.

8) Inquiries on the JT-60 Tokamak machine were made in May 1977 to two firms. Their estimates and specifications were examined; negotiations are proceeding with one firm. A contract study of the power supplies and control system is in progress. A contract for the study of diagnostic equipment was concluded.

9) A contact restudy of the JT-4 design was made on the basis of engineering studies completed by the previous year. The results are being studied at present.

Key words: Annual Report, Plasma Confinement, Plasma Physics, Tokamak, JFT-2, JFT-2a(DIVA), Diagnostics, Neutral Beam Injector, RF Heating, Surface Study, Superconducting Magnet, Reactor Design, JT-60, JT-4, Sputtering, Impurities

JAERI－M 8059

核融合研究部および大型トカマク開発部年報
（昭和５２年度）

日本原子力研究所東海研究所
核融合研究部・大型トカマク開発部

（１９７８年１２月２６日受理）

核融合研究部と大型トカマク開発部の昭和52年度における研究開発の現況とその成果をとりまとめたものである＊。両部における研究は密接な連けいのもとに進められている。その概要は次のとおりである。

1) トカマク閉込めの解析を，計算に力点をおいて進めている。とくにトカマクの磁気流体的ふるまいを扱う計算機コードシステムの開発を始めた。

2) JFT－2では低域混成波加熱により50～60％のイオン温度の上昇が得られた。また，プラズマと壁との相互作用に関する実験により，壁への粒子束及び熱束と閉込めとの関係を調べた。ＪＦＴ－２ａ（ＤＩＶＡ)では，イオン・スパッタリング，アーキング，蒸発を同定し，不純物イオンによるスパッタリングが現在のトカマクで主な金属不純物発生原因であることを示した。比較的高温，高密度プラズマにおいてダイバータの研究を行ない次のようなダイバータ作用を明らかにした。ダイバータは輻射損失を⅓に軽減し，エネルギ閉じ込め時間を２.５倍に増加した。種々の計測器は充分に動作し，その結果ＪＦＴ－２およびＪＦＴ－２ａ（ＤＩＶＡ)の研究の上で有用な情報を得た。

3) ＪＦＴ－２およびＪＦＴ－２ａ（ＤＩＶＡ）は，注意深い保守により，計画通り運転された。真空壁面のチタンコーティング，放電洗浄，予備電離等の技術改良を行った。

4) ＪＴ－60用粒子入射加熱装置原型ユニットの詳細設計を行った。また，イオン源およびビームライン関連機器の開発を続行した。

２００ kW，６５０MHzのＪＦＴ－２用高周波加熱装置を完成し，ＪＦＴ－２による低域混成波加熱の実験を成功裏に実施した。

＊ 既刊されている年度は，ＪＡＥＲＩ－Ｍ４６５４（昭和４５年度），５０２９，５５６４，５８８８，６３５９，６９２６および７４７９（昭和５１年度）である。

5) 粒子－表面相互作用の研究では，2種類のイオン加速器を用いてスパッタリング及び表面侵食の分野で成果を得た。真空排気や壁の清浄化の研究を開始した。

6) 超電導クラスター・テスト装置およびテスト・モジュール・コイルの改良設計がトロイルコイル開発の為に行われた。大電流超電導導体のテスト装置が実験室に設置された。超電導トロイダルコイル開発のためのＩＥＡ協力，Large Coil Taskが概略検討された。

7) １９７７年４月よりトカマク型核融合実験炉第２次予備設計を開始した。また，実験炉の主要機器，システムについての安全性解析を第１次予備設計に基づいて行った。

8) 昭和52年４月ＪＴ－60 本体の引合を産業界２社に行った。その見積書及び見積仕様書の評価を行い，うち一社の契約接渉を行っている。電源及び制御系に関係する設計の見直しを行っており，一方，計測系に関する検討契約を完了した。

9) ＪＴ－４

前年度までに完了した予備設計及び技術開発へ成果を基礎として調整設計を産業界に発注し完了した。その評価を現在進めている。

PREFACE

A brief summary of activities in the divisions of Thermonuclear Fusion Research and Large Tokamak Development in the fiscal year 1977 is as follows.

JT-60: Most of the necessary procedures and negotiation for a contract of construction of JT-60 in its tokamak part were finished in this fiscal year. However, the actual contract with Hitachi Co. was slipped to the next fiscal year, April 17, 1978. The design of power supply system and plasma control system were under re-evaluation, scheduled to be finalized by September 1979. The electric grounding system was designed in detail.

JT-4: A detailed design was finished; JT-4 is a tokamak with non-circular cross section and divertors to study high beta limit and impurity control.

JFT-2: High density operation became possible by gas puffing and Ti evaporation to the wall; confinement was improved in the operation. Lower hybrid reonance heating of 140 kW at 650 MHz for 20 ms demonstrated ion temperature rise of 60 %, from 270 eV to 420 eV, and no increase of impurity and no adverse effect to confinement were observed during the heating.

JFT-2a(DIVA): Toroidal field was upgraded to 20 kG from 10 kG in April 1977. Operating regime of the plasma increased drastically and divertor mechanism was studied in more detail; scaling law of T_e in the scrape-off layer was elucidated and impurity was decreased to 20 - 50 % by the divertor.

Diagnostics: The diagnostic system had been strengthened to the extent that most of the data of JFT-2 and JFT-2a were double checked.

Computation: A magneto-hydrodynamic toroidal plasma code system, TRITON, was being developed.

Heating Technology-1 (Neutral Beam Injection): Three test stands, ITS-1, 2 and 3, were in operation. Typical data in this year were 75 keV and 3 A proton beam for 0.1 s and with 1.2 degree in divergence and continuous proton beam of 30 keV and 3.8 A for 7.5 s.

Heating Technology-2 (RF): Construction of a 150 kW oscillator of 650 MHz or 750 MHz for 20 ms, having a four waveguide array coupling system, was finished, and it was applied to JFT-2 plasma successfully. Design study of 1 MW klystron for JT-60 was performed.

Surface Study: Sputtering yield of Mo in low energy proton bombardment (0.2-6 keV) was measured with improved accuracy.

Superconducting Magnet: Construction of a test facility of high current SC cables was begun; the facility became available in the middle of 1978. Design of a cluster test facility was performed. The cluster test coil in the design was one half of the LCT coil; LCT, Large Coil Task, is an IEA agreement on coil tests in toroidal assembly at ORNL.

Reactor Design Study: The design of JAERI's experimental fusion reactor, JXFR, entered upon its phase II in this fiscal year in which the phase I design would be revised in order to obtain a more practical design. (S. Mori)

CONTENTS

目　　次

I. PLASMA THEORY AND COMPUTATION

1. Introduction

Theoretical and computational studies have been continued on tokamak confinement and heating in close connection with experimental projects.

On the basis of the experience obtained during the preceding years, we have started from this fiscal year the project TRITON, a fluid model numerical code system for tokamak equilibrium, stability, and transport. Two dimensional MHD stability codes, NOTUS and ZEPHYrus, advanced well. With the collaboration of Dr. R. Gruber of Lausanne who stayed at JAERI in March 1978, the ERATO code was implemented in the JAERI computer system.

Heat transport due to collisionless drift tearing mode turbulence was studied with quasilinear theory. Since the saturation of the mode is not expected within this approximation, we calculated the heat generation and cross-field heat transport by considering the early phase of the instability growth. A two-fluids code was applied to the propagation of lower hybrid waves. We observed the distortion of the ray in the presence of density fluctuations due for example to the drift instability. A new method was proposed to suppress the grid instability in the particle simulation.

2. MHD Stability

2.1 Numerical analysis of linear MHD stability of a toroidal plasma

Analysis of linear MHD stability is now carried out extensively by many authors to determine the critical beta values of high beta tokamaks[1]-[4]. We have been developing two kinds of computational codes for the MHD stability in the project TRITON. One is called NOTUS which is based on the variational principle and the other is called ZEPHYrus which is an initial-value code. NOTUS code can be used for both symmetric and asymmetric equalibria with respect to the median plane of the torus.

In this fiscal year we completed almost all components of both the codes except for several subroutines for the interface with numerical equilibria and vacuum contributions.

A stability code similar to NOTUS (ERATO[5]) was adapted to the JAERI computer system by the cooperation of R. Gruber who stayed in our laboratory for three weeks in March 1978. The results by using NOTUS agreed with ones by ERATO in the case of a plasma with a circular and elliptic cross-sections in straight geometry. The results by using ZEPHYrus showed good agreement with the one by ERATO for the Solov'ev equilibrium (Fig. I.2.1-1).

2.2 Numerical analysis of nonlinear MHD stability of a toroidal plasma[6]

For a tokamak plasma with high beta value and noncircular cross-section as JT-4, the problems of the nonlinear saturation of a ballooning mode and an axisymmetric (positional) mode become very interesting and important ones. In the project TRITON we are mapping out to develop a fully three-dimensional nonlinear stability code including a resistive effect. To study the nonlinear MHD behaviors of a plasma, calculations based on an initial-value problem are useful.

In this fiscal year, we studied the algorithm for the nonlinear stability calculations of an ideal axisymmetric toroidal plasma, and developed a prototype code of a three-dimensional one. We tested it in the region of a linear theory in the case of a fixed boundary. The results obtained by this code agreed well with the ones by the two-dimensional codes (NOTUS and ZEPHYrus).

2.3 High-m ballooning mode in a tokamak[7]

A reduced equation describing MHD oscillations with high mode number

was derived for an axisymmetric tokamak configuration. Assuming a simplified model equilibrium with circular cross-section[8], we have examined analytically high-m ballooning mode. It was shown that the stabilizing effect due to magnetic well deepening, when β becomes large, is the same order as the destabilizing ballooning effect[9].

References

(1) Todd,A.M.M., et al.: Phys. Rev. Letters 38 (1977) 826.
(2) Bateman,G., Peng,Y-K.M.: Phys. Rev. Letters 38 (1977) 829.
(3) Berger,D.: "Numerical computations of the ideal magnetohydrodynamic stability of small aspect ratio tokamaks", Thesis presentad to Ecole Polytechnique Federale de Lausanne.
(4) Tsunematsu,T., Takeda,T., and Kurita,G.: "Numerical analysis of magnetohydrodynamic stability of high beta tokamaks with noncircular cross-section", to appear in JAERI-M.
(5) Gruber,G.: to be published in Computer Physics Communications.
(6) Kurita,G., et al.: private communication.
(7) Tuda,T.: in preparation.
(8) Shafranov,V.D. and Yurchenko,E.I.: Soviet Physics JETP 26 (1968) 682.
(9) Furth,H.P., et al.: "Plasma Physics and Controlled Nuclear Fusion Research" (IAEA, Vienna, 1966) vol.1, p.103.

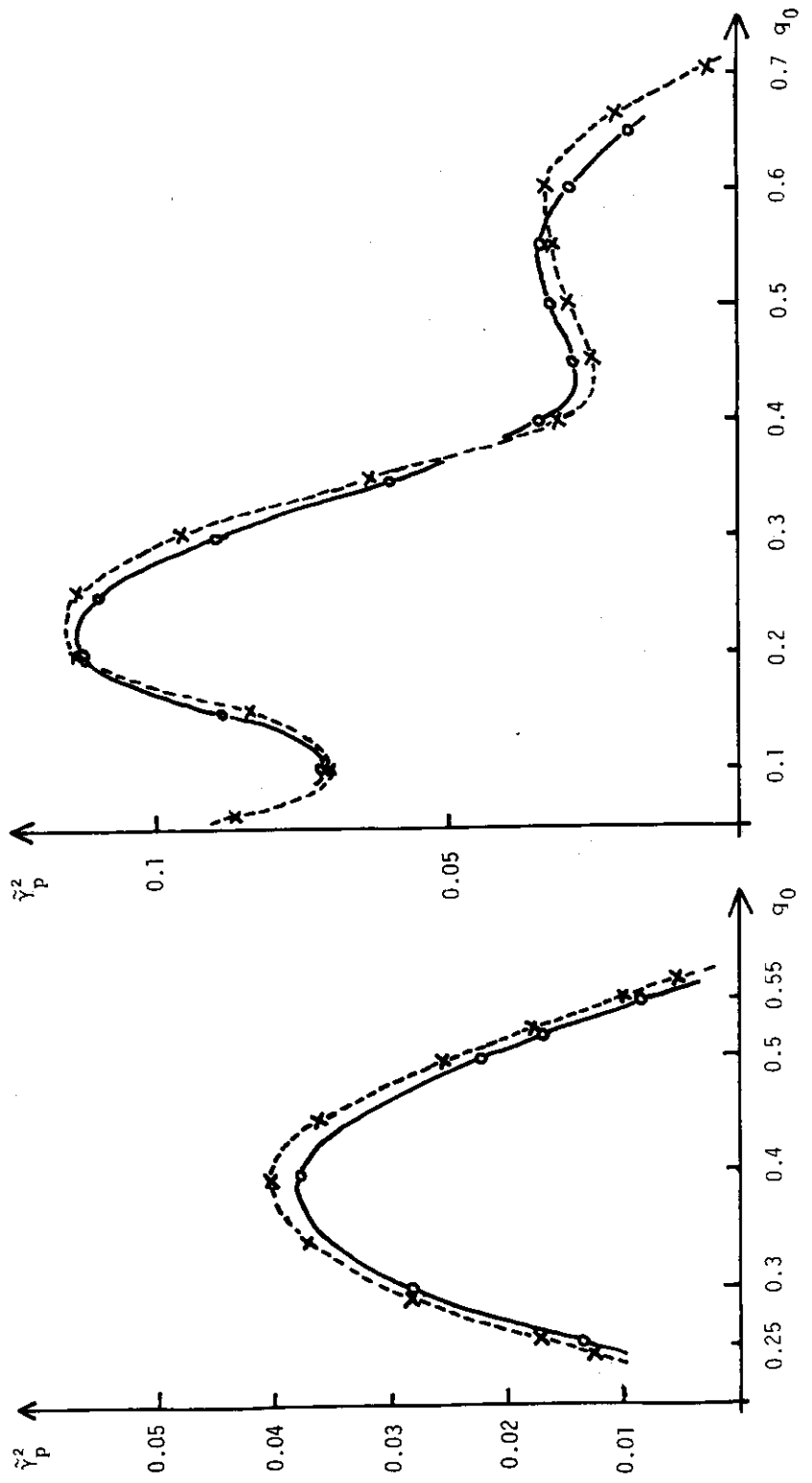

Fig.I.2.1-1 Normalized growth rates versus safety factor at magnetic axis. Solid curves are our results and dotted curves are obtained by ERATO code developed by Lausanne group for the cases, aspect ratio; R_0=3., ellipticity; E=1. and toroidal wave number (a) n=2 and (b) n=3 respectively.

3. Heating and transport

3.1 Numerical simulation of lower hybrid wave propagation[1]

Concerning the LHRH (Lower Hybrid Resonance Heating) in a tokamak, a numerical simulation is made of the propagation of a lower hybrid wave. By solving the system of two-fluid equations and Poisson's equation, ray trajectories of the lower hybrid waves are traced. The cases of cold plasma approximation, linear approximation and nonlinear two-fluid model are examined. The effect of density fluctuation due to the presence of a drift wave on the conical ray trajectories is also studied.

3.2 Effect of finite wavelength of the pump on the parametric threshold of lower hybrid wave[2]

The effect of the finite wavelength of the pumping wave on the threshold of the parametric instability of lower hybrid wave is studied theoretically. A general dispersion relation is derived for the coupling of four electrostatic waves, assuming that the pump is a lower hybrid wave. The analysis of the dispersion relation shows that the finiteness of the pump wavelength has an insignificant effect on the parametric threshold to excite another lower hybrid wave and a low frequency mode, whereas it plays an important role to excite high frequency modes.

3.3 Heat transport due to collisionless drift-tearing mode turbulence[3]

Heat generation and its transport due to collisionless drift-tearing mode turbulence are analyzed in the case of slab geometry. Turbulent state is assumed within a singular layer. A diffusion equation of the distribution function in the velocity space is deduced from the quasi-linear Vlasov equation and a time-dependent equilibrium distribution function of electrons is obtained. The distribution function becomes a kind of flat-top type instead of the Maxwellian one. A rate of the heat generation is greater than that of the wave-energy generation by about $\Sigma k_0^2/k^2$, where k_0 is inverse of the electron skin depth. Gradients of the temperature and of the number density modify the rate spatially. The temperature gradient is found to relax itself. Since perturbed magnetic field lines are bent in the direction of inhomogeneity, the generated heat is guided along the field lines in the direction of inhomogeneity. Convection and diffusion are considered

and both are shown to be equally important. These two mechanisms are caused by the gradient of number density as well as the temperature gradient. The obtained heat transport coefficient is larger than the one in MHD regime. For example PLT parameters are considered, the coefficient becomes about 20 times larger than that in MHD regime.

References

(1) Okamoto, M.: JAERI-M 7313 (1977).

(2) Okamoto, M.: J. Phys. Soc. Japan 43 (1977) 1105.

(3) Yamanaka, K.: JAERI-M 7314 (1977).

4. Numerical Analysis and Computing

4.1 Two-dimensional tokamak transport codes[1]

Two-dimensional tokamak transport codes (APOLLO-series codes in the TRITON system) are being developed. Neoclassical transport coefficients and a simplified source term of particles are incorporated in the first version APOLLO code. The basic idea of the numerical model is based on the Grad-Hogan theory, where the radial transport phenomena are calculated for a sequence of separately calculated toroidal equilibria. In the near future we will incorporate different types of transport in the APOLLO code, refine the source term of particles, and apply the code to the analyses of tokamak plasma with higher beta value.

4.2 A binary collision model for plasma simulation with a particle code[2]

A binary collision model by the Monte Carlo method is proposed for plasma simulations with particle codes. The model describes a collision integral of the Landau form. Collisional effects in spatially uniform plasmas are simulated, and the results are in good agreement with theoretical ones.

4.3 Suppression of grid instability in particle simulation[3]

Unphysical instabilities of the type of total energy being increased are often excited in particle simulation by the use of the spatial grid whose size Δ exceeds the Debye length λ_D[4],[5]. In a widely used method, NGP, CIC, or DP method, the profile of the electric field created by a charged cloud is assumed to vary artificially in accordance with the cloud position relative to the grid point. This variation brings grid instabilities.

We devise a method to reduce this variation and to suppress the grid instability. The charge density of a cloud is shared at three points in the one-dimensional simulation; at the nearest grid point (distance δ from the center-of-charge of the cloud) by $\varepsilon \equiv [0.5-(\delta/\Delta)^2]^{1/2}$, at a grid point (distance $\Delta-\delta$) by $[1-\varepsilon+(\delta/\Delta)]/2$, and at a grid point (distance $\Delta+\delta$) by $[1-\varepsilon-(\delta/\Delta)]/2$. Combination of this method with the interlaced-grid method[6] brings a remarkable reduction of undesirable variations.

Comparison of the results of simulation (errors in the total energy $\delta H/H_0$) are shown in Fig. I.4.3-1, where $\Delta = 64\lambda_D$. In the figure (I) CIC

method, (II) interlaced method, (III) the present method, and (IV) combination of (III) with (IV).

4.4 Large-scale matrix-handling subroutines "ATLAS"[7]

Subroutine package "ATLAS" has been developed for handling large-scale matrices. The package is composed of four kinds of subroutines, i.e., basic arithmetic routines, routines for solving linear simultaneous equations and for solving general eigenvalue problems and utility routines. The subroutines are useful in large-scale plasma-fluid simulations.

4.5 OLYMPUS system and development of its pre-processor[8]

The OLYMPUS SYSTEM developed by K. V. Roberts et al. was converted and introduced in computer system FACOM 230/75 of the JAERI Computing Center. A pre-processor was also developed for the OLYMPUS SYSTEM. The OLYMPUS SYSTEM is very useful for development, standardization and exchange of programs in thermo-nuclear fusion research and plasma physics. The pre-processor developed by the present authors is not only essential for the JAERI OLYMPUS SYSTEM, but also useful in manipulation, creation and correction of program files.

4.6 Special I/O routine based on the BSAM level[9]

A Special I/O routine "FORTXDAM" has been developed, which is based on the BSAM Level. Program "FORTXDAM" is useful in input-output of large quantities of data, random access (direct access), usage of the double (or multi) buffers technique or asynchronous input-output. Written in FASP language available for the computer system FACOM 230/75 of JAERI, it consists of six basic sub-programs which can be called in FORTRAN language. FORTXDAM is useful especially in large-scale computer simulations in thermo-nuclear fusion and plasma physics research.

4.7 A method to solve the impurity diffusion equation with ionization and recombination source terms[10]

Diffusion equations of impurities with ionization and recombination source terms are solved numerically by the splitting and fractional-step method for noncommutative operators. Diffusion equations without source terms and rate equations are solved successively and the very small time

step for calculation determined by fast ionization processes can be avoided by solving the rate equation as an eigenvalue problem. The time step is determined by the diffusion process and it is possible to follow the time evolution of impurities for a long time. The present method is second-order accurate in Δt.

References

(1) Takeda, T., et al.: private communication.
(2) Takizuka, T. and Abe H.: J. Comp. Phys. 25 (1977) 205.
(3) Takizuka T.: in preparation.
(4) Langdon, A.B.: J. Comp. Phys. 6 (1970) 247.
(5) Okuda, H.: ibid. 10 (1972) 475.
(6) Chen, L., et al.: ibid. 14 (1974) 200.
(7) Tsunematsu, T., et al.: JAERI-M 7573 (1978).
(8) Okamoto, M., et al.: JAERI-M 7228 (1977).
(9) Okamoto, M., et al.: JAERI-M 7337 (1977).
(10) Okamoto, M., et al.: J. Comp. Phys. 26 (1978) 80.

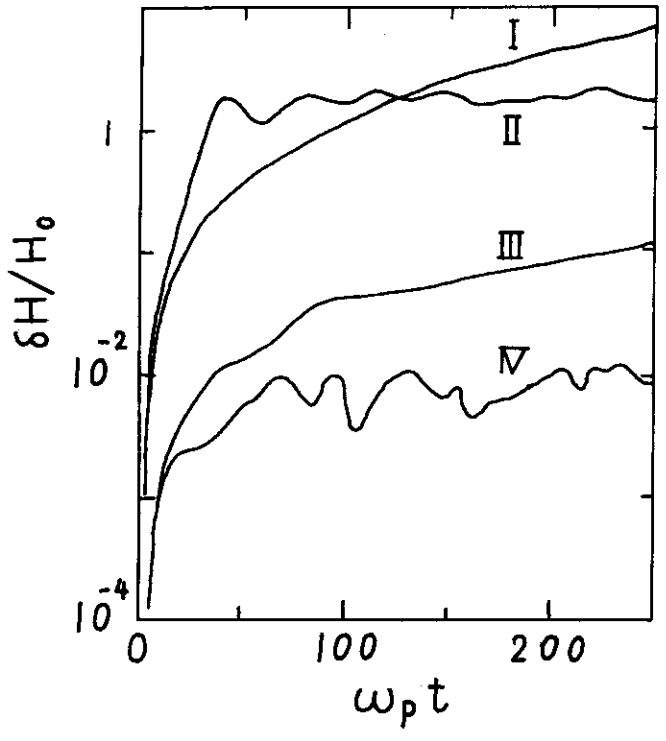

Fig.I.4.3-1 Errors in total energy due to grid instabilities.

5. Project TRITON[1]

"Project TRITON" was mapped out and a part of the project was started in this fiscal year. The project is composed of developments of the fluid-model numerical code system TRITON and supporting system for the development of the numerical codes PEGASUS (Fig. I.5-1). The TRITON system is an inclusive fluid-model numerical code system for the analyses of a tokamak plasma and the main part of the TRITON system is a subsystem ASTRAEA which consists of numerical codes for MHD stability analyses, multi-dimensional transport calculation, and MHD equilibrium calculations (Fig. I.5-2). TRITON system also contains subsystems PARIS (a subroutine package for large-scale numerical analyses) and ARGUS (an assembly of graphic I/O subroutines). The PEGASUS system is composed of assembly of supporting numerical codes, such as, automatic code generators written in a formula manipulation language "REDUCE-2", preprocessors for large-scale matrix handling and so on.

Time schedule of development of the codes in the ASTRAEA subsystem is shown in Fig. I.5-3. Development of individual codes in this fiscal year is described in other subsections.

References

(1) Takeda, T., et al.: unpublished (1977).

PROJECT TRITON

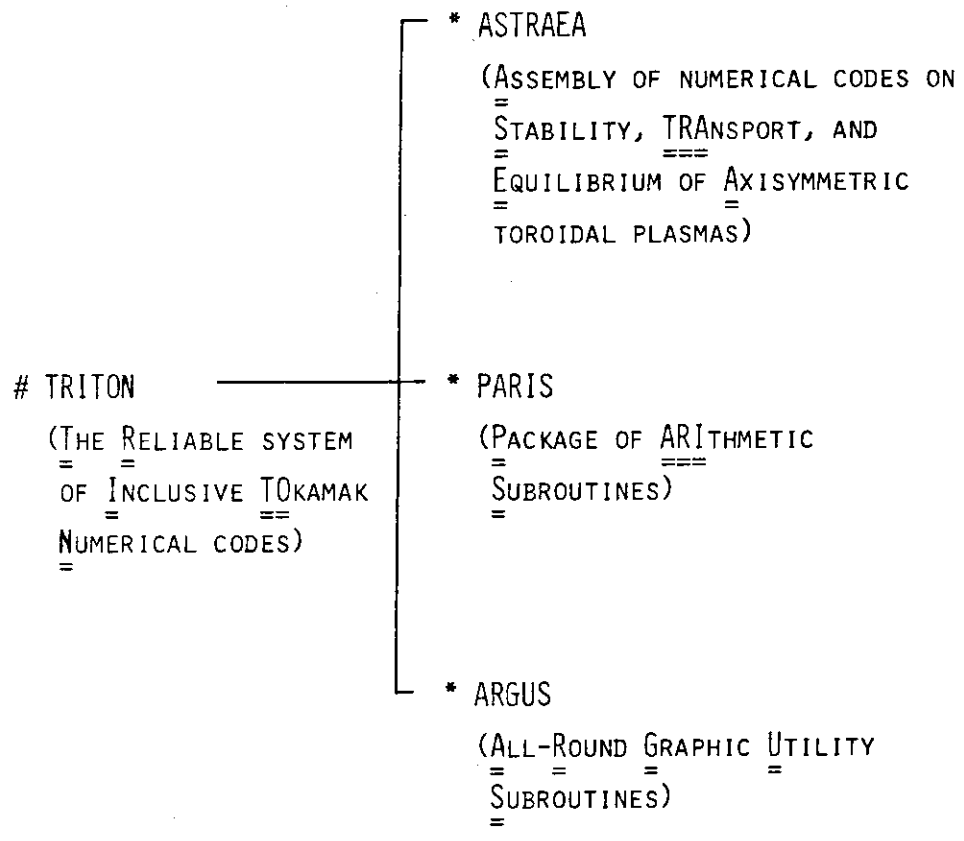

PEGASUS
(PROGRAMMING LANGUAGES FOR FORMULA EXPANSION AND CODE GENERATION: A SUPPORTING SYSTEM)

Fig.I.5-1 Project TRITON

ZEPHYRUS	: 2D ideal MHD instability (initial value problem).
NOTUS	: 2D ideal MHD instability (variational principle).
EURUS	: Group of codes to investigate numerical scheme.
BOREAS	: High-m ballooning mode (variational principle).
AEOLUS	: 3D nonlinear (dissipative) MHD instability (initial value problem).
SELENE	: High speed, high accuracy calculation codes of MHD equilibrium.
APOLLO	: 2D tokamak transport code.

Fig.I.5-2 Numerical codes in the ASTRAEA subsystem

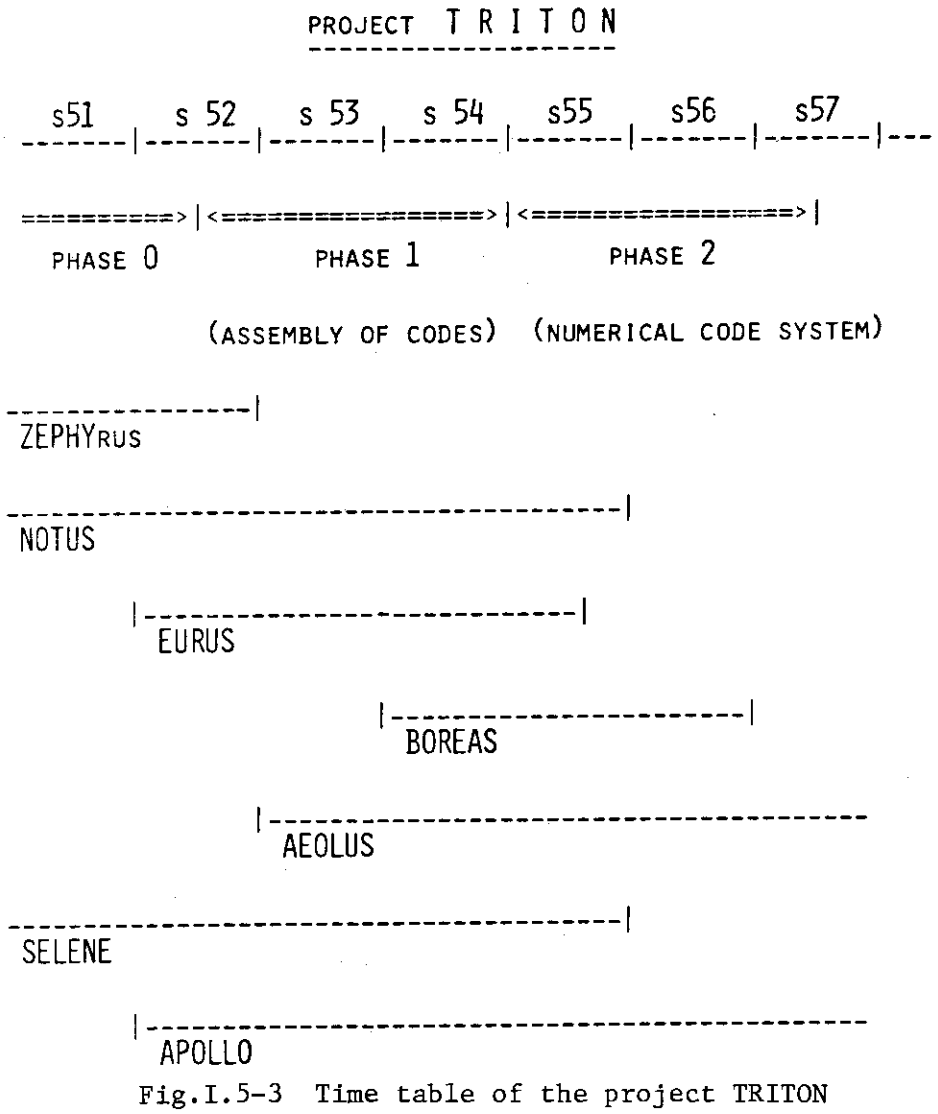

Fig.I.5-3 Time table of the project TRITON

II. TOROIDAL CONFINEMENT EXPERIMENTS

1. JFT-2

1.1 Introduction

JFT-2 is a low aspect ratio confinement device of the tokamak type with plasma major radius 90 cm and minor radius 25 cm, a magnetic field of 18 kG, a plasma current of 0.16 MA corresponding to a surface q of 4. The main experiment is supplemental heating (neutral injection, LHRH).

The neutral beam heating experiment started from September 1976 has been completed in April 1977. In June and July, preliminary plasma-wall interaction experiments have been carried out; reduction of impurities by titanium gettering, high density discharges, particle and energy fluxes at scrape-off layers, limiters of different materials, and so on. The lower hybrid heating experiment has started in October 1977.

1.2 Plasma-surface interaction experiments

1.2.1 Improvement of plasma parameters by titanium gettering[1]

In order to suppress the impurity (mainly oxygen) influx, the wall and the limiter were gettered by titanium. A pronounced decrease was observed in line intensities of oxygen (1/5-1/10) as well as metals (i.e. Fe and Mo, ∿1/10). The radiation loss power, which cools the plasma periphery decreased to 1/2, which resulted in (1) a broader electron temperature profile. This improved the energy confinement time by a factor of about 1.6. (2) A higher electron density (line-of-sight averaged density of 6.3×10^{13} cm^{-3}) was obrained (B_t: 1.8 T, I_p: 110 kA, limiter radius: 20 cm). The factor k of the maximum density scaling law; $n_e = kB_t(T)/R(m)$ is improved from 2 (without gettering) to 3.1 (with gettering).

Density limitation is usually preceded by the abrupt increase in the amplitude of m = 2 oscillations which seems to cause the rapid rise of the radiation loss, which triggers the MHD disruption. By increasing n_e, the net input power ((Joule heating power) - (radiation and charge exchange loss power)) decreases to some threshold which seems to limit the density maximum.

1.2.2 Particle and energy fluxes observed in the scrape-off layer[2]

Particle and energy fluxes in the scrape-off layer produced by poloidal limiters were observed by a combined Langmuir thermoprobe and by an infrared

camera. It was found that the electron density in the scrape-off layer decays exponentially with leaving plasma column in the minor radius direction. The cross-field diffusion coefficient determined by the e-folding length is of the order of Bohm diffusion.

The energy flux in the scrape-off layer can be devided into two categories. The one is determined by a sheath of Maxwellian particles formed in front of a material surface. The heat flux of this kind was observed 1 cm behind the limiter edge radius. The other, which was observed near the limiter edge radius, depends strongly on accelerated electrons. It therefore depends on the electron density of the main plasma.

1.2.3 Gross particle confinement characteristics determined by the scrape-off plasma[3]

The scrape-off plasma in JFT-2 tokamak are investigated experimentally by using an electrostatic probe, The density of the scrape-off plasma is about $2.2 \times 10^{12} - 1.0 \times 10^{13}$ cm^{-3} and decays like an exponential in radial direction. The electron temperature is about 30 eV and keeps almost constant value in the scrape-off layer.

With use of a simple scrape-off model of tokamak plasma to be representable by a finite straight coaxial cylinder, we can show that the density decays in exponential like and also can give the cross field diffusion coefficient by the gradient of the density profile. The e-folding length of the density profile can be expressed

$$\lambda = D^{1/2}\left(2\frac{v_s}{L} - n_n\langle\sigma v\rangle\right)^{-1/2},$$

where D is the cross field diffusion coefficient, v_s the ion sound velocity, L an effective interval of the straight cylinder (which becomes $2\pi R \cdot q_a$ in the rail limiter region, where q_a is an order of the safety factor and $2\pi R$ in the aperture limiter region), n_n the number of the neutral gas in the scrape-off layer and $\langle\sigma v\rangle$ the rate coefficient for electron ionization.

The parallel flux absorbed by the limiters is accelerated by the sheath potential, which is expressed

$$\Gamma_{//} = n\, v_s \ .$$

The perpendicular flux absorbed by the wall is expressed

$$\Gamma_{\perp} = -D \nabla n \ .$$

By integrating the particle flux over the surface of the limiters and the wall, which contact with the plasma, the total loss flux to the limiters and to the wall can be estimated.

The gross particle confinement time is also determined deviding the total particle number of the main and scrape-off plasma by the total loss flux.

1.2.4 On the origin of gaseous impurities measured by mass spectroscopy[4]

The origin of neutral gas species outside a plasma in the JFT-2 tokamak was investigated and its correlation to light impurities in a plasma was studied. The source of the gas species can be identified by titanium gettering which will reduce the contribution of the wall and/or the limiters.

The principal gases measured by a quadrupole mass spectrometer during and after a discharge are water, carbon monoxide, and methane, whose partial pressure rises are of the order of 10^{-7} Torr. The wall supplies oxygen impurity to the plasma in the form of water vapour. The measurements of a boundary plasma [ref. 3] and titanium coating indicate that the limiter mainly contributes to the production of carbon monozide and methane. There is no relationship of light impurities to methane and carbon monoxide. As for carbon and silicon carbide limiters [ref. 6], the formation of methane after a discharge results from the chemical reaction of implanted hydrogen atoms with the hot limiter [ref. 2].

1.2.5 Thermal load of a limiter[5]

Surface temperature of a limiter in the JFT-2 plasma was measured by an infra-red scanning camera with a time resolution of 0.625 msec. The heat flux to the limiter was estimated on the basis of one-dimensional heat conduction to the bulk. The maximum surface temperature rise and heat flux density during a discharge with a electron density of 1.3×10^{13} cm^{-3} are about 300 degrees and 2.3 kW/cm^2, respectively. They decrease by increasing electron density.

The correlation between the time behaviours of the heat flux density and the X-ray intensity emitted from the limiter indicates that the accelerated electrons play an important role in the heat flux to the limiter periphery.

Temperature of the limiter during a discharge is considerably lower than the temperature at which the evaporation of Mo becomes serious. Time behaviour of the spectrograph of Mo(XIII) line has no relation to the temperature rise of the limiter even in a low electron density. Evaporation due to heat load from the plasma is not a mechanism of metal impurity production in normal discharge.

Immediately before the negative voltage spike, the heat flux to the limiter increases abruptly. The surface temperature rise of the limiter near the plasma edge is about 140 degrees at that time. The heat flux density is about ten times as large as the one before the abrupt increase. Thermal energy to the limiter due to the accelerated electrons from the plasma is order of 5 % of plasma energy. The surface temperature decrease of the limiter is found in phase of the negative voltage spike.

1.2.6 Carbon and silicon carbide limiter experiment[6]

Pyrolitic graphite (PG) and silicon carbide were used for the limiter. The discharge characteristics with these limiters were the same as those with the molybdenum limiter except that the CV line radiance was 1.3 to 6 times larger with the PG and SiC limiters than with the Mo limiter. This is because the main impurity in the plasma was oxygen with all the limiters. For these conditions, the maximum surface temperature of the limiter during the discharge was 1900°C for PG and 1000°C for SiC, as observed by an infrared camera.

Residual gas analysis during and after the discharge showed that chemical reaction between the plasma and the limiters is not responsible for generation of the limiter materials to the plasma. It is supposed that physical sputtering by ions plays a major role in impurity generation from the limiters.

1.3 Ion heating experiments near lower hybrid frequency[7]

Lower hybrid heating experiment on the JFT-2 tokamak was started from October 1977. Net RF transmitted power at power level up to 135 kW had been applied for 20 msec at 650 MHz. The power was coupled by means of a phased array of four waveguides. Characteristics of lower hybrid heating in the JFT-2 are summarized in Table II.1.3-I.

To investigate the efficiency of coupling and penetration of slow waves into a plasma, the dependence of the total power reflection coefficient R as

a function of the phase difference $\Delta\phi$ between adjacent waveguides were measured at a power level P_{RF} = 3 kW in Fig. II.1.3-1(a), where $P_{RF} = P_{in} - P_{ref}$; the incident power P_{in} and the reflected power P_{ref}. Experimental points on the total reflection coefficient from a quadruple waveguide array are well fitted to the theoretical curve calculated from the Brambilla theory which uses the plausible density gradient from the density measurement of the scrape-off layer plasma $\nabla n_e = 3 \times 10^{13}$ cm^{-4}. In this case the net transmitted power P_{RF} is set at constant power level. Optimum coupling is obtained experimentally and theoretically for the quadruple array with 90 degrees phase shift between adjacent waveguides. Some data for the power reflection coefficient versus phase difference $\Delta\phi$ between adjacent waveguide of the quadruple array as a function of the net transmitted power are given in Fig. II.1.3-1(b). Reflection coefficient is greatly reduced with increasing the input power. Apparently, coupling feature becomes rather insensitive to phase difference $\Delta\phi$, although it has still an expected tendency. Coupling improves as the net transmitted power increases and is saturated over 40-50 kW power level. It is noted here that at the saturated region good coupling efficiency around 90% was obtained.

When a RF power of 135 kW has been applied for 20 msec, 650 MHz, the loop voltage shows a negligible increase by 2-3 %, the plasma current does not vary, the perpendicular ion temperature increases from 270 eV to 420 eV, the application of RF also results in an increase in the average electron density by 20 %, as shown in Fig. II.1.3-2, a high energy tail appears on the energy spectra of the charge-exchange neutrals, and the radiation of impurity lines and soft X-ray emission are not observed to change during RF.

Figure II.1.3-3 shows the body temperature increase ΔT_i during 10-15 msec where two pumping frequencies 650 MHz (closed circles) and 750 MHz (open circles) were used when $\omega_0/\omega_{LH}(0) < 1.3$ ($\omega_{LH}(0)$ correspond to the lower hybrid frequency at the center). The temperature rise is seen to increase with increasing RF power normalized by the average density. Also shown in the figure (the only cross point) is the ion temperature obtained from Doppler broadening of impurity lines (in the case presented here, O VII line at 1623 Å). The temperature given by this measurement is lower than that given by charge exchange and the radial maximum of O VII emission is found to be around r = 6-8 cm from the center by scanning vertically the monochromator looking at the horizontal chord of plasma.

Several conclusions may be stated from the observations before now.

(1) A phased array of four waveguides has been used with success. Coupling characteristic is well explained by Brambilla theory. Transmission efficiency of 90 % was easily obtained without any use of matching device.
(2) Parametric instability is observed during the RF pulse, which is correlated with generation of high energy ions and is not responsible for the bulk ion heating. This parametric process occurred in the vicinity of the plasma edge in front of the launcher and has a low saturation level, so that this parametric instability may not disturb the penetration of the pump wave into the interior rather at high power level.
(3) Effective ion heating $\Delta T_i / T_i$ = 50-60 % has been obtained on the application of 135 kW power and the temperature increase is seen to be proportional to the input RF power.
(4) Efficient ion heating has been observed when the turning point is in the plasma.
(5) An average electron density increase by $\Delta\bar{n}_e/\bar{n}_e$ = 20 % at the rate of $\Delta\bar{n}_e/\Delta t_{RF} = 1.1 \times 10^{14}$ cm^{-3} sec^{-1} was observed and loop voltage increases by less than 2-3 % at the power level of net transmitted power 135 kW, 20 msec. However, this smaller density increase cannot explain the observed heating. A quantitative measurements are needed to evaluate heating of the ions due to an influx of impurities.

References

(1) Konoshima,S., Fujisawa,N., Maeno,M., Suzuki,N., et al.: to be published in J. Nuclear Mater.
(2) Gomay,Y., Fujisawa,N., Maeno,M., Suzuki,N., et al.: to be published in J. Nucl. Fusion.
(3) Uehara,K., Gomay,Y., Yamamoto,T., Suzuki,N., et al.: to be published in Plasma Physics.
(4) Hirayama,T., Fujisawa,H., Gomay,Y., Maeno,M., et al.: to be published in J. Nuclear Mater.
(5) Maeno,M., Kawamura,K., Gomay,Y., Fujisawa,N., et al.: to be submitted to Jap. J. Appl. Phys.
(6) Gomay,Y., Konoshima,S., Fujisawa,N., Kasai,S., et al.: to be submitted to J. Nucl. Mater.
(7) Nagashima,T., and Fujisawa,N.: to be presented at Joint Varenna--Grenoble International Symposium on Heating in Toroidal plasma (1978).

Table II.1.3-1 Lower hybrid heating in the JFT-2 tokamak at JAERI.

JFT-2 MACHINE PARAMETERS	
Major radius	90 cm
Minor radius	25 cm
Minor wall radius	29 cm
Toroidal magnetic field	10-18 kG
PLASMA PARAMETERS	
Plasma	Hydrogen plasma
Plasma current	100 kA
Ohmic heating power	160-250 kw
Peak electron density	$(1\text{-}4.5) \times 10^{13}\ \mathrm{cm}^{-3}$
Peak electron temperature	600-1000 eV
Peak ion temperature	180-320 eV
Effective ionic charge	2-6
RF HEATING SYSTEM	
RF frequency	650 and 750 MHz
Maximum RF power	200 kw
RF pulse duration	1-100 msec
Coupling system	a phased array of four waveguides
Parallel refractive index	13 (maximum)
Launcher-limiter separation	1.5-3.0 cm

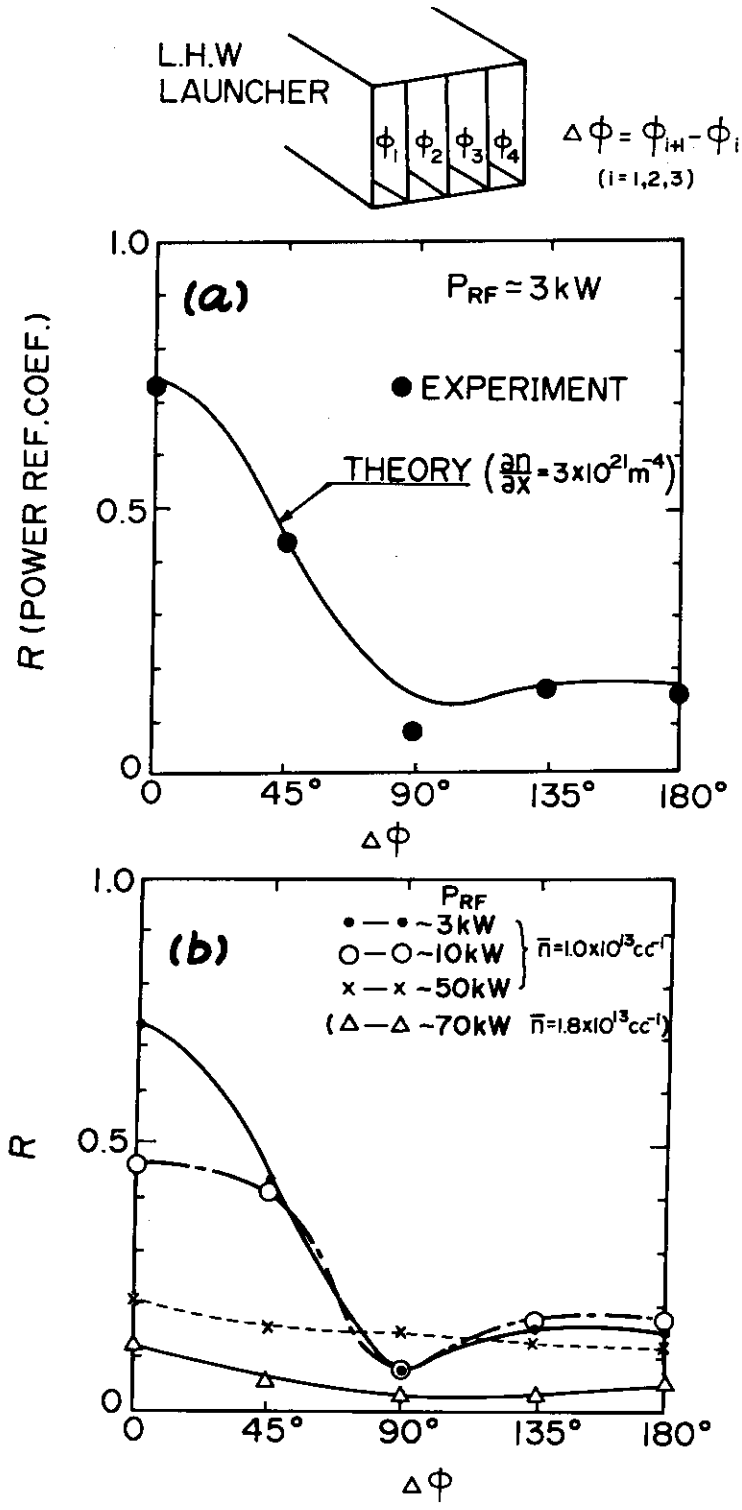

Fig.II.1.3-1 Dependence of the reflection coefficient on the phase angle between adjacent waveguides (a) a comparison between the theory and the experiment: $\nabla n=3\times10^{13}$ cm^{-4}, (b) as a function of the transmitted power.

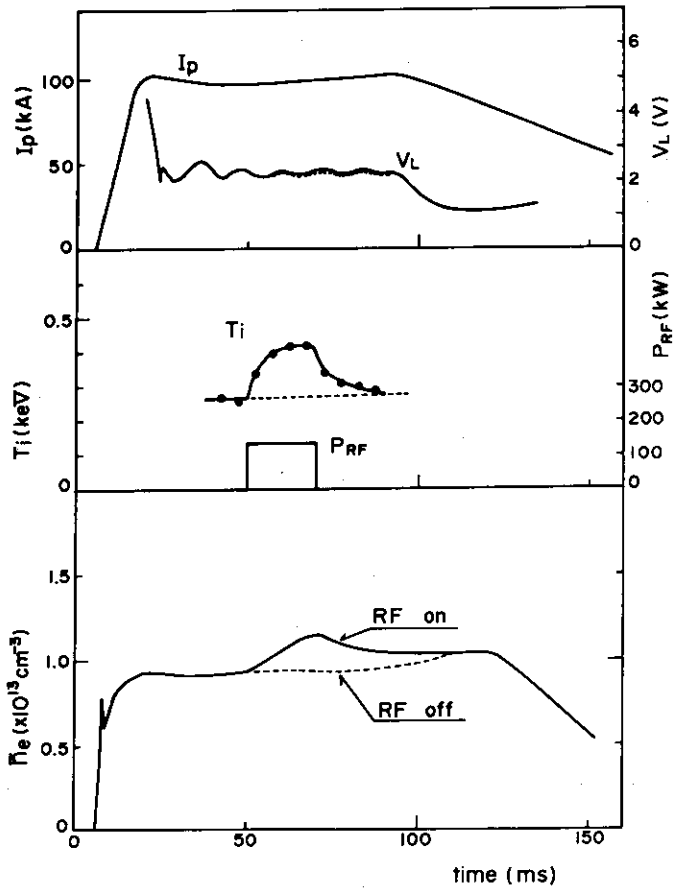

Fig.II.1.3-2 Time evolution of the plasma current, loop voltage perpendicular ion temperature determined from charge-exchanged neutrals, transmitted power at 650 MHz and the average density with (solid curve) and without (dotted curve) the RF.

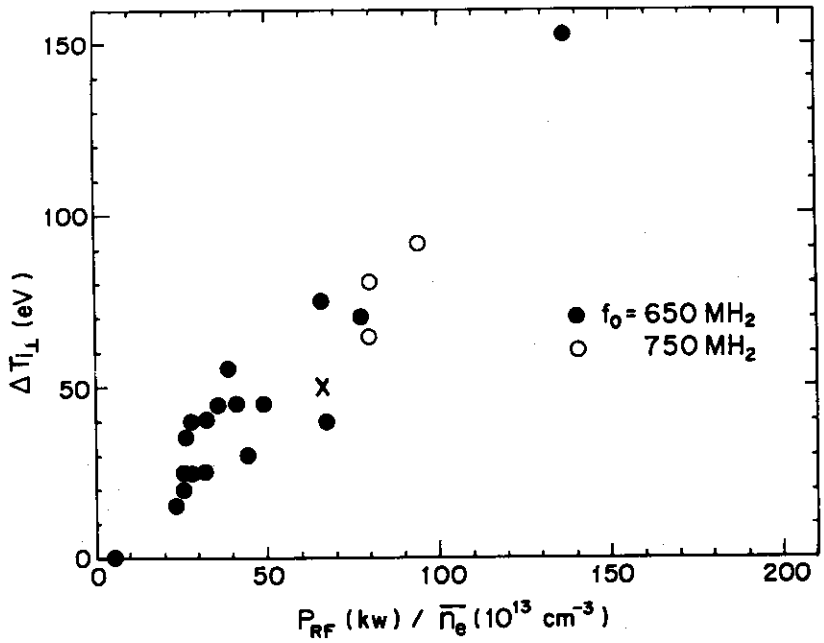

Fig.II.1.3-3 Incremental perpendicular temperature rise at 650 MHz and 750 MHz. The abcissa is transmitted RF power divided by the average density (in units of 10^{13} cm^{-3}).

2. JFT-2a (DIVA)

2.1 Introduction

The toroidal magnetic field was increased to 2T from 1T in April 1978 and divertor experiments had been completed. 100 kW ICRF heating experiment was prepared and will start in May 1978.

After increasing the toroidal magnetic field, a wide range of plasma parameters has been obtained as follows: electron temperature T_{e0} = 200 - 700 eV, ion temperature T_{e0} = 60 - 300 eV and density n_{e0} = (1.5-8.0) $\times 10^{13}$ cm^{-3} in the main plasma, and T_{es} = 20 - 100 eV, T_{is} = 20 - 60 eV and n_{es} = (1.5-5.0) $\times 10^{12}$ cm^{-3} in the scrape-off layer plasma. Over the wide range plasma parameters following subjects are studied[1]~[14]. Some of them extend the results of earlier effort in this device with 1T[15]~[23].

a) Divertor effects on the main plasma.
   - radiation loss
   - energy confinement time
   - particle confinement time
   - transport coefficient

b) Divertor actions
   - plasma diversion and reduction of plasma wall interactions
   - impurity shielding

c) Impurity behavior
   - impurity transport and recycling
   - impurity back flow from the divertor

d) Scrape-off layer
   - scaling for a scrape-off plasma
   - control of a scrape-off plasma

e) Metallic impurity origin and wall erosion.

The main results are summarized as follows.

a) The divertor reduces the radiation loss by a factor of 2-4 and hence increases the energy-confinement time by a factor of 2.5. The divertor does not significantly affect particle and heat transport coefficients.

b) The divertor reduces plasma-wall interactions near the main plasma by guiding loss plasma into the divertor chamber. A maximum divertor

efficiency is 35% for particle flux and 75% for heat flux. The shielding efficiency is 70% for alminum and 50% for carbon.

c) Both gaseous and metallic impurities have a confinement time comparable to the particle confinement time. Therefore, impurities flow always into the main plasma during a discharge. It is shown that carbon impurities recycle, and aluminum elements lose onto the wall and new elements are produced on the wall. Impurities are easily ionized and accelerated by the field particles and the space potential in the scrape-off layer plasma. Therefore impurities produced in the divertor flow hardly into the main chamber, i.e. the back flow is small.

d) In a scrape-off layer plasma, particle flow velocity is a few times less than the sound velocity, heat transmission rate is consistent with a sheath model, the particle diffusion coefficient is about 10 times less than the Bohm diffusion value. These results give simple formula of scalings for electron temperature, density and width in a scrape-off layer plasma. The relation between ion temperatures in the scrape-off layer and in the main plasma is also obtained. Control of a scrape-off layer plasma is investigated by using gas injection.

e) Ion sputtering, arcing and evaporation are identified. Evaporation is important in a low density discharge, and arcing in a disruptive discharge and in a discharge with dirty surfaces. The ion sputtering is demonstrated to be dominant in a normal discharge for metallic impurity origin.

These results are detailed described in the following subsections. Impurity control in a large fusion device is also discussed.

2.2 Improvement of plasma parameters by the divertor[2][3][9][10][11][13]

In order to know the divertor effects on plasma-confinement, radiation loss P_R, energy-confinement time τ_E, average particle-confinement time $\bar{\tau}_p$ and ion temperature T_i with and without the divertor are investigated over a wide range of plasma parameters, i.e. toroidal magnetic field B_T = 0.8 - 2.0 T, I_p = 10 - 53 kA, safety factor q_a = 2.6 - 5.9 and mean electron density $\bar{n}_e = (1.5 - 5.0) \times 10^{13}$ cm^{-3}. Results are summarized in Fig. II.2.2-1. A relation between radiation loss-power P_R and plasma current I_p is shown in Fig. II.2.2-1(a). Sum of radiation loss and

charge-exchange loss is measured by scanning a calibrated pyroelectric detector and charge-exchange loss is calculated by a three dimensional Monte Carlo method. Charge-exchange loss is less than 13 kW and the radiation loss P_R shown in Fig. II.2.2-1(a) is the main part of loss power measured by the pyroelectric detector. It is shown that the radiation loss is reduced by a factor of 2 - 4 by the divertor. The radiation loss increases monotonically as increasing the plasma current I_p without the divertor but saturates at I_p = 26 kA with the divertor. It is clearly shown in Fig. II.2.2-1(b) that the divertor increases the energy-confinement time by a factor of 2.5 which has the functional dependence of the ALCATOR scaling as follows: $\tau_E = 1.5 \sqrt{q_a}\, \bar{n}_{14}$ ms without the divertor and $\tau_E = 4.0 \sqrt{q_a}\, \bar{n}_{14}$ ms with the divertor where $\bar{n}_{14} = 10^{-14} \bar{n}_e$. The average particle-confinement time shown in Fig. II.2.2-1(c) is calculated from the total particle loss-flux measured as the total ion saturation current onto the shell, protection plates and burial chamber. The result is contrast to that of the energy-confinement time i.e. a large improvement by the divertor is not observed on this average particle-confinement time. The average particle-replacement time is roughly given by the ALCATOR scaling for the energy-replacement time, i.e. $\bar{\tau}_p = 2.0 \sqrt{q_a}\, \bar{n}_{14}$ ms without the divertor and $\bar{\tau}_p = 3.0 \sqrt{q_a}\, \bar{n}_{14}$ ms with the divertor. The ion temperature shown in Fig. II.2.2-1(d) agrees with the Artsimovich scaling law with and without the divertor as expected.

The results show that the divertor reduces the radiation loss. This is the same effect observed in the previous experiment[15][16] in which a low-z free plasma was obtained[21] and the radiation loss was mainly due to pseudo continuum[18][20]. The pseudo continuum is considered due to gold because it increases as inserting a gold plate into the plasma and has a good correlation with AuI- and AuII-lines. The recent experiment up to now is done during the first few months after completing the modifications which forced to open the vacuum vessel to the atmosphere for a few months and low-z impurities may not be neglected. In order to study impurities, radiations are spectroscopically investigated in both discharges with and without the divertor under the conditions in which plasma density n_e, plasma current I_p and toroidal magnetic field B_T are appreciably the same. Peak electron temperature and ion temperature are 700 eV and 270 eV with the divertor and 540 eV and 240 eV without the divertor, respectively. Figure II.2.2-2 shows radial profiles of intensities of

pseudo continuum at 100 Å and oxygen lines and loss power P_{py} measured by the pyroelectric detector. Influx of oxygen is reduced by a factor of about 3 because intensity of OV-line decreases by a factor of 3 with the divertor. It is suggested that oxygen content is also reduced by the divertor because oxygen influx is decreased and confinement time of oxygen is roughly equal to the particle confinement time which is not strongly affected by the divertor. The pseudo continuum was observed only in the range of 120 Å - 250 Å in the previous experiment with a low temperature plasma and is observed in the range of 45 Å - 250 Å in these experiments. The divertor reduces gold content at least by a factor of three because radiation loss due to gold decreases by a factor 3 and increases monotonically as increasing electron temperature from 200 eV to 1000 eV from calculated results[24]. The profile of P_{py} suggests that both of oxygen and gold are influential to the radiation loss as expected.

The divertor increases the energy-confinement time by a factor of 2.5 which seems a result of lowering the radiation loss. The radiation-loss power is not a large portion of the total energy loss, i.e. 30 - 40 % of the ohmic power without the divertor and 15 - 30 % with the divertor. Electron temperature profiles, however, are strongly affected by the radiation loss, i.e. by the divertor, as shown in Fig. II.2.2-3. The divertor increases the radius of the hot column by reducing the radiation loss and increases the energy-confinement time because internal energy of a plasma is concentrated in the hot column. Calculated heat-diffusion coefficient from the experimental data is about 4×10^3 cm^2/s without the divertor and about 3×10^3 cm^2/s with the divertor. This small difference in the heat-diffusion coefficient is consistent with the conclusion, i.e. the divertor increases the energy-confinement time by increasing the effective radius, and is also consistent with the small divertor effect on the average particle-confinement because the density profile is not strongly changed by the divertor.

2.3 Divertor actions

2.3.1 Plasma diversion[20]

Plasma-wall interactions can be removed to a remote neutralizer plate from a limiter. In Table II.2.3-1, a typical particle- and heat-balance with and without operating the divertor are shown for plasma with the same minor radius, density, plasma current and toroidal magnetic field. The

divertor reduces the particle flux to the first wall by a factor of 2 and the heat flux carried with conduction and convection by a factor of 8.

The plasma diversion is ruled by transport process along and across magnetic field lines in the scrape-off which is discussed in II.2.4.

2.3.2 Impurity shielding[4][8]

Shielding action was observed in the previous experiment[16]. Impurity shielding is studied by injecting methane of the room temperature and aluminum of around 5 eV at the farthest point from the burial chamber along the magnetic field line. The injected carbon is ionized and ionized ions with the state of around CIV flow into the divertor chamber (Fig. II.2.3-1). Consequently, the divertor reduces the radial impurity influx towards the plasma center by a factor of 2-3 during the successive ionization process from CIII to CV (Fig. II.2.3-2). The accumulation of the injected aluminum is 3-4 times less in a diverted discharge than that in a nondiverted discharges as shown in Fig. II.2.3-3. These results demonstrate the shielding action by the divertor plasma.

Pumping-out of the guided impurities into the burial chamber is considered essential in a divertor device. However, the gaseous impurities are easily reduced as shawn in experiments. and metallic impurities stick naturally on a material surface. Therefore an artificial pumping system for impurity exhaust does not seem necessary.

The impurity transport in the main plasma is studied by comparing numerical results to the observed impurity profile and it is shown that the impurity confinement time is comparable to the particle confinement time and the neoclassical effect is masked by the anormal transport effect[21]. Therefore, the time behavior of injected impurities (Fig. II.2.3-2, 3) shows that carbon recycles and aluminum sticks on the wall.

2.3.3 Impurity back flow[12]

Impurity behavior in a scrape-off layer is very important concerning not only shielding action but also impurity back flow. Behavior of injected impurities is studied. Accumulation of aluminum injected in the burial chamber is less by a factor of 10 or more than that of aluminum injected near the main plasma Fig. II.2.3-4. This result shows that impurity efflux at the neutralizer plate induces only a little increase of impurity contents in the main plasma than the same amount of impurity

efflux at the limiter or the first wall does. This result may be explained by two different phenomena. One is that the scrape-off layer is too thin to ionize impurities and the other is that ionized impurities do not hardly flow into the main chamber. Impurity flow in a scrape-off layer was studied by measuring intensities of carbon lines in the burial chamber and in the main chamber and the result is shown in Fig. II.2.3-1. In the main chamber, sudden increase of CII-, CIII- and CIV-line intensity indicates the spread of the injected impurity ions in the edge of the main plasma column. In the burial chamber, no increase of CII-line intensity is found and the largest increase is observed in CIV-line emission. These observations make clear that injected carbon is ionized and flow into the burial chamber with the state of around CIV. Thus, the excursion time of carbon ions into the burial chamber is roughly equal to the ionization time of CIII or CIV which is roughly equal to the excursion time of the field particles. This result shows that impurity ions are easily accelerated by the field particle and the space potential into the burial chamber and that impurities produced in the burial chamber do not hardly flow into the main chamber. This process can give a high energy for a multi-ionized and heavy ion which is several times higher than proton temperature. This behavior has been confirmed by a numerical simulation[25] as shown in Table II.2.3-1. These results show that the divertor remove the surface mainly interacting with a plasma from the limiter to the remote neutralizer plate and the released impurities in the divertor flow hardly into the main chamber.

2.4 Scaling for a scrape-off layer[1]

It is generally believed that plasma-wall interactions become more serious in a future large tokamak because plasma temperature of the scrape-off layer increases as increasing temperature of the main plasma. Thus, the scaling for scrape-off layer plasmas is very important. From this point of view, scrape-off layer plasmas have been investigated in DIVA and the following results were obtained in the previous experiment: 1) Particle flow velocity to a limiter or a neutralizer plate $v_f \simeq 0.3\ v_s$ where v_s is the sound velocity[17][23]. 2) Heat flux q agrees with the value calculated from a simple sheath model and $q = \gamma T_e f_p$ where γ is a numerical factor, T_e is the electron tempera ture and f_p is the particle flux[19][23]. 3) Diffusion coefficient across magnetic field lines D

is 10 times smaller than the Bohm diffusion coefficient but the parameter dependence of the diffusion coefficient is unknown[19][23].

Important plasma parameters in the scrape-off layer, i.e. mean electron temperature $\bar{T}_{es}$, width of the scrape-off layer d and mean electron density $\bar{n}_{es}$ are given as follows:

$$\bar{T}_{es} = \frac{3\bar{\tau}_p (P_{in} - P_{cx} - P_R)}{2\tau_E P_{in}\gamma} (\bar{T}_e + \bar{T}_i) \tag{1}$$

$$d = \sqrt{D_\perp L / v_f} \tag{2}$$

$$\bar{n}_{es} = \frac{L\bar{n}_e a}{2 v_f \bar{\tau}_p d} \tag{3}$$

where P_{in}, P_{cx}, P_R, $\bar{\tau}_p$, τ_E, $\bar{T}_e$, $\bar{T}_i$, $\bar{n}_e$, a and L are the input power, cx loss-power, radiation loss-power, average particle-confinement time, energy-confinement time, mean electron temperature of the main plasma, mean ion temperature, mean density, minor radius and length of magnetic field lines to a material surface, respectively. In this section, $\bar{\tau}_p/\tau_E$, $D_\perp$ and γ are studied to obtain the scaling for scrape-off layer plasmas and characteristics of the scrape-off layer is briefly discussed. Average particle confinement time $\bar{\tau}_p$ is calculated from the total electron number and the total particle loss flux which is measured as the sum of ion saturation currents onto four sectors of the shell, three pieces of the protection plate and the burial chamber[17]. The average particle-confinement time has the functional dependence of the Alcator scaling for the energy-confinement time. The relation between the average particle-replacement time and the energy-confinement time is shown in Fig. II.2.4-1 and $\bar{\tau}_p/\tau_E \simeq 1.5$ without the divertor and $\bar{\tau}_p/\tau_E \simeq 0.8$ with the divertor. The difference is mainly due to the difference in the electron temperature profile, i.e. the profile becomes broad and the energy-confinement time increases by operating the divertor.

Parameter dependence of the diffusion coefficient is studied by measuring the divertor efficiency for the particle flux which is given by the following equation:

$$\eta = \mathrm{Erf}(y), \qquad y = \sqrt{\frac{\Delta^2 v_f}{4\pi D_\perp q_a R}} \tag{4}$$

where Erf, R, q_a and Δ are error function, safety factor and the distance

between the separatrix magnetic surface and the wall surface, respectively. The result shows that the diffusion coefficient has the functional dependence of the Bohm diffusion (Fig. II.2.4-2).

γ is obtained from equation (1) which is rewritten as follows:

$$\gamma \bar{T}_{es} = \frac{P_{in} - P_{cx} - P_R}{F_p} \tag{5}$$

where F_p is the total loss flux. $(P_{cx} + P_R)$ is measured by scanning a calibrated pyroelectric detector, F_p is measured as the ion saturation current and the electron temperature is measured by using electrostatic methods. The electron temperature near the surface which collects the main part of the heat flux is employed as $\bar{T}_{es}$. The result is shown in Fig. II.2.4-3 and $\gamma \simeq 7$.

The experimental results given $v_f \simeq 0.3\ v_s$, $\bar{\tau}_p/\tau_E \simeq 1$, $D \simeq 0.1\ D_B$ and $\gamma \simeq 7$. Thus, equation (1) is simplified as follows:

$$\bar{T}_{es} \simeq 0.2 \frac{(P_{in} - P_{cx} - P_R)}{P_{in}} (\bar{T}_e + \bar{T}_i) \tag{6}$$

This equation shows that temperature at the edge is extremely high in a high temperature tokamak with $P_{in} \gg P_{cx} + P_R$ and sputtering by ions becomes serious. Therefore it is very important to control the scrape-off plasma in a large fusion device as discussed in II.2.6. For example, the edge cooling is necessary to mitigate the plasma-wall interactions. This scheme is tested by feeding cold gas into the scrape-off layer[12]. With the gas feeding the Fig. II.2.4-4 shows that the outer edge of the scrape-off plasma is cooled down by a factor of 2, thereby causing the reduction of floating potential of the first wall. This appears that the observed reduction of impurity generation is attributed to the suppression of the ion sputtering yield by reducing the potential difference (sheath potential) between the plasma and the first wall. The experimental result shows that slight cooling of the outer edge plasma nearest to the first wall effectively suppresses the metallic impurity release from the wall, thereby reduces the contamination by first wall material.

Ion temperature is also investigated and flowing result is obtained[14].

$$T_{is} \sim 0.2\ T_{i0}$$

2.5 Ion sputtering, arcing and evaporation

2.5.1 Metallic impurity origin[5][6][7]

A gas-impurity-free-plasma was easily obtained by clearing the vacuum wall[22]. Therefore, the impurities of the wall material (usually metal) is important in both present and future devices. In order to control these impurities in a large fusion device, it is necessary to know the metallic impurity origin.

The metal impurities was investigated by using the aluminum test target. The aluminum target located normal to the magnetic field in the divertor is pulsely biased with the time duration of 2 ms when the plasma reaches its quiet phase. The probe characteristics of the target, the time evolution of the target current and the variation of the intensity of Al-III line radiation are measured. From the experimental results, the three different types of the metal impurity release are identified, i.e., arcing, evaporation and ion sputtering. It must be pointed out that the experimental method using there is time-resolved one. Therefore the dominant process for the metal impurity release in the quiet phase can be identified by this method. Ion sputtering is the dominant process of the release of the metal impurity from the limiter contacting to the quasi-stationary scrape-off plasma in tokamak. Arcing occurs only when the target surface is dirty, but can be easily suppressed by discharge cleanings. Arcing may occur when the negative spikes appear. By using a high speed camera, several lightning due to arcing are clearly observed on a shell surface only at the moment of disruptions. Evaporation may occur when the heat flux to the limiter is increased to the level about ten times greater than the normal heat flux by the stationary plasma. Although these processes may occur under the special condition of the plasma and the limiter surface, they do not occur when the plasma becomes its stationary state.

The shell coated by gold is pulsely biased with respect to the plasma in spite of the previous aluminum test target in order to know the origin of the real impurity, i.e. gold. The scrape-off plasma parameters are as follows; T_e = 40 - 60 eV, T_i = 50 - 70 eV and $n_e = 2 - 5 \times 10^{12}$ cm^{-3}. The similar measurements to the previous letter[6] are done. And the same result is obtained for ion sputtering as shown in Fig. II.2.5-2. In the figure the intensity of the Au-I line radiation, that correlates to the

the quantity of the metal impurity efflux by ion sputtering, is plotted as a function of the applied voltage to the shell. These results suggest that when the accelerating potential is below 400 V, the main part of the ion sputtering may be caused by the impurity ions and above 400 V, the ion sputtering by the hydrogen may become dominant, because the energy gained by the ion of charge Z is Z-times greater than the energy gained by the hydrogen. On this point of view, the sputtering yields of H^+, Au and Ne on Au are shown in the same figure. Data are taken from the reference. Unfortunately, data on oxygen are not available and neon is shown for an example to see the rough dependence of sputtering yield of oxygen on Au. These traces are obtained assuming the effective charge $\bar{Z}$ of Au and Ne are 10 and 3, which values are probably true in the present scrape-off plasma parameters. The horizontal axis for Au and Ne are divided by $\bar{Z}$ because the energy of these impurity incident fluxes to the target is $\bar{Z}$ times the potential difference between the plasma and the target. These traces remarkably resemble the experimental results on Au obtained by biasing the shell coated by gold, in which there are two threshold energies, i.e., a few hundreds eV and a few tens eV. It is difficult to estimate the fluxes of Au and oxygen onto the shell surface experimentally, however, the ratio is fairly well consistent with the values estimated from the impurity content of the main plasma.

From these considerations, it can be said that the high-Z impurity ion sputtering must be dominant when the sheath potential is as low as in an usual scrape-off plasma, i.e., $\phi \sim 150 \sim 200$V[26]. The contribution of the sputtering by the neutral atoms to the metal impurity contamination is concluded to be very little because of the electrical potential dependence on the metal impurity release.

Because ion sputtering is dominant, the honeycomb structure can reduces the impurity production[27]. The plane target is replaced by the honeycomb target (Fig. II.2.5-2) and the comparison of the metal efflux with the plane target is performed. In Fig. II.2.5-3 the efflux of Al vs. applied voltage to the honeycomb target is shown, comparing to those of the plane target. This result shows that 30 - 40 % of the metal efflux is reduced by employing a honeycomb structure as a neutralizer plate. According to the calculation[27], in which the sputtered metal is free from ionization and travels straight from the surface as a neutral particle, the reduction must be 70 - 80 %. The discrepancy between the observed and

the calculated values may be explained by taking into account the ionization of the sputtered atoms in the scrape-off plasma in front of the honeycomb target. Figure II.2.5-4 shows the trapping efficiency of the honeycomb structure as a function of a mean free path λ of the sputtered atom.

It is difficult to determine the mean free path of the sputtered aluminum atoms experimentally, however, some crude estimation can be given as following. Assuming the energy of the sputtered aluminum atoms to be some reasonable value of 3 eV and using the ionization rate coefficient in the present scrape-off plasma parameters (n_e = 2 - 5 × 10^{12} cm^{-3}, T_e = 40 - 50 eV), the mean free path λ is calculated to 7 mm. Because of this finite λ, the trapping efficiency is reduced from 80 % to 45 % and is consistent with the experimental results. This result shows that the size of a honeycomb has to be small not only because of thermal problems but also because of ionization processes. This experiment suggests that the honeycomb structure is also as effective in reducing metal effluxes from a neutralizer plate as in reducing them from the first wall surrounding the main plasma.

Since gold has a high sputtering yield and a poor thermal property, plasma-wall interactions in DIVA simulates those in a higher temperature scrape-off plasma in a large machine with a suitable wall material.

2.5.2 Wall erosion[6][7]

Wall erosion is also important in a large fusion device. Ovservation of surfaces exposed to a plasma is not a time-resolved one and is not always suitable to investigate the impurity origin. The method, however, is very important to know the wall erosion.

Fig. II.2.5-5 shows the scanning electron micrograph picture of a gold protection plate surface attached to the shell. It is deposited to the plasma over 10000 shots. The cone like formations due to the ion sputtering are clearly observed in the region some distance apart from the edge of the protection plate, although the cones in the edge region are destroied by the damage due to the evaporation and/or arcing. This photograph indicates that the ion sputtering really occurs on the surface of the protection plate in a real tokamak.

Damage of the shell surface is also investigated. Figure II.2.5-6 shows the spacial intensity distribution of the Au-I line radiation and

the scanning electron micrograph pictures of various area of the shell coated by gold. The shell is desposed to the plasma over a few ten thousands shots. There is also the picture of the shell before the desposure to compare with the photographs after the desposure. The cone loke formations due to the ion sputtering is more clearly observed in the area of the maximum intensity of Au-I line radiation. Gold is the dominant metal impurity in DIVA. There is a fairly good correlation between the area of the maximum intensity of the metal line radiation and the area of the maximum growth of the cone like formations due to the ion sputtering. It also indicates that the ion sputtering is the dominant process of the metal impurity release from the first wall. A one-shot-exposed target, where the target is electrically floated, indicates (Fig. II.2.5-7) clear arc tracks as observed in other tokamaks and arcing is important for wall erosion.

It is only when the electrically floated target is so placed to accept high energy electrons from the main plasma that the SEM (scanning electron micrographs) picture of the target surface indicates many melted spots (Fig. II.2.5-8) in the present experiments. In this case the target may be evaporated due to the concentrated heat flux.

2.6 Impurity control in a large fusion device[3][26]

The erosion of a limiter or a neutralizer plate is very serious in a large fusion device as discussed below even if we assume molybdenum which has a low sputtering yield. Without cooling the edge plasma, the edge temperature is a few keV which gives about 3×10^6 g/year for the erosion rate in a typical EPR[3]. Even if we assume the area of the neutralizer plate of 300 m^2, the average erosion rate is about 1 mm/year. The maximum erosion rate may be several times larger than the average value. The erosion is very serious and other mechanisms such as evaporation, arcing and self-sputtering may enhance the erosion. This situation is not different in a conventional tokamak. The erosion can be mitigated by cooling the edge plasma.

Even if the serious erosion is permitted in a large device, the temperature of a plasma contacting a material surface has to be rather low as discussed below.

The total number of high-Z impurities is given by the following equation:

$$\frac{dN_Z}{dt} = (R_S - 1)\frac{N_Z}{\tau_Z} + F_Z$$

where N_Z, R_S, τ_Z and F_Z are the total number of high-Z impurities, their re-cycling rate, their confinement time and their influx caused by other particles such as charge-exchange particles, protons and low-Z impurities and by evaporation. When $R_S > 1$, N_Z increases exponentially; $R_S < 1$ refers to the steady state. R_S is given by the following equation:

$$R_S = \alpha S(E_Z)$$

where α is the probability of ionization and trapping of heavy atoms by the main plasma, and $S(E_Z)$ is the sputtering yield by heavy ions with energy E_Z; reflection is included in $S(E_Z)$. To satisfy $R_S < 1$, E_Z has to be low because high E_Z gives very high sputtering yield. E_Z is given by the following equation:

$$E_Z \simeq ZV_S + T_Z$$

where z, V_S and T_Z are the charge number, the sheath potential and temperature of the heavy ion, respectively. Since V_S and z increase with increasing electron temperature, the electron edge temperature, T_e, has to be low in steady state.

The heat flux to a material surface is carried mainly by electrons, from Langmuir's sheath theory, and is approximately given by:

$$P_L \simeq \gamma T_e F_p$$

where F_p is the particle flux to the limiter and γ is a numerical constant. The particle flux to the limiter coincides with the particle flux from the main plasma because the recombination rate is negligible for $T_e > 10$ eV; F_p is re-written as follows:

$$F_p = \frac{N_e}{\tau_p}$$

where N_e and τ_p are the total number of electrons and the gross particle confinement time of the main plasma column, respectively. P_L is not strongly

changed by increasing machine parameters because N_e proportional to the major radius and the square of the minor radius, τ_p is also proportional to the square of the minor radius, and T_e is limited as was discussed above. The power input, however, is expected to increase strongly with increasing machine parameters. Thus, the power loss to the limiter is a small fraction of the power input in a future large tokamak, which suggests that radiation loss dominates the energy balance if charge-exchange loss is small. The relation between the radiation loss and the heat loss to the limiter is explained by a natural feedback mechanism as follows: When the radiation loss and charge-exchange loss are small, P_L has to be large to satisfy the energy balance. Large P_L is provided by high T_e, which gives a high energy for E_z because of a high sheath potential and a high ionization level. R_s can easily increase to more than one because of the very high self-sputtering yield with high E_z. Thus, the high-Z impurities and the radiation loss increase while P_L decreases until a value of R_s less than unity is achieved. After this situation has been attained, the impurity contamination level does not change without change of impurity emission by other mechanisms or a change in the plasma parameters. P_L, however, can be smaller than the estimated upper limit with the estimated maximum electron temperature, when another mechanism of impurity emission, and/or low-Z impurities are dominant.

A simple estimation shows that the electron temperature has to be around several tens eV at the plasma edge in a conventional tokamak which is consistent with the observed temperature[23]. By introducing the divertor, the permissible electron temperature becomes higher. By shileding action, however, the scrape-off layer can easily ionize the sputtered impurities and this situation is essentially similar to that in a conventional tokamak.

The above two different considerations give that controlling the plasma contacting to a material has to be controlled cool even in a divertor device.

In a fusion reactor, the wall temperature is high enough to clean the vacuum surfaces and impurities are originated only from the wall materials. Therefore, dominant mechanisms of impurity release are ion sputtering, neutral particle sputtering and evaporation. Evaporation can be rather easily eliminated by spreading the heat flux onto a large area. Both sputterings can be reduced by cooling the edge plasma. Moreover impurity influx from the wall can be screened by the shadow plasma of a limiter in a conventional tokamak as well as by the scrape-off layer plasma in a

divertor tokamak. The screened impurities flow onto the limiter surface where metallic impurities stick naturally. Therefore, screening action in a conventional tokamak is the same as in a divertor tokamak if the shadow plasma is well controlled. In a conventional tokamak, impurity control depends on a control of the periphery plasma.

If the impurity level is higher than a permissible level after controlling the edge plasma, the divertor or another method is needed.

There are a few types of divertors for controlling impurities as summarized in Fig. II.2.6-1. The classical divertor collects not only a large portion of the particle flux but also that of the heat flux without cooling the edge plasma. Therefore the guided plasma into the divertor has an extremely high temperature, typically a few keV, and cooling the diverted plasma[28] or a direct convertor[29] is required in the divertor chamber. The flow velocity is very high and the line density in a scrape-off layer is low. Thus, the shielding efficiency is low and neutral particle density in the main chamber has to be kept low to reduce impurity release at the first wall. Thus, the classical divertor requires a large pumping system and a special fueling method without producing neutral particles and is complex and expensive. There are few experimental data which we need to design a classical divertor.

A more realistic divertor is a non-heat-exhaust divertor. The periphery plasma is cooled and a large fraction of the total power loss is converted to the radiation and charge-exchange loss at the edge. Therefore, the guided power into the divertor is low and the plasma temperature is also low. The impurity contamination is strongly reduced by the non-heat-exhaust divertor because the impurity source moves from a limiter to a remote neutralizer plate and impurities released from the neutralizer plate do not hardly flow into the main chamber as shown by the experiments and a numerical simulation. Some additional methods controlling plasma-wall interactions can be added to it. For example, the honeycomb structure can be rather easily applied because of the low density for the heat flux. The non-heat-exhaust divertor is simple and compact and is rather easily designed because of easy extension of the present divertor experiment. If the impurity level is still high, the left origin of impurity, i.e. sputtering by charge exchange particles, has to be eliminated. In this case, the divertor becomes again complex and expensive, i.e. the large pumping system and the special fueling are necessary.

References

(1) Shimomura, Y., Maeda, H., Kimura, H., et al.: Scaling for Scrape-off Layer Plasma in Tokamak, Japan Atomic Energy Research Institute Report JAERI-M 7457.

(2) DIVA Group, Recent Results in the DIVA Experiment, Japan Atomic Energy Research Institute Report JAERI-M 7610.

(3) Shimomura, Y., Maeda, H.: Proc. 3rd Int. Conf. on Plasma Surface Interactions in Controlled Fusion Device, Culham (1978) Paper R5.

(4) Nagami, M., et al.: ibid Paper 28.

(5) Ohasa, K., et al.: ibid Paper 47.

(6) Ohasa, K., et al.: to be published in Nuclear Fusion 18 (1978).

(7) Ohasa, K., et al.: to be publiished in Jurnal of Phys. Soc. of Japan (1979).

(8) Nagami, M., et al.: to be published in Nuclear Fusion 18 (1978).

(9) DIVA Group, Nuclear Fusion,18(1978) 1619.

(10) DIVA Group, Internal Report (1977).

(11) Yamamoto, S., Maeda, H., Shimomura, Y., Odajima, K., Nagami, M., et al.: in Controlled Fusion and Plasma Physics (Proc. 8th Europ. Conf., Prague, 1977) 2 (1977) 234.

(12) Sengoku, S., et al.: to be submitted to Journal of Physical Society of Japan 45 (1978) 1385.

(13) Sugie, T., Takeuchi, H., Kasai, S., et al.: Ion Temperature Characteristics of Upgraded DIVA, to be published in Journal of Physical Society of Japan 44 (1978) No. 6.

(14) Odajima, K., Kimura, H., Maeda, H. and Ohasa, K.: Measurement of ion Temperature in Scrape-off Layer with Katsumata Probe, Japan Journal of Applied Physics, 17 (1978) 1281.

(15) Maeda, H., Fujisawa, N., Shimomura, Y., Funahashi, A., Ohtsuka, H., et al.: in Plasma Physics and Controlled Nuclear Fusion Research (Proc. 6th Int. Conf., Berchesgaden, 1976) 2, IAEA, Veinna (1977) 289.

(16) Maeda, H., Ohtsuka, H., Shimomura, Y., Yamamoto, S., Nagami, M., et al.: in Plasma Wall Interaction (Proc. Int. Symposium, Julich, 1976) Pergamon Press, Oxford (1977) 537.

(17) Kimura, H., et al.: Japan Atomic Energy Research Institute Report JAERI-M 6861 and 6971 (1977).

(18) Shiho, M., Odajima, K., Sugie, H., Maeda, H., Kasai, S., et al.: Spectroscopic and Bolometric Measurement of Radiation Loss in DIVA Japan Atomic Energy Research Institute Report JAERI-M 7397 (1977).

(19) Kimura, H., Maeda, H., Ueda, N., Seki, M., Kawamura, H., Yamamoto, S., et al.: Heat Flux to the Material Surfaces in a Tokamak, Nucl. Fusion, 18 (1978) 1195.

(20) Odajima, K., et al.: Nucl. Fusion 18 (1978) 1337.

(21) Nagami, M., et al.: Internal report (1977).

(22) Nagami, M., et al.: Nuclear Fusion 18 (1978) 529.

(23) Ohtsuka, H., et al.: Plasma Physics 20 (1978) 749.

(24) Post, D.E., et al.: PPPL-1352 (1977).

(25) Azumi, M.: private communication.

(26) Shimomura, Y.: Nuclear Fusion 17 (1977) 1377.

(27) Yoshikawa, M.: JAERI-M 5849 (1974).

(28) Yoshikawa, M.: JAERI-M 4494 (1971).

(29) Mills, R.G., et al.: MATT-1050 (1974).

Table II.2.2-1 Particle flux and heat flux.
Discharge condition is shown in Fig.II.2.2-1.

Divertor	Particle Flux (10^{18} ms^{-1})		Heat Flux (kw)			
			Conduction and Convection		Radiation	Charge-Exchange
	Divertor	Limiter and Wall	Divertor	Limiter and Wall		
off	0	2.1	0	200	102	10
on	0.5 (33%)	1.0	75 (55%)	25	30	10

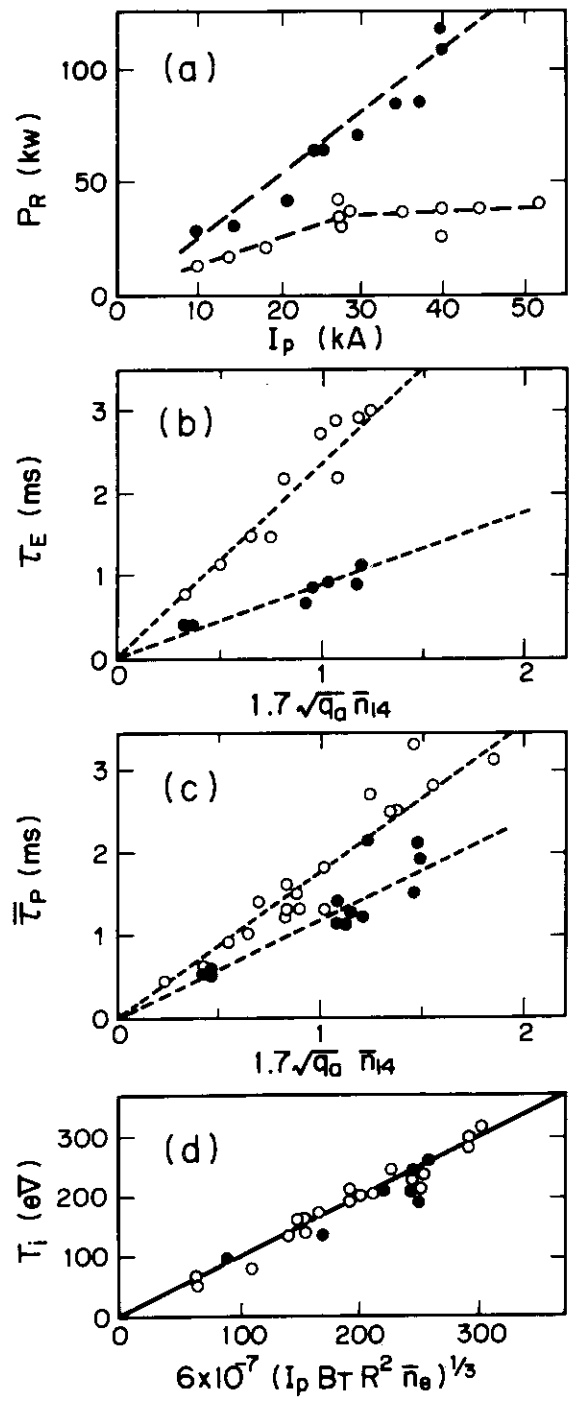

Fig.II.2.2-1 Radiation loss power P_R, energy-confinement time τ_E, average particle-confinement time τ_p and central ion temperature T_i with the divertor (○) and without the divertor (●). I_p: plasma current, q_a: safety factor, $\bar{n}_{14}=\bar{n}_e/(10^{14}\ cm^{-3})$ and $(I_p B_T R^2 \bar{n}_e)$ in $(A\cdot G\cdot cm^2\cdot cm^{-3})$.

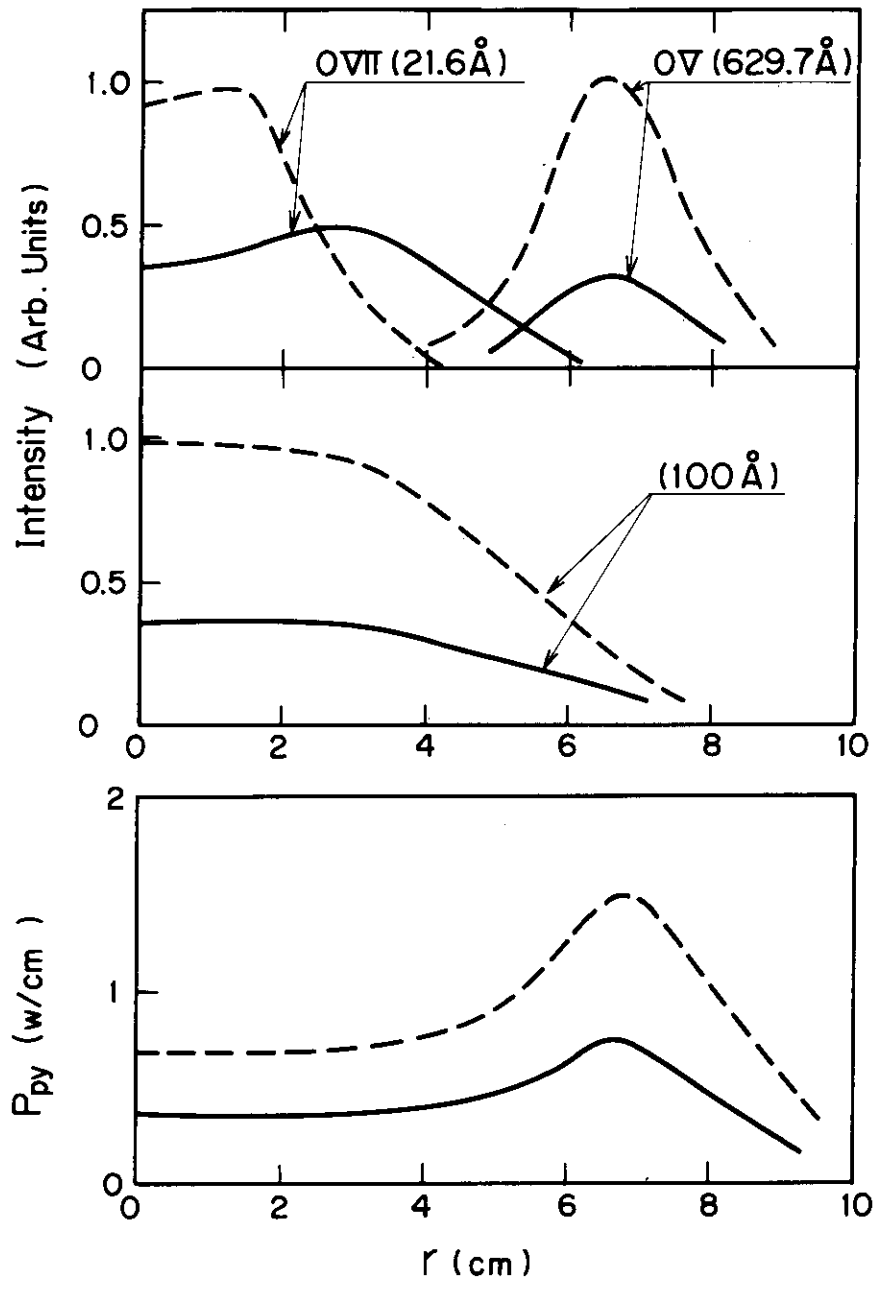

Fig.II.2.2-2 Radial profiles of intensities of OV- and OVII-lines and pseudo continuum at 100 Å and the total radiative loss-power P_{py} including charge-exchange loss with the divertor (——) and without the divertor (– – – –) where I_p=40 kA, B_T=2 T and $\bar{n}_e$=3.5×10^{13} cm^{-3}.

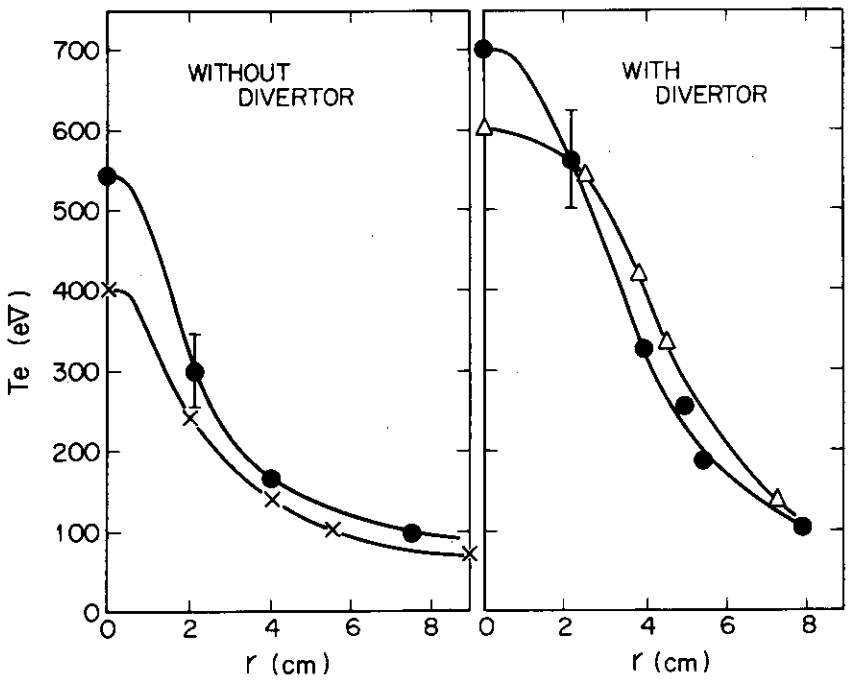

Fig.II.2.2-3 Typical profiles of electron temperature T_e with and without the divertor.

Table II.2.3-1 Ionization state and energy of swept carbon ions into the divertor.

	$\bar{Z}$	E(CIV)	E(CV)
Experiment	∿3	40 eV	80 eV
Calculation	3.3	50 eV	70 eV

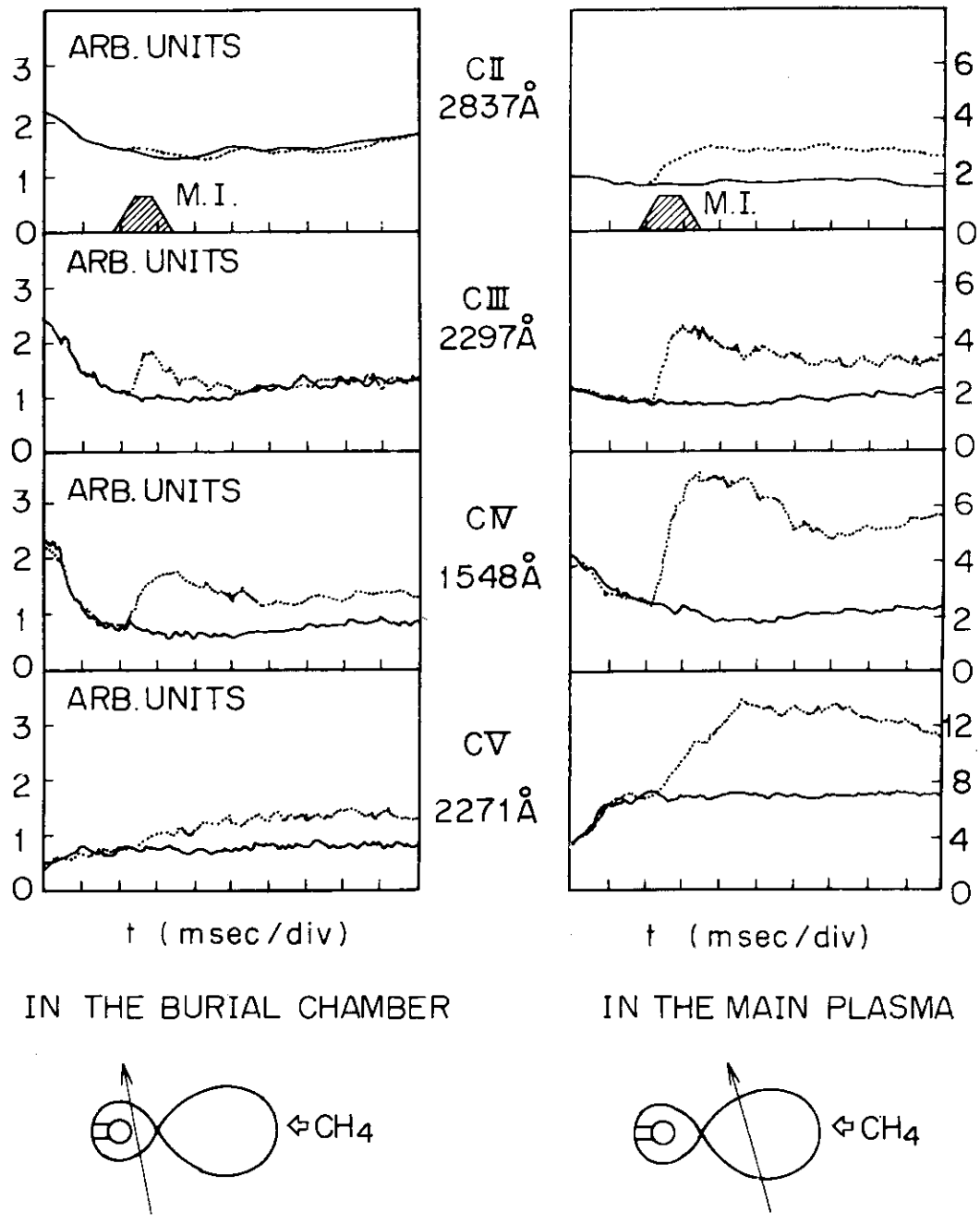

Fig.II.2.3-1 Time development of the increase of line intensity from respective ionization states of carbon ions in the burial chamber and in the main plasma with the methane injection (M.I.) in diverted discharge. —— : without injection, - - - - : with injection.

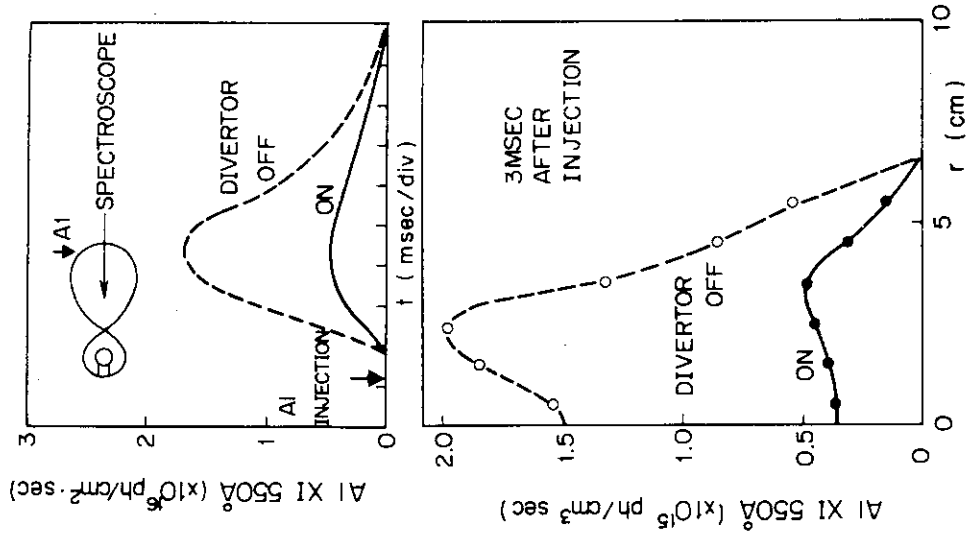

Fig.II.2.3-3 (a) Time development of the line integrated emissivity of AlXI 550 Å with the aluminum injection, (b) Abel-inverted volume emission of AiXI 550 Å after 3 msec from the injection. Accumulation of the injected aluminum ions in the central region of the plasma is reduced by factor 3-4 by the divertor action.

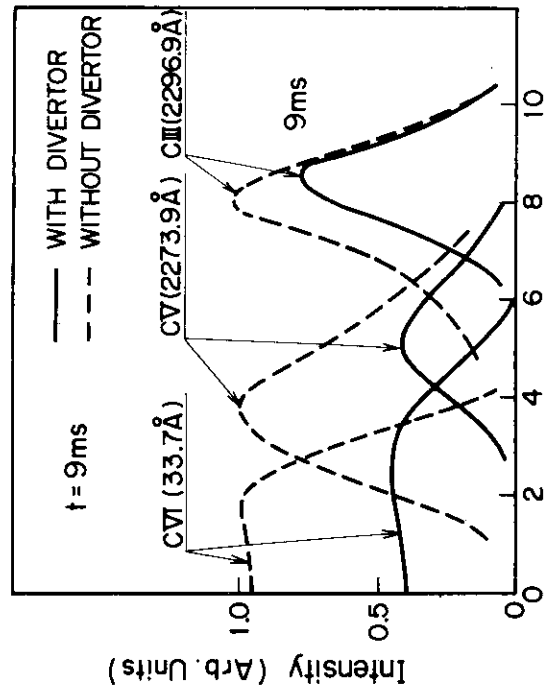

Fig.II.2.3-2 Radial profiles of CVI-, CV- and CIV-line intensity increased with methane injection,

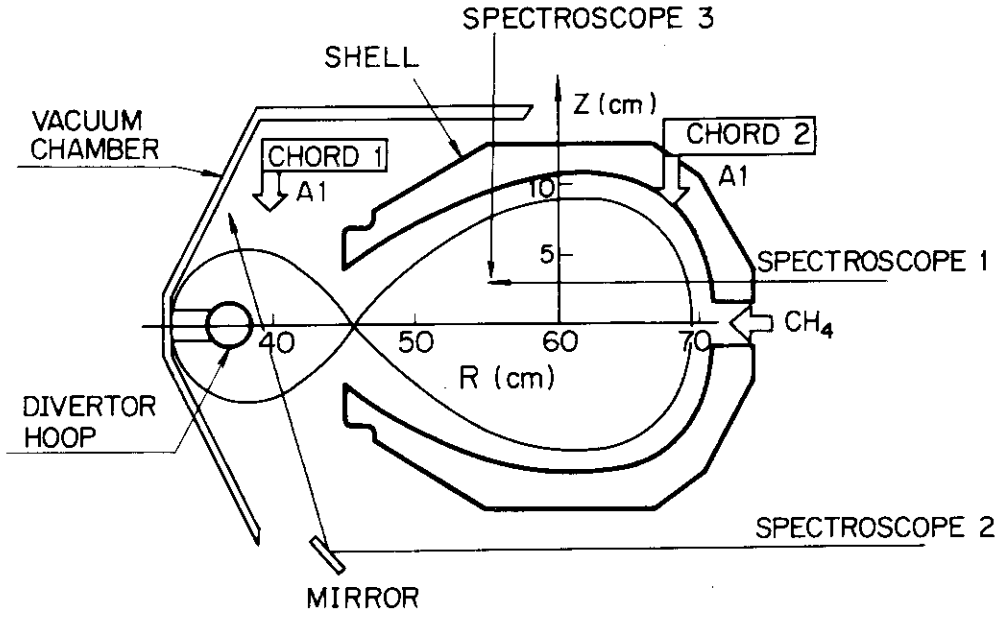

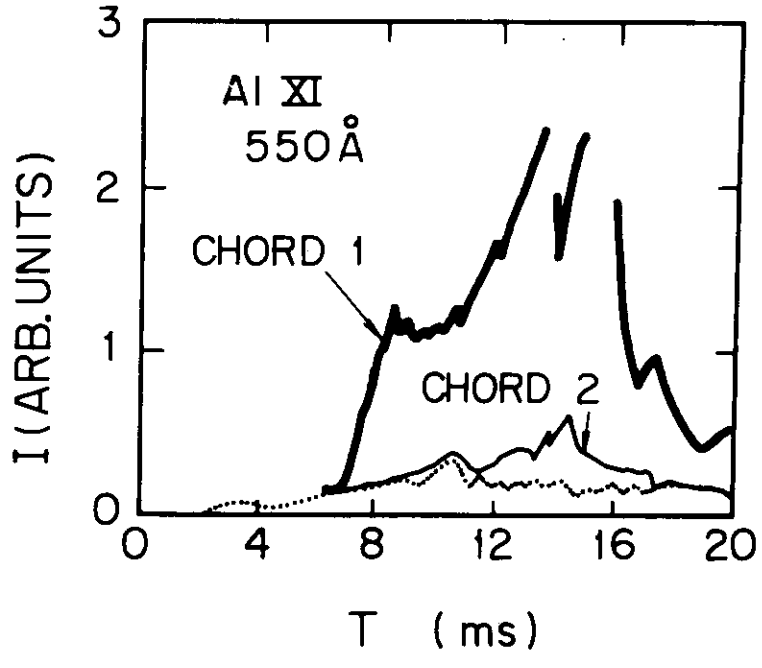

Fig.II.2.3-4 Demonstration of the back flow of the aluminum ions from the burial chamber into the main plasma; solid lines indicate with the injections along the chords 1 and 2 and dotted line indicates the background level of the AiXI 550 Å line emission.

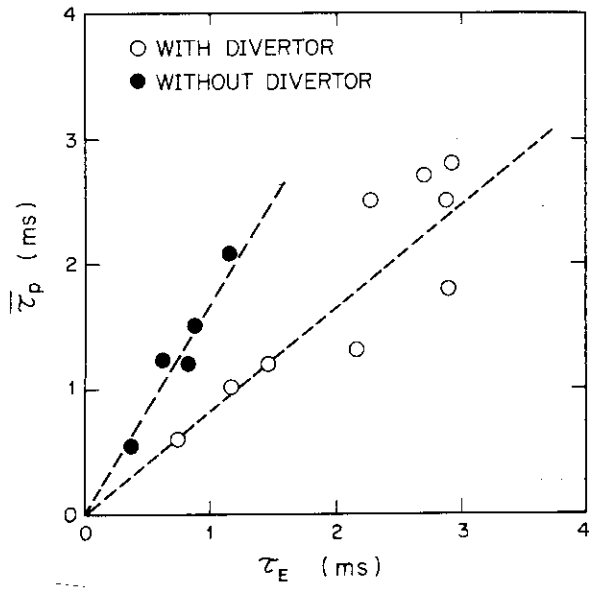

Fig.II.2.4-1 Relation between the average particle-confinement time $\bar{\tau}_p$ and the energy-confinement time τ_E with and without the divertor. B_T=0.8-2.0 T, I_p=10-53 kA, q_a=2.6-5.9, $\bar{n}_e$=(1.5-5.0)×10^{13}cm ^{3}, T_i=80-300 eV.

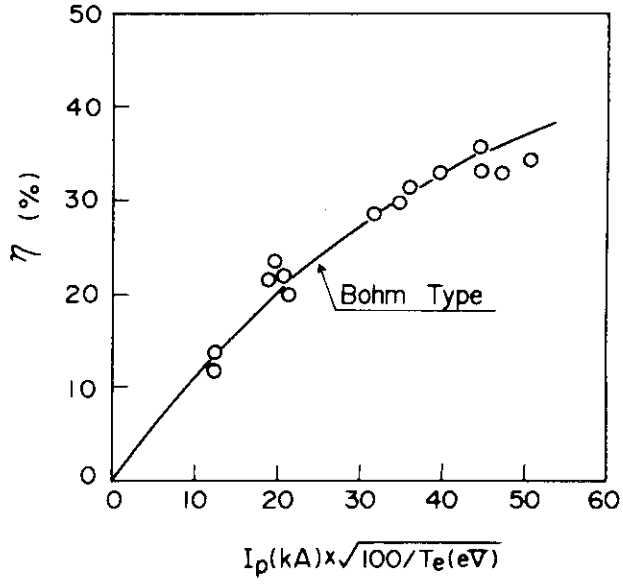

Fig.II.2.4-2 Particle divertor efficiency η. B_T=0.8-2.0 T, $\bar{n}_{es}$=(1-4)×10^{14} cm^{-3} and T_{es}=20-100 eV.

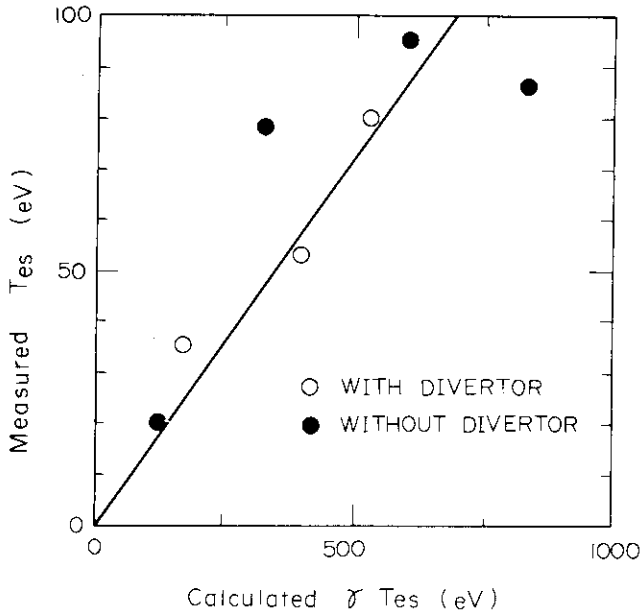

$$\left[\gamma Tes = 1.5 \times \frac{\bar{\tau}_p}{\tau_E} \frac{P_{in}-P_{CX}-P_R}{P_{in}} (\bar{T}_i + \bar{T}_e) = \frac{P_{in}-P_{CX}-P_R}{F_p}\right]$$

Fig.II.2.4-3 Measured electron temperature $\bar{T}_{es}$ in scrape-off layer plasmas and calculated $\gamma\bar{T}_{es}$ from equation (1).

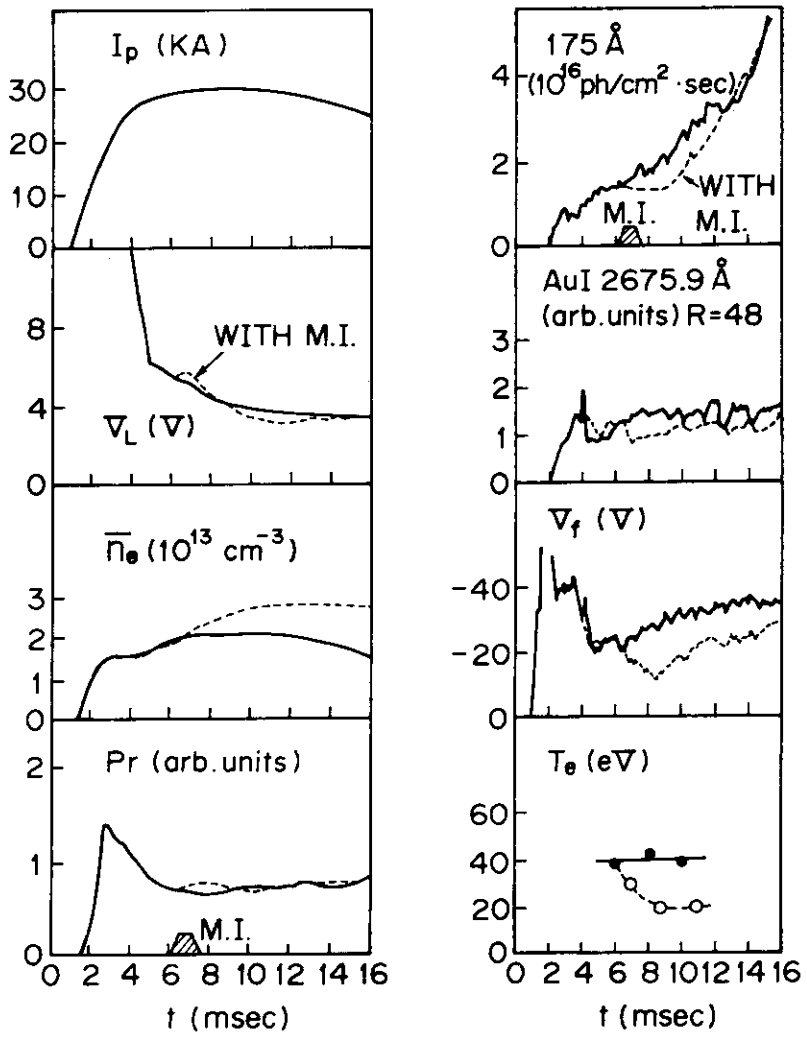

Fig.II.2.4-4 (a) Time evolutions of plasma current I_p, plasma loop voltage V_L, line-averaged electron density $\bar{n}_e$, the total radiation power P_r, and (b) the line integral (across the minor diameter) of photon signals of 175 Å (bandwidth 1 Å), AuI 2675.9 Å line emission near the divertor throat (R=48 cm), floating potential of the shell with respect to the vacuum chamber and the electron temperature of the scrape-off plasma at 5 mm from the first wall at the divertor throat with (solid lines) and without (dotted lines) methane injection (M.I.).

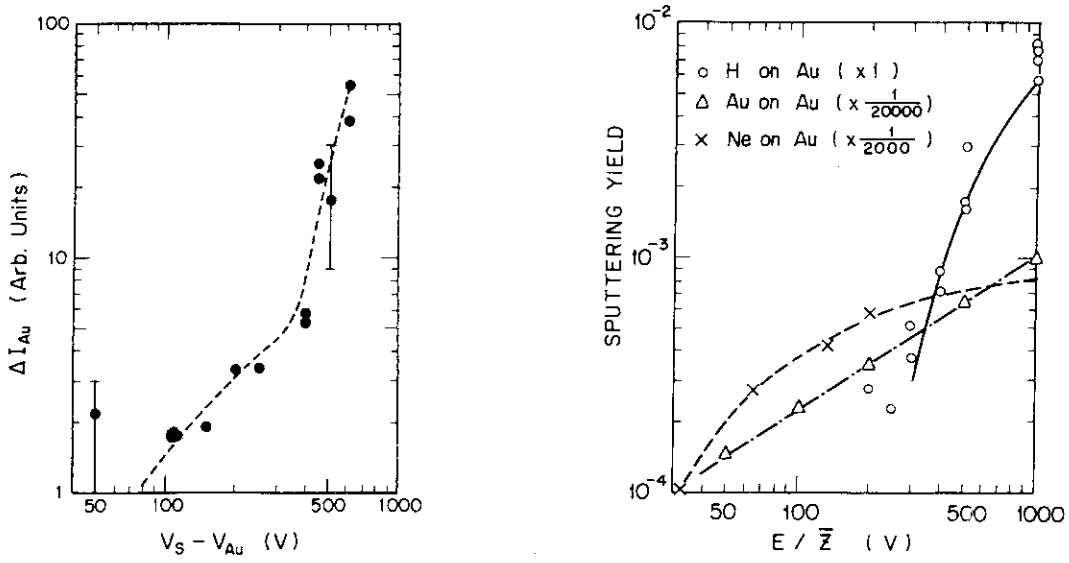

Fig.II.2.5-1 Dependence of the intensity of Au-I line radiation on the applied voltage to the gold plated shell. V_S-V_{au} means the potential gap between the plasma space potential and the gold plated shell. Sputtering yields of H^+, Au and Ne on Au.

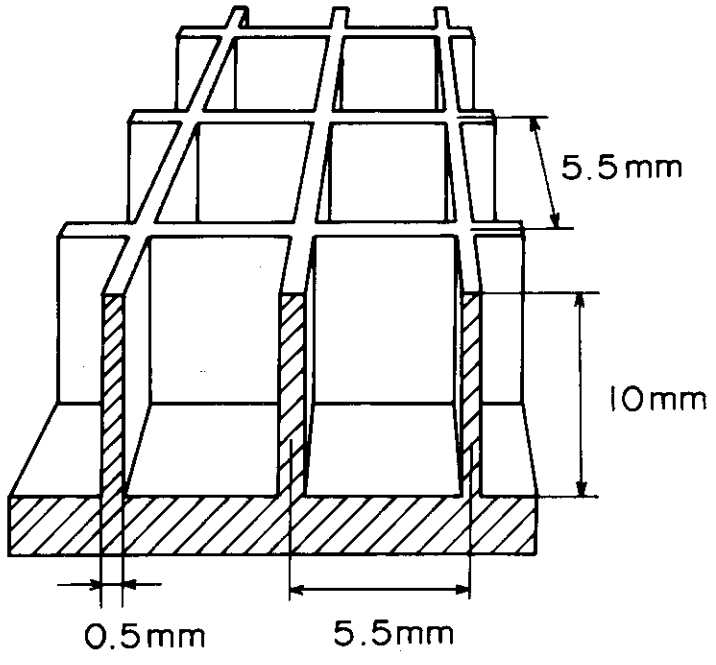

Fig.II.2.5-2 Schematic drawing of a honeycomb target.

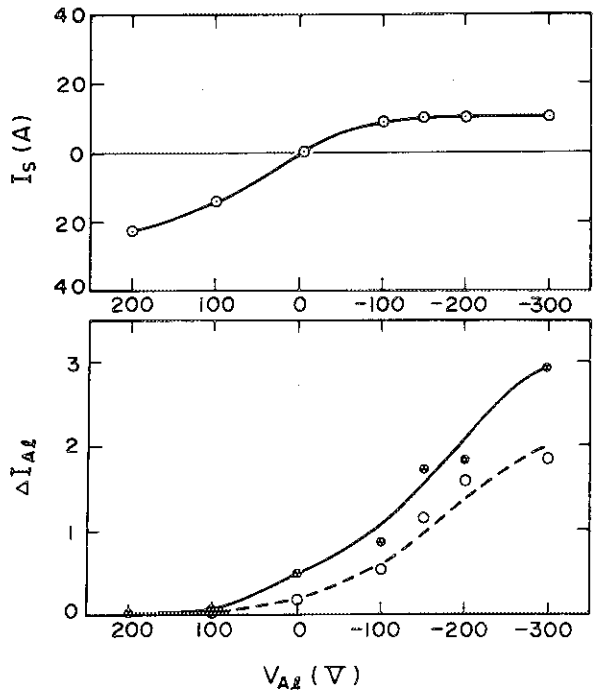

Fig.II.2.5-3 Efflux of aluminum from the honeycomb target. Open circles correspond to the honeycomb target and closed circles correspond to the plane target. The top trace shows the target current vs voltage.

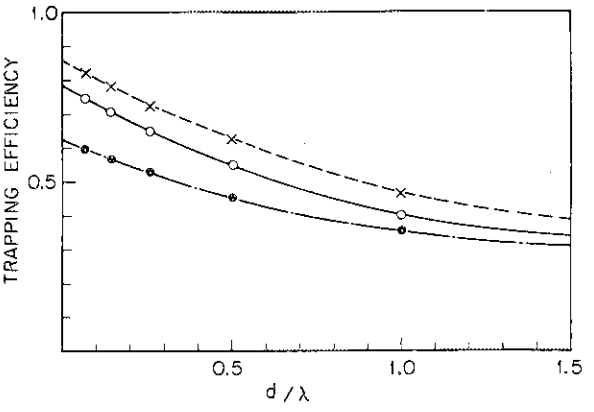

Fig.II.2.5-4 Trapping efficiency of the honeycomb structure as function of the mean free path λ of the sputtered neutral atom calculated using the Monte Calro Method. D is the depth of the honeycomb and d is the width of the honeycomb. Angular distribution of the sputtered atom is assumed to be cosine distribution (open and closed circles). The case of homogeneous distribution is also calculated and shown by the crossed points.

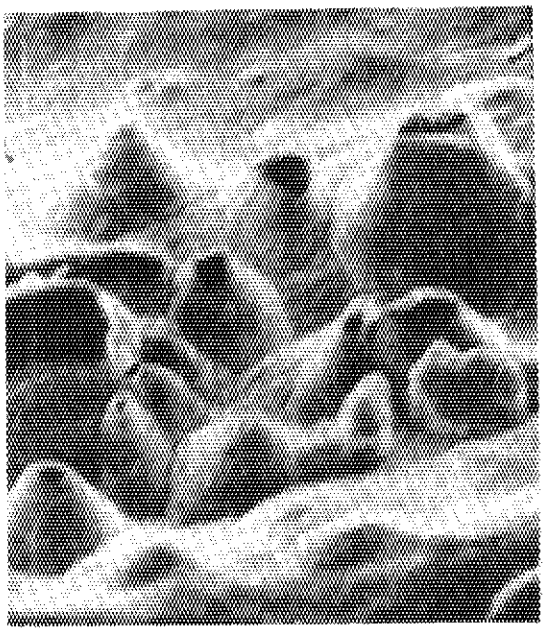

Fig.II.2.5-5 Sputtered corns observed on the gold protection plate exposed to about 100,000 discharges.

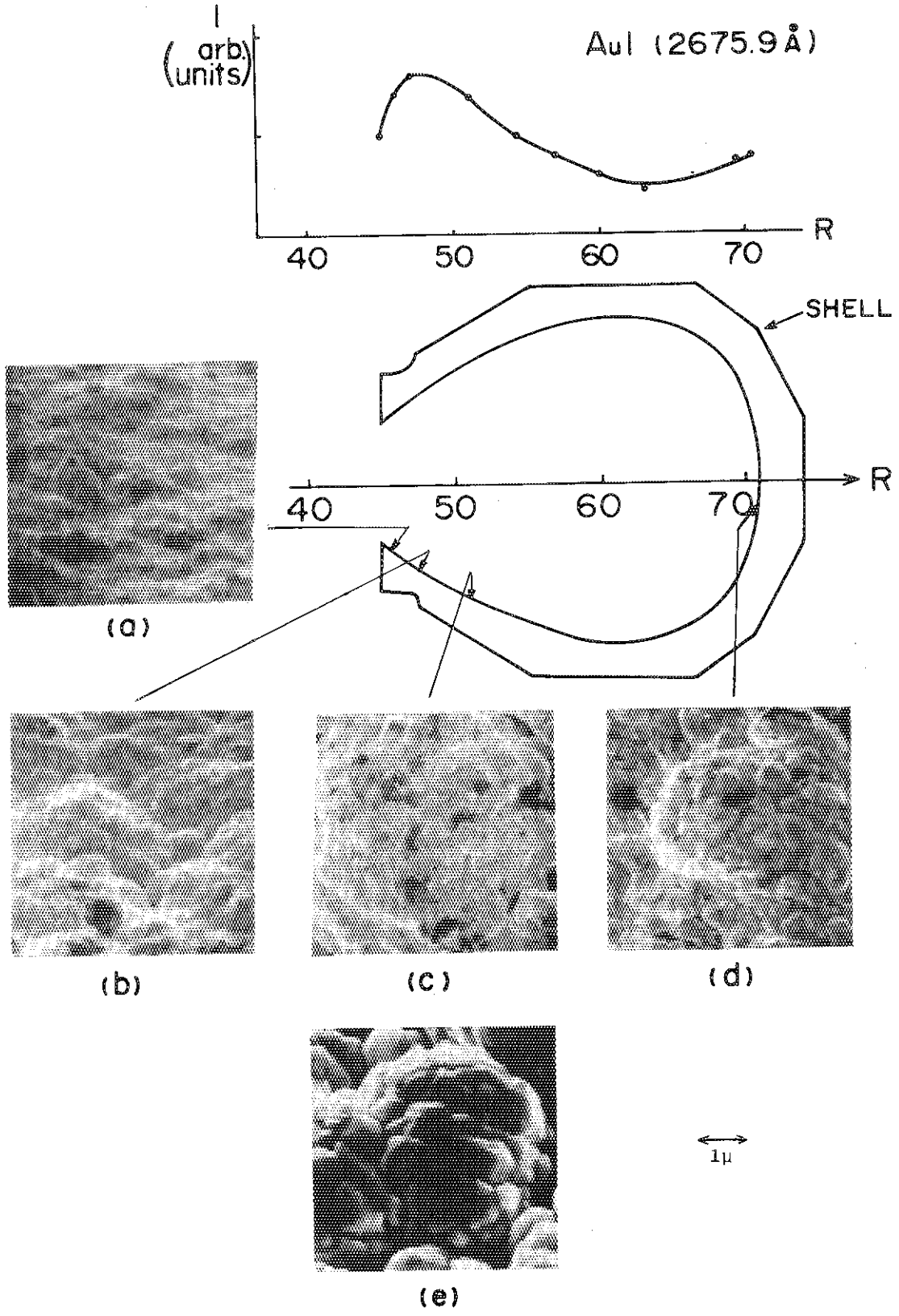

Fig.II.2.5-6 Profile of Au-I line intensity and the damage of the gold plated shell surface.
(e) is the surface before operating the device.

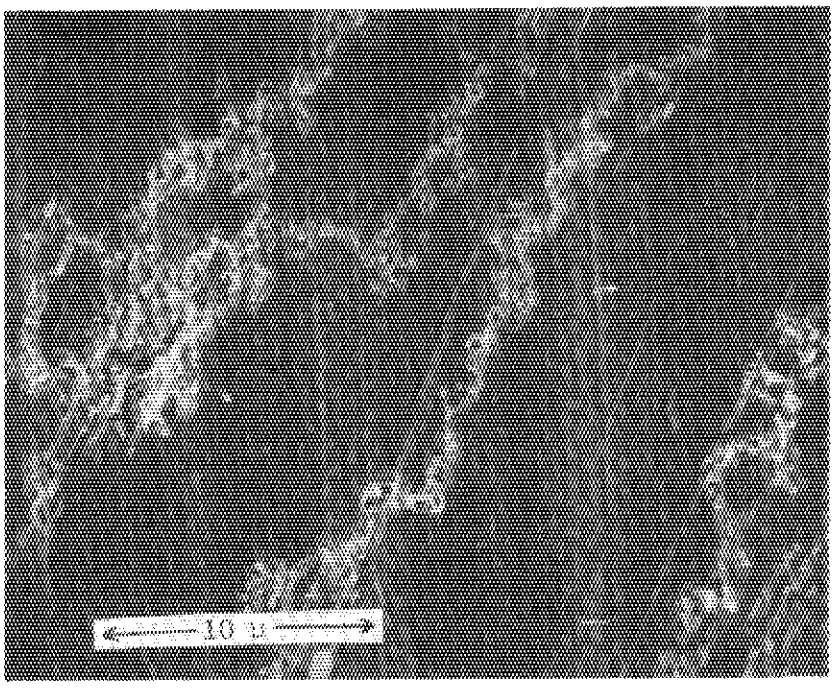

Fig.II.2.5-7 Scanning electron micrographs of arc tracks on the electrically floated aluminum target located in a divertor.

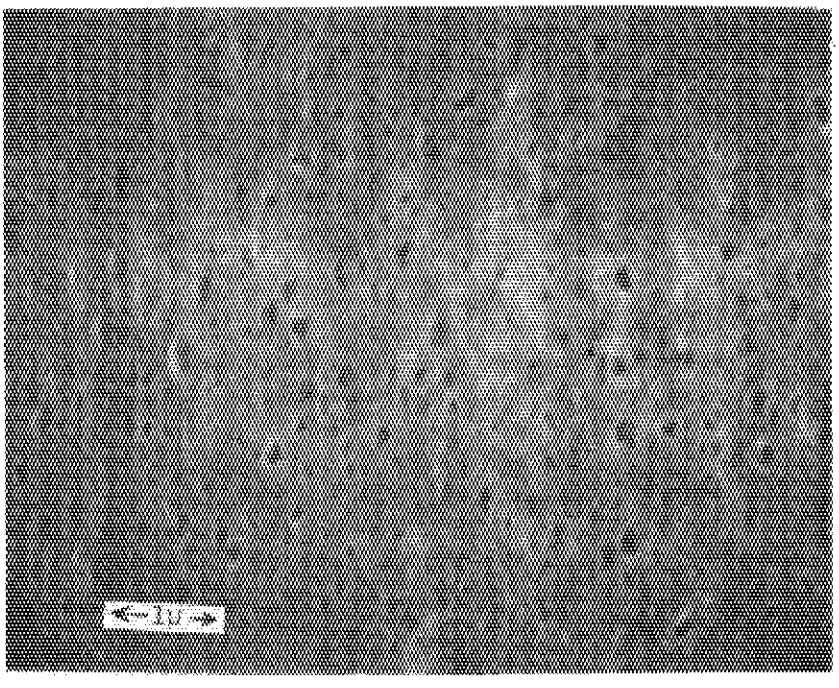

Fig.II.2.5-8 Scanning electron micrographs of the many melted spots on the electrically floated aluminum target in a divertor. These spots are created by high energy electrons from the main plasma.

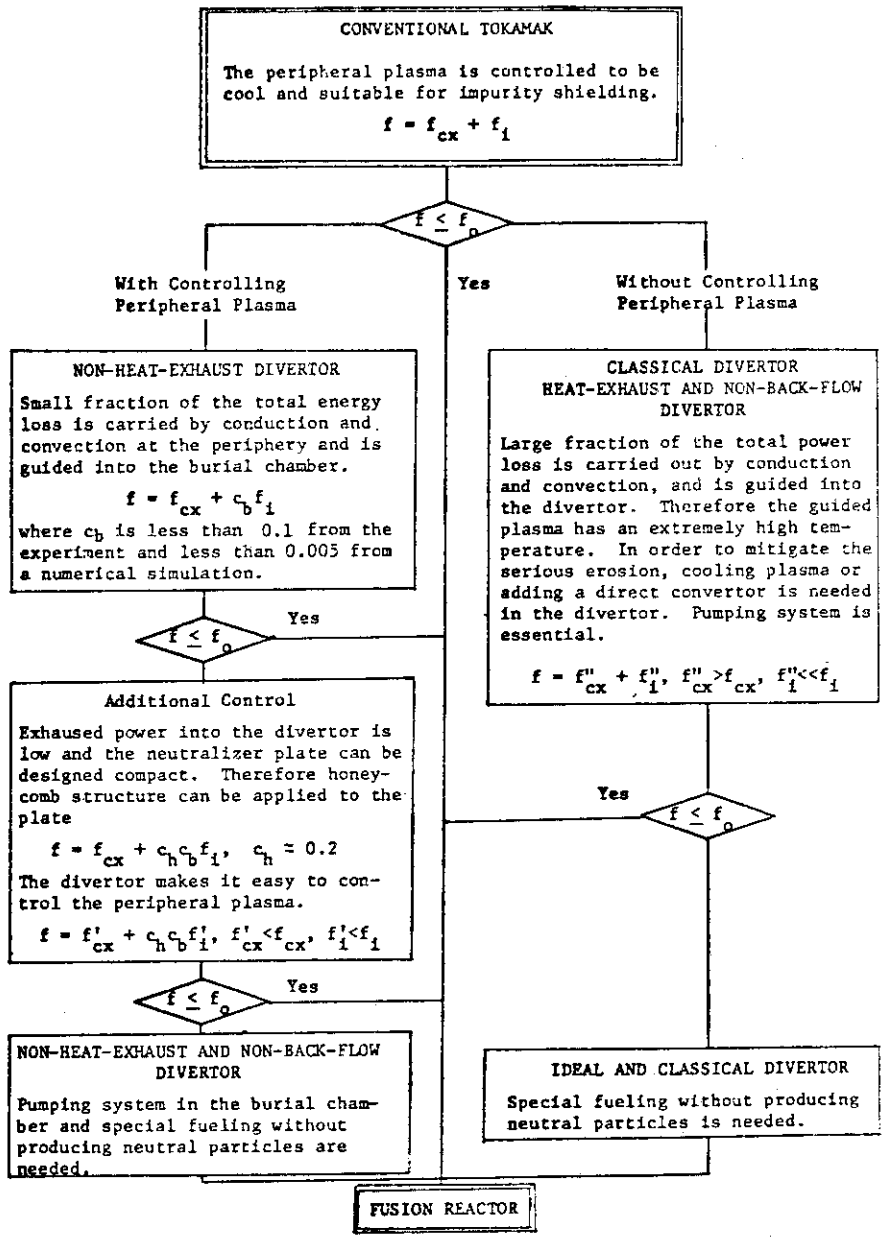

Classification of divertors for impurity control. f is fraction of impurities in a reactor plasma. f_{cx}: due to charge exchange neutral particle, f_i: due to ions, f_o: permissible level of impurities.

Fig.II.2.6-1 Classification of divertors for impurity control. f is fraction of impurities in a reactor plasma. f_{CX}: due to charge exchange neutral particle, f_i: due to ions, f_o: permissible level of impurities.

3. Diagnostics

3.1 Study on proton behavior in the JFT-2 tokamak from analyses of charge-exchanged fast atoms

Proton behavior in the JFT-2 hydrogen plasma under an 18 kG and 160 kA discharge was investigated from analyses on charge-exchanged atoms measured with a multi-channel neutral particle energy analyser .

The radial profiles of the transferred power from electrons to protons $Q_{ep}(r)$, charge exchange energy loss $Q_{cx}(r)$, and stored energy in protons $P_p(r)$ were determined from the experimental data. Expressions of Q_{ep}, Q_{cx} and P_p

$$Q_{ep}(r) = 4\sqrt{2\pi}\cdot e^4\cdot \ln\Lambda(r)\ \frac{n_e(r)\cdot n_p(r)\cdot\sqrt{m_e}}{m_p}\ \left(\frac{T_e(r)-T_p(r)}{T_e(r)^{3/2}}\right) \tag{1}$$

$$Q_{cx}(r) \simeq 4\left(\frac{2}{m_p\pi}\right)^{1/2}\cdot n_p(r)\cdot n_o(r)\cdot\langle\sigma_{ex}\rangle\cdot T_p(r)^{3/2} \tag{2}$$

and

$$P_p(r) = \frac{3}{2}\, n_p(r)T_p(r)\ . \tag{3}$$

Here the proton temperature $T_p(r)$ was measured with the 10-channel nautral particle energy analyser which observed horizontally different chords of the minor cross-section, the proton density $n_p(r)$ was determined from impurity concentrations measured by a vacuum ultraviolet spectroscopic measurements, the electron temperature $T_e(r)$ was measured with a Ruby Laser scattering, the electron density $n_e(r)$ was obtained from an Abel transformation of a line averaged density measured with a 4 mm microwave interferometer and the cold hydrogen atom density $n_o(r)$ was obtained by an Abel-transformed intensity of H_α line intensity and also the density near the plasma was determined from the charge-exchange neutral. The experimentally determined $Q_{ep}(r)$, $Q_{cx}(r)$, $P_p(r)$ are shown in Fig. II.3.1-1. The transferred power from electrons to protons was 33 kW, the charge-exchange loss was 16 kW, the thermal flux (involved the convection and condition) energy loss was 17 kW and the stored energy in protons was 470 J.

The radial distribution of energy conduction coefficient $\chi_{pex}(r)$ for the thermal (conduction and convection) flux is given by

$$\chi_{pex}(r) = \frac{\int_0^r \left(\frac{\partial P_p(r)}{\partial t} - Q_{ep}(r) + Q_{cx}(r)\right) r dr}{r\,\frac{\partial P_p(r)}{\partial r}}\ . \tag{4}$$

By using Eq. (4) the value of $\chi_{pex}(r)$ was experimentally determined from $P_p(r)$, $Q_{ep}(r)$ and $Q_{ex}(r)$ shown in Fig. II.3.1-2. The obtained $\chi_{pex}(r)$ is shown by the hatched area and found to be (5---8) $\times 10^3$ $cm^2 \cdot sec^{-1}$ through the minor radius. The width of $\chi_{pex}(r)$ corresponds to the ambiguity of $Q_{ep}(r)$ resulting from errors of electron temperature profiles.

The radial distributions of the various experimentally-estimated collision frequencies ($\nu_{p1}(r) = \frac{v_{Tp}(r)}{R\ q(r)} (\frac{r}{R})^{3/2}$: boundary collision frequency between a banana and plateau regions, $\nu_{p2}(r) = \frac{v_{Tp}(r)}{R\ q(r)}$: boundary collision frequency between a plateau and collisional regions, $\nu_p(r) = \nu_{pp}(r) + \nu_{pi}(r)$: proton collision frequency, $\nu_{pp}(r)$: proton-to-proton collision frequency, and $\nu_{pi}(r)$: proton-to-impurity ion collision frequency) are shown in Fig. II.3.1-3 on the JFT-2 plasma. Here $\nu_{pi}(r)$ was determined from density profiles of oxygen ions (OIX, OVIII, OVII and OVI) measured with a grazing incidence vacuum monochromator, because the other impurity (C, Fe, Mo) ions were below one percent of oxygen through the minor radius. From the figure it is found that the proton collision frequency $\nu_p(r)$ exists in the plateau region.

The thermal conductivity on protons in the banana or plateau region from the neoclassical theory is given by

$$\chi_{pth}(r) = \frac{0.68}{1 + 0.36\ \nu_p^*(r)} n_p(r)\nu_p(r)\rho_\theta^2(r)(\frac{r}{R})^{1/2} \qquad (5)\ ^2$$

where $\nu_p^*(r) = \frac{\nu_p(r)}{\nu_{p1}(r)}$, R major radius and ρ_θ poloidal Larmor radius. By using the equation the theoretical thermal conductivity $\chi_{pth}(r)$ is calculated from the values of $n_p(r)$, $\nu_p(r)$ and $\nu_{p1}(r)$ (shown in Fig. II.3.1-3) and ρ_θ. The value of ρ_θ is calculated from the current distribution which is assumed to be proportional to $[T_e(r)]^{3/2}$ and $[Z_{eff}(r)]^{-1}$. The value of $\chi_{pth}(r)$ is shown by the dotted line in Fig. II.3.1-2. It is found from the figure that the experimental value $\chi_{pex}(r)$ has approximately the same magnitude and radial dependence as the theoretical value by Hinton et al. $\chi_{pth}(r)$ within a factor of 2.

Since the over-all convection energy loss estimated from the particle confinement time of protons was about $\frac{1}{4}$ of the total thermal loss, the convection loss does not play an important role to the present analyses. Considering the enhancement of the H_α-line intensity at r > 20 cm, however the difference in a peripheral region between the value of χ_{pex} and χ_{pth} may be interpreted by the convection energy loss. Consequently the proton thermal conductivity seemed to agree with that predicted from the neoclassical

theory within a factor of 2. Thus the proton behavior in the JFT-2 plasma could be explained by the neoclassical theory.

3.2 Ion temperature characteristics of upgraded DIVA

In order to confirm the reliability on measurements of ion temperature and to determine ion temperature profiles on hydrogen plasmas in the upgraded DIVA, the spectrum of charge-exchanged atoms and Doppler broadening of impurity ion lines were simultaneously measured[3]. The radial profiles of spectral intensities emitted from various impurity ions with different ionic charges were beforehand measured to confirm that the emission intensities had their localized peaks at a specified position of the minor cross-section. Then the broadenings of the spectral lines in a vacuum uv or ultraviolet region were measured with a 1 meter Czerny-Turner type vacuum monochromator. The ion temperatures were spectroscopically determined from Doppler broadenings of impurity lines OVII(1623 Å), NV(1239 Å), CIV(1548 Å), CV(2271 Å), CIII(2297 Å) and CII(2837 A). Charge-exchanged fast hydrogen-atoms leakaged from DIVA hydrogen-plasmas were analysed with a 10-channel neutral particle energy analyser.

The central ion temperatures were also investigated in the wide parameter ranges of the toroidal magnetic fields $6 \leqq B_t \leqq 20$ KG, plasma currents $10 \leqq I_p \leqq 48$ KA and averaged electron densities $0.6 \leqq n_e \leqq 3.8 \times 10^{13}$ cm ^{3}.

Measurements of ion temperature profile were made on the hydrogen plasma under the condition of toroidal field 20 KG, maximum plasma current 28 KA and ratio of divertor current to plasma current 1.2. Figure II.3.2-1 shows the radial profile of temperature (a) from charge-exchanged atoms and from Doppler broadenings of impurity lines as well as the localizations (b) of spectral emissions from the impurity lines, at 10 milliseconds. In this figure the domains denoted by oblique lines present Doppler temperatures determined from the measured broadenings and localizations of different impurity line emissions, and cross points refer to temperatures from energy spectra of charge-exchanged atoms measured on the lower half plane.

Figure II.3.2-2 shows that the central ion temperature scaling of DIVA is found to be

$$T_i(0)[\text{in eV}] = 5.5\times10^{7}\cdot(I_p\cdot B_t\cdot\overline{n_e}\cdot R^2)^{1/3} \quad , \tag{6}$$

where I_p is in ampere, B_t in Gauss, $\overline{n_e}$ in cm^{-3}, and the major radius R in

cm (R = 60 cm for the DIVA device). The ion temperature scaling did not change whether with or without the divertor. Accordingly the experimental result suggests that the divertor does not influence remarkably the ion confinement.

3.3 Absolute calibration of a grazing-incidence vacuum monochromator

A 3-m grazing-incidence monochromator was absolutely calibrated in a wavelength region from 40 to 1100 Å by using a branching-ratio method on JFT-2 and DIVA hydrogen discharges[4]. The monochromator was equipped with a platinum-coated, 600 grooves/mm, ruled grating and with a windowless photomultiplier (Cu-Be photo-cathode). Table II.3.3-1 shows branching line-pairs used to calibrate the vacuum monochromator. Most of the values in the table were quoted from Ref. 5 by Wiese et al. and the transition probability of the 40.73 Å CV line was taken from the value calculated by Drake and Dalgarno[6]. Because of a limited wavelength resolution of the vacuum monochromator, impurity lines from the sub-levels of the multiplet in the table, except the CV line, were measured without resolving their fine structures. The ratio of transition probabilities was calculated under the assumption that the sub-levels were populated according to their statistical weights. Figure II.3.3-1 shows the sensitivity $S(\lambda_{nm})$ obtained for the 3-m grazing-incidence vacuum monochromator and detector system in the wavelength region of 40 to 1100 Å. The sensitivity is indicated in $mV/photon \cdot sec^{-1}$. Filled (or open) circles were the experimental sensitivities determined on JFT-2 (or DIVA) discharges. Due to the limited wavelength-resolution of the vacuum monochromator, it was found that the measured intensity of the 40.73 Å CV line ($^1S_0$-$^3P_1{}^0$) included the 40.27 Å CV line ($^1S_0$-$^1P_1{}^0$). The decomposition of these two CV lines was carried out by using the intensity ratio of the 40.73 Å to 40.27 Å lines observed photographically with the discharges whose electron temperatures were of a few hundred eV. The sensitivity curve in Fig. II.3.3-1 was obtained by drawing a curve fitting the experimentally determined results. The maximum sensitivity of the curve at about 500 Å seems to be due to an increase in photoelectric yield of the Cu-Be photo-cathode detector. The blaze effect of the grating appears as an increase of the sensitivity curve near 100 Å.

Considering errors in the geometrical factors for the experimental setup and in calibration of the visible monochromator with the standard lamp, uncertainties in the transition probabilities, and the reproducibility of

JFT-2 and DIVA discharges, errors in the calibration experiment were estimated to be typically within several ten percents and were largely ascribable to a lack of the accuracy in the values of transition probabilities.

3.4 Spectroscopic measurements of impurities on upgraded DIVA

We studied spectroscopically the concentration and the radiation loss due to low-Z and high-Z impurities[7] in the upgraded DIVA hydrogen plasma with a divertor under its magnetic field of 20 kG and peak plasma current of 40 kA. During the discharge the ratio of divertor current I_D and to the plasma current I_p was held to be 1.2. The central electron temperature and density of the DIVA plasma were 700 eV and 8.2×10^{13} cm^{-3}, respectively. Spectroscopic measurements were made in the region of 10 to 1300 Å by using an absolutely calibrated 3-m grazing-incidence vacuum monochromator. The absolute calibration of the monochromator was described in sub-section 3.3.

Figure II.3.4-1 shows a microphotometer trace of the spectrograph in a wavelength region of 10 to 350 Å. Identified spectral lines were mainly ones emitting from low-Z impurity ions such as oxygen, carbon and nitrogen. Resonance-lines of the OVIII (18.97 Å), NVII (24.78 Å) and CVI (33.74 Å) originated from the 1^2S-2^2P^0 transition of hydrogen-like ions were quickly identified and the OVII (21.60 Å), NVI (28.79 Å) CV (40.27 Å) lines were emitted from the 1^1S-2^1P^0 transition of helium-like ions. Intercombination lines of the helium-like ions due to the 1^1S-2^3P^0 transition were identified as the OVII (21.80 Å), NVI (29.08 Å) and CV (40.73 Å) lines. Metal-impurity lines such as Au, Cu, et al. could not be clearly identified in the region of 10 to 350 Å since atomic data for their metalic ions were extremely lacked. In the spectrographic measurements, a very interesting emission spectrum was one due to closely-crowded many lines observed in the region of 42 to 200 Å just like a continuum spectrum. Most of the emission spectrum of the many lines were found to be originated from highly ionized Au ions from the fact that their emission was increased by injecting pure gold into the plasma with a laser blow-off technique[8].

Figure II.3.4-2(a) shows radial profiles of the ground-level population density of carbon and oxygen ions at 10 msec obtained on the basis of the coronal model. Profiles of the electron temperature and density are shown by a broken and a dashed-dot curves in the figure, respectively. Their values at the plasma center were 700 eV and 8.2×10^{13} cm^{-3}. Solid curves

show radial profiles of ground-level population density of the O^{+7}, O^{+6}, O^{+5} O^{+4} and C^{+5} ions. The densities of the O^{+7} and O^{+6} ions were an order of 10^{12} atoms$\cdot$cm^{-3}, and those of the O^{+5} and O^{+4} ions were much lower by two and three orders than the O^{+7} and O^{+6} ion densities. The C^{+5} ion had its density of 2×10^{11} atoms$\cdot$cm^{-3}. Although a radial profile of the C^{+4} ion was not measured in the present experiment, the average density of the C^{+4} ion was estimated to be about 1×10^{11} atoms$\cdot$cm^{-3} from the line-radiance measured through the plasma center. Considering contributions from the O^{+8} and C^{+6} ions, the total contents of oxygen and carbon impurities were approximately 2 % and at most 1 % of the electron density integrated over the whole minor cross-section in the DIVA plasma. Also, the effective ionic charge was found to be (2.4--3) at 10 msec and this value agreed fairly with that derived from the plasma conductivity and the electron temperature. This result indicated that oxygen was a dominant impurity which defined the plasma conductivity of the upgraded DIVA tokamak and that the gold impurity did not play an important role in the conductivity.

Figure II.3.4-2(b) shows the radial profile of line-radiation power from oxygen ions in each charged state (solid curves). The value on the ordinate in the figure was the radiation power multiplied by $4\pi^2 rR$, where r is the minor radius and R the major radius of the DIVA device, i.e., R = 60 cm. In the figure, the broken curve is sum over the radiation power from O^{+7} to O^{+4} ions. Integrated this line-radiation power for oxygen ions over the minor radius, the total line-radiation power was obtained to be 25 kW. Also, the radiation power due to carbon ions was estimated at most to be 5--10 kW. Therefore, the total line-radiation power loss due to low-Z ions from the DIVA plasma was estimated to be approximately 30--35 kW. This value was corresponding to 21--25 % of the Joule-input power of 140 kW.

Figure II.3.4-3 shows the time-evolution of the radiance per unit wavelength for the many line emission (in Watt$\cdot$cm$^{-2}\cdot$sr$^{-1}\cdot$Å^{-1}) against the observed wavelength. The radiance in the figure was that measured along the central horizontal-chord. This radiance was determined by unfolding the lights in the second-order of the many line emission from 42 to 100 Å and in the third-order of the emission from 42 to 67 Å from the measured emission intensity. The central electron temperature T_{eo} is also presented in the figure. In the initial phase of the discharge, when the central electron temperature was less than 200--300 eV, the intense radiation of the many lines concentrated in the region above 120 Å. As the electron temperature

increased in time the emission of the many lines above 120 Å was intensified and simultaneously the spectrum extended towards a shorter wavelength region. After 8 msec when the central electron temperature was more than 600 eV, the spectrum of the many lines was found in the region below 110 Å in addition to one in the region of 120 to 200 Å. The emission at 8--14 msec was found that there were three luminous peaks at 42--65 Å, 80--110 Å and 120--200 Å. Also, it was evident that the spatial distribution of their radiation indicated a peaked profile at a shorter wavelength and a hollow profile at a longer wavelength. As shown in Fig. II.3.4-2(b), the rdiation power due to the many lines (dashed-dot curve) was found to be accumulated in the intermediate region near the minor radius of 3--6 cm, where the electron temperature was 400--200 eV. Integrated the radiation power over the minor radius, the total radiation power loss due to the many lines (42--200 Å) was estimated to be 27 kW which corresponded to 19 % of the Joule-input power. The total radiation power loss due to low-Z and high-Z impurities corresponded to 41 ∿ 44 % of the Joule-input power.

3.5 Estimation of oxygen diffusion flux from spectroscopic measurements

The radial profiles of impurity ion densities were determined by the coronal model from the absolute intensity of the first resonance line emission of the impurity ions which was measured by the calibrated 3 m grazing incidence vacuum monochrometer[9].

Once the radial profiles of the particle densities are known, the radial profile of the particle flux Γ_i^{EXP} (i indicates electron, proton or impurities) is readily derived from the following particle conservation equation:

$$\frac{\partial n_i}{\partial t} = -\frac{1}{r}\frac{\partial}{\partial r}(r\Gamma_i) + \begin{array}{l}\text{creation or anihilation of particle}\\ \text{by atomic processes such as ionization}\\ \text{and recombination}\end{array} \qquad (7)$$

Present observation of particle difusions were summarized as follows:

IMPURITIES (oxygen; Fig. II.3.5-1, 2)

1) The neo-classical transport theory including the multi-ion components explain the observed radial profiles of the $\Gamma^{exp}(0)$ considerably well. Oxygen-oxygen collision play an important role in the oxygen transport, which prevent any peculiar accumulation of oxygen ions in the central

region of the plasma.

2) The magnitude of $\Gamma^{EXP}(0)$ is one order of magnitude larger than that predicted by the neo-classical theory $\Gamma^{NC}(0)$.

PROTONS (Fig. II.3.5-3)

3) In the inner region of the plasma ($r < 15$ cm), proton appears to diffuse in a fashion of the neo-classical transport including the impurity effect. The main diffusion process is due to the temperature gradient.

4) In the outer region of the plasma ($r > 15$ cm), anomalous diffusion is observed.

ELECTRONS (Fig. II.3.5-4)

5) In the whole region of the plasma the electron diffusion is greately enhanced than that expected by the neo-classical theory.

6) At about $r < 10$ cm the electron diffusion is of the order of that expected by the dissipative trapped electron instability. At other region of the plasma the observed diffusion is much larger than that due to the dissipative trapped electron mode.

7) In the central region of the plasma ($r < 10$ cm) the enhanced electron diffusion has a correlation of the enhanced impurity diffusion.

8) In the outer region of the plasma ($r > 15$ cm), the enhanced diffusion of electrons has a correlation with the enhanced proton diffusion.

References

(1) Takeuchi, H., Shoji, T., Funahashi, A. and Takahashi, K.: J. Phys. Soc. Japan 44 1363 (1978).

(2) Hinton, F.L., Wiley, J.C., Düchs, D.F., Furth, H.P. and Rutherford, P.H.: Phys. Rev. Letters 29 698 (1972).

(3) Sugie, T., Takeuchi, H., Kasai, S., Funahashi, A., Takahashi, K. and Kimura, H.: J. Phys. Soc. Japan 44 1960 (1978).

(4) Kasai, S., Funahashi, A., Konoshima, S., Nagami, M., Sugie, T. and Mori, K.: Japan. J. appl. Phys. 17 (1978) 1625.

(5) Wiese, W.L., Smith, M.W. and Glennon, B.M.: Atomic Transition Probabilities (National Bureau of Standards, Washington, 1966) vol.1.

(6) Drake, G.W.F. and Dalgarno, A.: Astrophys. J. 157 (1969) 459.

(7) Kawai, S., Funahashi, A., Nagami, M., Sugie, T. and Yamauchi, T.: to be published in J. Phys. Soc. Japan.

(8) Yamauchi, T., Nagami, M., Sengoku, S. and Kumagai, K.: JAERI-M 7809 (in Japanese).

(9) Shiho, M., et al.: in preparation for publication.

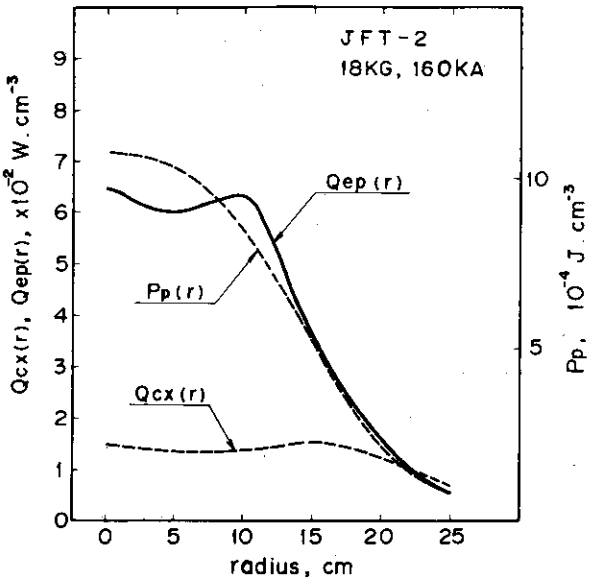

Fig.II.3.1-1 Radial distributions of transferred power from electrons to protons $Q_{ep}(r)$, stored energy in protons $P_p(r)$ and charge exchange loss $Q_{cx}(r)$.

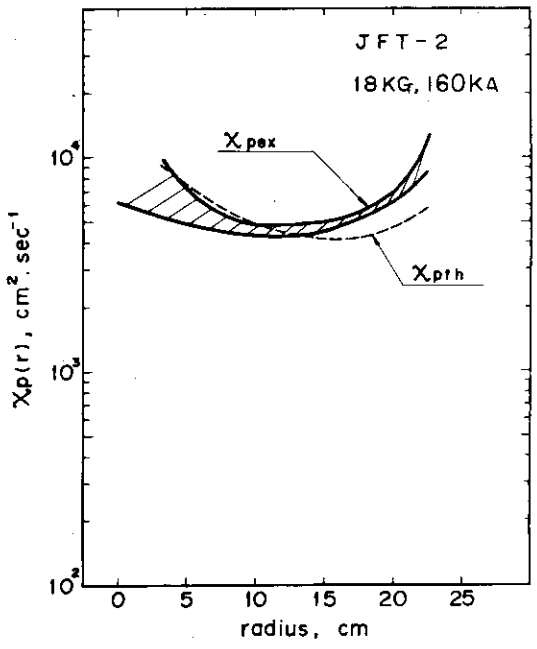

Fig.II.3.1-2 Comparison between the experimentally-determined thermal proton conductivity $\chi_{pex}(r)$ and the theoretical one $\chi_{pth}(r)$ by Hinton et al.

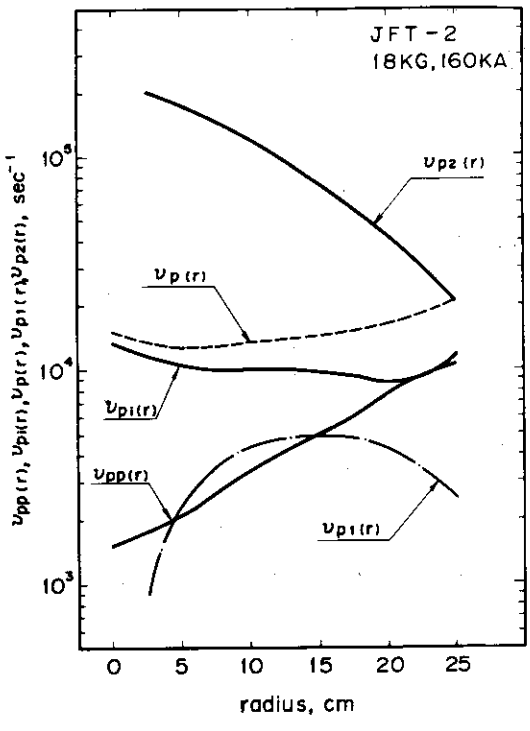

Fig.II.3.1-3 Radial distributions of various proton collision frequencies ($\nu_{p1}(r)=(\frac{r}{R})^{3/2}\frac{v_{TP}}{Rq(r)}$, $\nu_{p2}(r)=\frac{v_{TP}}{Rq(r)}$, $\nu_{pp}(r)$; proton-to-proton collision, and $\nu_{pi}(r)$; proton-to-impurity ion collision, with the safety factor q(r)).

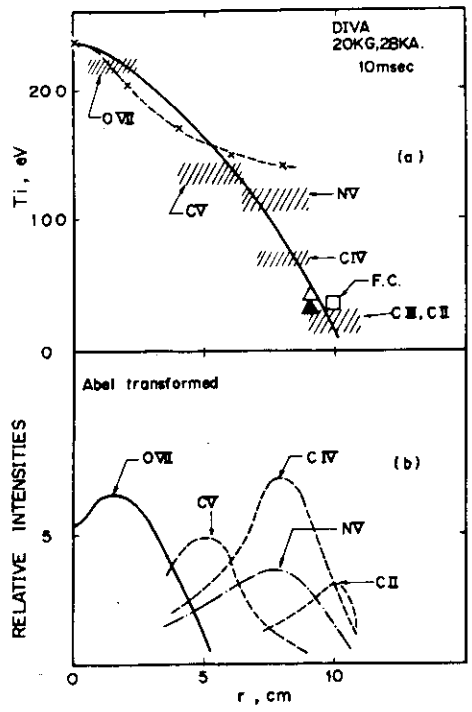

Fig.II.3.2-1 Radial profile of ion temperature (a) and localization of emission intensities from impurity lines (b) at 10 msec.

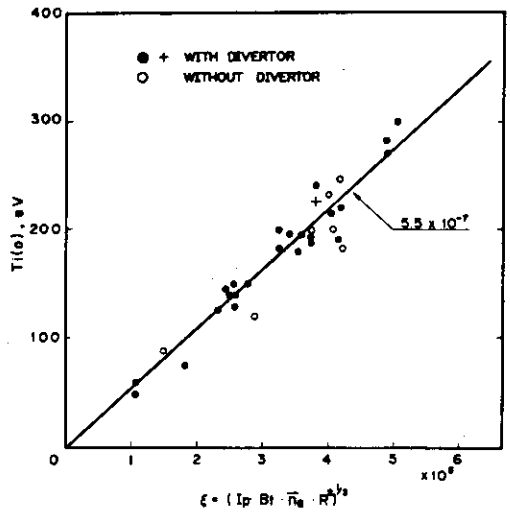

Fig.II.3.2-2 Scaling low of central ion temperatures obtained on the DIVA device.

Table II.3.3-1 Branching line-pairs used in the calibration experiment.

	Vacuum Ultra-Violet Lines			Ultra-Violet and Visible Lines		
	Wave-Length (Å)	Transition	Transition Probability (S^{-1})	Wave-Length (Å)	Transition	Transition Probability (S^{-1})
CV	40.73	$1s^2\ ^1S_0 - 2p\ ^3P_1^o$	2.84×10^7	2277.92	$2s\ ^3S_1 - 2p\ ^3P_1^o$	5.65×10^7
OVI	150.09	$2s\ ^2S_{1/2} - 3p\ ^2P_{3/2}^o$	2.59×10^8	3811.35	$3s\ ^2S_{1/2} - 3p\ ^2P_{3/2}$	0.513×10^8
	150.12	" $_{1/2}$ - " $_{1/2}$	"	3834.24	" $_{1/2}$ - " $_{1/2}$	0.503×10^8
OIV	238.57	$2p\ ^2P_{3/2}^o - 3d\ ^2D_{3/2}$	3.50×10^8	3411.76	$3p\ ^2P_{3/2}^o - 3d\ ^2D_{3/2}$	1.15×10^8
	238.36	" $_{1/2}$ - " $_{3/2}$	3.00×10^8	3403.58	" $_{1/2}$ - " $_{3/2}$	0.96×10^8
	238.58	" $_{3/2}$ - " $_{3/2}$	5.9×10^8	3413.71	" $_{3/2}$ - " $_{3/2}$	0.191×10^8
CIV	312.42	$2s\ ^2S_{1/2} - 3p\ ^2P_{3/2}^o$	4.57×10^8	5801.51	$3s\ ^2S_{1/2} - 3p\ ^2P_{3/2}^o$	0.319×10^8
	312.46	" $_{1/2}$ - " $_{1/2}$	4.55×10^8	5812.14	" $_{1/2}$ - " $_{1/2}$	0.316×10^8
OIII	320.98	$2p^2\ ^1D_2 - 3d\ ^1F_3^o$	1.90×10^8	3961.59	$3p\ ^1D_2 - 3d\ ^1F_3^o$	1.28×10^8
OII	515.50	$2p^3\ ^2P_{3/2} - 3d\ ^2D_{3/2}$	1.5×10^8	4943.06	$3p\ ^2P_{3/2}^o - 3d\ ^2D_{3/2}$	1.06×10^8
	515.64	" $_{1/2}$ - " $_{3/2}$	1.2×10^8	4941.12	" $_{1/2}$ - " $_{3/2}$	0.83×10^8
	515.64	" $_{3/2}$ - " $_{3/2}$	2.4×10^8	4955.78	" $_{3/2}$ - " $_{3/2}$	0.256×10^8
H	1025.72 (L_β)	1 - 3	5.575×10^7	6562.8 (H_α)	2 - 3	4.410×10^8

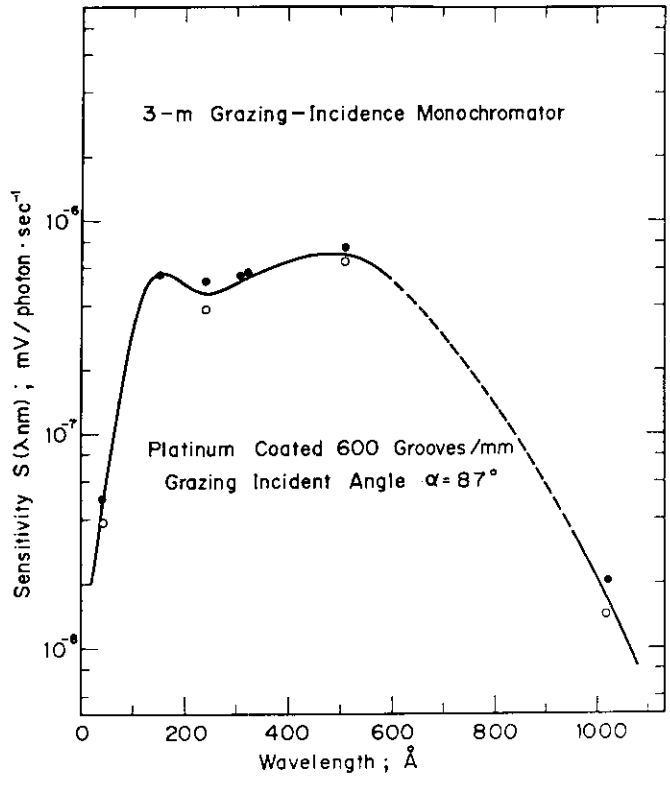

Fig.II.3.3-1 Sensitivity of a 3-m grazing-incidence vacuum monochromator-detector system.

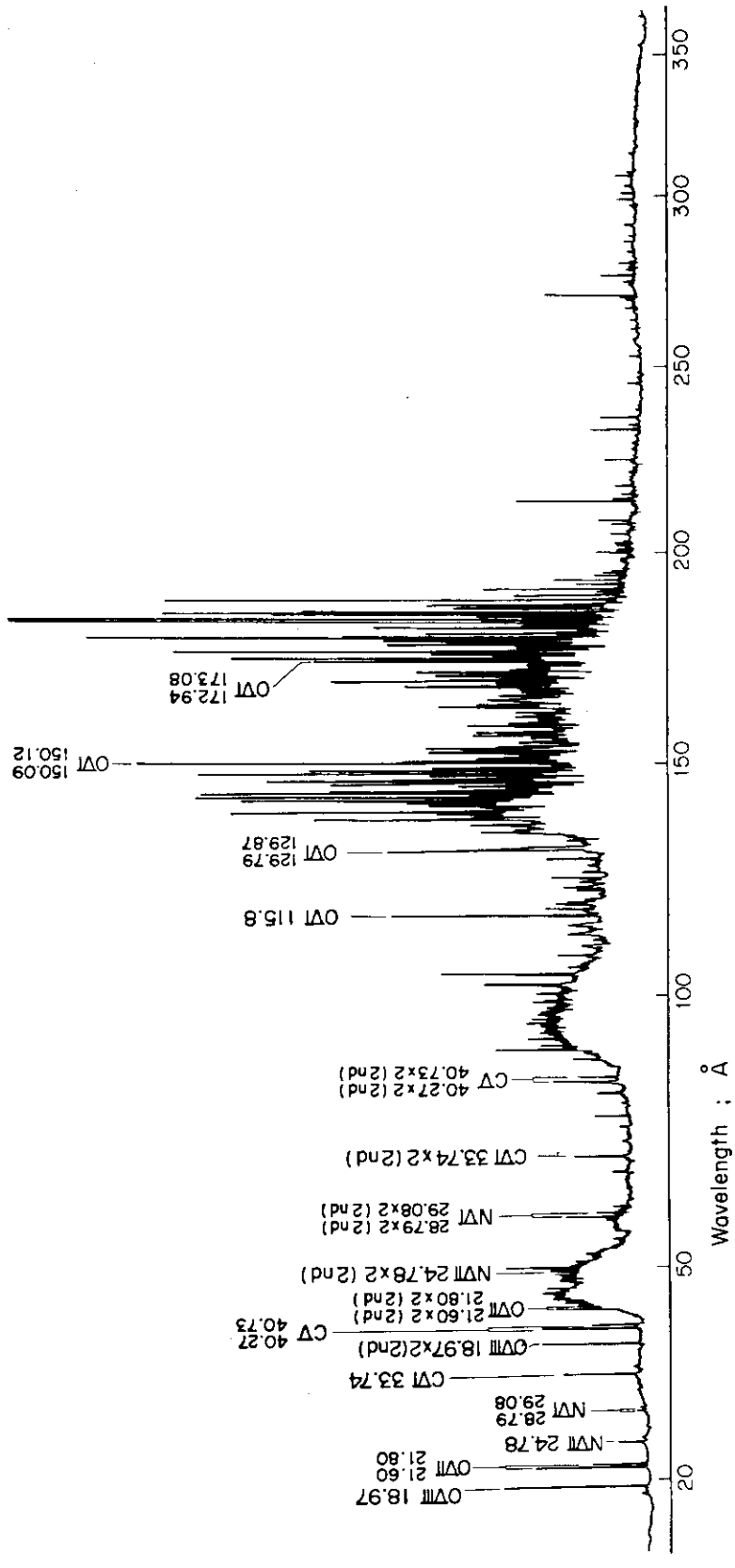

Fig.II.3.4-1 Microphotometer trace of the spectrograph of the emission spectrum measured on the DIVA plasma.

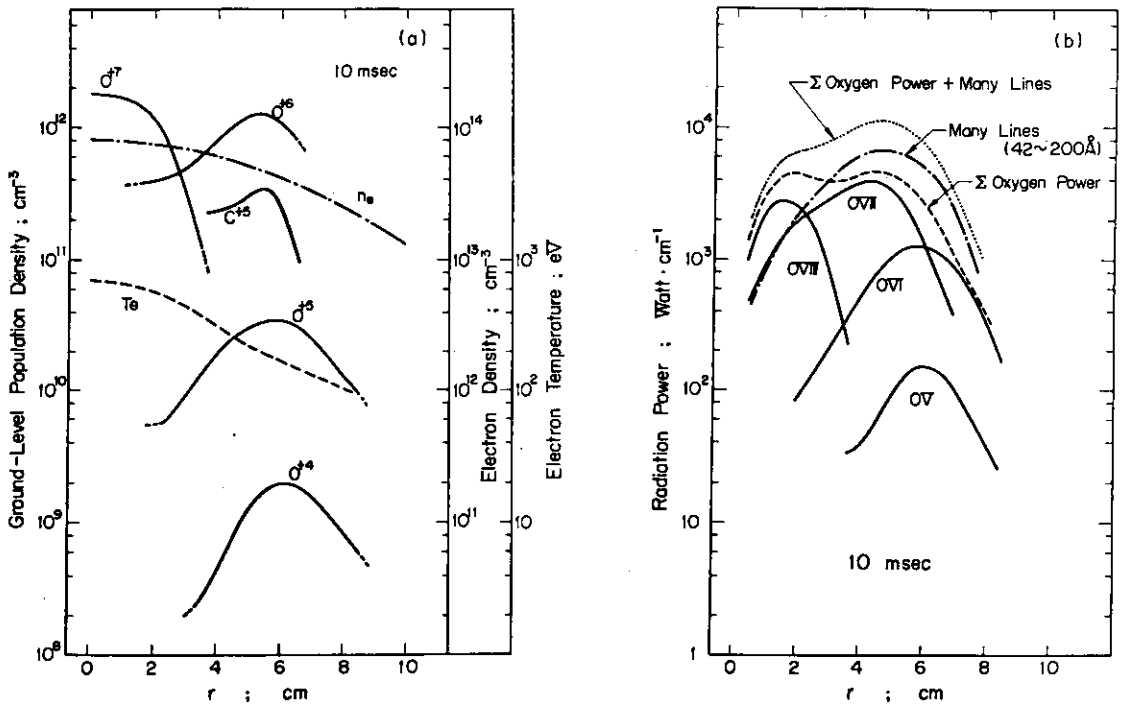

Fig.II.3.4-2 Radial profiles of population density of oxygen and carbon ions in various ionized states at 10 msec. The broken curve indicates the profile of electron temperature and the dashed-dot curve indicates the profile of electron density (a), and radial profiles of radiation power multiplied by $4\pi rR$ (b).

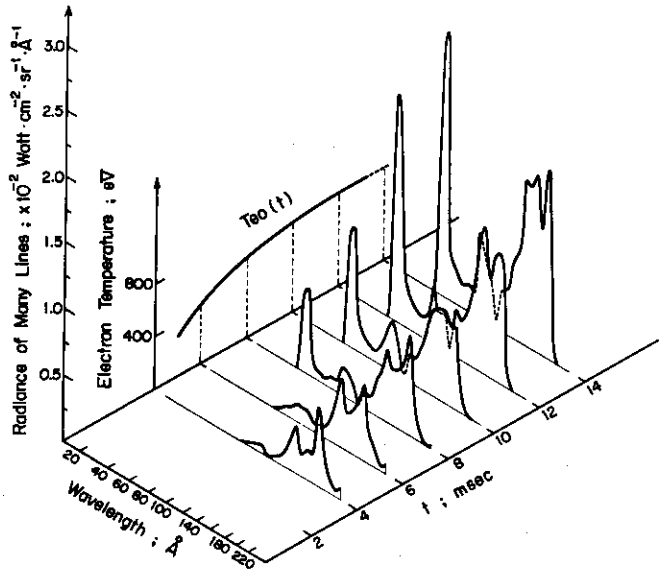

Fig.II.3.4-3 Time-evolution of the weavelength distribution of radiance of the many lines.

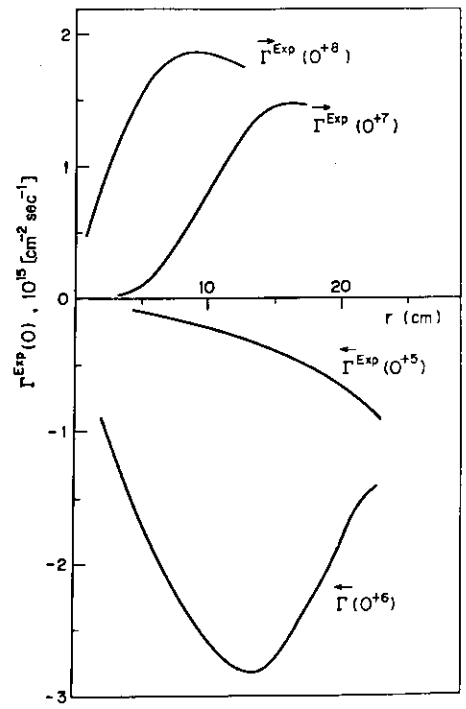

Fig.II.3.5-1 Radial profiles of experimental oxygen flux $\Gamma^{EXP}(0)$ derived by the particle conservation equation.

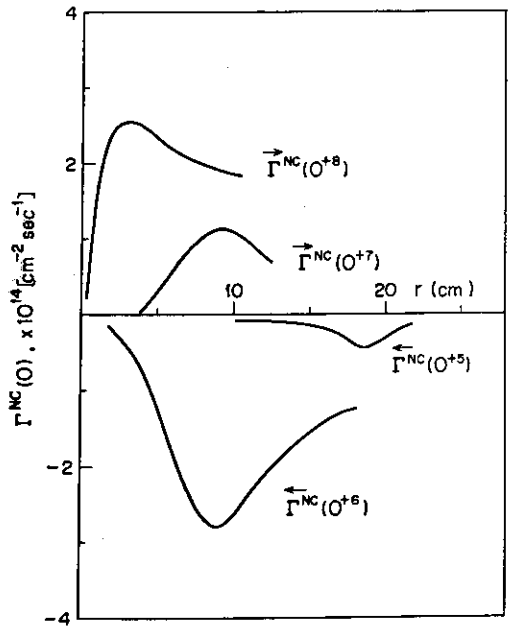

Fig.II.3.5-2 Radial profiles of theoretical oxygen flux $\Gamma^{NC}(0)$ calculated by the neoclassical theory in the collisional regime.

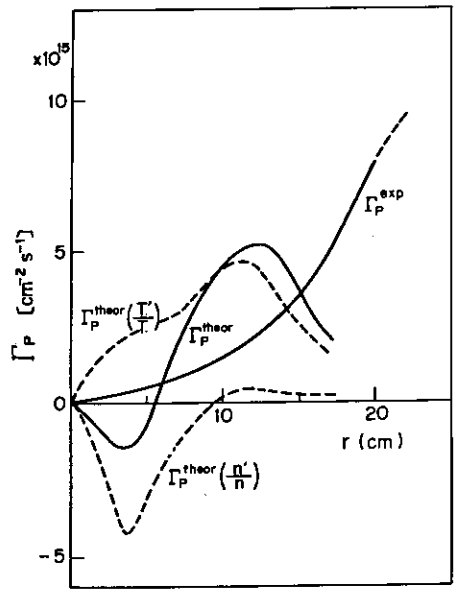

Fig.II.3.5-3 Radial profiles of experimental proton flux Γ_p^{EXP} and theoretical one Γ_p^{theor}. which is calculated by the neoclassical theory in plateau regime.

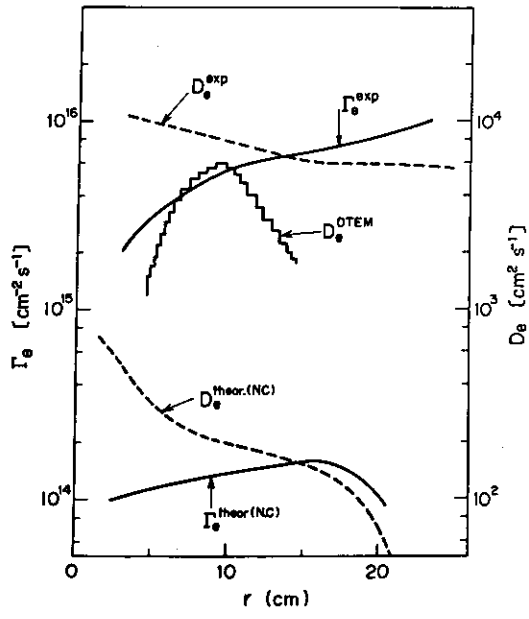

Fig.II.3.5-4 Radial profiles of experimental electron flux Γ_e^{EXP} and theoretical ones which are calculated by the neoclassical theory Γ_e^{NC} in plateau-bananna transition region and anomalous theory (DTEM) Γ_e^{DTEM}.

III. OPERATION AND MAINTENANCE

1. Introduction

Facility Operation and Engineering Section is engaged in operation and maintenance of JFT-2 and JFT-2a tokamak and development of auxiliary equipments and instruments.

In the fiscal year 1977, a 21,740 kW flywheel motor-generator was used in common to JFT-2 and JFT-2a machines. The JFT-2 machine was operated in cummulative total 200,000 shots since its start in 1972. Co-operative work was made in remodelling of JFT-2 such as power supply, control and vacuum system. JFT-2 and JFT-2a were operated on schedule with careful maintenance.

2. Operation and maintenance of JFT-2

JFT-2 was operated in schedule and for many experiments (Fig. III-1). Operation was suspended for removal of a neutral beam injection system, installation of a lower hybrid resonance heating system, recovery in insulation of M-G.

In summer the cooling water system was remodelled to stainless steel pipes, spiral type heat exchanger and new cooling towers. The thyrister trigger of ignitrons in capacitors was rebuilt to simplify the sequence control. Cathode wires of tungsten of electron beam pre-ionization equipment failed, but with many consideration such as 1.2 kV high voltage between vacuum chamber and wires and careful TIG welding on wires, it successfully functioned.

Insulation of DC generator #2 of M-G dropped to 0.1 MΩ at 500 V DC. It was overhauled and cleaned of carbon dust by steaming in Hitachi, Ltd., so its insulation was thus restored to 0.9 MΩ.

3. Operation and maintenance of JFT-2a

JFT-2a was also operated on schedule and performed experiments satisfactorily (Fig. III-2). After upgrade to 20 kG, the toroidal field power was supplied by M-G and thyrister power was used for discharge cleaning. The 20 kG discharge became a normal tokamak discharge after some improvement on JxB type pre-ionization gun. To prevent cooling water fluctuation of toroidal coils a water tank was installed.

4. Development of equipments and instruments

4.1 JFT-2

(1) In plasma-wall interaction experiments, means of reducing the impurity concentration is very important. For the purpose, titanium coating equipment for the surface of vacuum chamber was designed and set in JFT-2. Its specifications are: a movable titanium ball going in and out the chamber in each shot, total usable titanium 35 g, maximum sublimation rate 0.5 g/h, operation life time 70 hours, power supply 750 W, stroke length 180 mm by 3--5 kg/cm^2 pneumatic control (Fig. III-3). The oxygen contamination was thus reduced to 1--2 % of plasma density[1].

(2) Low power, high repetition rate discharge cleaning (Taylor type discharge cleaning: TDC) is effective for removal of oxygen from the chamber. In JFT-2, a TDC device consists of constant toroidal field and ohmic power supplied by capacitors was installed. Constant toroidal field about 2 kG was achieved by changing the sequence control. Ohmic power was supplied by two 10 kV, 200 μF capacitor banks, ignitrons and controllers, and the maximum repetition time is 0.5 msec (2 pulse per 1 sec) (Fig. III-4). Its effects is now studied by experiment[2] and preliminary results suggest the effectiveness (Fig. III-5).

(3) JxB gun type pre-ionization equipment was designed in power supply; 10 kV, 100 μF capacitors, and electrodes with tungusten tips. A preliminary experiments was done.

(4) In remodelling of JFT-2, power supply and control system for horizontal and vertical positions of plasma were designed and studied in detail. These were ordered to Hitachi, Ltd. in March 1978. In final design horizontal position control of plasma is made by 0.4 kG constant vertical field (B_{vd}) supplied from a 196 kW thyrister rectifier, pulse vertical field (B_{vp}) supplied from a 140 kJ capacitors and 0.1 kG control vertical field (B_{vc}) supplied from a 800 kW thyrister rectifier controlled by digital computer HIDIC-80 system (Fig. III-6). Vertical position control of plasma is made by 60 G horizontal field (B_h) controlled by digital computer like B_{vc}.

(5) The purpose of remodeling JFT-2 is mainly for plasma-wall interaction experiments, so an extremely ultra high vacuum system is necessary. A schematic diagram of the system finally designed is shown in Fig. III-7. Two turbomolecular pumps (TMP) i.e; 1,700 1/s N_2 of TVP-6000 and 1,900 1/s N_2 of TPH-2000, and 2,700 1/s N_2 of 20 °K Cryo-pump from two pumping lines. The total pumping speed at the vacuum chamber port is 1,680 1/s N_2. The seals use metal gasket bakable at 250 °C between TMP and vacuum chamber. The system aims at base pressure 1×10^{-8} Torr and total helium leak rate 5×10^{-5} Torr.l/s for the vacuum chamber of 3,000 litre volume and 3×10^{5} cm^2 surface.

(6) Lower hybrid resonance heating (LHRH) system was installed in August 1977. A vacuum system and cooling water system were designed in cooperation on Plasma Heating Labolatory.

4.2 JFT-2a

(1) An upgrade of toroidal field from 10 kG to 20 kG was achieved in April 1977 by Hitachi, Ltd. Its specifications are follows: coil number 16, maximum ampere-turn 6,000 kAT, maximum current 11,720 A, repetition time at maximum operation 5 minutes.

(2) To control the flow of gas during the discharge, the piezoelectric PV-10 valve was used and its specifications are followed; control voltage is 0--100 V DC, gas flow at maximum is 5--10 Torr.l/s, minimum time from closed to full open of PV-10 is 2 msec. This gas flow system could control the plasma density and its duration for requirement of experiments.

(3) In JFT-2a Taylor type discharge cleaning (TDC) device was installed March 1978. Its constant toroidal field 1.5 kG is supplied by thyrister power. Its ohmic power is supplied by 5 kV, 200 μF capacitors and repetition time 1--3 sec. Its effectiveness and utility appeared in the shortening of necessary discharge cleaning time.

(4) ICRF heating device was designed and fabricated. Cooperative works with Plasma Experiment Laboratory was performed, specially on the sequence control. In March 1978 its system was installed and functioned successfully at 25 MHz & 50 MHz and maximum power is 150 kW.

Month	APR	MAY	JUN	JUL	AUG	SEP	OCT	NOV	DEC	JAN	FEB	MAR
Operation Mode	NBI Heating Experiment	Vacuum Chamber was broken	Plasma – Wall Interaction experiments		Vacuum chamber was broken		LHRH experiments			stopage	LHRH experiments	
Maintenance & Installation	◦B vp coil insulation was broken	◦Ti-coating equipment was installed ◦MG was used in commo JFT-2 & 2a	◦ Cathode wires of electron beam pre-ionization equipment had troubles		◦Periodical maintenance was done	◦Thyrister trigger set of ignitrons was set	◦OH circuit had some troubles					

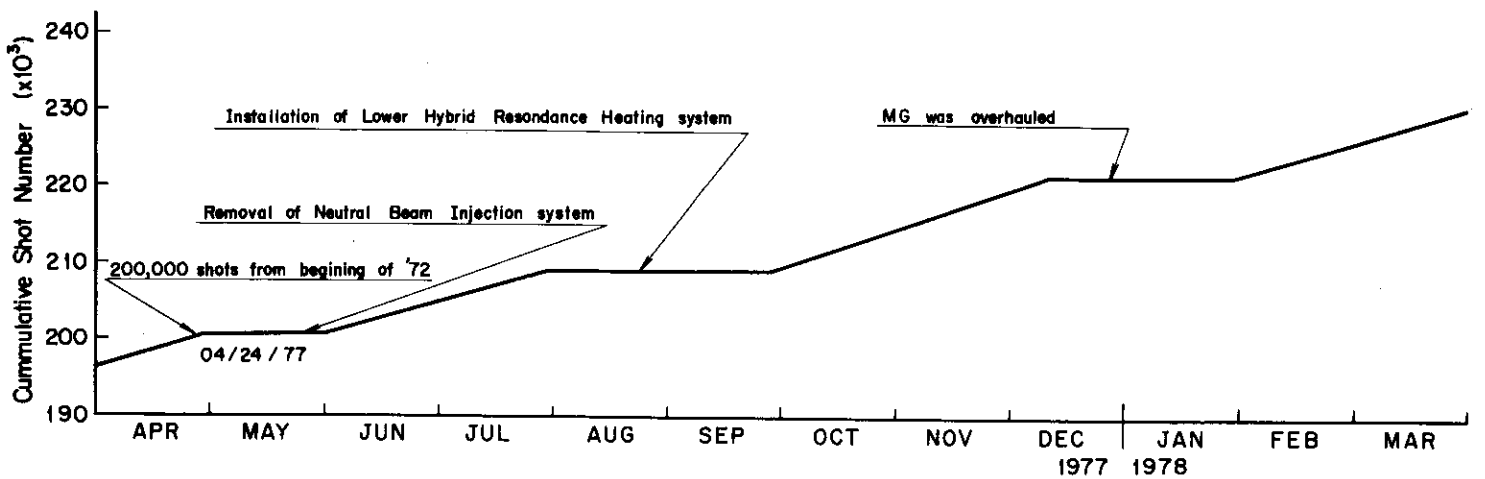

Fig. III-1 Operation of JET-2.

Month	APR	MAY	JUN	JUL	AUG	SEP	OCT	NOV	DEC	JAN	FEB	MAR
Operation Mode	Upgrade of toroidal field 20 kG		20 kG Divertor tokamak experiment							stopage	experiments	
Maintenance & Installation	∘ Installation of new 20 kG toroidal field coil		∘ J x B gun type pre-ionization equipment had troubles	∘ Ti-balls were set						∘ The periodical maintenance was done ∘ TDC type discharge cleaning device was installed ∘ CO_2 fire extinguisher system was installed		

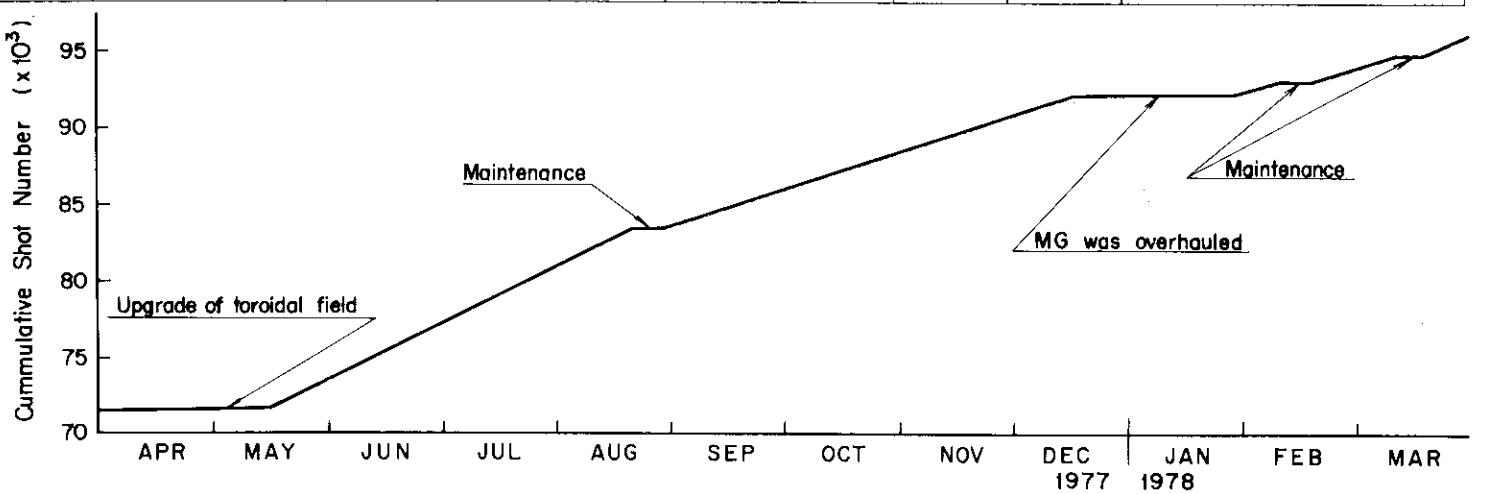

Fig. III-2 Operation of JFT-2a (DIVA).

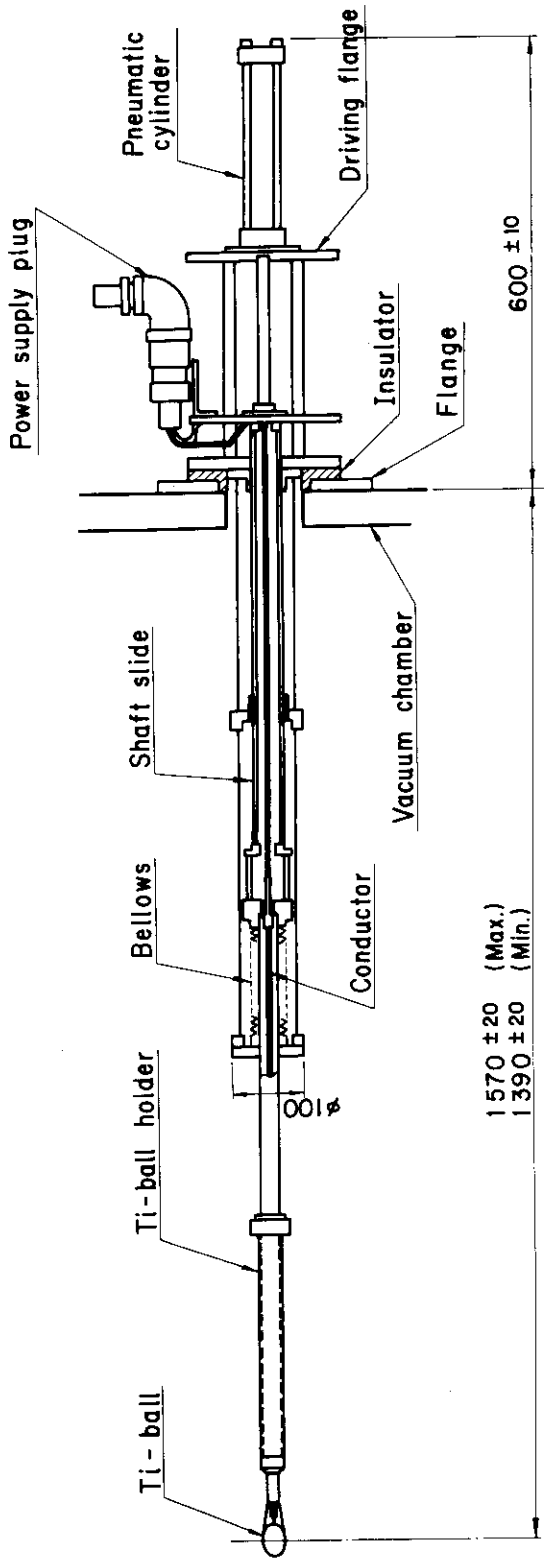

The driving mechanism of Titanium ball

Fig. III-3 Mechanism of movable Titanium flash instrument.

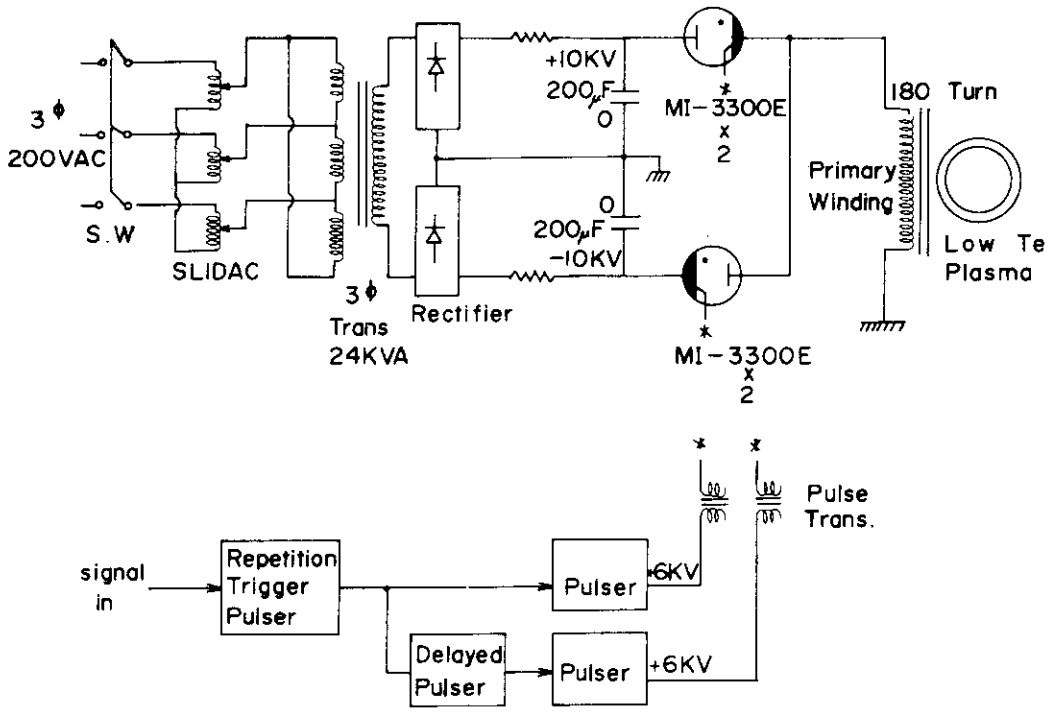

Fig. III-4 The circuit of Taylor type discharge cleaning.

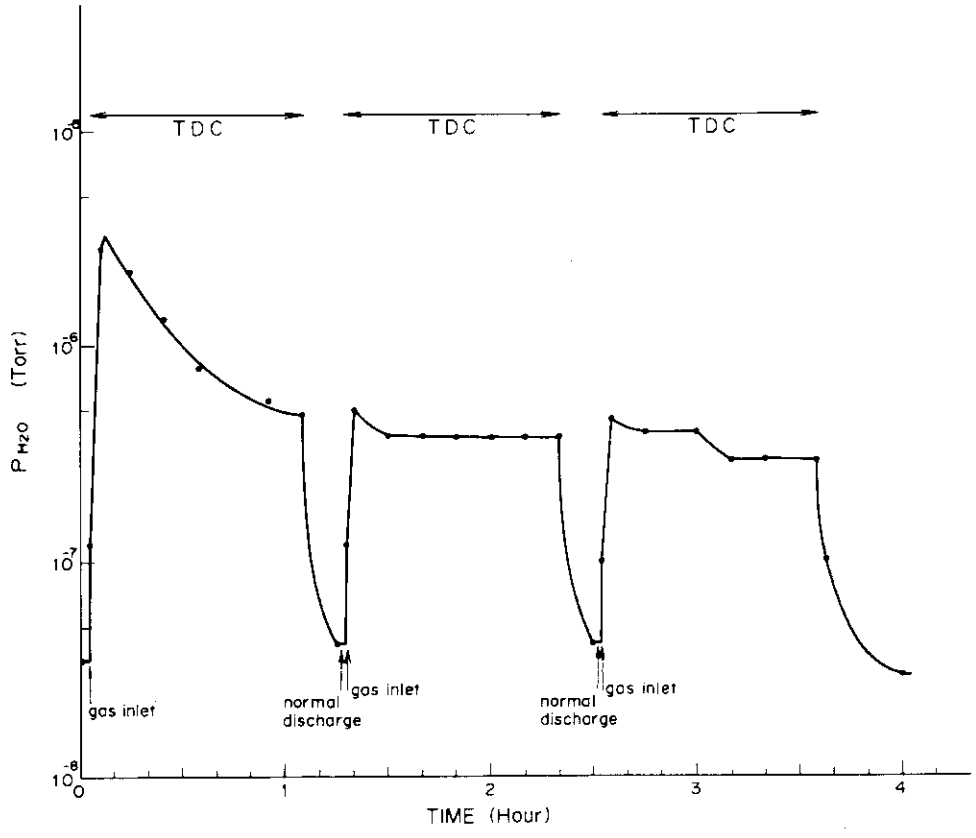

Fig. III-5 Time behavior of partial pressure M/e = 18 in TDC.

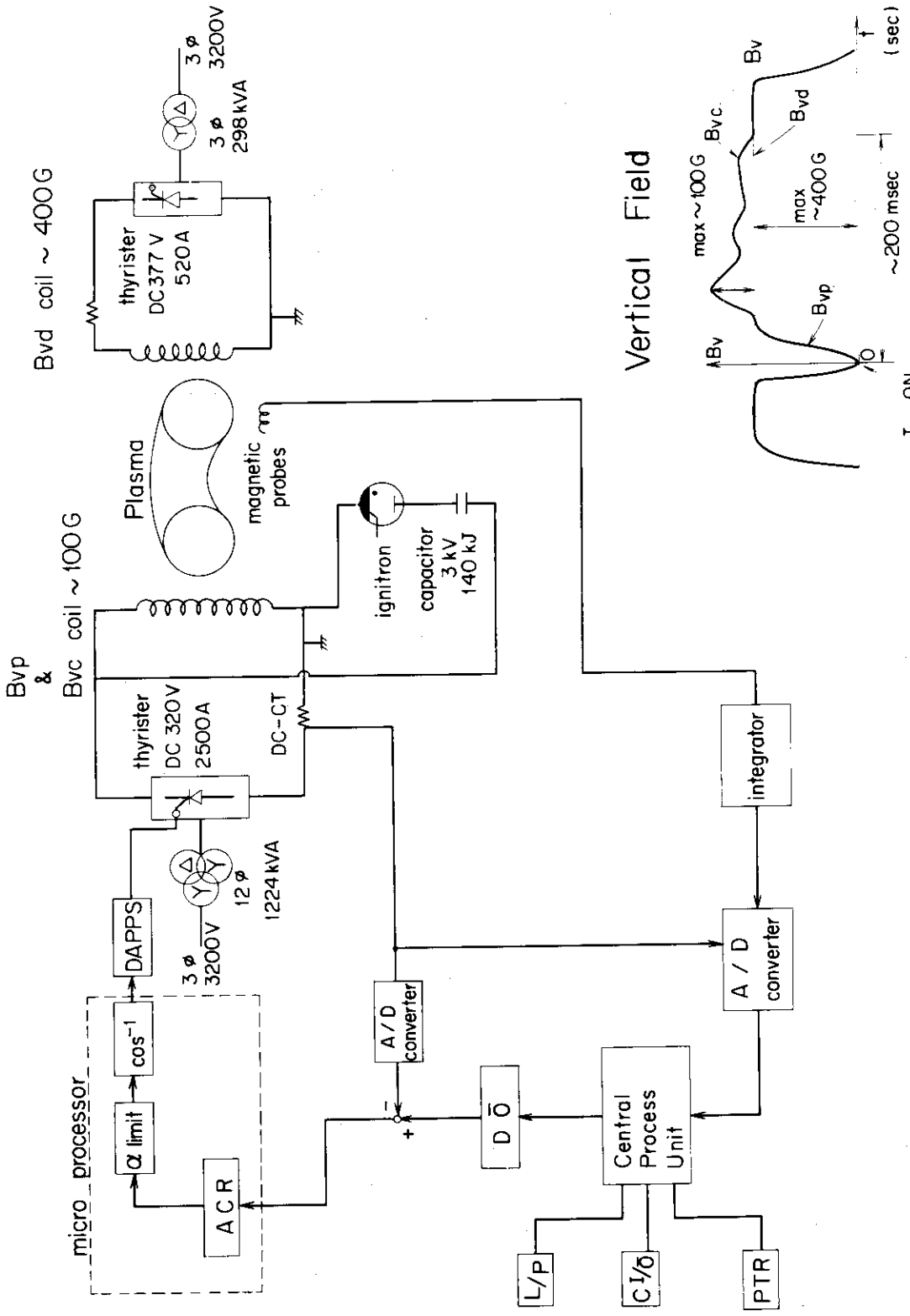

Fig. III-6 The block diagram of positional control of Plasma.

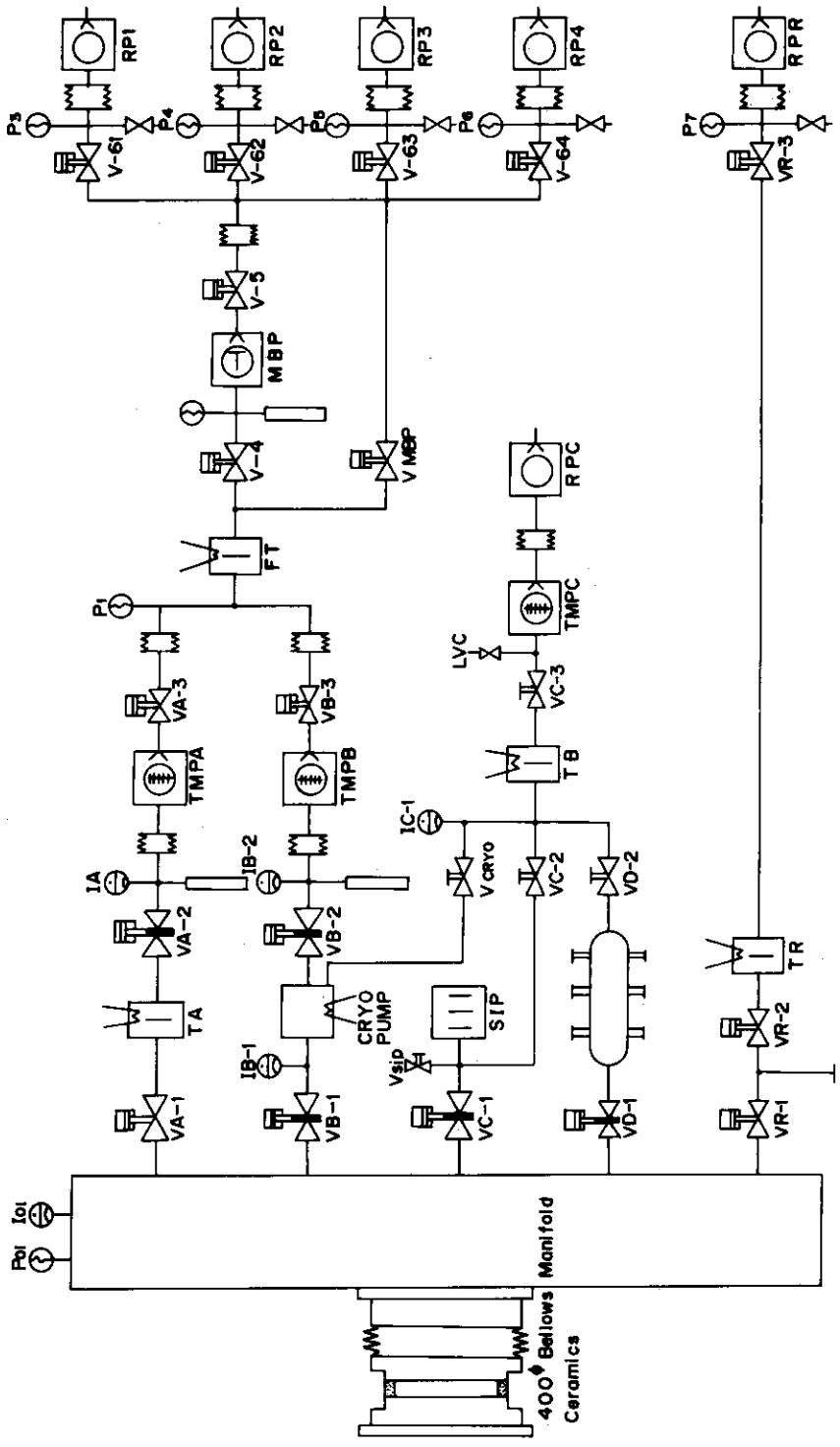

Fig. III-7 New pumping system in modification of JFT-2.

IV. DEVELOPMENT OF PLASMA HEATING SYSTEM

1. Introduction

Neutral beam injection and radiofrequency (RF) heating systems are under development for supplementary heating of JT-60 and JFT-2 plasmas.

In the neutral beam injection, ion source development and beam line studies for JT-60 injectors have continued, using test stands ITS-1 and ITS-2[1]. A hydrogen beam of 3.0 A (current density 0.27 A/cm^2) at 75 keV with divergence 1.2 degree was extracted by using the two-stage ion source of 6.6 cm diameter. These experimental results satisfy the specifications of the JT-60 ion source concerning the acceleration voltage and the current density. To further intensify the ion source development, a test stand ITS-3[2] was built in December 1977 and source plasma studies were started.

Based on the conceptual design of the neutral beam injectors for JT-60 made by JAERI personnel taking about two years, detailed design of the prototype unit for the JT-60 injectors was made by four industrial firms respectively under JAERI's supervision.

In the RF heating, a 200 kW, 650 MHz (and 750 MHz) RF heating system for JFT-2 was completed in September 1977, and the lower hybrid heating experiment was started on JFT-2. In this experiment, the RF coupling efficiency of 90 % was obtained by using the phased array of four wave guides. Effective ion heating (ion temperature rise of 50 - 60 %) has been obtained on application of 135 kW power.

2. Neutral Beam Injection System

2.1 Ion source development and beam line studies

2.1.1 Beam optics and grids heat loading in the two-stage acceleration system

Next generation fusion experiments will require tens of amperes equivalent of neutral hydrogen atoms at energies greater than several tens of keV for heating a torus plasma. To maintain high power density at high energy, it is necessary to use post-acceleration system because of limitations due to vacuum breakdown among extraction grids. Here, the beam optics of the two-stage acceleration system is investigated experimentally[3], using a JAERI 7-cm duoPIGatron plasma source shown in Fig. IV.2-1.

The two-stage acceleration system is composed of four grids called

plasma grid, gradient grid, suppressor grid and exit grid, respectively (See Fig. IV.2-2). The ion source is operated with a continuous hydrogen gas flow from the hot cathode region. The ion beam up to 3.0 A was extracted stably in the range of total acceleration energy 50 - 75 keV. The duty cycle of beam extraction is 1/10 - 1/30, and the beam pulse length up to 1 sec was obtained successfully.

Figure IV.2-3 shows the beam divergence as a function of perveance per hole in the case of d_{ext} = 6 mm, d_{acc} = 8 mm, aperture diameter = 3.5 mm and $V_{ext} + V_{acc}$ = 50 keV, where perveance per hole is defined by $I_{acc}[V_{ext} + V_{acc}]^{-3/2}$ divided by the number of apertures. This result shows that the reduction of the ratio V_{ext}/V_{acc} makes the minimum beam divergence ω_{min} decrease for the fixed gap distances, while the reduction of optimum perveance P_{opt} is inevitable. The latter is defined by the perveance that gives the minimum beam divergence when the extraction current I_{acc} is changed. It also shows that the divergence increases very gradually above the optimum perveance. Such tendency is not observed in the single-stage acceleration. This is preferable to obtain a low divergent and high perveance beam. Furthermore, the influence of source plasma density fluctuation on the beam divergence can be reduced when the dependence of beam divergence on the perveance is weak. Figure IV.2-4 summarizes wide variety of data from the view point of the dependence of minimum beam divergence and optimum perveance on the field intensity ratio f, defined by $f = V_{ext}d_{acc}/d_{ext}(V_{acc}+V_{dec})$, that is, the ratio of electric field intensity in the extraction gap to that in the acceleration gap.

From this figure, it is seen that the decrease of f makes ω_{min} and P_{opt} decrease, as is expected by the analytical and numerical estimation. In conclusion, it is preferable that f should take the value about 0.3 - 0.5, to obtain a high perveance and low divergent beam. Table V.2-1 summarizes the typical beam properties obtained.

The heat loading of the extraction grids, which is one of the critical problems limiting beam pulse duration at high power level, has been investigated experimentally in the two-stage acceleration system[4]. The heat loading is measured calorimetrically by the temperature difference between the inlet and outlet cooling water.

Figure IV.2-5 shows the heat loading of each grid as a function of extraction current I_{acc}, when the gas pressure in the vacuum chamber is low enough, below 1×10^{-3} Torr. The gradient grid current I_g, suppressor grid

current I_{dec} and e-folding half-width beam divergence are also shown. The heat loading of each grid has minimum value at I_{acc} = 2 A, where beam divergence is close to its minimum, and with increasing I_{acc}, the heat loading and I_g increases rapidly. Figure IV.2-6 shows the heat loading as a function of the pressure in the vacuum chamber. Most part of the heat loading on the gradient and the plasma grids is attributed to the inpinging high energy electrons accelerated backward. These electrons are born as a result of secondary emission at the suppressor grid due to back streaming ion bombardment from the downstream beam-plasma region. In general, the heat loading depends largely on extraction current and the gas pressure; it decreases with improvement of the beam optics and with decrease of the pressure. In optimum operating modes, its level is typically less than 2 % of the total beam power or 200 W/cm^2 at beam energy of 50 - 70 keV.

2.1.2 Source plasma study

The plasma source should be capable of producing a quicent, uniform and dense plasma over the large extraction area. For this reason, we have undertaken a study to improve the source plasma of an axisymmetric 15 cm diam. duoPIGatron ion source. Figure IV.2-7 shows the schematic of the modified duoPIGatron ion source with an axial button and a set of line cusp confinement magnets. Figure IV.2-8 shows a typical example of the density profiles of the source plasma in the original duoPIGatron ion source, which has neither the button nor line cusp confinement. As shown in this figure, uniformity is improved by lowering the magnetic field, but the density becomes too low to produce high-current ion beams. As a first step of the improvement of the source plasma, the copper button was installed about 2.5 cm downstream of the nozzle snout. Figure IV.2-9 shows variations of density profiles with various size of the axial button. It is seen that the source plasma is improved by installing the button of the proper size. To increase the plasma density without impairing uniformity, it is necessary to reduce a loss rate of charged particles from the PIG plasma to walls of the arc chamber. For this purpose, we have made the modified duoPIGatron with the line cusp field around the arc chamber. This effect is shown in Fig. IV.2-10, operating the ion source at higher arc current level (about 300 A). It is seen in this figure that the characteristics of the source plasma is significantly improved. We are planning to extract ion beams under this operating conditions.

2.1.3 Electrode cooling

In order to obtain the design data for extraction grids of ion source for JT-60 neutral beam injector, heat removal experiments from a extraction grid[5] and that from a beam target simulating the extraction grid[6] were performed. One of the time response of temperature at the grounded electrode is shown in Fig. IV.2-11, when the beam of 30 keV, 4 A was extracted for 7 sec. In this figure the temperature at the grid center saturated at about 200°C which corresponds to boiling point of the coolant water. In this example the average heat flux of copper electrode was 130 W/cm^2. One of the time response of temperature of the target is shown in Fig. IV.2-12. In this case beam of 30 keV for 7 sec was applied on the target of 0.5 cm thickness. The upper curve shows the heighest temperature and the lower at the 4 cm off the highest point. The average heat load of the target was 220 W/cm^2 and that of the coolant surface was about 570 W/cm^2.

2.1.4 Cryopump

In the neutral beam injector for the JT-60, cryogenic pumps that have pumping speed of 10^6 1/sec for hydrogen will be installed in beam lines. To develop these cryopumps we have built a small scale cryopump of 6×10^4 1/sec[7]. It consists of a pair of liquid helium cooled panels (60cm×60cm), the liquid nitrogen cooled chevrons and radiation shields. The pumping speed was obtained by measuring the flow of hydrogen and the pressure in the cryopump. The results are shown in Fig. IV.2-13. The pumping speed and the equilibrium pressure agree with the design values. The rate of liquid helium consumption was also obtained by measuring the boil-off helium when the hydrogen was bein pumped. From those result the heat load due to condensation of hydrogen gas is 0.12 ± 0.02 J/Torr. l and can be explained by the energy difference of hydrogen between 80 K and 4.2 K.

This cryopump has been connected with the ion source test stand ITS-2 beam line to investigate the pumping and heat loading problems associated with thermal radiation and backscattered hydrogen in the pressure of the beam dump[8]. The maximum hydrogen beam power of 71.3 kW (26.4 kV 2.7 A, pulse length 100 msec, duration 1 sec) was introduced to the water cooled beam dump placed in the cryopump. The pressure in the pump was sustained about 5×10^{-5} Torr. The hydrogen beam did not change it, and did not affect the pumping speed. The heat inputs to the chevron and cryopanel were measured with the gas flow meters for nitrogen and helium. These maximum averaged

powers were 62.2 W and 0.19 W, respectively. These values were well agreed with the results from the Monte Carlo simulation[9]. This Monte Carlo simulation was done by the code which calculates the following; (1) energy distribution and reflection efficiency of the backscattered particles from the beam dump, (2) molecular flow rate and energy distribution of the backscattered energetic particles through the chevron baffle, and (3) radiation transmissivity of the chevron baffle.

2.1.5 Energy converter

Neutral beam injector in near future will require energy recovery system to improve the power efficiency. From the computer simulation[10] of the electro-static deceleration system, it was shown that high voltage negative electrode is necessary to prevent space charge neutralizing electrons from being accelerated to a recovery electrode. The negative electrode bombarded by ions will cause secondary electrons and they may reduce the recovery efficiency. Therefore it is very advantageous if the beam plasma electrons are magnetically confined. We undertook preliminary tests to see the effect of magnetic field. The experimental setup is shown in Fig. IV.2-14. The hydrogen ion source has extraction area of 8 cm dia. and the beam target is made of copper. The magnet has pole faces of 13 cm × 10 cm and the pole gap is 13 cm. The gas pressure varies from 0.3×10^{-4} to 1.5×10^{-4} Torr during gas pulse length of 80 msec. The voltage of the target increases with the magnetic field and the extracted ion current. This is shown in Fig. IV.2-15 for beam energy of 27 keV.

2.2 Design of the JT-60 neutral beam injection system[11]

Effective heating of the plasma beyond 5 keV requires following main performances for the neutral beam injector.

(1) 20 MW hydrogen atoms into the torus (at 75 kV acceleration)

(2) Permissible cold gas influx into the torus:

a value corresponding to 15 % of the fast neutral atoms

Neutral beam of hydrogen atoms are injected into the plasma through fourteen ports placed at seven azimuthal positions. One injector unit is connected to each port. Two units are placed at an azimuthal position stacked vertically one over the other.

A conceptual scheme of the beam line is shown in Fig. IV.2-16.

Cylindrical vacuum tank made of stainless steel, 2.5 m in dia, and 5 m high, contains all the hardware items necessary to treat ion and neutral beams and concomitant cold gas. Each tank is connected to one of the drift tube of the JT-60 vacuum vessel through the connection bellows and gate valve. Retractable calorimeter is used as a neutral beam target during source conditioning. The vacuum tank of the lower injector unit also plays a role of supporting base for the upper unit. Two ion sources are stacked in each unit. The ion beams extracted from the source and introduced to the subsequent neutralizer cell. Cryopump is used to pump out almost 98 % of the cold and dumped hydrogen. A reflecting magnet will be placed near the center of the vacuum tank, and at this point the tank is divided into two rooms, P_1 and P_2 room, respectively. A cylindrical small chamber is welded to the main tank. This chamber is names as P_3 room and contains a small cryopump and the fast shutter, On both ends of this room two beam limiters are situated, the 1st, and the 2nd limiter, respectively. In the main tank, residual ion beams are guided to the beam dump. To prevent sputtered particles from attaching the cryopump and to reduce heat loading on the cryopump due to backscattered hydrogen and thermal radiation, sputtering shield is installed along this ion drift path.

2.2.1 Power efficiency

The most important parameter that determines the overall power efficiency of the neutral beam system is the neutralization efficiency. We envisage the standard ion spacies H^+ : H_2^+ : H_3^+ to be 75:20:5, and we adopt 38 % conversion efficiency corresponding to 87 % equilibrium cell.

The next important is a divergent loss of neutral beams due to geometrical limitations of the beam line. Although we would desire the ion sources to be installed as close to the injection port as possible, hardware items that have to be housed in the beam line require 8.25 meter for the total beam line length. Ideally, 10 % of the neutral beam is intercepted before reaching the torus, if there are no obstacles other than entrance aperture of 44 cm diameter. However, overall calculations including beam limiters show about 20 % of the total beam is lost due to the beam divergence.

There is additional loss of fast neutrals due to collision with ambient cold hydrogen gas, We estimate this effect to be 5 %, since the total line density of cold hydrogen is well below 1.1×10^{-2} Torr·cm.

Thus the overall power efficiency is about 30 %, so that primary ion

beam amounting to 70 MW would be necessary to generate 20 MW neutral beam. The above value corresponds to 5 MW ion beam output per each injector unit. Accordingly, 75 kV, 66.6 A net output is required for the ion source.

2.2.2 Gas consideration

Multiply divided long gas cell gives high gas efficiency. However, if the cross section of the cell is too small, fraction of the beam that otherwise enters the torus is intercepted by the wall of the cell. It should be designed taking into account matching with the injection port, namely, beam acceptance of the drift tube and the acceptance of the gas cell must be chosen nearly equal. For this reason together with improving a packing factor of the ion source grid area, we have changed our former design using four cylindrical cells in each beam line unit to two larger rectangular cells. The neutralizer must sustain enough line density while keeping the entrance gas pressure below some permissible level, which is determined by the heat loading of the extractor grid. The cell has a conductance of 2300 1/s for room temperature hydrogen. The line density necessary for 87 % cell is 0.32 Torr·cm, hence the gas pressure at the entrance of the cell P_0 is 2.85×10^{-3} Torr. The gas flux rate Q_c from the cell is then $Q_c = P_0 \cdot C =$ 6.57 Torr.1/s per source and 13.1 Torr.1/s in total.

On the other hand, dumped ions would produce thermal hydrogen gas amounting to 4.63 Torr.1/s, so that the cryogenic pumping system has to pump out the gas throughput of 17.7 Torr.1/s.

To handle this throughput with a reasonable pumping speed, a differential pumping system is adopted. Conceptual gas flow diagram is shown in Fig. IV.2-17 where p denotes the pressure, S the pumping speed, C the conductance, Q the cold gas flux rate, Γ the fast particle flux, respectively. The ion beam is extracted from the 12 cm × 27 cm grid and each beamlet is assumed to be Gaussian. Since most of the beam fraction that hit the wall of the drift tube cannot be pumped by the NBI cryopump, they cause an unnegligible effect on the total gas influx to the torus. We search for reasonable solutions by changing geometry of the limiters, beamlet focal length, steering length. By the parametric study changing S_1, and S_2, we obtain the optimum parameters of the vacuum system as

$S_1 = 4\times10^5$ 1/s, $S_2 = 4\times10^5$ 1/s, $S_3 = 3\times10^4$ 1/s

$P_1 = 3.3\times10^{-5}$ Torr, $P_2 = 1.3\times10^{-5}$ Torr, $P_3 = 9.2\times10^{-6}$ Torr, $P_s = 7\times10^{-5}$ Torr

$P_i = 1\times10^{-2}$ Torr, $P_G = 3\times10^{-3}$ Torr, and $P_0 = 1.15\times10^{-3}$ Torr, respectively.

Taking into account the design basis, operational flexibility, and unexpected degradation of pumping properties, about 50 % margin is added to each pumping speed, in particular for prototype injector unit. Namely, our design pumping speeds are chosen as

$S_1 = 6.3\times10^5$ 1/s, $S_2 = 6.3\times10^5$ 1/s, and $S_3 = 4.5\times10^4$ 1/s, respectively for the prototype unit.

2.2.3 Ion source and neutralizer

Two ion sources are mounted in each injector unit. The main performance is written as follows;

Type of plasma production:	rectangular duePIGatron with cusp magnetic field and button
Extraction current:	75 kV, 35 A current density 0.27 A/cm^2
Beam divergence:	0.9-1.0 degree (e-folding)
Pulse width:	2 msec - 10 sec
Duty cycle:	1/30
Transparency:	40 %, 12 cm × 27 cm
Ion species:	$H^+:H_2^+:H_3^+$ = 60:30:10 - 75:20:5
Method of beamlet focusing:	aperture displacement

To adjust beam axis toward injection port, bellows and the pulse motor driving system serves to change directions of each ion source within accuracy of ±0.1 degrees. The ion sources are magnetically shielded against external field. The outer shield structure made of mild steel is connected magnetically to the outer shield of the neutralizer cell. The shield factor needed for the ion source is 200 against perpendicular magnetic field of 100 Gauss. This specification is based on our recent measurement on the source plasma shift due to external field.

The neutralizer cell is a copper tube with a 14 cm × 29 cm rectangular cross section and is 225 cm long including gate valve, joint bellows. It must be magnetically shielded with the mild steel and high permeability materials against stray magnetic field to the level of 0.17 Gauss. The wall loading to the neutralizer is about 120 kW in most cases and the design specification is 300 kW.

2.2.4 Ion deflector magnet

Design of the ion deflector magnet has been made extensively using two

dimensional computer code. In a simple reflecting magnet, ion beams at off axis are easily bent toward the pole as they travel across the magnetic field and finally hit the wall of the magnet poles. The bending magnet on the other hand tends to focus ion beams and as a result, imposes high heat flux constraint on the beam dump. A 270° reflecting magnet also gives a convergent beam but the magnetic flux density required becomes large. A special reflecting magnet with 32 cm gap length and chamfered at 45° is designed to overcome these difficulties. As a result, distribution of the heat loading to the beam dump becomes broad. Furthermore, since the direction of the ion beam to the beam dump is nearly parallel to that of magnetic lines of force, the effect of stray magnetic field on the ion trajectory is appreciably small. Therefore, the magnetic shield along the ion drift region appears unnecessary. We are choosing this design provided its performance is verified by the small model test.

2.2.5 Calorimeter and beam pump

Calorimeter and beam dump must cover a wide range of heat load corresponding to variety of operation. They are formed like a V type shape to reduce effective heat flux to the dump surface. The maximum heat loading to these target are 2.5 MW for the calorimeter (75 kV, 80 A drain current, ion species are 60:30:10) and 5.2 MW for the beam dump (100 kV, 73 A drain current, ion species are 75:20:5). Dimensions of the calorimeter are 100 cm high, 80 cm long along the beam axis, and 30 cm wide opening to the beam. The maximum heat flux is 0.58 kW/cm^2 perpendicular to the dump surface. The beam dump has a V type shape, 160 cm high, 80 cm long and 100 cm opening. The heat flux is the same as that of the calorimeter. A silver annexted copper or ZrCu, CCu alloy is recommended, since they push forward the softening point of usual copper toward higher temperature. Array of cooling pipes with fin on their backs will be chosen for the dumper structure, because the temperature gradient across the material is small and hence thermal stress can be kept low.

2.2.6 Cryopump

The cryopump has a total pumping speed of 1.3×10^6 l/s and hence the required pump area is about 14.5 m^2. Since typical operation pressure at the cryopump is below 5×10^{-5} Torr ($P_3 = 9.2 \times 10^{-6}$ Torr), the temperature

of the cryopanel should be less than 3.6 K. The cryopump is divided into three groups and are housed in P_1, P_2 and P_3 room, respectively. Two types of cryopanels are being evaluated. The one is composed of a set of aluminum pipes with fin plate of about 10 cm wide, and the other is the stainless steel kilting vessel. The former is cooled by the two phase flow helium, and the latter is cooled by the liquid helium pooled in the vessel. Heat loading to the cryopanel is estimated for the former case and is tabulated in Table 1.

Table 1 Heat loading to the cryopanel

	Pulse Load	Continuous Load
1. Radiation from 77 K plate		9.9 w
2. Radial from room temperature materials	9.5	19.0
3. Support loss		2.0
4. Condensation of H_2 gas 30 Torr.l/s	3.6	0.12
5. Backscattered hydrogen	0.1	0.003
6. Cyclotron radiation	25	0.42
7. Eddy current	15	0.25
	53.2 w	31. 7w

Thus the pulse load occupies an unnegligible fraction of the total load. Choise of the type of the cryopump is closely coupled with the helium refrigeration system.

References

(1) Ohga, T., et al.: JAERI-M 7604 (1978) (in Japanese)
(2) Itoh, T., et al.: JAERI-M (to be published)
(3) Ohara, Y., et al.: Proc. 7th Symp. on Engineering Problems of Fusion Research, Knoxville. (1977) p.273.
(4) Okumura, Y., Ohara, Y. and Ohga, T.: JAERI-M 7696 (1978) (in Japanese).
(5) Kondoh, U., et al.: JAERI-M 7612 (1978) (in Japanese).
(6) Horiike, H., et al.: to be submitted for publication.
(7) Shibata, T., Okumura, Y. and Sakuraba, J.: JAERI-M 7869 (1978) (in Japanese).
(8) Sakuraba, J., Ohga, T. and Shibata, T.: to be published in JAERI-M

(9) Sakuraba, J. and Shibata, T.: JAERI-M 7611 (1978) (in Japanese)

(10) Horiike, H. and Ohara, Y.: to be submitted for publication.

(11) Matsuda, S., et al.: JAERI-M 7655 (1978) (in Japanese)

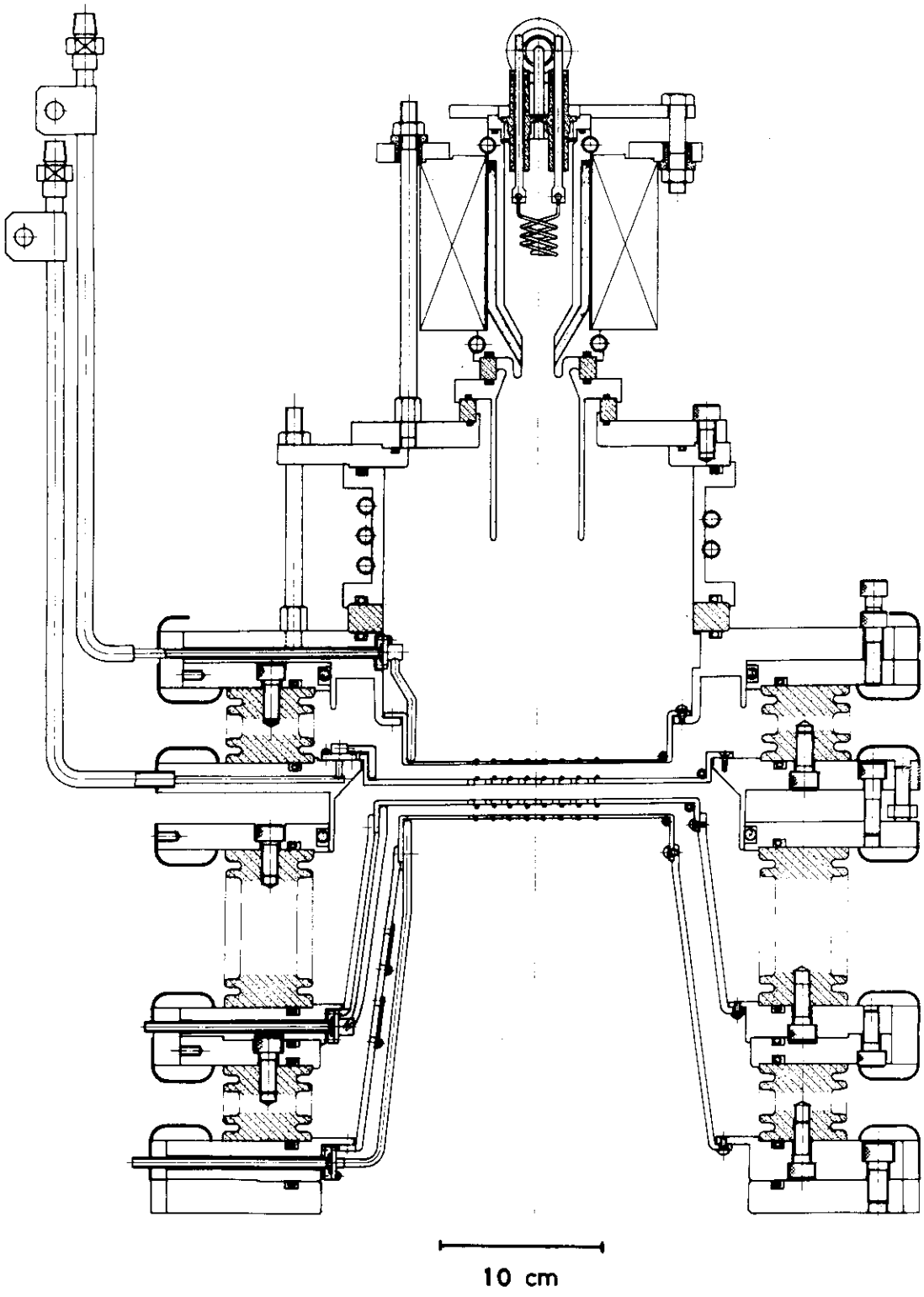

Fig.IV.2-1 DuoPIGatron ion source with two-stage acceleration system.

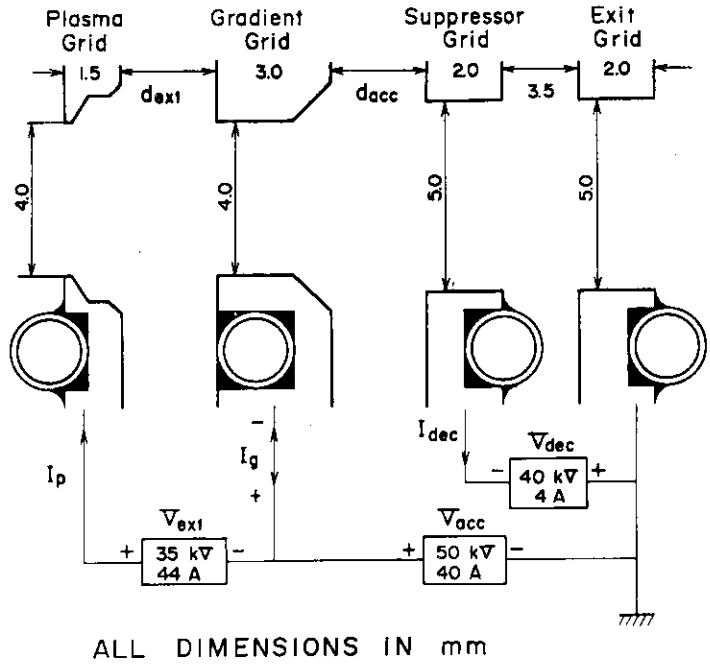

Fig.IV.2-2 Schematics of the two-stage acceleration system.

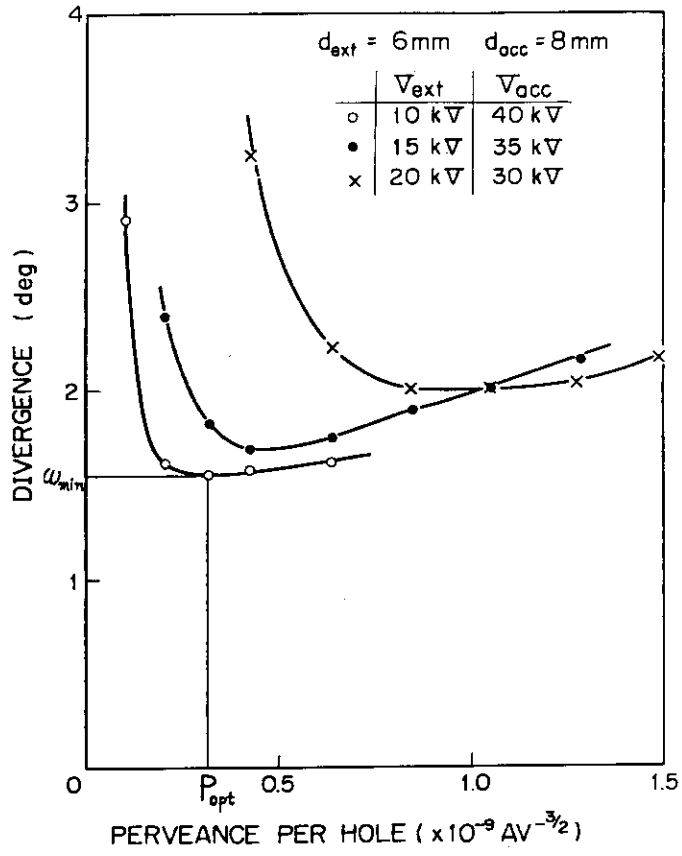

Fig.IV.2-3 Beam Divergence as a function of preveance per hole, where total beam energy is fixed to 50 keV.

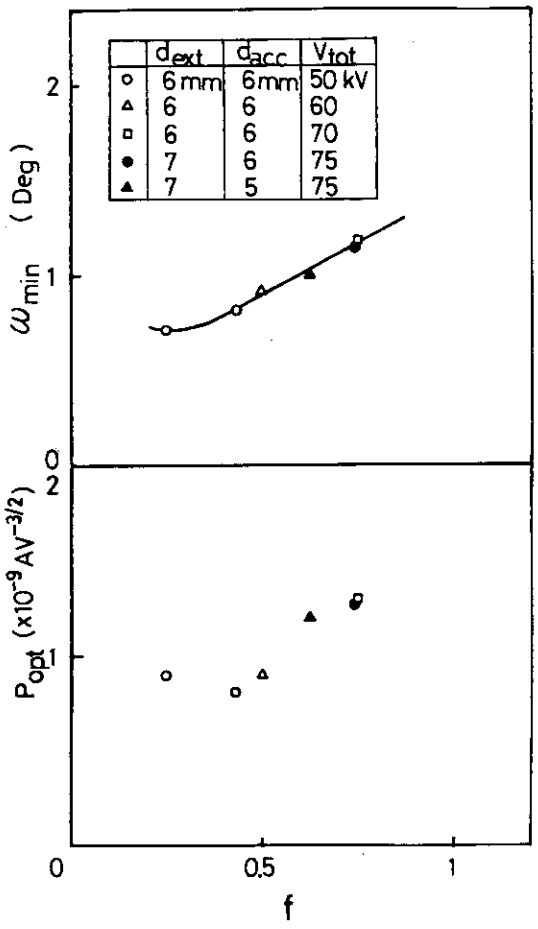

Fig.IV.2-4 Dependence of minimum beam divergence ω_{min} and optimum perveance Popt on the field intensity ratio.

Table IV.2-1 TYPICAL PROPERTIES OF TWO-STAGE ION SOURCE

EXTRACTION GRID	5 cmϕ (3.5mmϕ x 83)		6.5 cmϕ (4.0mmϕ x 87)				JT-60 NBI 12cm x 27cm
TRANSPARENCY (%)	43		32				40
SPECIES	H_2		H_2				H_2 or D_2
BEAM ENERGY (keV)	50	70	50	60	70	75	75
BEAM CURRENT (A)	0.6	2.0	0.9	1.5	3.4	3.0	35
CURRENT DENSITY (mA/cm^2)	75	250	80	140	310	270	270
e-FOLDING DIVERGENCE	1.0°	1.4°	0.8°	0.9°	1.4°	1.2°	1.0°
DURATION (sec)	0.1	0.1	0.1	1.0	0.5	0.1	10

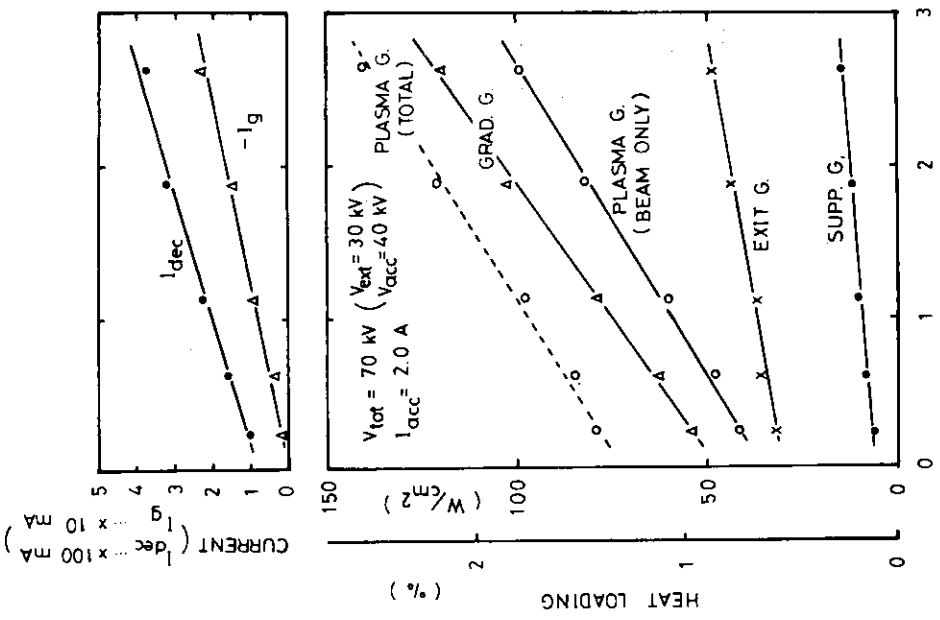

Fig.IV.2-6 Heat loading of each grid and beam dumper, beam divergence and grid current vs. the pressure in the vacuum chamber, where (V_{ext}+V_{acc})=70 kV and I_{acc}=2 A.

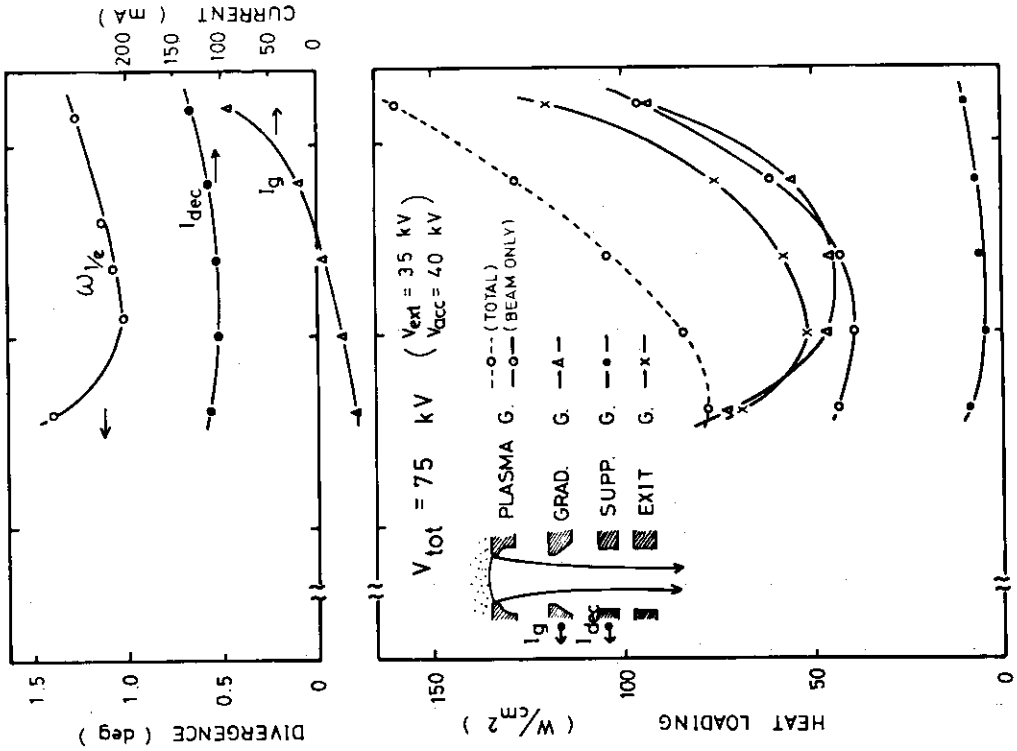

Fig.IV.2-5 Heat loading of each grid and beam dumper, beam divergence and grid current vs. extraction current I_{acc} where (V_{ext}+V_{acc})=70 kV.

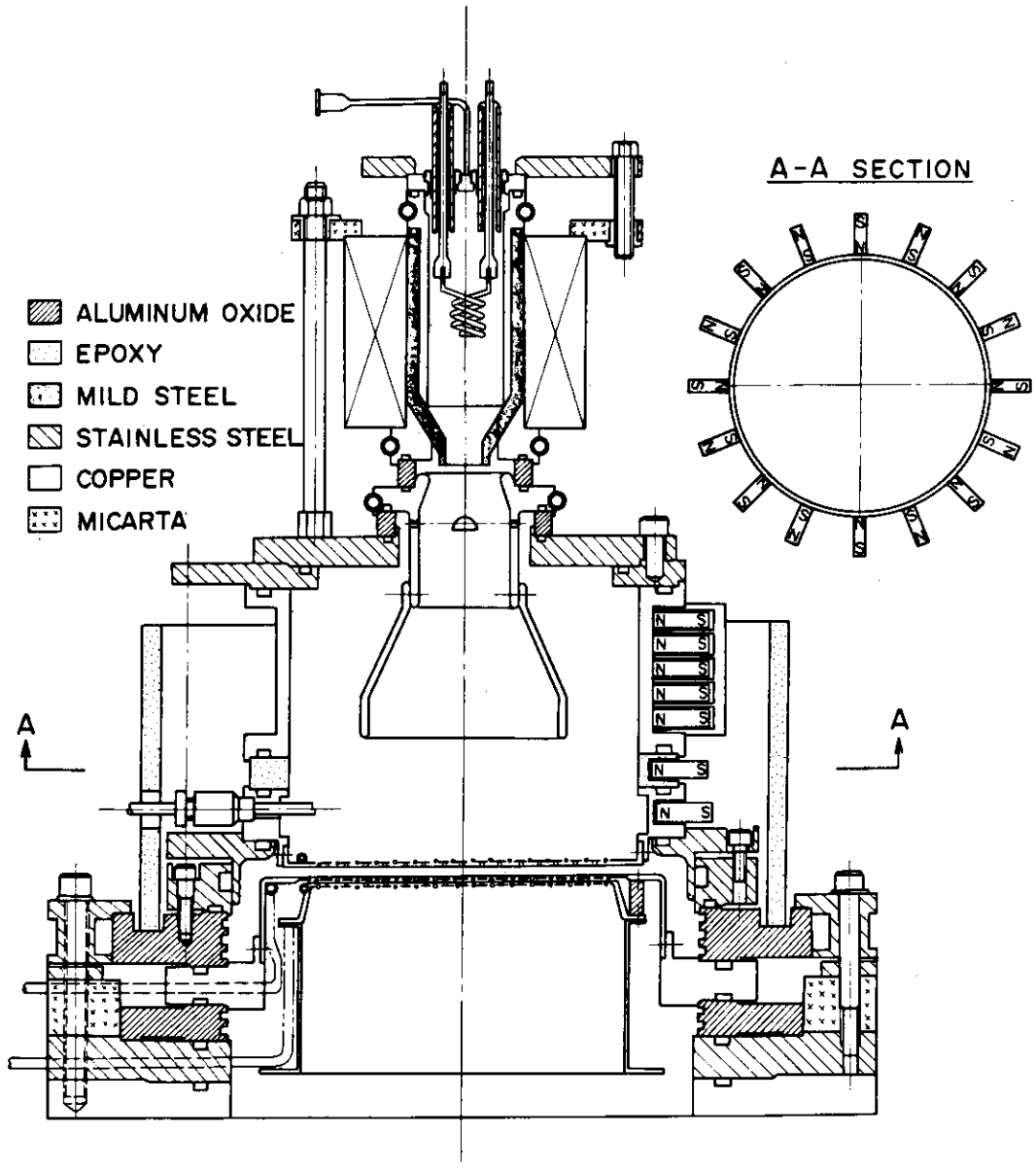

Fig.IV.2-7 An axisymmetric 15 cm diam. duoPIGatron ion source.

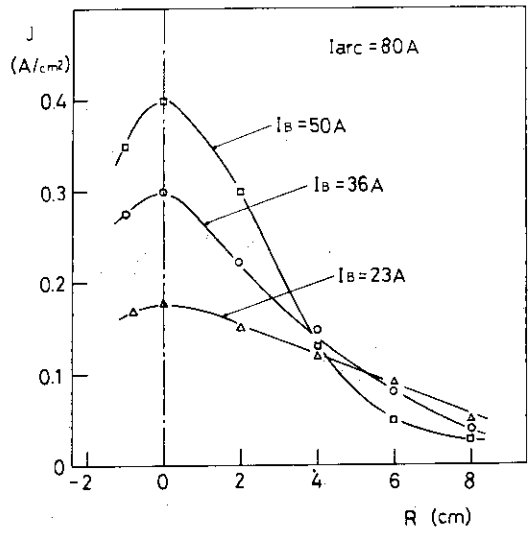

Fig.IV.2-8 Density profiles of the source plasma before improvement.

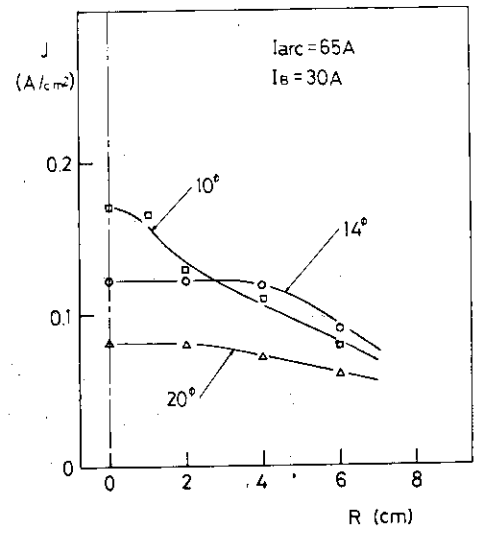

Fig.IV.2-9 Variations of density profiles with various size of axial button.

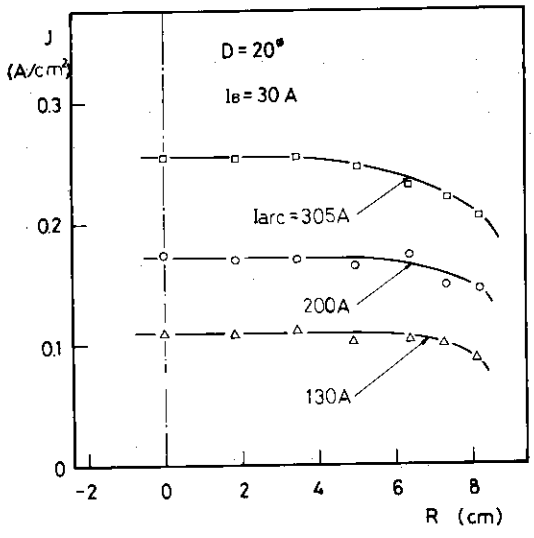

Fig.IV.2-10 Density profiles in the ion source with the axial button and line cusp confinement.

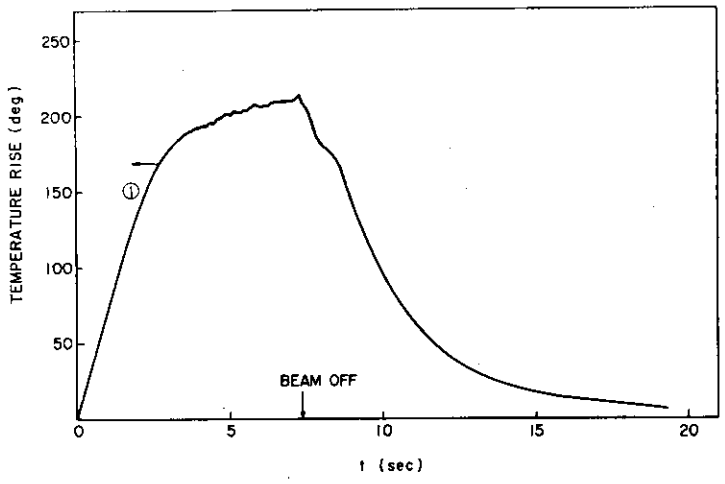

Fig.IV.2-11 The time response of temperature at the grounded electrode.

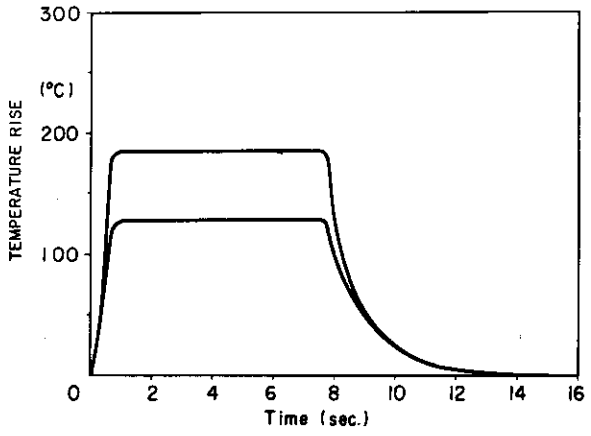

Fig.IV.2-12 The time response of temperature of the target.

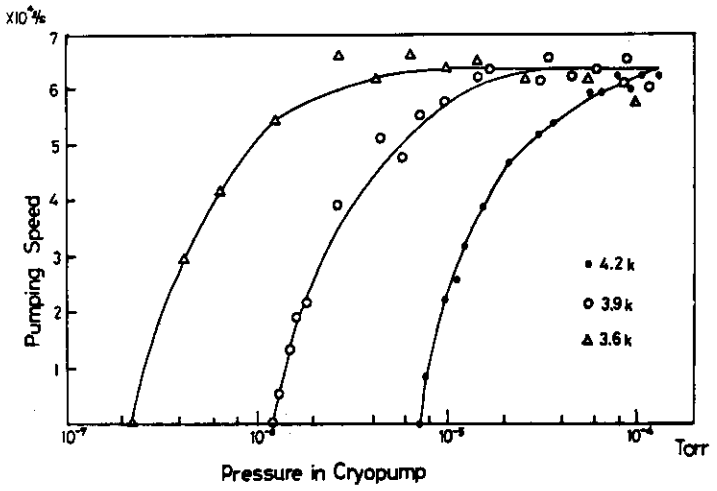

Fig.IV.2-13 The pumping speed of the 6×10^4 l/sec cryopump.

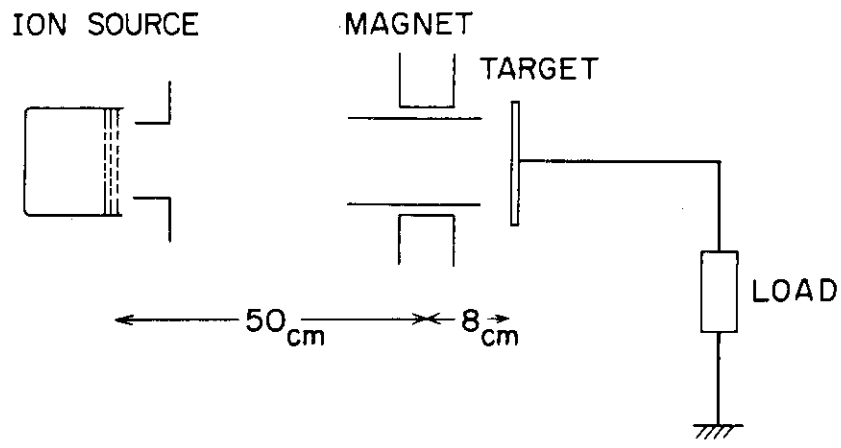

Fig.IV.2-14 The experimental setup of energy converter using the magnetic field.

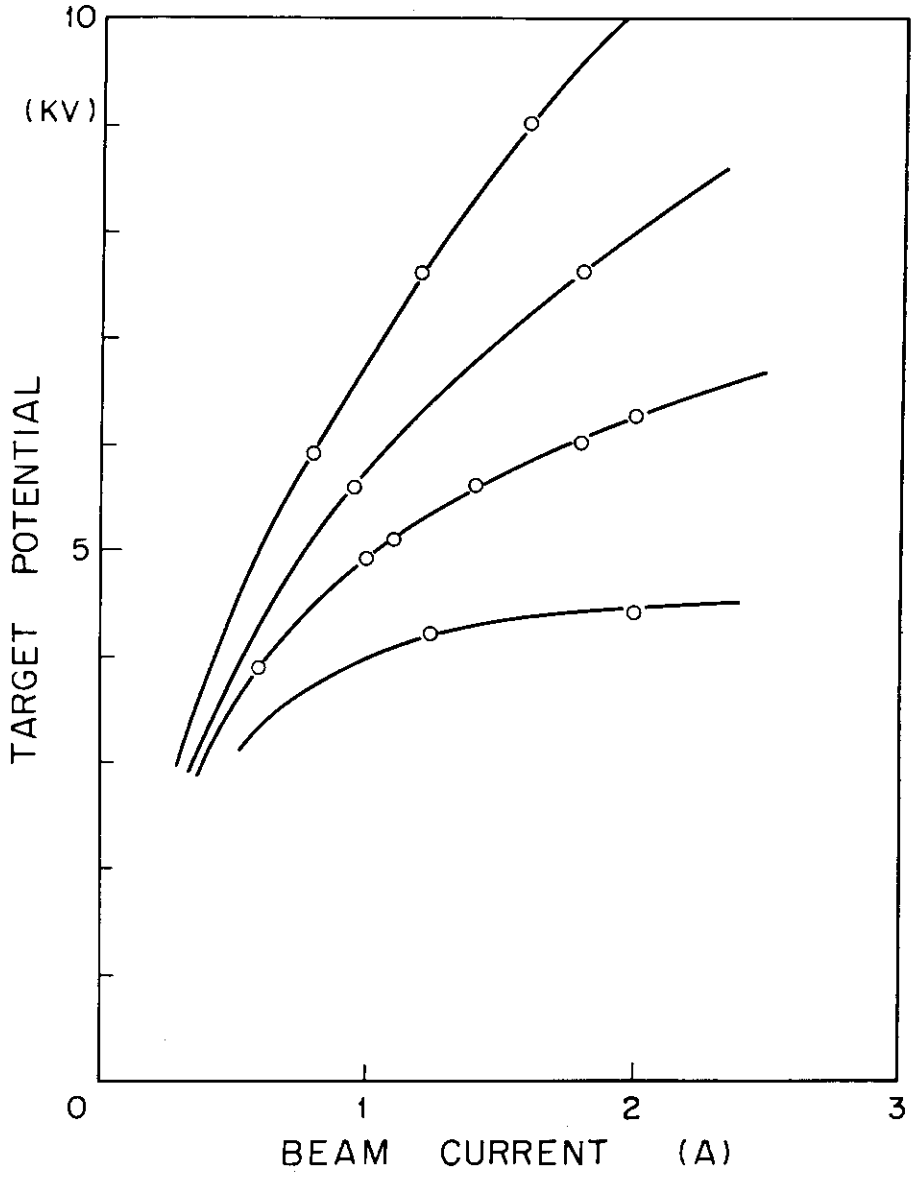

Fig.IV.2-15 Target potential as a function of beam current.

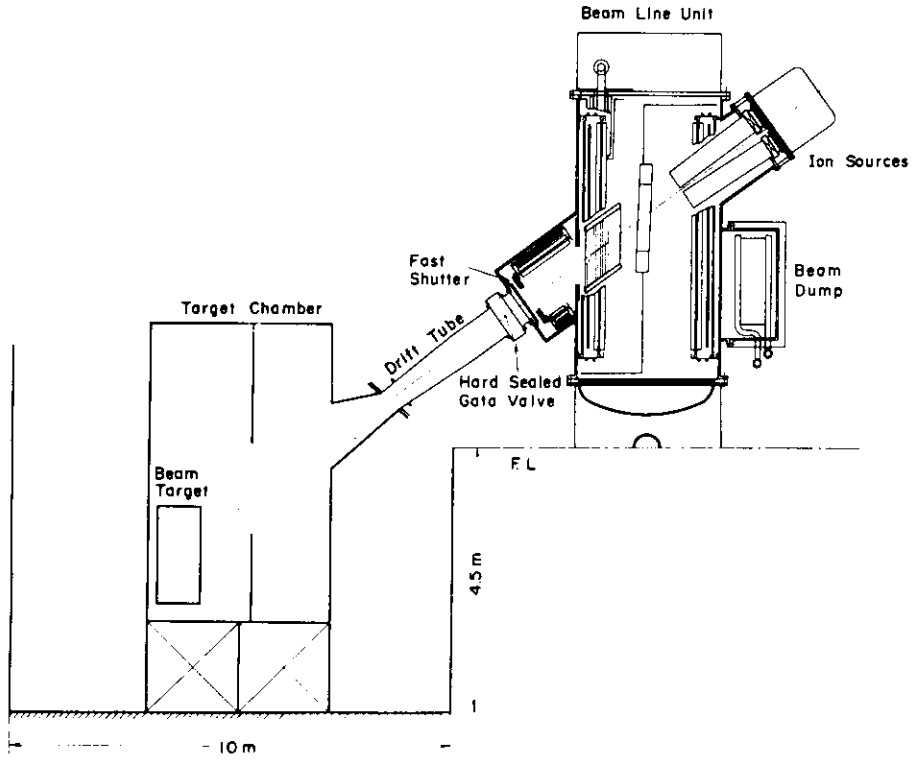

Fig.IV.2-16 Conceptual scheme of the beam line, a prototype unit is shown with a target chamber.

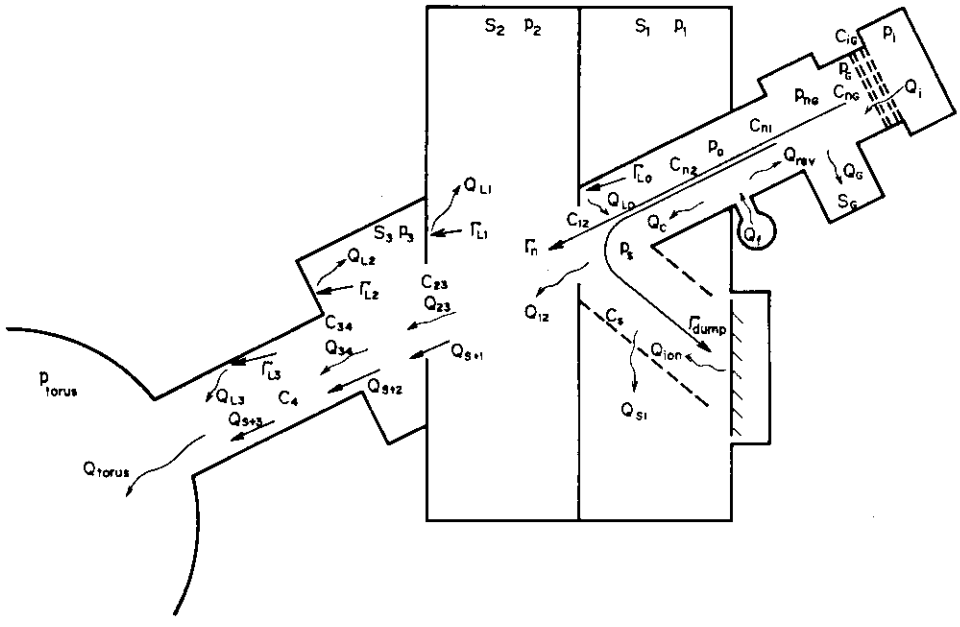

Fig.IV.2-17 Gas flow diagram.

3. Radiofrequency Heating System

3.1 Lower hybrid heating system for JFT-2

A power source of 200 kW, 650 MHz (and 750 MHz) and a phased array of four waveguides as a coupling system had been selected for the lower hybrid heating system employed on JFT-2. The final work on the design of the system was completed in the middle of 1976. After that the system began to be constructed and was installed in JFT-2 in September of 1977. The first experiments on ion heating were started from the begining of October 1977. An available power will be increased to 300 kW in the spring of 1978.

Main parameters of the lower hybrid heating system for JFT-2 are listed in Table IV.3.1-1. A block diagram of the RF system is shown in Fig. IV.3.1-1. The heat of the RF system is an E 3765 klystron amplifier. This is a 5 cavity, electromagnetically focused klystron. This tube is rated at approximately 60 kW of RF out put. Four klystrons are utilized in this system. High power RF out put from the klystron is transmitted to the coupling section through a circulator, coaxial line (WX-77D) and non-standard 95 mm × 340 mm rectangular waveguide.

The most important part of the lower hybrid heating system is the coupling system. A phased array of four waveguides which is the most advanced coupler theoretically and experimentally, was selected[1]~[3]. The schematic arrangement of the coupler is shown in Fig. IV.3.1-2. The size of each open waveguide (Al) is 14 mm × 290 mm as shown in Fig. IV.3.1-3. Two types of vacuum windows (Al_2O_3), seen in Fig. IV.3.1-4 (seal ① and seal ②), were tested and finally vacuum seal ① was chosen. The differential pumping system of waveguides were also prepared to reduce the RF break down at the ceramic window and in the waveguides.

An efficient coupling of RF power to a plasma by use of the phased array was obtained. Reflection co-efficient was less than 10% at a power of 137 kW[4]. But, in the early stage of the heating experiments, maximum RF power to couple to the plasma was less than 50 kW. This limit was possibly due to the following reasons; (1) break down at the surface of the ceramic and/or between the iris, (2) multipactoring discharge inside the waveguide, (3) arc discharge at a junction of the waveguide. In order to suppress these kinds of break down, the differential pumping of the waveguides was performed by a turbo moleculer pump of 1000 l/sec with the vacuum seal ① in Fig. IV.3.1-4, and the contact of waveguides

were improved. After these improvements, a power of 140 kW could be coupled to the plasma. Now, maximum power is likely to be limited mainly by (2). The importance of the material and its surface condition has been recognized. The further improvement of the launcher is necessary to increase an available launching power.

3.2 Ion cyclotron range of frequency heating system for JFT-2a

RF heating experiment in the ion cyclotron range of frequency (ICRF) is planned. The RF power can be up to 200 kW, and the frequency range separated in two bands, i.e. 25-30 MHz the cyclotron frequency for hydrogen ω_{CH} or the second harmonic cyclotron frequency for deuterium $2\omega_{CO}$ and 48-60 MHz for $2\omega_{CH}$. The RF power is transmitted to a launching structure by a two-stub impedance matching network allowing optimum transfer for loading impedance. The launching structure is a half turn antenna, which is insulated by a ceramic cover and protected by molybdenum guard limiters from the direct view of the plasma.

The generator has a phase locked feedback system which is almost the same as that of the TFR. The frequency can be changed ±5% within 30% variation of the RF power for the full operation.

The main objectives of the ICRF programme in DIVA is as follows; (1) heating by the magnetosonic wave at $\omega = 2\omega_{Ci}$ without minority component at the fundamental resonance, and comparing with the heating in a deuterium plasma with the minority component (H^+) at the fundamental resonance; (2) heating with mode tracking; (3) heating without impurity influx.

3.3 Design study of radio frequency system for JT-60

We have a program to develop a high power 1 MW - 10 sec klystron at 1-2 GHz for the RF heating system on the JT-60. Prior to the construction of the klystron the survey of technological problems expected during R & D had been made by Nippon Electric Co., Ltd. and Tokyo Shibaura Electric Co., Ltd. under the contact with JAERI. The conceptual design of the klystron at 1.3-1.4 GHz was done.

References

(1) Brambilla, M.: Nuclear Fusion 16 (1976) 47.

(2) Imai, T., Nagashima, T. and Azumi, M.: Numerical Studies of Lower Hybrid Wave Propagation in JFT-2, JAERI-M 6902, (February 1977), 39 pp. (in Japanese).

(3) Bernabei, et al.: Nuclear Fusion 17 (1977) 929.

(4) Nagashima, T. and Fujisawa, N.: To be presented at Joint Varenna-Grenoble International Symposium on Heating in Toroidal plasma (1978).

Table IV.3.1-1 Summary of JFT-2 lower hybrid heating system.

RF Source	
Frequency	650 and 750 MHz
RF power output	200 kW
Pulse width	1 msec 100 msec
Pulse repetition frequency	1 pulse/2 min
Power droop during pulse	5 %
Coupling System	
A phased array of four waveguides	

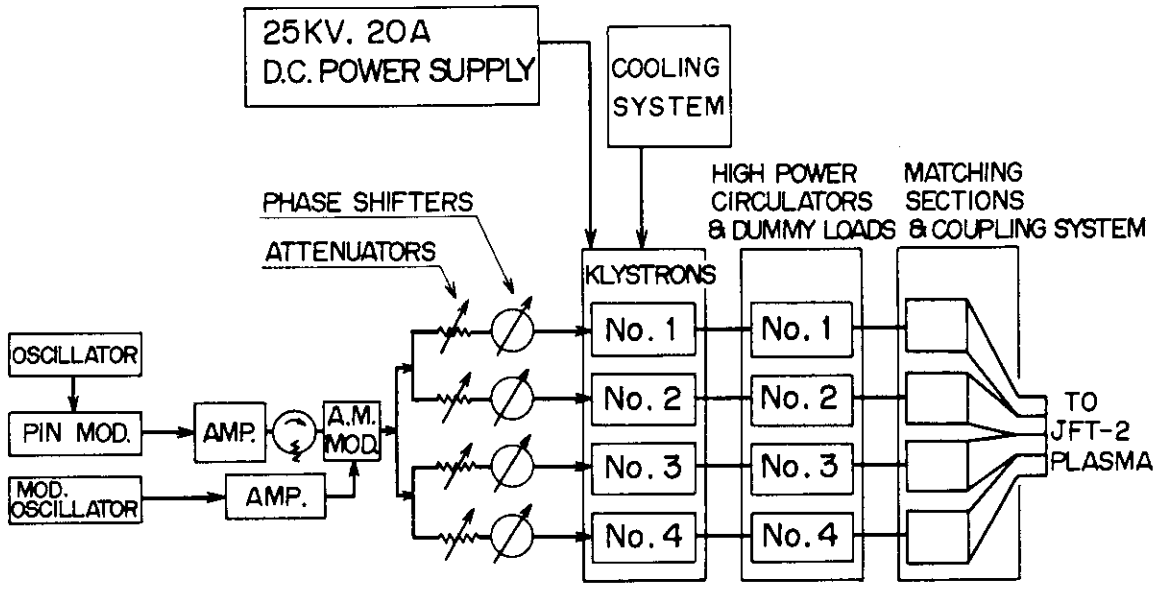

Fig.IV.3.1-1 Simple block diagram of lower hybrid heating system JFT-2 tokamak.

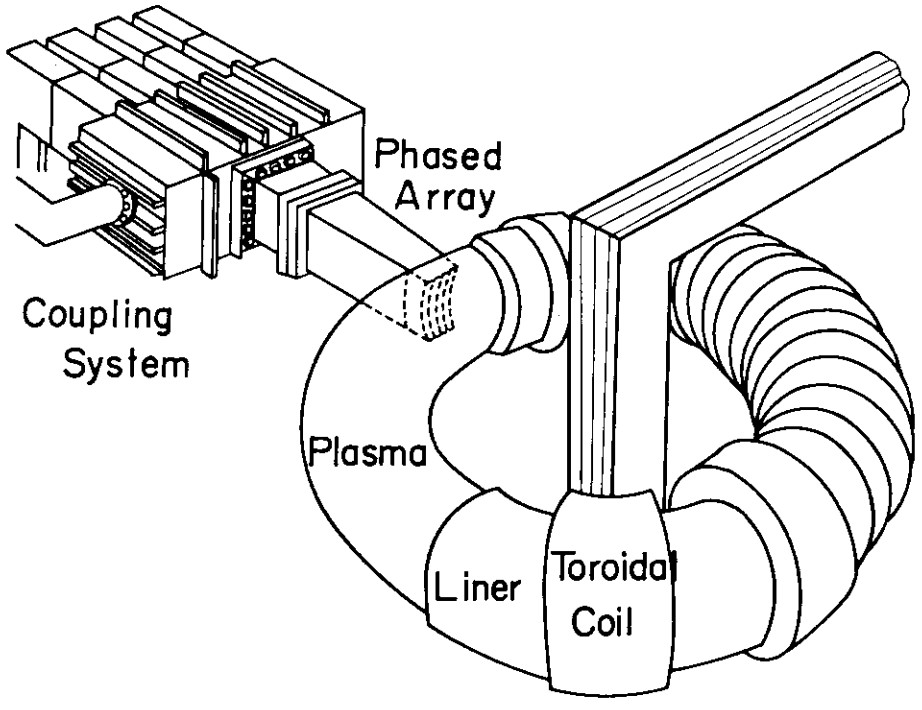

Fig.IV.3.1-2 Schematics of a waveguide coupling system for the JFT-2 tokamak.

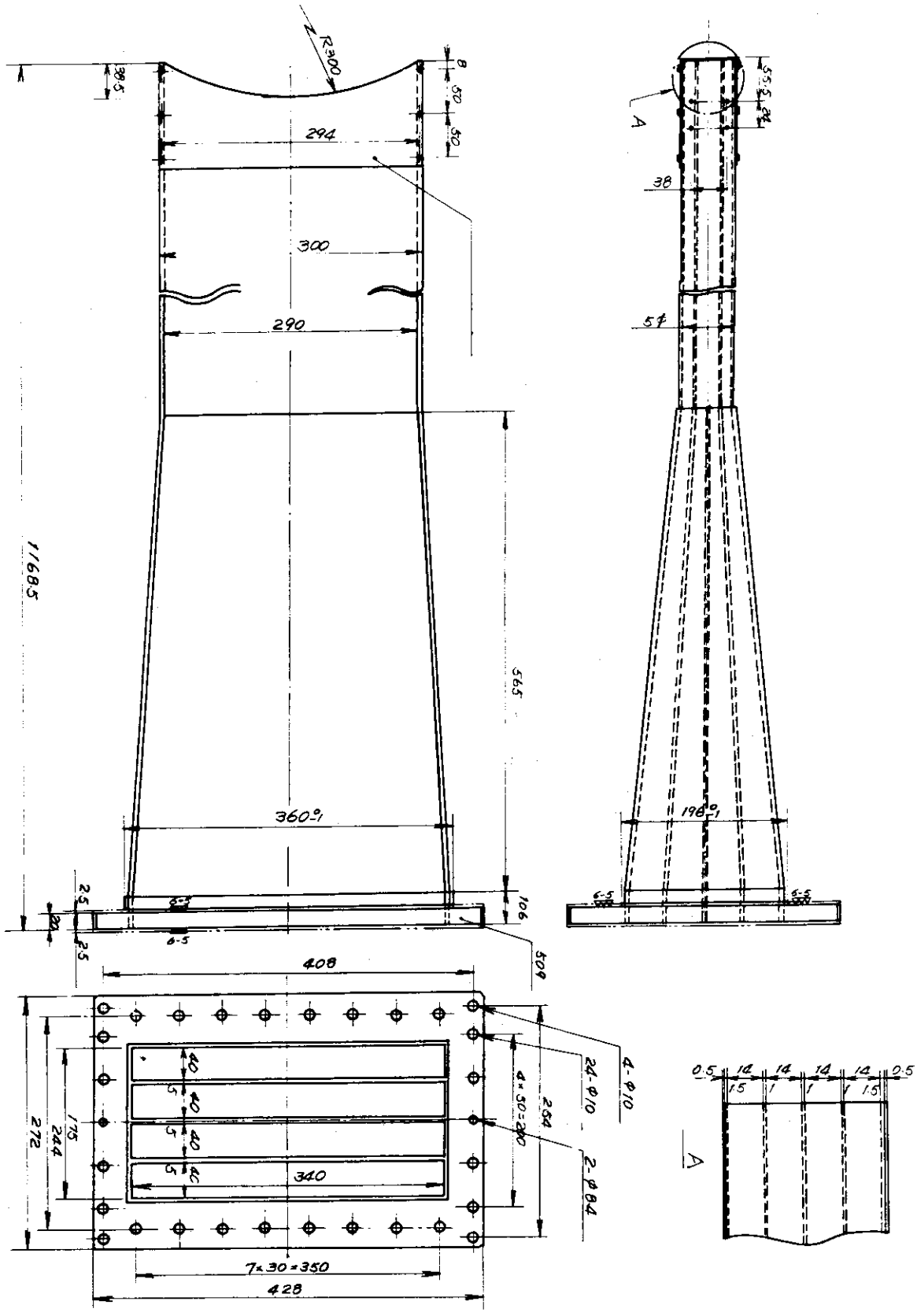

Fig.IV.3.1-3 A phased array of lower hybrid heating.

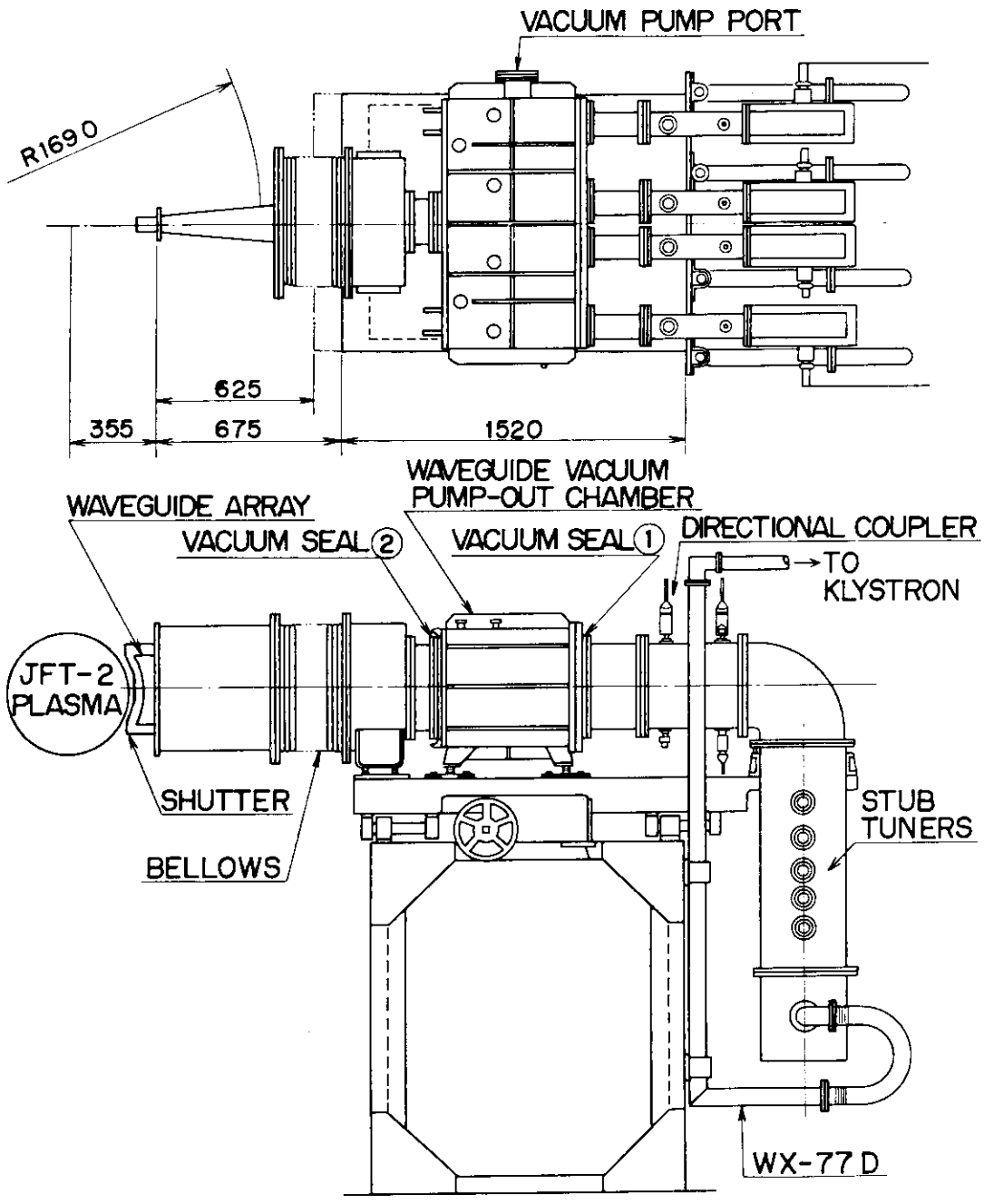

Fig.IV.3.1-4 Coupling section of lower hybrid heating system.

V. SURFACE SCIENCE AND VACUUM TECHNOLOGY

1. Introduction

The particle-surface interaction program in the division of thermonuclear fusion research was started in April 1975, and has been continued in close connection with the JT-60 program.

The main objective of this program is to investigate the individual effects in plasma-wall interaction which are very important problems in tokamak devices. Impurity atoms are released from the first wall which is bombarded with energetic and/or chemically activated particles leaking from a tokamak plasma through complicated processes including chemical reaction, sputtering, desorption of adsorbed gases, and blistering. Backscattering, trapping and reemission of the fuel particles are also great concerns for the investigation of the recycling processes in plasma-wall systems.

In the fiscal year of 1975, two ion accelerators, LSP and HSP, were designed and constructed[1]. If the year of 1976 is regarded as that of a significant step forward in the particle-surface interaction program making the initiation of the preliminary experiments[2], the following year of 1977 is to be remembered as a year of even greater significance in that fruitful results have been obtained in the fields of sputtering and surface erosion by using the two ion accelerators. The main results are as follows;

(1) precise measurements of the sputtering yield of molybdenum by Auger electron spectroscopy,
(2) angular distribution of sputtered atoms by Ne^+ ion bombardment,
(3) dose and characterization effects on surface topography change and sputtering yield in polycrystalline molybdenum for the bombardment with 2 keV Ne^+ ions, and
(4) reduction of erosion by blistering in molybdenum surface with a multi-groove microstructure,

Parallel to the above experiments, a specially designed scanning electron microscope has been constructed and connected to an exclusive beam line of the HSP[3]. This will be a powerful instrument for the in-situ and continuous observation of sample surface during ion bombardment.

In order to control the light impurities in large tokamaks, vacuum technological developments must be accompanied with the study of the particle-surface interaction. One of the staff members, in cooperation with the JT-60 group, began to investigate the vacuum pumping and wall cleaning problems

which are very much important to the design and operation of the actual machine. A new torus pumping system has been proposed for the JT-60, in which 18 K refrigerator cryopumps and turbomolecular pumps are connecting in series for the reduction of backstreaming of light impurities from the system. Concerning the development of large vacuum pumps, a palladium-alloy membrane pump has been proposed for the pumping of a large amount of hydrogen isotopes in thermonuclear fusion devices.

Figure V-1 is a summary of the surface effects-related research and development. Some of these are in progress or planned for the next few years.

2. Interaction of Energetic Particles with Wall Materials

2.1 Sputtering experiments with low energy ions

2.1.1 Sputtering yield measurement by Auger electron spectroscopy[4]

Metal impurities in the tokamak plasma are considered to play an important role in future thermonuclear fusion research. In this respect measurement of sputtering yields of high-Z materials by using Auger electron spectroscopy (AES) was started in our laboratory in 1976, laying emphasis on low energy proton impact. The preliminary result was obtained for polycrystalline molybdenum by normally incident protons in the energy range 0.15 - 6 keV[5]. So far, above 1 keV Finfgeld had obtained sputtering yields of molybdenum by neutron activation analysis[6]. The fact that our proton sputtering data were about three times as large as Finfgeld's sug-gusted that the application of AES to the sputtering yield measurement must be fully studied as compared with the other established methods.

One of the problems in the AES method is the selection of substrate material. In our previous work tungsten was chosen as a substrate material because of the uniform deposition of molybdenum[7]. However, if the uniform deposition is indispensable for the measurement, a serious limitation on the use of this method is implied. We have attempted to use silver as the substrate material in the present study. Figure V-2 shows the intensity of the AES signal of molybdenum atoms on the silver substrate as a function of the number of sputtered particles. Good linearity and reproducibility may permit us to neglect the effect of the agglomeration of the deposited particles, even if it existed. The molybdenum signal in Fig. V-2 was noramlized by the substrate AES signal for the sake of better reproducibility.

However, deviation from the linear relation appears with an increase in the number of deposited particles. The measurement of proton sputtering was made by deposition of 0.1 - 0.2 monolayers, which is in the linear region in Fig. V-2.

Silver substrate has several favorable points for the measurement. Simple Auger spectrum of Ag can eliminate overlapping with sample material, and this brings about a better signal to noise ratio. If the surface of the substrate is covered by residual gases, quantitative measurement of the deposited particles may fail in the normalization. Thus, silver has been expected to have good characteristics in view of the surface contamination.

Another problem relevant to the AES method is the angular distribution of sputtered particles. As far as we use an identical calibration curve such as in Fig. V-2, the method requires the same angular distribution for all energy ranges of incident beam because, in this experiment, the substrate was located at a fixed point where the total number of deposited particles represents the total number of sputtered ones. It is tacitly assumed that the angular distribution does not vary significantly because of the normal incidence of the primary beam.

The molybdenum sputtering yield obtained in the course of this work is shown in Fig. V-3. The difference of the present result from the previous one has come from correction of calibration factor (reduced to 0.6 from reexamination of the neon sputtering yield) and the above-mentioned improvement by using the silver substrate. Bay et al. have recently measured the sputtering yield by the weightloss method[8]. A small discrepancy still can be seen between our data and Bay et al.'s, the reason for which has not yet been clarified. We are able to conclude, however, that the AES method is proved to be a useful tool for the measurement of the sputtering yield of metals. This method has some advantages, namely high sensitivity and high spacial resolution. From the availability of this method being confirmed, the former may be applied to, for example, the measurement of sputtering yield under different surface conditions (e.g. oxidized surface), and the latter to the measurement of the angular distribution of sputtered particles.

2.1.2 Angular distribution of sputtered atoms by Ne^+ ion bombardment

Angular distributions of sputtered particles have been measured by

collecting the particles on inner surface of a semi-sphere whose radius is 38 mm and by analyzing with a densitometer and an atomic absorption spectrometer. Molybdenum targets were bombarded by Ne^+ ions which were defined with a slit of 4.5 mm and their energies were 0.6 and 1.5 keV. The angles of incidence were 0 and 45° with respect to the surface normal. These results are shown in Figs. V-4 - 6. At the normal incidence of 1.5 keV Ne^+ ions the angular distribution is symmetrical to normal of surface and obeys cosine law. On the other hand, for the oblique incidence, target atoms are easily sputtered toward the specular direction. The angle at the maximum in the angular distribution with respect to the surface normal becomes large with decreasing incident energy for the oblique incidence as shown in Figs. V-5 and 6. At oblique ion incidence ion-etched hillocks parallel to the ion beam direction were observed by scanning electron microscopy.

2.1.3 Dose and characterization effects on surface topography change and sputtering yield in polycrystalline molybdenum for the bombardment with 2 keV Ne^+ ions[9]

Dose effect on surface topography change and sputtering yield have been investigated under 2 keV Ne^+ ion bombardment in the LSP. Three kinds of molybdenum samples (see Table V-1) were chosen to study the characterization effect on them. The current density of 2 keV Ne^+ ions was 50 - 70 $\mu A/cm^2$ at the target. The irradiation dose ranges 0.8 - 12 $\times 10^{18}$ ions/cm^2. The ion beam was normally incident to the target. The target temperature during bombardment was ambient. The amount of sputtered material was determined by the weight loss of the target measured with a microbalance.

The typical results of surface topography changes of the three samples are shown in Figs. V-7 - 9. Up to 4 $\times 10^{18}$ ions/cm^2 in Fig. V-7, the grain boundaries come to appear with increasing dose because sputtering yield depends on the crystallographic orientation of grains[10]. Above 4 $\times 10^{18}$ ions/cm^2 cones appear on the surface, and the number density and the height of cones increase with dose. In contrast to this, Figs. V-8 and 9 show that large deformation textures parallel to the original direction are engraved by the bombardment at dose of 1.2 $\times 10^{19}$ ions/cm^2. From Figs. V-7 - 9, it appears that cones are localized, i.e., there are lines of cones along grain boundaries and aggregated cones on specific grains. As low sputtering atoms are considered to be a origin of cone formation[11], we

used the electron probe X-ray micro-analyzer to examine whether low sputtering tungsten atoms gather at the cones on the irradiation surface or not. The results showed that there was no correlation between tungsten atoms distribution and the cone distribution. It suggests that the low sputtering tungsten atoms are not the main origin of cone formation because of its similar localized distribution on non-irradiated surface to the cone distribution.

The results of weight losses of molybdenum targets of the three samples by the sputtering with 2 keV Ne^+ ions is shown in Fig. V-10 as a function of dose. We can conclude from Fig. V-10 that there is no dose effect on sputtering yield up to a dose of 1.2×10^{19} ions/cm^2. Moreover, we can say that there is no sample characterization effect on the sputtering yield, even though the topographic features of surface of the three samples become considerably different from each other by irradiation. It is thought that microroughing which can result in change of sputtering yield such as micro-honeycomb[12] are not fully developed in our radiation dose and sample characterization. The sputtering yield of molybdenum for mobardment with 2 keV Ne^+ ions obtained from Vig. V-10 is 0.90 ± 0.10 atoms/ion for three kinds of molybdenum samples.

2.2 Reduction of erosion by blistering in molybdenum surface with a multi-groove microstructure[13]

Blistering of surfaces of solid materials due to implantation of gaseous ions is a very undesirable erosion, when it develops into flaking and exfoliation with increasing ion fluence. Blistering caused by bombardment with helium ions in polycrystalline molybdenum has been reported[14][15]. More recently, it has been found in molybdenum that grain ejection occurs near a temperature of 200°C after bombardment with a high flux hydrogen ions with energies of 25 keV[16]. It is very important to find out how to reduce the erison by blistering, and there have been some propositions made to answer this problem[12],[17]~[21]. We have reported that surface erosion by helium blistering can be effectively reduced on surfaces roughned unidirectionally by sandblastering[22],[23]. A criterion for the reduction of surface erosion has been estimated from the experiment. Here we verify this criterion using a molybdenum surface with a multi-groove microstructure, where the width and the depth of the grooves are controlled.

Polycrystalline molybdenum targets with regularly multi-grooved surface

were prepared by the well-known chemical dry etching technique, which is commonly used for integrated circuit micropatterning. The microstructure consisted of a number of parallel rectangular grooves (see Fig. V-11); the width w, λ and the depth d were distributed to be 3 - 7 μm, 10 - 14 μm, respectively. A target was bombarded with a helium ion beam from the HSP. The beam was normally incident on the target surface. The current density was 30 - 60 $\mu A/cm^2$. The helium re-emission rate during bombardment was also measured by using the set-up shown in Fig. V-12. A small chamber with a volume of 2.5 ℓ and a slit 5 mm in diameter was connected to the main chamber for the detection of re-emitted helium atoms. Re-emitted helium was detected with a quadrupole mass spectrometer. The target temperature was measured with a thermocouple, which was alternatively used to measure the beam current after the temperature became saturated.

We show scanning electron micrographs of multi-grooved molybdenum surfaces bombarded with 100 keV helium ions to a fluence of 1×10^{19} ions/cm^2 (Fig. V-13) and 400 keV helium ions to a fluence of 5×10^{18} ions/cm^2 (Fig. 14) at room temperature. From Fig. V-13 is found the fact that the smaller width prevents formation of blisters with a large diameter. Although blisters are formed, flaking and exfoliation do not occur upto a fluence of 1×10^{19} ions/cm^2, at which considerable flaking occurs on the smooth surface[22),(23]. Very severe exfoliation occurs both on the smooth and chemically dry etched surfaces, whereas it is completely suppressed on the top surface of the multi-grooves because of its small width (Fig. V-14). The model which has been proposed by us predicts that blistering can be suppressed for a multi-groove microstructure when the width is narrower than $10R_p$ and the depth is larger than R_p, where R_p is the projected range of ions. From the LSS theory the projected ranges of helium ions in molybdenum are 0.35 and 1.1 μm, for 100 and 400 keV energies, respectively[24]. Therefore, this criterion is well verified in Figs. V-13 and 14.

In Fig. V-15 are shown the scanning electron micrographs of surfaces after bombardment with 100 keV helium to a fluence of 1.4×10^{18} ions/cm^2 at various target temperatures from room temperature to 850°C both for multi-grooved and smooth surfaces. In this case the widths d and λ-d of the grooves are both ≃7 μm, which does not satisfy the above criterion for the suppression of blistering. With increasing temperature of the target, blisters with larger diameter are formed on the smooth surface, which has a tendency to flake due to reduction of the strength of the material[14].

As seen in Figs. V-15e and 15f significant flaking occurs on smooth surfaces at 350 and 500°C, where the size of the flakes is beyond 7 μm. On the top surface of the multi-grooves flaking is very much reduced. It is seen at 850°C that dense pinholes are observed on both smooth and multi-grooved surfaces.

The result of the helium re-emission rate at various temperature is shown in Fig. V-17 as a function of the fluence of helium ions of 100 keV incident energy for multi-grooved and smooth surfaces. Some remarkable features are observed as follows; (1) for the smooth surface an initial overshoot of the re-emission curve is seen, whereas in the multi-grooved surface it is not seen below 500°C; (2) at 850°C the re-emission curve for the multi-grooved surface is almost the same as for the smooth surface; (3) the saturation level of the re-emission rate is always lower for the multi-grooved surface than the smooth one; (4) the critical fluence shifts to a higher value for the multi-grooved surface compared to the case of the smooth one within the experimental accuracy; (5) the temperature dependence curve of the critical fluence for the multi-grooved surface is located at higher temperatures than that for the smooth surface; and (6) the initial overshoot is not seen for the re-damaged surface. Bauer and Thomas[25] have concluded that the initial overshoot indicates a helium re-emission burst which is connected with the surface deformation, but no surface deformation was observed by scanning electron microscopy at the same fluence as that at which the initial re-emission overshoot appears[22],[23]. This overshoot is therefore not directly related to surface deformation. When the concentration of trapped helium atoms exceeds the helium solubility, the abrupt increase in re-emission rate occurs. However, a gradual increase in new trapping sites is produced by irradiation damage with increasing helium ion fluence[26]. These make the initial overshoot appear. The damage due to chemical dry etching is thought to be equivalent to irradiation damage in its capability for helium trapping. The reason why no overshoot is seen below 500°C on the multi-grooved surface may be that the initial surface was severely roughened by dry etching which causes the number of trapping sites to have been saturated before helium bombardment. The above discussion can be applied to understanding observations (3) and (6) in the same way as (1). The high diffusivity of helium atoms and annealing can explain observation (2). The temperature dependence of the critical fluence is determined by the balance between helium diffusivity and solubility. As the

diffusivity in the multi-grooved surface is smaller than in a smooth surface, the critical fluence shifts to higher value, which explains (4). As the high trapping ability in a multi-grooved surface reduces diffusion of helium atoms at high temperature compared to that in a smooth surface, the balancing temperature between the diffusivity and solubility shifts toward the higher side for an endothermic metal such as molybdenum, the solubility of which is larger as the temperature becomes higher. Observation (5) is due to this fact. Further measurements of the helium re-emission rate in 400 keV helium bombardment will be made for the above observations.

3. Vacuum Technological Development

3.1 Alternative torus pumping system for JT-60

In order to control the light impurities in large tokamaks, vacuum technological developments must be accompanied with the study of the particle-surface interaction. We, in cooperation with the JT-60 group, began to study the vacuum pumping and wall cleaning problems for the design and operation of JT-60.

Large tokamaks impose unique vacuum pumping problems involving extreme cleanliness requirements and high pumping speeds. The torus pumping system must perform the following functions in the JT-60 system:

(a) Remove impurities liberated during bakeout, high temperature oxidation and reduction, and discharge cleaning of the vacuum vessel interior.
(b) Provide the initial ultra-clean vacuum environment for plasma formation with minimal impurities.
(c) Evacuate the spent plasma constituents at the end of each pulse prior to initiation of the next plasma pulse. The interval between the pulses is planned to be 10 minutes.

The influx rate of contaminants from the pumping system to the vacuum vessel will be required to be comparable to the total leak and outgassing rate of the vessel. Here, the contaminants include water vapor, oxygen, carbon monoxide and hydrocarbons.

In order to fulfill these requirements, we proposed an alternative pumping system after a detailed study, which comprises of 18K refrigerator cryopumps and turbomolecular pumps connecting in series. The conceptual deisgn of the system is shown in Fig. V-17.

The sticking probability of active gases such as oxygen and carbon monoxide on clean metal surfaces is fairly large. Therefore, if these gases flow into the vacuum vessel after a discharge cleaning, they are adsorbed on the molybdenum wall almost completely. In this case, the wall acts as a large ideal pump or a gas sink. From this point of view, we have evaluated the backstreaming rate of such contaminants from the turbomolecular pump system. A final contaminant gas composition at the inlet port of the pump is typically 3×10^{-10} Torr of water vapor, 1×10^{-10} Torr of carbon monoxide, 3×10^{-11} Torr of carbon dioxide, and a small amount of hydrocarbons. If we apply these values to the JT-60 system, the backstreaming rate of the contaminants would be as follows;

	backstreaming rate (number of oxygen atoms)
without liquid nitrogen traps	4.5×10^{14} atoms/s
with liquid nitrogen traps	1.5×10^{14} atoms/s
with refrigerator cryopumps	8×10^{12} atoms/s

where the rate is indicated in oxygen atom equivalent. The backstreaming rate from the pumping system with refrigerator cryopumps is comparable to the leak and outgassing rate of the vacuum vessel.

Although cryopumps offer outstanding advantages for this application, several special problems which are associated with pumping gases from the torus vacuum vessel must be considered. One of the important problems is a relatively large heat input to the cryopanels due to impingement of energetic particles and deposition of cyclotron radiation from the plasma, and eddy current induced by magnetic flux change across the panels. We have made an estimation on these heat loads to the cryopanels comparing with the common heat loads such as due to radiation from surrounding environment and conduction by residual gas molecules.

Another problem is the desorption of previously pumped gas molecules by energetic particles. Since the molecular binding energies of the condensate are less than 1 eV, each hot particle could desorb hundreds of previously pumped gas molecules. We have also made an estimation on this effect.

3.2 Palladium-alloy membrane pump for hydrogen pumping[27]

We have proposed a palladium-alloy membrane pump for the pumping of a large amount of hydrogen isotopes in thermonuclear fusion devices. The performance of the pump was estimated from both the kinetic and chemical processes involved. This pump essentially consists of a heated membrane of palladium alloy, which acts as a pumping surface and is positioned airtightly between the vacuum chamber to be evacuated and the pump chamber with an oxygen inlet and a liquid nitrogen trap (see Fig. V-18). In order to reduce the hydrogen concentration at the backside (pump chamber side) of the membrane, we offer a new idea which implies that the diffused hydrogen should be removed through chemical reaction at the membrane-gas interface.

The results derived from the theory and the experimental values show that the pumping speed per unit projected area at 10^{-5} Torr is about 7 - 15 $l/sec \cdot cm^2$ if a 0.1 mm thick membrane is corrugated to increase the effective area by 5 - 10 times. The pumping speed per unit power input at 10^{-5} Torr is comparable to that of large cryopumps.

References

(1) Annual Report of the Divison of Thermonuclear Fusion Research, JAERI, for the Period of April, 1975 to March, 1976, JAERI-M 6926, p. 109.
(2) Annual Report of the Division of Thermonuclear Fusion Research and Division of Large Tokamak Development, JAERI, for the Period of April, 1976 to March, 1977, JAERI-M 7479, p. 144.
(3) Obara, K., Abe, T. and Sone, K.: JAERI-M 7797 (1978) (in Japanese).
(4) Ohtsuka, H., et al.: J. Nucl. Materials 76 & 77 (1978) 188.
(5) Sone, K., et al.: Proc. Internal. Symp. Plasma Wall Interaction (Pergamon Press, 1977) p.323.
(6) Finfgeld, C. R.: ORO-3557-15 (1975)
(7) Tarng, M. L. and Wehner, G. K.: J. Appl. Phys. 44 (1973) 1534.
(8) Bay, H. L., Roth, J. and Bohdansky, J.: J. Appl. Phys. 48 (1977) 4722.
(9) Yamada, R., et al.: J. Nucl. Materials _in press).
(10) Nelson, R. S. and Mazey, D. J.: Radiation Eff. 18 (1973) 127.
(11) Wehner, G. K. and Hajick, D. J.: J. Appl. Phys. 42 (1971) 1145.
(12) Ziegler, J. F., Cuomo, J. J. and Roth, J.: Appl. Phys. Letters 30 (1977) 268.
(13) Sone, K., et al.: J. Nucl. Materials 76 & 77 (1978) 240.

(14) Erents, S. K. and McCracken, G. M.: Radiat. Eff. 18 (1973) 191.
(15) Thomas, G. J. and Bauer, W.: J. Nucl. Materials 53 (1976) 134.
(16) Nakamura, Y., Shibata, T. and Tanaka, M.: J. Nucl. Materials 68 (1977) 253.
(17) Das, S. K. and Kaminsky, M.: Appl. Phys. Letters 27 (1975) 197.
(18) Das, S. K. and Kaminsky, M.: J. Nucl. Materials 63 (1976) 292.
(19) Wilson, K. L., Thomas, G. J. and Bauer, W.: J. Nucl. Materials 61 (1976) 113.
(20) Behrisch, J. Roth R. and Scherzer, B. M. U.: J. Nucl. Materials 57 (1975) 365.
(21) Evans, J. H.: J. Nucl. Materials 61 (1976) 117.
(22) Sone, K., et al.: Proc. 7th Internal. Vac. Congr. and 3rd Internal. Conf. on Solid Surfaces (IUVSTA, 1977) p.375.
(23) Saidoh, M., et al.: JAERI-M 7182 (1977).
(24) Sone, K. and Shiraishi, K.: JAERI-M 6094 (1975).
(25) Bauer, W. and Thomas, G. J.: J. Nucl. Materials 53 (1976) 127.
(26) Bottiger, J., et al.: J. Appl. Phys. 48 (1977) 920.
(27) Murakami, Y. and Ohtsuka, H.: Vacuum 28 (1978) 235.

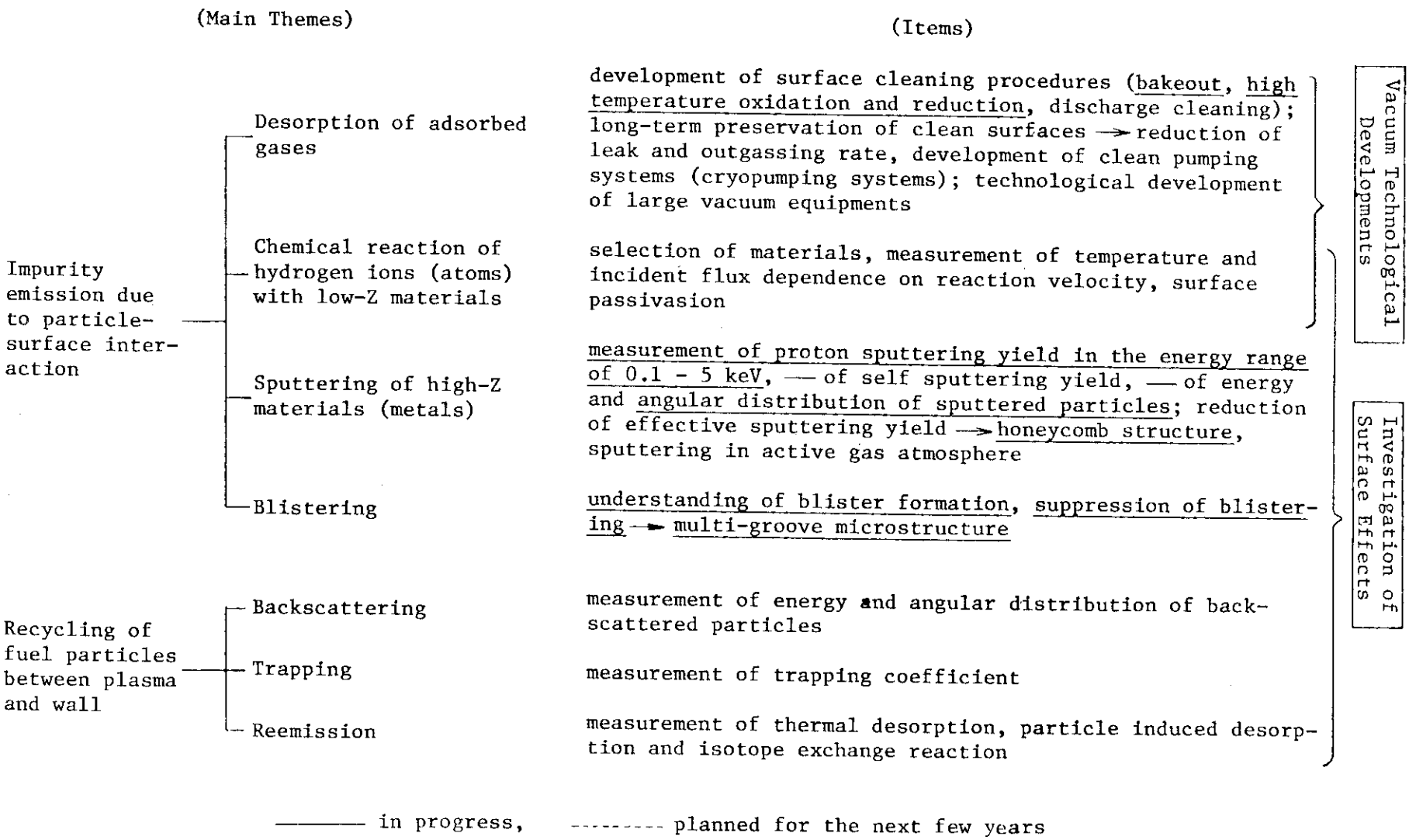

Fig.V-1 Summary of the surface effects-related research and development.

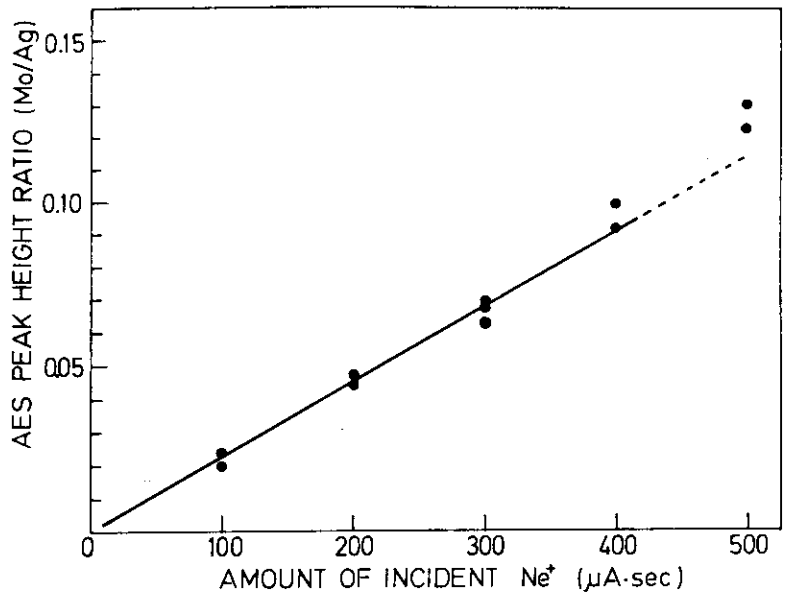

Fig.V-2 Intensity of the AES signal of Mo (186 eV) normalized by the substrate Ag (351 eV) as a function of Ne ion dose which is proportional to the number of sputtered particles.

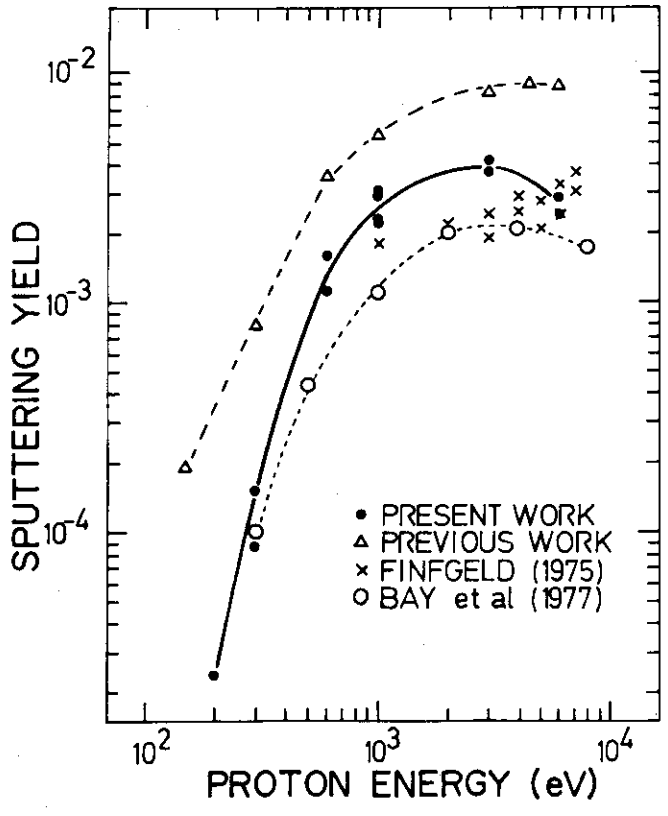

Fig.V-3 Sputtering yield of molybdenum by protons as a function of energy.

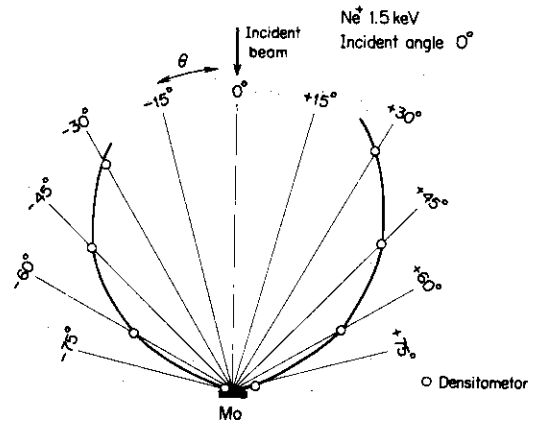

Fig.V-4 Angular distribution of sputtered molybdenum atoms; incident beam -- 1.5 keV Ne^+, incident angle -- 0°.

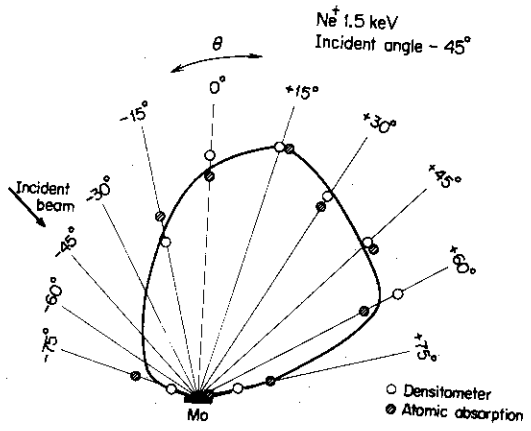

Fig.V-5 Angular distribution of sputtered molybdenum atoms; incident beam -- 0.6 keV Ne^+, incident angle -- 45°.

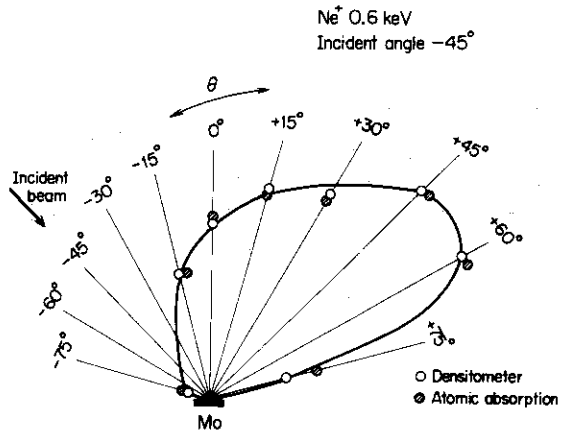

Fig.V-6 Anglular distribution of sputtered molybdenum atoms; incident beam -- 0.6 keV Ne^+, incident angle -- 45°.

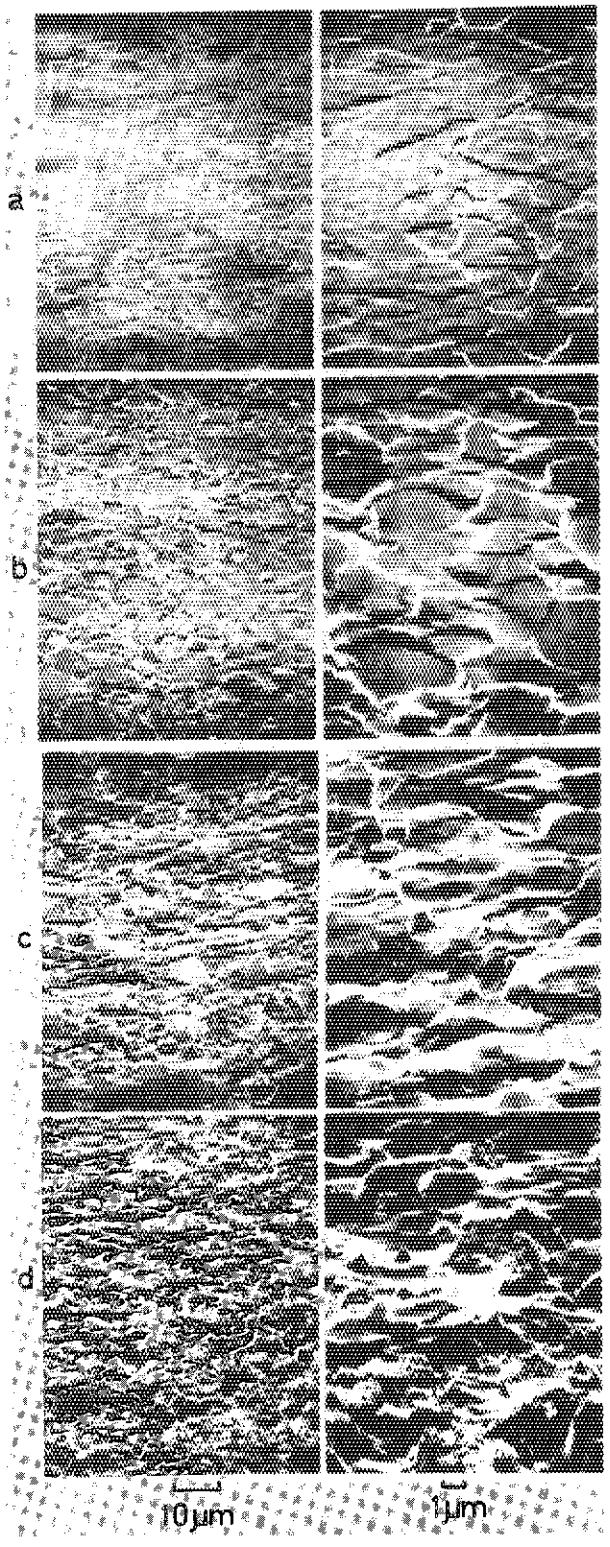

Fig.V-7 SEM micrographs of sputtered surfaces of No.1 sample as a function of 2 keV Ne^+ ion dose; (a) 0.8×10^{18}, (b) 1.7×10^{18}, (c) 4.5×10^{18}, and (d) 1.2×10^{19} ions/cm^2.

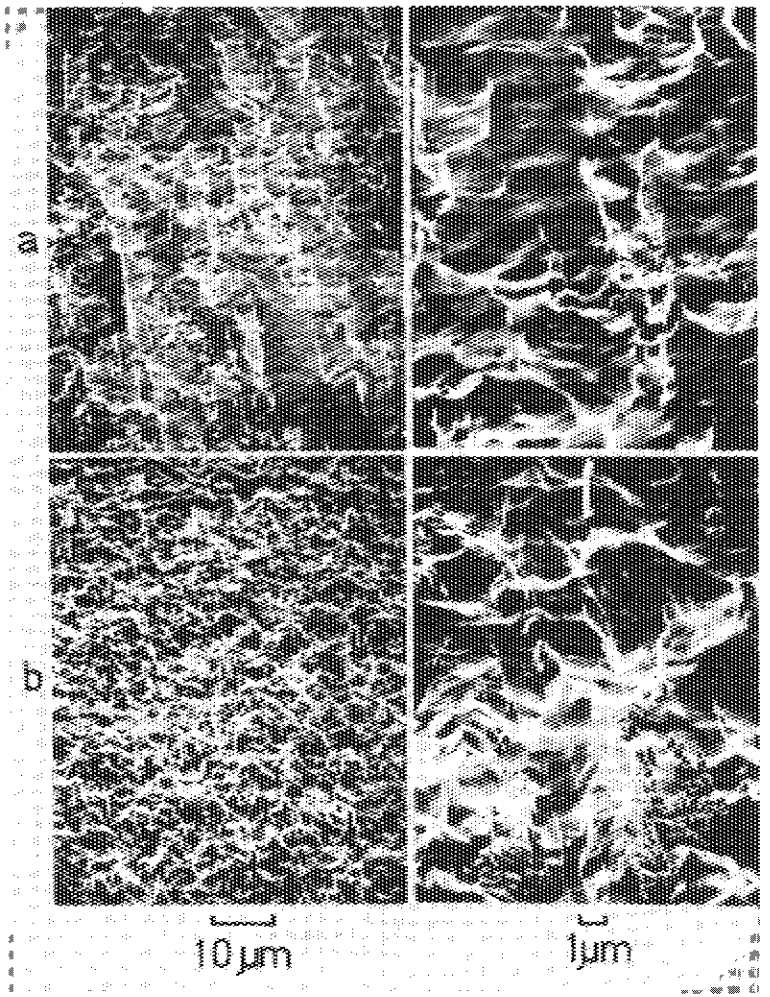

Fig.V-8 SEM micrographs of sputtered surfaces of No.2 sample by 2 keV Ne^+ ions; (a) 4.5×10^{18} and (b) 1.2×10^{19} ions/cm^2.

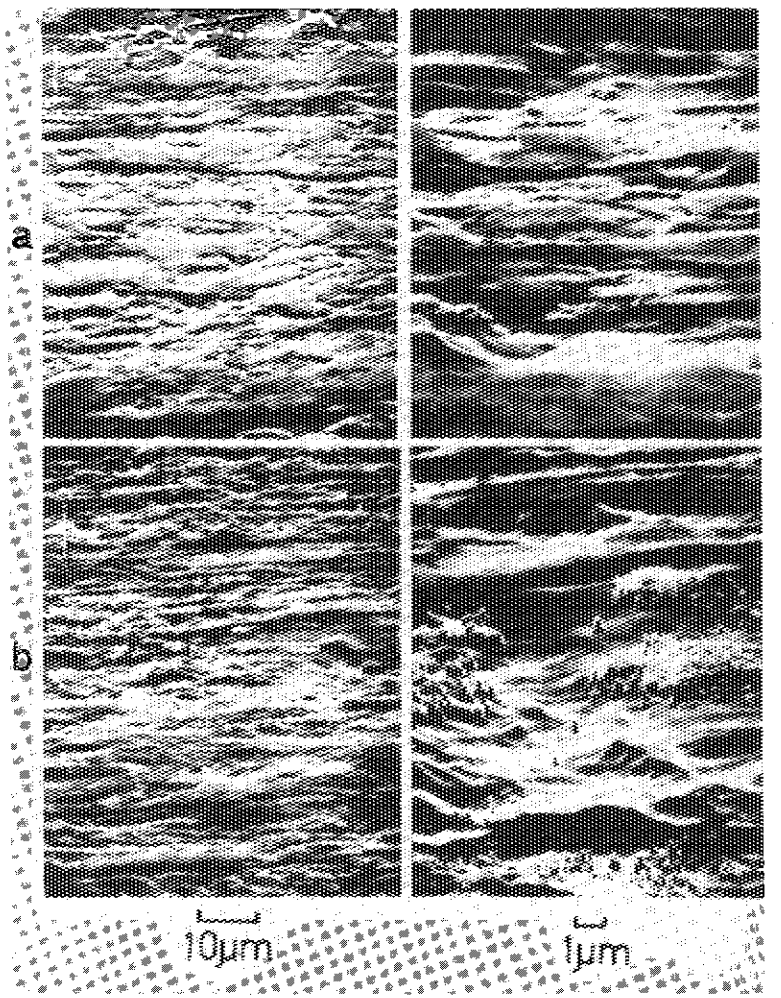

Fig.V-9 SEM micrographs of sputtered surfaces of No.3 sample by 2 keV Ne^+ ions; (a) 4.5×10^{18} and (b) 1.2×10^{19} ions/cm^2.

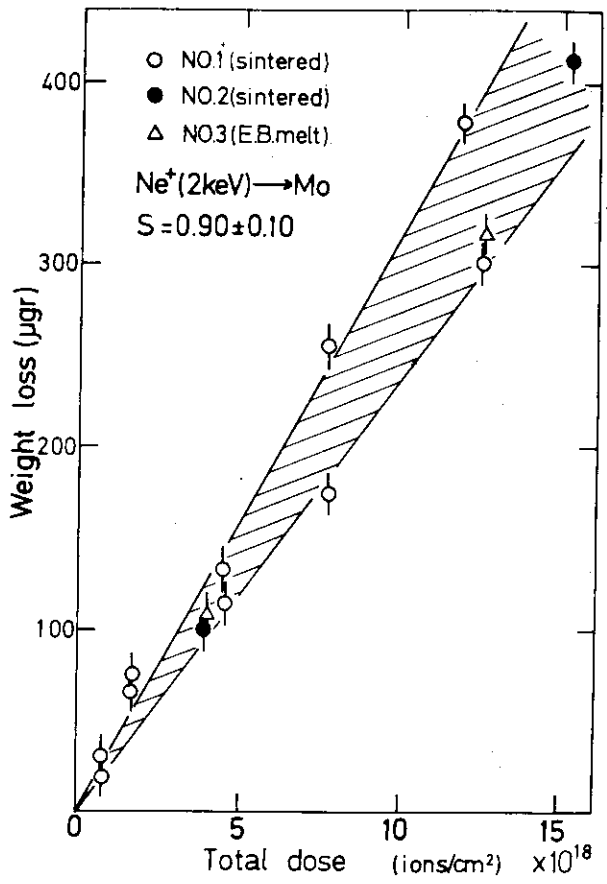

Fig.V-10 Weight losses of the samples by the sputtering with normally incident 2 keV Ne^+ ions as a function of dose. Their sputtering yields are 0.90±0.10 atoms/ion.

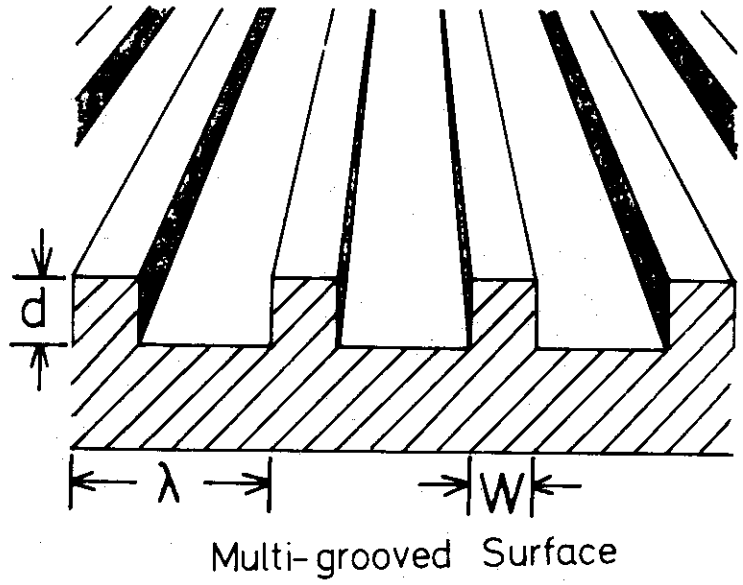

Fig.V-11 Schematic representation of a perspective view of a molybdenum surface with regular microscopic multi-grooves, where d is the depth of the grooves, w the width of the protruding part, and λ the periodic length of the multi-grooves.

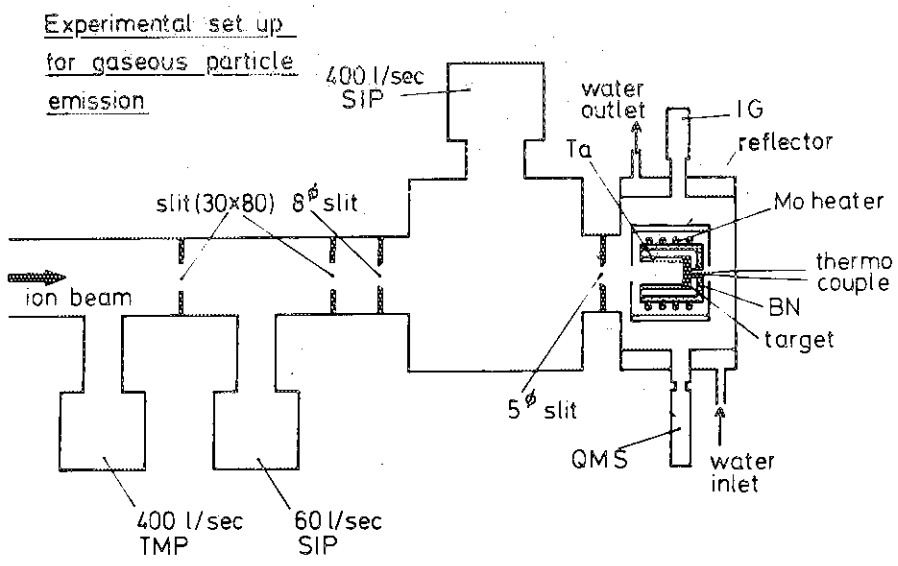

Fig.V-12 Schematic representation of the experimental set-up for the measurement of helium re-emission during bombardment. SIP; sputter ion pump, TMP: turbo-molecular pump, IG: ionization gauge, QMS: quadrupole mass spectrometer, and BN: boron nitride insulator.

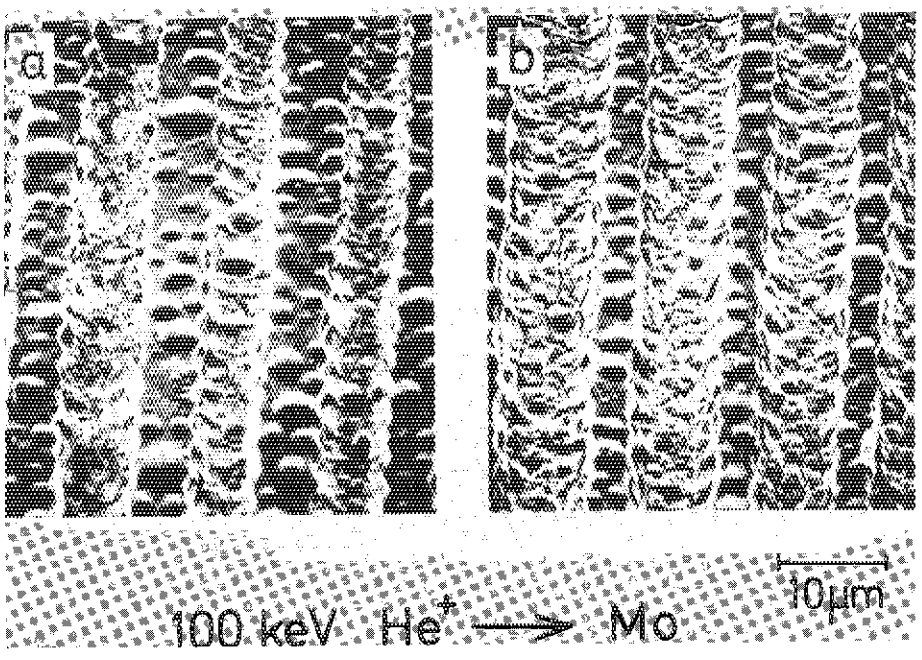

Fig.V-13 Scanning electron micrographs of regular multi-grooved molybdenum surfaces bombarded with 100 keV helium ions to a fluence of 1×10^{19} ions/cm^2. The width w is approximately 6 μm and 3 μm, in (a) and (b), respectively.

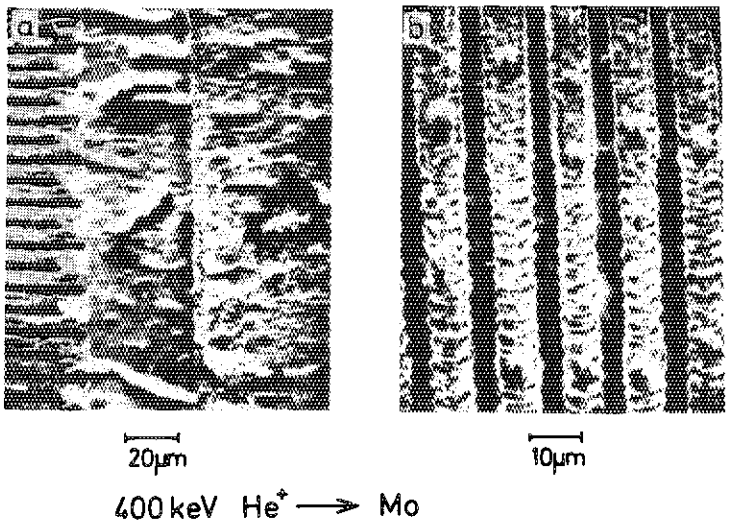

Fig.V-14 Scanning electron micrographs of molybdenum surfaces bombarded with 400 keV helium ions to a fluence of 5×10^{18} ions/cm^2. The micrograph (a) shows three different kinds of bombarded surfaces, i.e. the multi-grooved surface (left), the smooth surface (center), and the chemically dry etched surface (right). The central part of (a) is eroded most severely by exfoliation, while the multi-grooved surface (b) is little eroded.

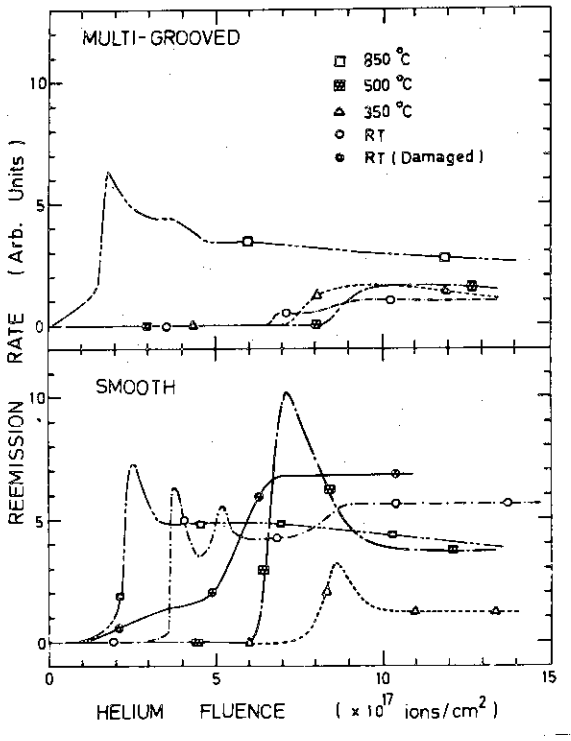

Fig.V-16 Helium re-emission rate as a function of the fluence of helium ions of 100 keV incident energy for multi-grooved and smooth molybdenum surfaces at various target temperatures. RT denotes room temperature bombardment, and RT (damaged) room temperature bombardment of molybdenum target pre-damaged with 100 keV helium to a fluence of 2×10^{18} ions/cm^2.

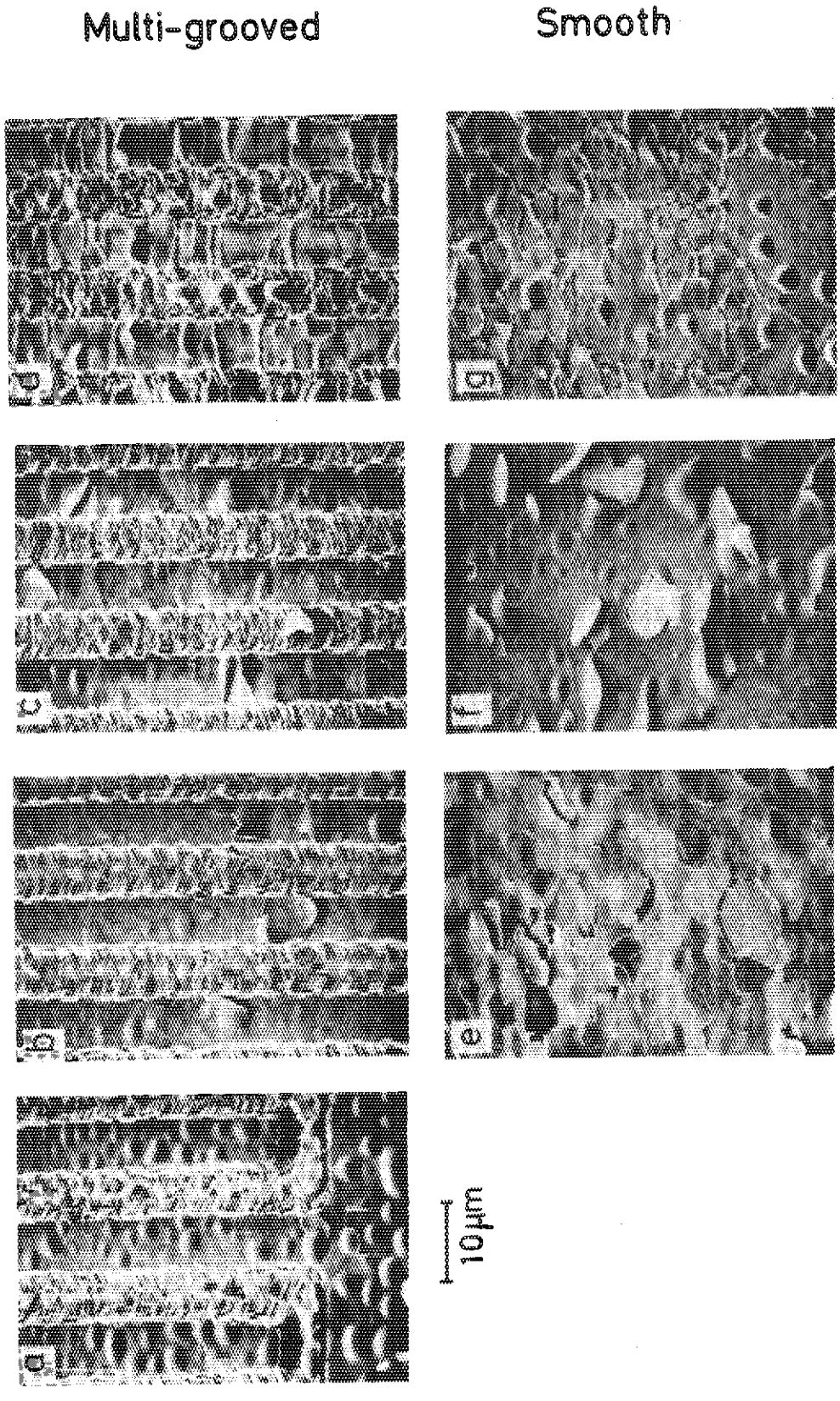

Fig.V-15 Scanning electron micrographs of molybdenum surfaces after bombardment with 100 keV helium ions to a fluence of 1.4×10^{18} ions/cm^2 at various target temperatures; (a) room temperature, (b, e) 350°C, (c, f) 500°C, and (d, g) 850°C.

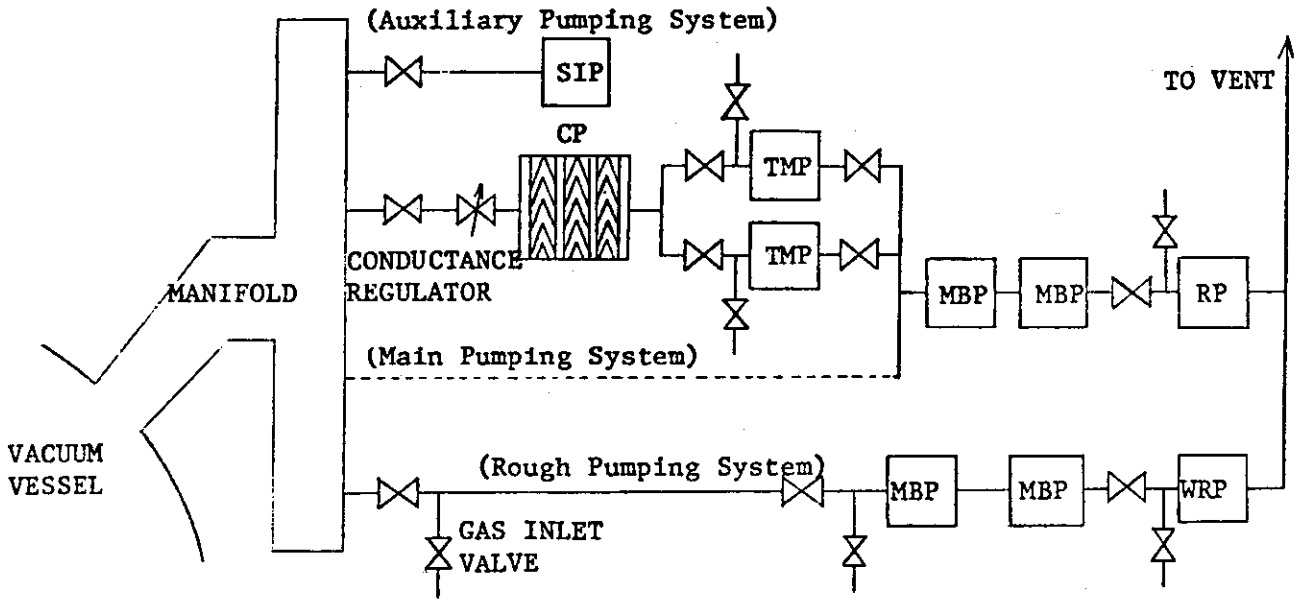

CP 18K cryocondensation pump
TMP turbomolecular pump (2000 l/sec)
SIP sputter-ion pump
MBP mechanical booster pump
RP rotary pump
WRP water ring pump

Fig.V-17 Conceptual design of an alternative torus pumping system for JT-60. This shows 1/4 of the full system.

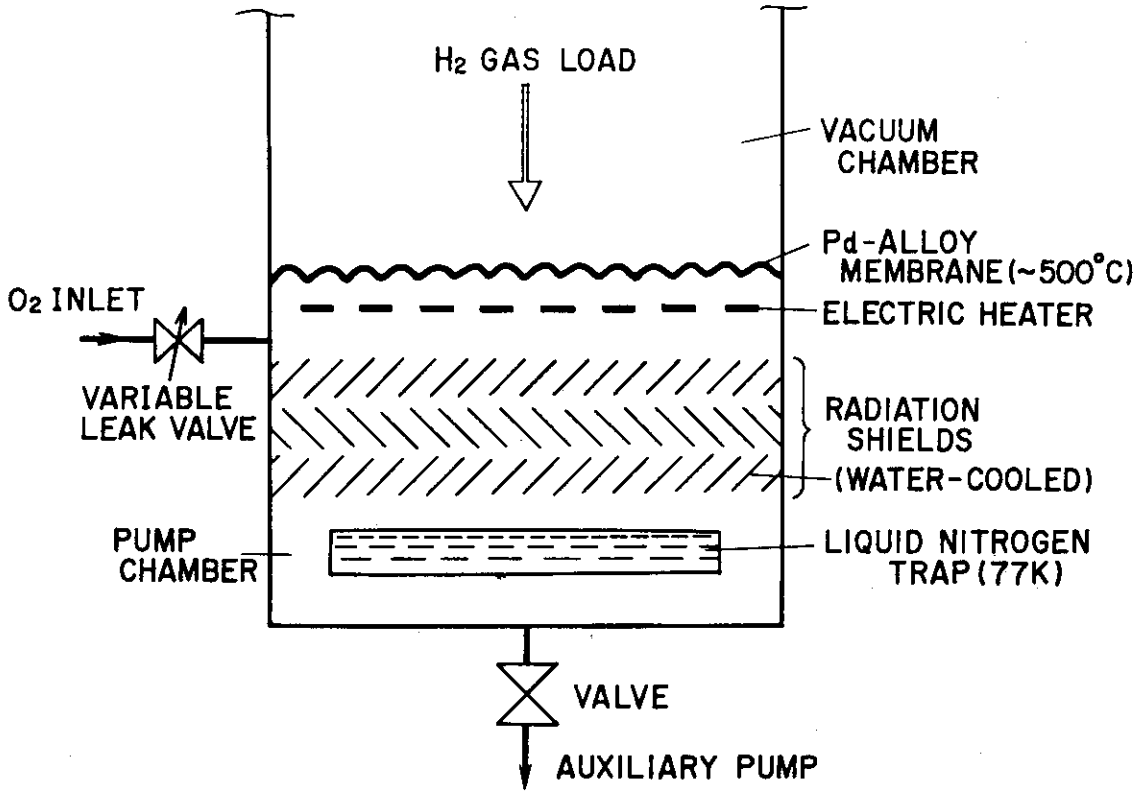

Fig.V-18 Schematic diagram of Pd-alloy membrane pump.

Table V-1 Characterization properties of three molybdenum materials; No.1--Plansee Co., No.2--Tokyo Tungsten Co., and No.3--Daido Steel Co.

	No. 1	No. 2	No. 3
	sintered	sintered	E.B. melt
	rolled	rolled	rolled
	1000°C 10 min annealed	as received	as received
Mo	99.96 %	99.96 %	99.96 %
W	200 ppm	200 ppm	150 ppm
Fe	50	40	2
Al	10	6	2
Si	5	15	88
C	15	7	40
N	5	5	12
O	20	17	8

VI. SUPERCONDUCTING MAGNET DEVELOPMENT

1. Introduction

The main purpose of development of superconducting magnet (SCM) for fusion research in JAERI is the construction of superconducting toroidal coil system for a device coming after JT-60 machine, named Fusion Engineering Power Reactor.

The strategy for this purpose is that the evolution of the development should be scaling up of superconducting toroidal coil from a size of coil bore~1 m to the post-JT-60 machine approximately by four stages, as cluster test, large coil task, superconducting tokamak test assembly and Fusion Engineering Reactor proto-type coil test.

In April of 1978, JAERI signed on the Implementing Agreement for a Programme of Research and Development of Superconducitng Magnets for Fusion Power, operated by International Energy Agency. In the Annex I of the Agreement JAERI participates in the Large Coil Task which will be carried out in Oak Ridge National Laboratory, U.S.A. The scientific activities on SCM in the fiscal year of 1977 are shown in the followings.

2. Advanced Design of Cluster Test Facility and Test Module Coil[1]

Following the preliminary design work of cluster test facility in the fiscal year of 1976, we carried out the advanced design of the facility and test module coil in relation with IEA-Large Coil Task.

The design conditions are a little modified from the work of 1976. The modified conditions are followings.

..... The current in a test module coil is 10,000 12,000 A

..... The maximum field in a test module coil is 8.0 T

..... The configuration of a test module coil is similar to IEA-LCT coil. The size is half of IEA-LCT coil.

The back ground coil, called as cluster test coil has 1.5 m mean diameter, the operational current of 2,150 A and the maximum field of 7 T in the winding with the operating test module coil.

The coil disposition and the dimension of the cluster test coil and the test module coil are shown in Fig. VI-1. In order to simulate the poloidal field effect on the test module coil, a separated system is designed as pluse poloidal coil, which is also superconducting. The principal

designed values of the cluster test coil and the test module coil are shown in Table VI-1.

This facility requires a refrigerator of 250 W at 4.2 K. The total cooling weight is about 25 tons.

With the cluster test facility the principal experimental simulation of toroidal coil can be carried out on conductor, stability, insulator, mechanical reinforcement, cooling system and varying field effect. In order to generate a high stress in a test module coil, a high current density coil may be constructed and tested with a fixed ampere turns.

3. Preliminary Analysis of Magnetic Field and Stress on IEA-LCT

Magnetic field and stress on IEA-LCT are have been studied on the basis of the ORNL specification. A computer code JAFUSAC, in which magnetic field is calculated by integral of Biot=Savart's Law and stress analysis is carried out by finite element method, is applied for this study.

As ampere turn in a LCT coil is not specified by ORNL, first the value, 6.75 MAT, was determined for the generation of 8 T on the horizontal line in a coil by varying the winding cross section and the current density. With this condition, all the analysis were started and as one of the results, Fig. VI-2(a) shows magnetic field distribution along the horizontal center line. It is revealed, by field calculation, that, though the peak field is defined on the horizontal line in the specification, the practical maximum field is generated in the corner of D shape. The field distribution along the inner-most layer is presented in Fig. VI-2(b) in which the maximum value is 8.3 T.

The Von Mises stress both in the conductor and in the structure is calculated on the conductor and in the structure is calculated on the several test conditions and the results in the normal test condition is shown in Fig. VI-3 in function of the coil perimeter. It is shown that the maximum stress value in the structure is 10 kg/mm^2 and in the conductor 7 kg/mm^2. These values are lower than the yield stress value.

4. Thermal Analysis on IEA-LCT

Thermal problems in the IEA-Large Coil Task have been studied[3], including stability, nuclear heating simulation, initial cool down and warm up.

The conditions for half turn recovery to the superconducting state after a normal transition have been obtained by a computer program TRUMP. Both linear heat transfer and boiling heat transfer characteristics have been considered. Fig. VI-4 shows one of the results in which there are two kinds of stable point, one is the superconducting state(○1) and the other is the heat balance point(● 2,3).

The resulting conditions are;

(1) The heat generation rate per unit length of the conductor should not exceed the cooling heat flux.

(2) Liquid Helium must be sufficiently supplied from surroundings. (over 1.6 g/sec-cm^2)

(3) The temperature when normal transition occurrs must be under 9.5 K.

In order to cool down a LCT coil within 120 Hr a flow rate of 72.5 g/sec is necessary, with the three steps of cooling gas, 100 K, 20 K, and 4.2 K. In order to warm up a LCT coil within 60 Hr the current of 180 A ∿ 190 A must be supplied.

Thermal stress in initial cooling has been analyzed by a computer program SAP-4[4]. Without active cooling system in structure material the stress in stainless steel wall would increase to the yield strength and the stress in superconductor exceeds the yield strength as shown in Fig. VI-5. In order to avoide a possibility of the breakdown, additional cooling in stainless steel wall such as by special cooling channel or extended cooling surface is necessary for initial cooling.

5. Development of Large Current Conductors

A forced cooled NB-Ti conductor and a reinforced Nb_3Sn conductor have been developed in order to study large current capacity for tokamak toroidal coil.

The forced cooled conductor, can have an advantage of more wetted perimeter between conductor and coolant than pool cooled one. Consequently, with this type of conductor a coil winding can have higher current density. The developed conductor[5], which has the operational current of 10 kA at 8 T, has 79 FM Nb-Ti strants, reinforcing material and copper stabilizer with cooling channel. Fig. VI-6 shows a cross sectional view of the conductor. The doncutor with stands an internal pressure of 50 kg/mm^2 with water pressure test. It has AC loss of 7.1 mW/m under magnetic field of 0.5 T, 1/150 Hz.

Reinforced MF Nb_3Sn conductor, shown in Fig. VI-7 has been developed . The conductor, rated as 10 kA at 13 T, consists of 5 monoliths of MF Nb_3Sn and reinforcement. The superconducting monolith contains 331 groups, each of which has 331 filaments. One filament diameter is approximately 5 μm and 0.6 μm thick Nb_3Sn layer is formed around it. These conductor was tested and the following characteristics were obtained. The critical temperature and the resistance ratio between 3000 K and 18 K are 17.5 K and 115 respectively. The critical current density in 0.6 m Nb_3Sn layer is 7×10^5 A/cm^2 at 7 T. The measurement of the critical current under tensile stress showed less effect of stress on critical current that without reinforcement.

6. Installation of Superconductor Test Facilities

In order to test large current and high field superconductor, the test facilities are installed in the laboratory.

A Nb-Ti solenoid of 8.5 T - 24 cm clear bore was designed by JAERI and manufactured in industry (Fig.VI-8). The winding of this magnet has 26 cm inner diameter, 41 cm outer diameter and 45 cm length. The inductance is 2.91 Henry and the weight 300 kg. The magnet quenches at the field of 9.3 T on the winding with the average current density of 11,000 A/cm^2 and the stored energy of 1.2 MJ. No quench is found with the charge rate of 8.5 T/ 8 minutes. This magnet will be used for the test of Nb-Ti large current conductor.

A Nb_3Sn solenoid of 13 T - 7 cm clear bored is being imported from a foreign industry. This magnet will be used for the development of multifine Nb_3Sn conductor.

A stress effect test facility was designed by JAERI and manufactured in industry.

This test facility can give 10 ton maximum force, 5.5 T transverse field and, 2,000 A current on a superconductor test piece. It will be used for the study of stress effect on Nb_3Sn materials and for the calibration of strain gage in magnetic field.

A 12 kA - 10 V power supply was installed in the laboratory. It consists of IVR, transformer, silicon diode, filter and transistor controller. The power supply will be used for short sample test of large current conductor with the solenoid mentioned above.

Cryogenic apparatus and electronic measurements were well equipped in the laboratory.

7. Conceptual Studies for Future Program

In the fiscal year of 1977, two conceptual studies were carried out in corporation with industries for future program of Tokamak superconducting toroidal coil development.

One is the conceptual stufies on the transportation and construction problems of large superconducting toroidal coil for the post JT-60 machine, named Fusion Engineering Power Reactor[7]. In this toroidal coil system, one coil weighs about 150 tons and the weight of the whole toroidal coil system is about 4300 tons. In order to construct such a heavy system, there are three solutions; each complete coil transportation from a factory, semi complete coil transportation from a factory and on-site winding & assembly. Difficulties in these methods are well pointed and discussed. The necessary utility capacity is shown for each case. This study report is delivered from an industry.

Another conceptual study is on the refrigeration system for the post JT-60 machine[8]. In order to cool down a coil system in one or two months the necessary condition for cool down are pointed out for three cases of cooling weight; 100 tons, 700 tons and 5000 tons. Nitrogen liquifaction system or refrigiration system in the laboratory is also discussed in comparison with a case of LN_2 purchase, in which there will be difficulty of transportation of enormous quantity by unit time. The necessary utility capacity and the layout of the system are shown for each case. This study report is delivered from an industry.

References

(1) The advanced designs on the Cluster Test Facility and the Test Module Coil are reported in collaboration with Toshiba Co., Hitachi, Ltd. and Mitsubishi Electric Corp. The reports are not published.

(2) Yoshida, K., Ando, T. and Shimamoto, S.: Magnetic Field and Stress Analysis for ORNL-LCT, JAERI-M 7543 (in Japanese).

(3) Hosoda, Y. and Shimamoto, S.: Study of Thermal Problem in ORNL-Large Coil Task, JAERI-M 7546 (in Japanese).

(4) Hosoda, Y. and Shimamoto, S.: Thermal Stress Analysis of Superconducting Magnet by SAP-4, JAERI-M 7675 (in Japanese).

(5) Development of Forced Cooled Alloy Superconductor for Toroidal Coil, a report in collaboration with Hitachi Cable Ltd. (not published).

(6) The Development of Compound Superconducting Conductor (Feb. 1978), a report in collaboration with Hitachi, Ltd. The report is not published but a part of this work will be presented in supplied Superconductivity Conference, Sept. 1978.

(7) Construction System Analysis for Superconducting Magnet, a report in collaboration with Mitsubishi Electric Corp. (not published).

(8) Refrigirator System Analysis for Superconducting Magnet of Fusion Device, a report in collaboration with Toshiba Ltd. (not published).

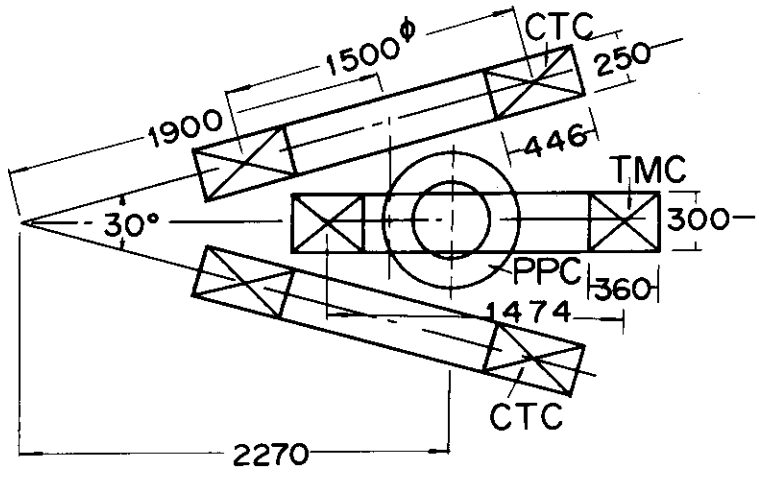

Fig.VI-1 Cluster test facility disposition.

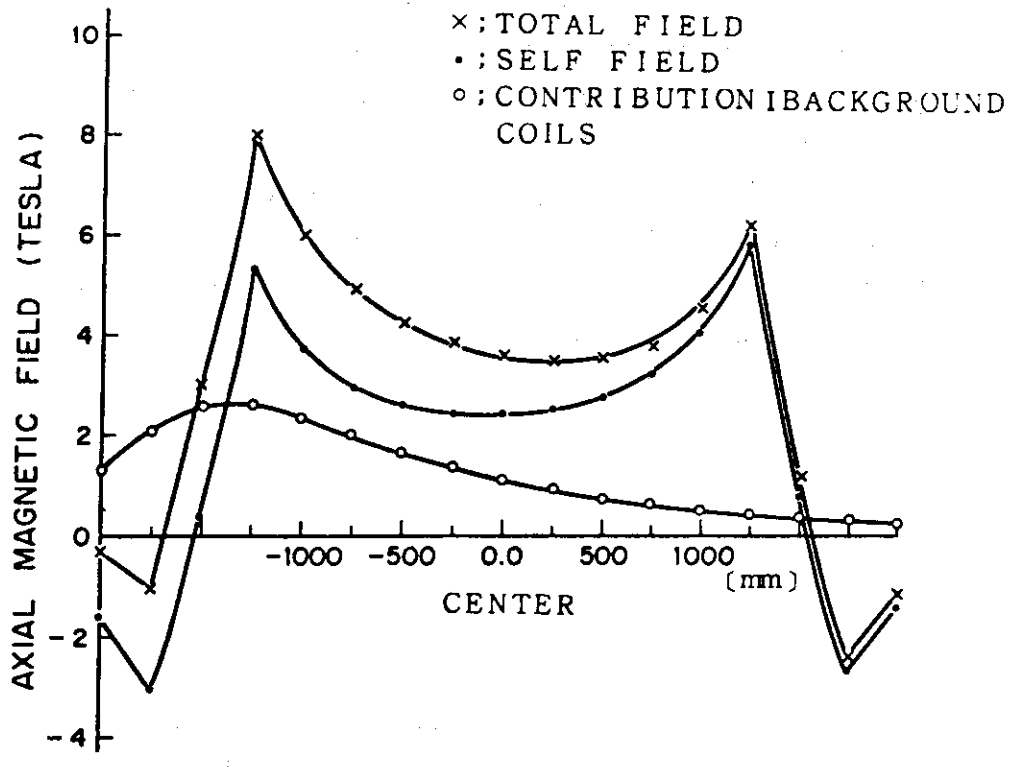

Fig.VI-2 (a) Magnetic field distribution along the horizontal center line.

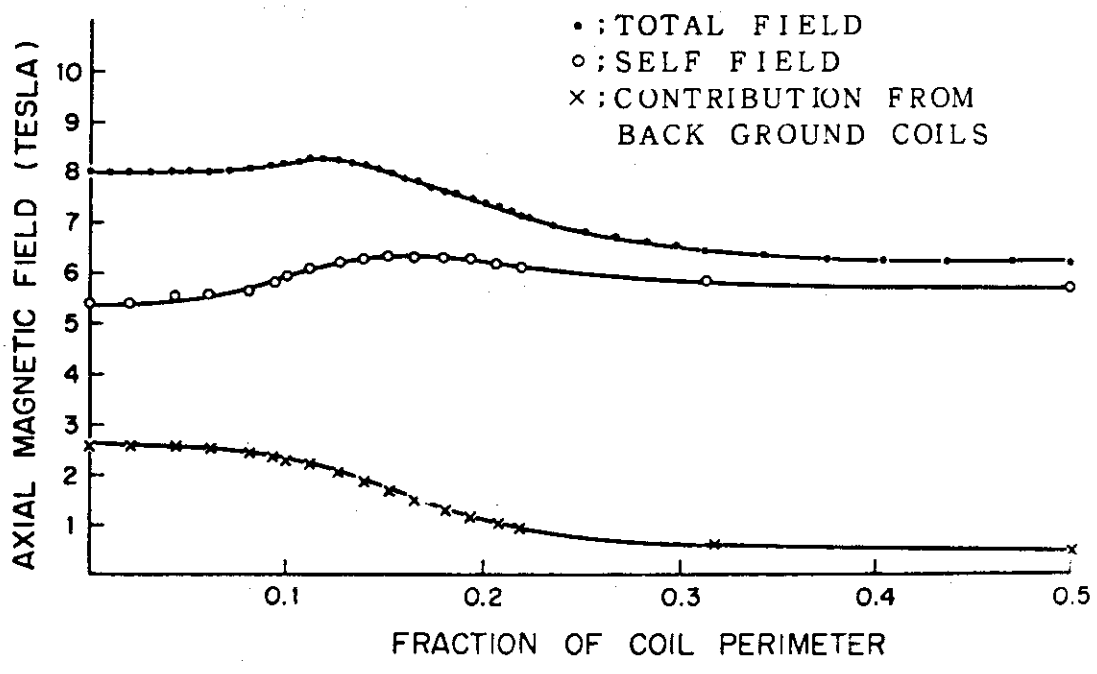

(b) Magnetic field distribution along the coil inner perimeter.

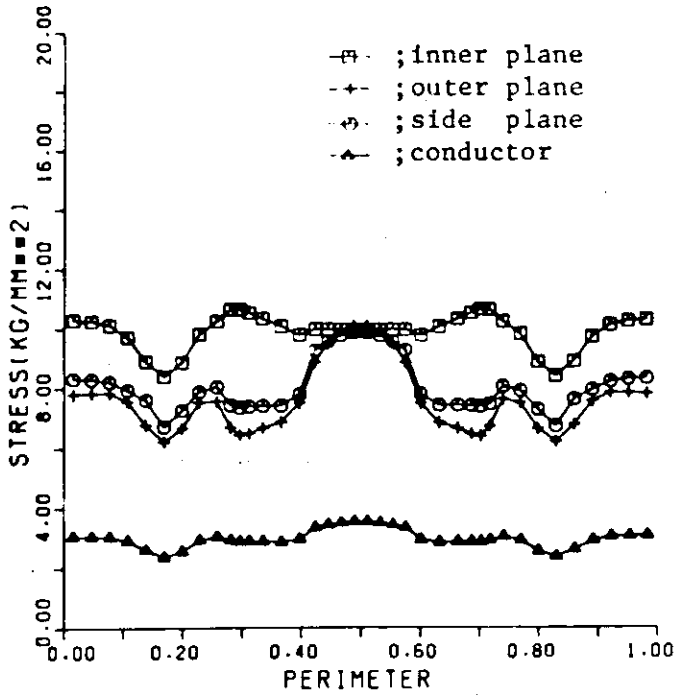

Fig.VI-3 Stress distribution under normal test condition.

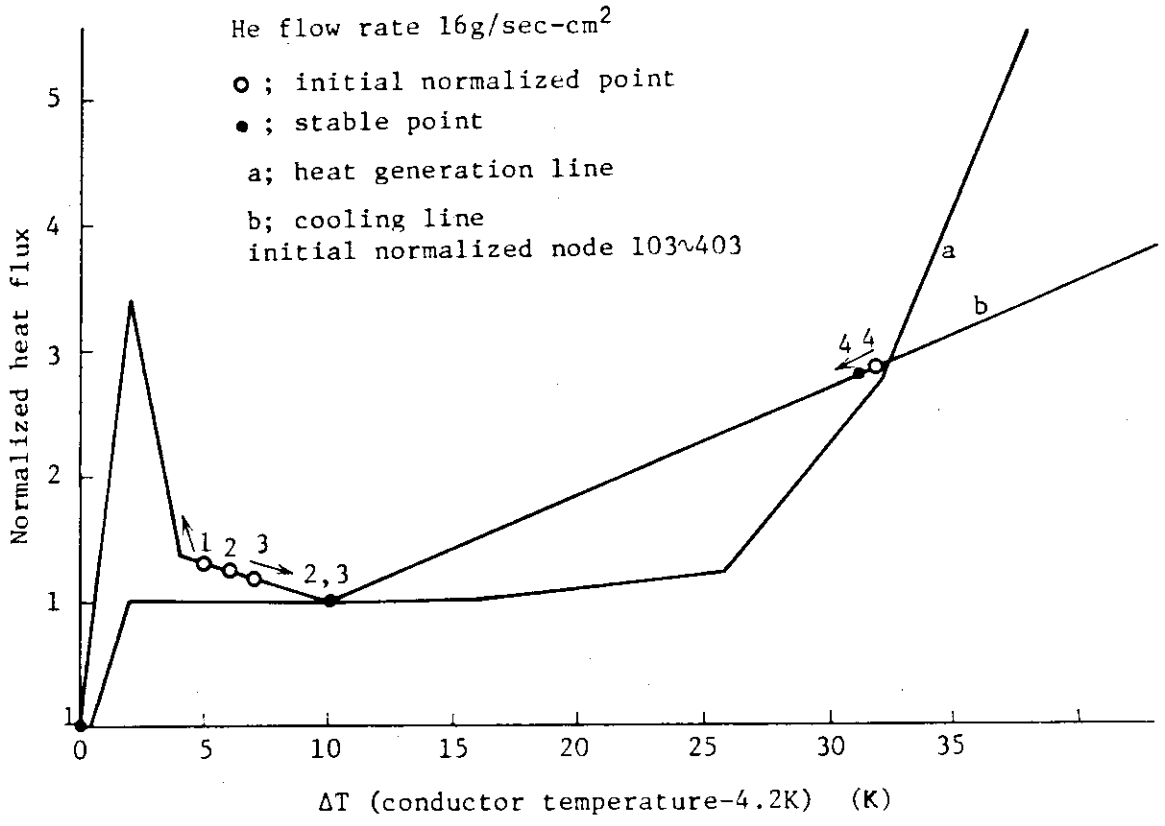

Fig.VI-4 Stability characteristics.

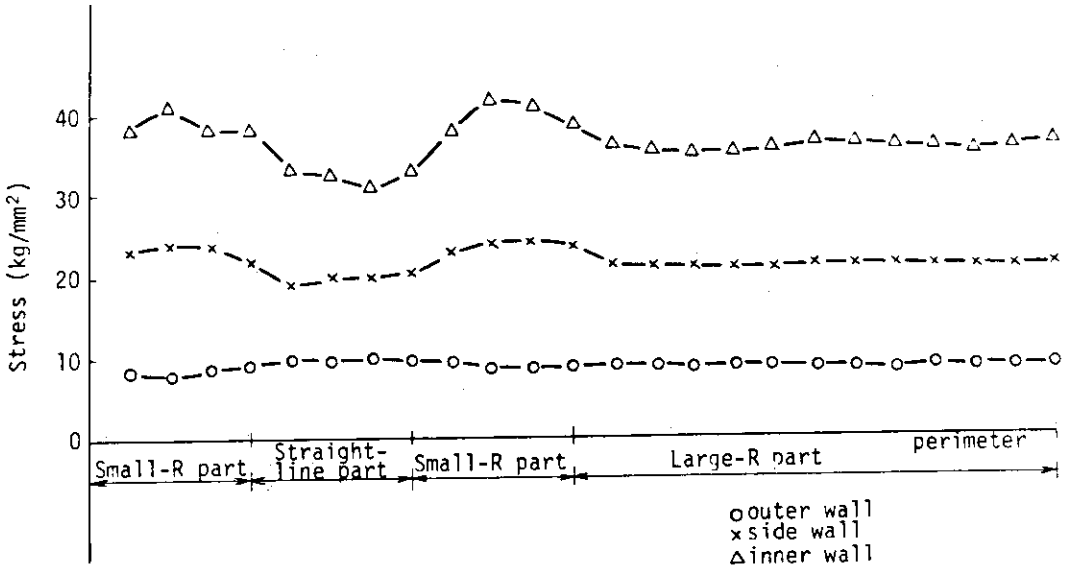

(a) (σ_{max} - σ_{min}) distributions in SUS wall

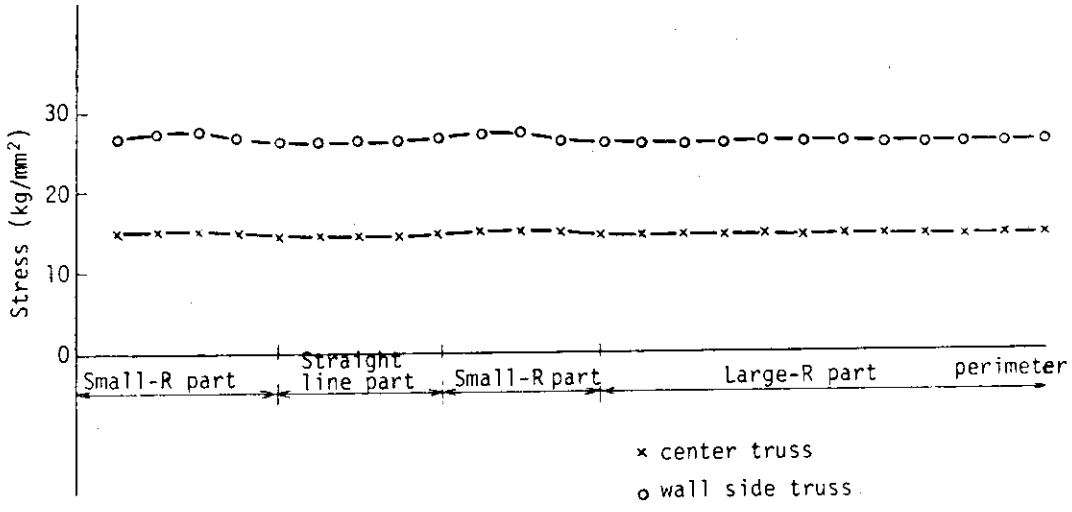

(b) Tensile stress distribution in superconductor

Fig.VI-5 Stress distribution in LCT coil

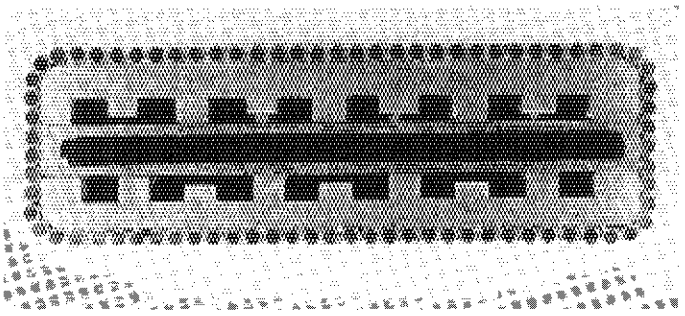

Fig.VI-6 The cross section of the forced cooled Nb-Ti conductor, operational current 10 kA at 8 T.

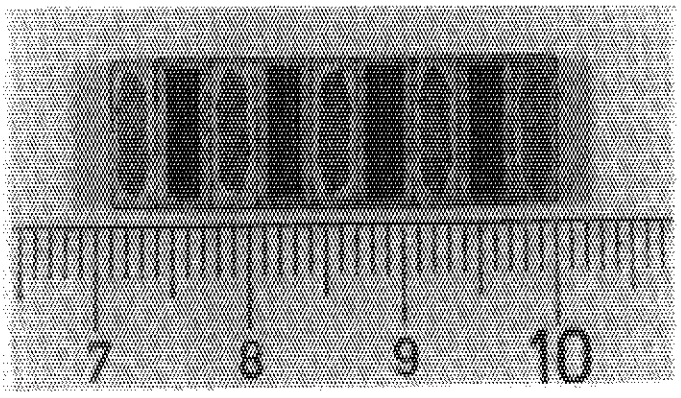

Fig.VI-7 The cross section of the MF Nb_3Sn, critical current of 8.5T-24cm for conductor test.

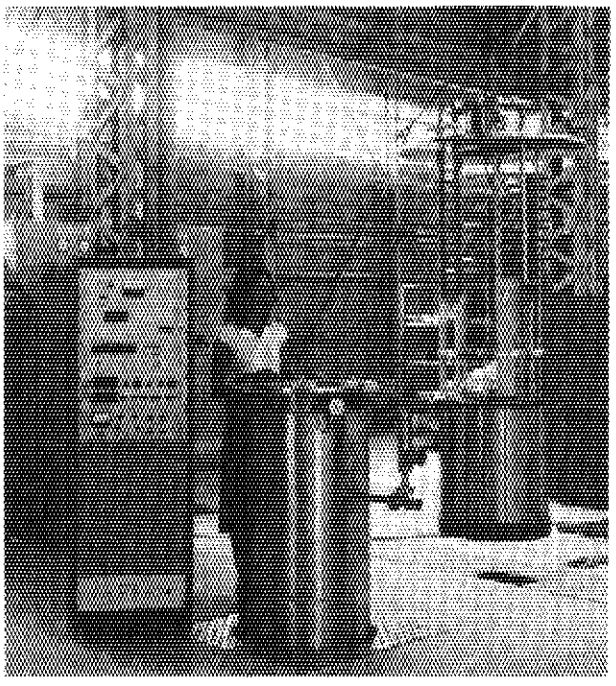

Fig.VI-8 The Nb-Ti solenoid of 8.5T-24cm for conductor test.

Table VI-1 Designed value of the test module coil and the cluster test coil

TMC

Coil Cross Section	(mm)	360×300
Coil Shape		Oval
Coil Size	(m)	1.47×1.97
Magnetic Field	(T)	8.0
Average Current Density	(A/mm^2)	30
Operating Current	(KA)	10-12
Stord Energy	(MF)	15
Centering Force	(ton)	1400
Winding Volume	(m^3)	0.589
Energy Density	(MJ/m^3)	30
Ampere-turns	(MAT)	3.24
Weight	(ton)	7
Minimum Winding Curvature	(m)	0.4
Number of Turn		3240
Wiere Length per Turn	(m)	5.53
All Wire Length	(m)	1792.
B_{max}/B_{min}		1.62

CTC

Magnetic Field	(G)	7.0
Coil Size	(m)	1.5
Ampere-turn	(MAT)	3.3×2
Current Density	(A/mm)	30
Total Energy	(MJ)	40

VII. REACTOR DESIGN STUDY

1. Introduction

The following three design works are now in progress.

1.1 Preliminary design of JXFR

The purposes of the design are as follows; (a) Elucidate the performance requirements of the experimental fusion reactor which operate with high duty cycle and plant availability. (b) Clarify the request to the plasma physics research. (c) Investigate the problems associated with the development of main components and subsystems of the reactor and provide bases for R&D planning. (d) Improve the designing techniques.

The first preliminary design of a tokamak experimental fusion reactor to be built in near future started in April 1975 and finished in March 1977. The design report has been completed as JAERI-M 7300 (Sept. 1977) and presented at the IAEAI Technical Committee and Workshop on Fusion Reactor Design (1977, Madison). This design covers an overall reactor system including plasma characteristics, reactor structure, blanket neutronics, shielding, superconducting magnets, neutral beam injector, electric power supply system, fuel (D-T) circulating system, reactor cooling and tritium recovery systems and maintenance scheme. By this design study, we revealed many design problems to be overcome.

The second preliminary design with special emphasis placed on developing realistic and credible solutions to the design problems was started in April 1977 and will de finished in March 1979. Then an overall evaluation of the design will be carried out for a year.

1.2 Design study of power reactor

The objectives of this design study are to make clear the concept of future tokamak power reactor and point out problem areas for the development. Another important objective of this design study is to provide the feedback information to the design of JXFR. A preliminary design study has been presented at the Second Topical Meeting on the Technology of Controlled Nuclear Fusion (CONF-760935-P2).

1.3 Safety analysis of JXFR

Safety analyses for the main components and systems of JXFR are carried out based on the first preliminary design. These analyses are closely inter-related with the reactor design itself and are becomming more detailed as the design progresses. So far, JXFR is evaluated to be a highly safe facility.

2. General Description of the Second Preliminary Design of the JAERI Experimental Fusion Reactor (JXFR)

Main design parameters of the reactor are given in Table VII.2-1. The reactor consists of eight reactor modules which can be withdrawn in the radial direction for repair. Each module has a blanket module which consists of blanket vessels and a vessel with the hole for the neutral beam injection and evacuation. Mechanical limiters employed are so designed that they may be withdrawn in case of failure. Four limiters and four injectors are alternately installed. Two vacuum pumps (cryo-pumps) are installed to every reactor module.

3. Design Studies

3.1 Plasma

3.1.1 MHD equilibrium

MHD equilibria for JXFR were obtained by the use of fixed-boundary MHD equilibrium calculation code. The parameters (β_p,q(a) and I_p) are obtained for various values of the profile exponent α in a circular plasma with dimensions (R=6.75 m, a=1.5 m) and toroidal field strength (B_T=5.5 T) and with the constraint q(0) > 1.

With the power balance analysis, the reference design parameters were chosen for the 100 MWt EPR;

(a)	Plasma Current	4.4 MA
(b)	Beta Poloidal	2.2
(c)	Safety Factor at the Plasma Surface	2.55
(d)	Beta Toloidal	0.025

3.1.2 One-dimensional transport computer code

One-dimensional simulation code for D-T tokamak plasma is being developed.

This code consists of particle balance equations including α-ion and impurities, energy balance equations and magnetic field equations. The equations are represented in generalized forms so that some other equations may be easily added. Crank-Nicloson's numerical method is adopted in this code.

This code has the following characteristics;

(1) An anomalous transport model is used in this code. Transport coefficients are based on the trapped ion mode in the low collision frequency region and pseudoclassical mode in the higher region.
(2) Plasma expansion in startup phase can be treated.
(3) Plasma current is computed by coupling to external circuit equations.
(4) The distributions of ionized impurities are computed under the assumption of ionization equilibrium.
(5) Radiation loss terms (bremsstrahlung, cychrotron and line radiations), ionization loss and recombination loss are taken into consideration. sideration.

3.1.3 Alpha heating

Two-dimensional confinement, loss and energy deposition rate of 3.52 MeV alpha particles produced in D-T reaction were studied using the drift kinetic equation of alpha particles. The effects of spatial distributions of plasma current, ion temperature and plasma density were examined; these changes have large influence on the results. The loss rate of alpha particles to the source quantity is larger in the outer region of plasma than in the inner region. The more peaked the distribution, the smaller becomes the total loss rate. The momentum increase caused by alpha particle loss was estimated. A manual on the computer program (ALPHA) was developed for the research.

3.2 Neutronics

3.2.1 Nuclear heat deposition in cryosorption pumps[1]

The nuclear heat depositions in the cryopumps for JXFR are evaluated by using Monte Carlo transport code MORSE-GG. The following conclusions are obtained,

(1) Nuclear heat deposition in the cryopumps is small and the refrigeration power increase due to nuclear heating is acceptable.

(2) The total heat deposition in the cryopumps for the neutral beam injection system is particularly small amounting to less than 1/10 of that for the main evacuating system.

(3) The nuclear heat deposition in the cryopumps is mostly due to gamma-rays.

3.2.2 Three-dimensional analysis of the effects of neutron streaming through neutral beam injection ports[2]

Effects of neutron streaming through neutral beam injection ports have been studied for JXFR. The radiation damage of toroidal field (TF) coils in the presence of cylindrical injection ports with 1.2 m diameter was estimated by three-dimensional Monte Carlo calculation.

To protect the TF coils from neutron streaming, 0.8 m thick shield is sufficient. The presence of the injection ports, however, increases substantially radiation damage of the TF coils.

3.2.3 Induced activities of fusion reactor structural materials[3]

Induced activity, biological hazard potential and decay heat of the JAERI Demonstration Fusion Reactor (JDFR) with molybdenum alloy as a blanket structural material and gamma-ray dose rates in and around the reactor after shutdown are calculated. Induced activities of other blanket materials, tantalum and tungsten used in molybdenum alloy, other fusion-reactor structural materials and impurities are also calculated to examine effects of the gamma-ray dose rates in reactor design. The quantities of radioactive wastes from JDFR and JXFR are estimated.

3.3 Reactor structure

Thermal and mechanical analysis for the blanket structure are performed. The electromagnetic force in case of the plasma disruption was also estimated. From the analysis and evaluation conducted, a feasibility of the blanket vessels for the experimental fusion reactor has been shown. However, more detailed studies including those on the problems in the fabrication process are believed to be necessary.

3.3.1 Thermal analysis[4]

Thermal and hydraulic analysis of the blanket first wall under normal

operation and abnormal conditions was carried out. The cases with and without a protection wall were studied and the effectiveness of the protection wall was demonstrated. Creep-fatigue interaction of the first wall based on the temperature changes was evaluated.

3.3.2 Stress analysis[4]

The stress analysis of a unit blanket vessel made of Type 316 stainless steel with a square shaped cross section under internal pressure of 12 kgf/cm^2 (design pressure) was carried out. Two-dimensional models for various corner radii and wall thicknesses and three-dimensional model of a typical blanket vessel were employed in the analysis. Both free-standing case and the case with interaction between adjacent blanket vessels were considered. It has been found that without the interaction between the vessels, the volume fraction of stainless steel becomes very large which may make the tritium breeding ratio of 0.9 unobtainable.

3.4 Superconducting toroidal magnet

Design and safety analysis are carried out on the electrical, structural and thermal aspects of the JXFR toroidal magnet. Detection systems and protection systems which are necessary to maintain the functions of the magnet against any potential accidents are considered. Analysis on coil stability, quench propagation and earthquake response is also performed. Operating experiences relating to the safety problems of existing superconducting magnet systems are investigated.

3.5 Superconducting poloidal magnet

The superconducting poloidal magnet design for JXFR was reviewed in the light of safety. Firstly the maximum repeated tensile stress at 4.2 K of 304 SS caused by electromagnetic force was lowered to the level of 24 kg/mm^2, reducing magnetomotive force of the air-core transformer from 60 MAT to 48 MAT, because the figure of 46 kg/mm^2 in the previous design was too high. As the result of this change, stability margine of the superconducting magnet was increased, that is, heat flux of the superconducting wire for normal transition could be reduced from 0.36 W/cm^2 to 0.24 W/cm^2.

Pressure increase in the liquid helium vessel due to deterioration of

vacuum jacket for thermal insulation was also analyzed, and safety valves and rupture discs were designed for this kind of accidents.

Finally, analysis of general failure of the superconducting poloidal magnet was done using event tree or fault tree techniques.

3.6 Neutral beam injection system

Further design study of the neutral beam injection system was carried out for JXFR taking into account maintainability of the system and replacement of ion sources. Atomic deuterium beams of 33 MW, 200 keV are injected from four injection ports. Six beam lines and a pumping system are installed in an injection unit. Each beam line consists of a 55 A ion source, a neutralizing cell, direct converter and a drift tube connected of the torus. Cryocondensation pump of 10^6 ℓ/s is used for an injection unit which is divided into four chambers and three of them are in operation while one is in regeneration.

One of the important problems found in the design study is effect of ions or electrons produced by ionizations and charge-exchange of remaining gas between accelerating electrodes. Divergence of these particles and broadening of ion energy spectrum may decrease efficiency of the direct converter and heat load of the ion source due to these particles may also be serious. Detailed design study of the ion source and the direct converter is still under way.

3.7 Tritium circulating system

System design and safety analysis for JXFR have been carried out. A three stage containment system of tritium bearing fuel is proposed to prevent tritium release to the environment. The primary containment system consists of the equipments, pipes and sweep gas jackets which are designed to minimize leakage into the secondary containment barrier. The secondary containment system which encloses most of primary containment system, has the structure similar to glovebox with an inert gas atmosphere. The tertiary containment system consists of the room enclosing the secondary containment system and tritium bearing gas processing system.

3.8 Reactor cooling system

Safety analysis of the reactor cooling system for JXFR has been carried out.

The main objectives in this study were to evaluate the tritium releases associated with the normal operation and accidents of the main cooling system, and to make a good choice of the tritium treatment and containment system for reducing its releases.

Performed here were (1) to evaluate the pressure and temperature behaviour in vacuum vessel during the piping failure of the primary cooling system, and then to analyze the behaviour of tritium adsorbed on cryosorption-panel, and (2) to evaluate the tritium releases from the main cooling system, and then to approach the method which would reduce the tritium releases.

3.9 Repair and maintenance system

Repair and maintenance design for JXFR has been studied. The reactor is in eight modules so that a damaged module alone can be separated from the other modules and transferred from the reactor room to a repair shop.

Design work covers overhaul procedure, dismounting equipments (overhead cranes, auto welder/cutter and remote handling equipments), transport system of a module (module mounting carriages and rotating carriage), repair equipment for blanket, earthquake-proof analysis of the reactor, reactor room structure, repair shop layout, management of radioactive wastes, time and the number of persons required for overhaul etc.

Though the repair and maintenance system is almost complete, there still remain problems for further study in joints of blanket cooling piping, auto welder/cutter and earthquake-proof strength in reactor disassemblage.

Table VII.2-1 Main design parameters of the JXFR

Operation Mode	
Fusion power (MW)	100
Operation period (s)	180
Burn time (s)	100
Load factor	0.3
Duty factor	0.6
Reactor dimensions	
Major radius (m)	6.75
Plasma radius (m)	1.5
First wall radius (m)	1.75
Plasma volume (m^3)	300
Plasma	
Mean temperature (keV)	7
Mean density (10^{14} cm^{-3})	1.1
Effective charge	∿2
Confinement time (s)	3.6
Injection power (MW)	30
Toroidal field (T)	5.5
Safety factor	2.5
Poloidal beta	2.2
Toroidal beta	0.025
Plasma current (MA)	4.4
Reactor Structure	
Reactor module/Reactor	8
Blanket cells/Reactor module	284
Injection and evacuation hole/ Reactor module	1
Nominal max. 1st wall temp.(°C)	550
Materials	
Structure material	316SS
Blanket fertile material	Li_2O
Reflector material	Stainless steel
Neutronics	
Neutron current at 1st wall (n $cm^{-2}s^{-1}$)	7.6×10^{12}
Neutron wall loading (MW m^{-2})	0.17
First wall displacement damage rate (dpa y^{-1})	0.7
Max. helium production rate in 1st wall (appm y^{-1})	8.7
Max. hydrogen production rate in 1st wall (appm y^{-1})	25
Tritium breeding ratio	0.9
Nuclear heating per DT neutron (MeV n^{-1})	16.1
Total induced activity at one hour after shutdown (Ci) (after one year operation)	7.3×10^{7}
SCM irradiation effects	
Max. copper displacement (dpa y^{-1})	6×10^{-6}
Max. nuclear heating rate (W cm^{-3})	4×10^{-5}
Total nuclear heating in SCM (kW)	0.68
Toroidal field magnet	
Number of coils	16
Bore, Width/Height (m)	7/11
Magnetomotive force (MAT)	186
Max. field strength (T)	11
Stored energy (GJ)	50
SCM material	Nb_3Sn
Primary winding	
Number of coils	20
Magnetomotive force (MAT)	48
Maximum field intensity (T)	8
Stored energy (GJ)	1.3
Flux change (Wb)	102
SCM material	NbTi
Vertical field magnet	
Number of coils	8
Magnetomotive force (MAT)	±8.3
Maximum field intensity (T)	8
Field intensity (T) at plasma center	0.30
Stored energy (GJ)	0.75
SCM material	NbTi
Neutral beam injector	
Number of ion sources	24
Deuterium beam energy (keV)	200
Ion beam output (MW)	240
Injection power (MW)	33
Power efficiency	0.40
Power supply (MW)	
for Toroidal coils	0.6
for Poloidal coils	6
For Refrigerator of SCM (Toroidal, Poloidal, IES)	12
for Neutral beam injector	85
for Vacuum exhaust system (Main pump, NBI pump)	3
for Blanket cooling system	40
for Auxiliary system	13
Total power	160
Fuel circulation system for rate (mgs^{-1})	
Tritium insertion rate	17.5
Deuterium insertion rate	11.7
Herium exhaust rate	0.24
Cooling system	
Number of loops	4
Coolant, Pressure (kg cm^{-2})	He, 10
Inlet/Outlet temp. (°C)	300/500
Flow rate (kg/s)	143
Secondary system	He, air-cooler
Tritium inventory (kg)	
Fuel recirculating system	0.3
Tritium recovery system including blanket	0.1
Total inventory including storage	0.5

VIII. DEVELOPMENT OF A LARGE TOKAMAK --- JT-60

1. Introduction

Upon completion by March 1977 of the preconstruction (detailed) design and the engineering development of JT-60, the request for quote of JT-60 machine (Tokamak System) was let to industry. After examining and evaluating the quote and design report in a period of June - July 1977, Hitachi was selected as the first choice, and the negotiation is being conducted. It is expected that the contract will be reached in April 1978.*

The design reexamination is continued under contract with Hitachi and Toshiba on the systems of JT-60 other than the machine. Their purpose is to reexamine, better, and modify, if necessary, the preconstruction design to reduce their cost and enhance their performance taylored to latest findings in their operation characteristics and plasma-physical knowledges.

Design works are continued on the other part of JT-60 including the prototype of neutral beam injectors, the diagnostic system, and the buildings.

2. Outline of the Progress of JT-60

For JT-60 project, the year of 1977 may be characterized as the preparatory year for the contract with a manufacturer. This year began with editorial work of specifications of the tokamak machine of JT-60. It was accomplished in March and proposed in May to Toshiba Corporation and Hitachi Limited. JAERI received their estimates in June and Hitachi made successful bid. JAERI began to examine technical specifications and estimated cost in details and long negotiation period began. They could not reach agreement in 1977 and their efforts continued until the next spring.

The technical specifications other than tokamak machine has been studied through the year by Power Supplies Group, Control Group and Auxiliary Facilities Group of Division of Large Tokamak Development.

Choice of the JT-60 site has been one of the problems disturbing the project. JAERI almost gave up the initially proposed government-owned land and had to find other sites. Fortunately, several local towns in Ibaraki Prefecture offered JAERI to invite JT-60. JAERI began to study about their location conditions.

---

* The contract was completed in April 17, 1978.

The detailed design of JT-60 was over in February and the full report of six volumes was published in August[1]. In the detailed design, emphases were put not only of JT-60 main components but on the system design such as system consistency, operation conditions, licensing or effects on envivonment.

The whole research and development programs of JT-60 components were accomplished in February and their many reports were published as described in the following chapters. The results of research and development were presented at IEA Workshop on Coil Technology, Stress Analysis, and Mechanical Structure in April. Tubes of vacuum circuit breaker developed in R & D Program were sent to PPPL and GA of U.S.A. as test samples.

In parallel with the negotiation with Hitachi for Contract in July, JAERI organized JT-60 Technical Steering Committee by specialists and authorities from outside of JT-60 Project to examine reliability of JT-60 design from objective view points. The Steering Committee and its Technical Sub-Committees worked intensively and submitted its preliminary evaluations and recommendations in December.

On the other hand, the safety analysis for environment was promoted. Especially about the estimate of X-ray and photo-neutron emissions at run-away electron mode operation[2]. The results were reflected on the design of building to keep extremely low level of radiation dose at the site boundary.

As an event of project management, JAERI hosted IEA Project Management Meeting of Very Large Experimental Devices in Tokyo in April.

Planning Coordination Group initiated program planning and coordination activities. Project activities were compiled to a Working Break-down Structure and the project flow chart and the time schedule were investigated. One of causes of uncertainty of the schedule is vague perspective of budget which has been partly approved year by year. Another condition to make project management complicate is involvement of several main manufacturers.

JAERI kept to discuss with Tokyo Electric Power Company Incorporated and the Japan Atomic Power Co. about the technical conditions to receive directly electric power of 180 MW as a part of power supply to toroidal field coils and they almost reach agreement.

The design of main buildings were initiated. Experimental Building naturally require the longest construction period and may be the critical path for the whole JT-60 project because of delayed selection of JT-60

location.

In Division of Large Tokamak Development, the new section responsible to tokamak machine and auxiliary systems is established and named JT-60 Project Office II in July. At the same time, JT-60 Program Office and Large Tokamak Administration Section were also established in the Division. The former is responsible to technical planning and coordination of JT-60 and JT-4 and the latter is to administration. JT-60 Project Office I keeps power supply and control system.

The contract with Hitachi for construction of the tokamak machine of JT-60 will be made early in the next year and the site will be finally decided in mid 1978.

References

(1) Div. of Large Tokamak Development: Internal report August, 1977.

(2) Aikawa, H., Ryufuku, H. and Hiraoka, T.: Internal report Dec., 1977.

3. Outline of Machine

3.1 Activity of tokamak machine group

Detailed design and engineering developments carried out in the previous year were evaluated spending the former half of fiscal 1977 and the results were summarized in about thirty JAERI-memos.

The design and engineering developments concerning the toroidal and poloidal field coil systems were presented to the IEA workshop on coil technology, stress analysis and mechanical structure held in Tokyo at April, 1977.

The design has been reviewed by JT-60 technical review committee and a lower sub-committee specialized in JT-60 tokamak machine.

Some of specifications of JT-60 machine were reconsidered through the useful discussions in these committees. Analyses and discussions of hypothetical fault conditions, for example, vacuum breaking of a vacuum vessel, short-circuit of field coils, and malfunction of main servovalves of a fast movable limiter, have been done in a latter half of the fiscal year.

The contract for construction of JT-60 machine is to be made separately since the other systems have not been approved for construction by the Government. Therefore, much effort has been made in deciding the boundary design conditions between the machine and the other systems.

Settlement of a spatial conflict among each component located in the experimental building and drawing of the layout in a machine room were done with energetic effort.

In parallel with the above works, official works on the course to the contract for machine constructions with an industry have been continued for the whole year in cooperation with Contract section II. Engineering evaluation of the specification proposed from industries and cost evaluation of each component of the machine were the most important and troublesome works in the activity of machine group.

3.2 Desgin of machine

3.2.1 Design condition

JT-60 machine is composed of a vacuum vessel, toroidal field coils, poloidal field coils, support structures, a primary cooling system, movable limiters, a vacuum pumping system, a plasma monitor system, a gas supply

system, and a preionized system. The latter four systems are described in Section 5 and 6.

The desgin conditions have been frozen by settling the conflict between the requirement of plasma physics and the present engineering technique. The results of the development of each component carried out from fiscal 1976 to fiscal 1977 have been partially taken into the present design. Main design conditions are as follows. (a) Total operation cycles of 3×10^5 and rated operation cycles of 5×10^4 are required for the machine life. (b) The total exposure, the maximum exposure intensity per shot, and the maximum energy of X-rays due to runaway electrons are 2×10^8 R, 10^5 R, and 10 MeV, respectively. (c) Typical plasma current of 2.7 MA decreases to zero in at least 50 msec. (d) The negative spike of plasmas induces the one-turn voltage of 3 kV with the pulse length of 100 $\sim$ 400 μsec. (e) The magnitude of the earthquake does not exceed 0.3 G.

The design has taken into account the assembly/disassembly, the matching between the components, the earthquake proof, the transportation from industries to the construction site, the environmental assessment, the reliability, faults and their interlocks, tests, and inspections during and after construction, and so on.

3.2.2 Vacuum vessel and its auxiliary components

Specifications of the vacuum vessel and its auxiliary components are shown in Table VIII.3.2-1 and Table VIII.3.2-2, respectively.

(1) Vacuum vessel

Fig. VIII.3.2-1 shows a cross-sectional view of the vacuum vessel. The material is Inconel 625. Electric resistance of a torus should be higher than 1.3 mΩ. The helium leak rate, the outgassing-rate and the ultimate vacuum pressure are lower than 5×10^{-7} torrℓ/sec, 10^{-11} torrℓ/sec$\cdot$cm^2 and 10^{-8} torr, respectively. The baking temperature will be above 500°C for the vacuum vessel and 250°C for the ports. The vacuum vessel is composed of U-shaped bellows and thick rings. The vacuum vessel is supported at the thick rings by bars extended from a support structure. The vessel is heated by nonmagnetic electric heaters and cooled by water pipes wound around it.

A vacuum vessel is loaded by centripetal forces both toward the major axis and toward the minor axis due to the atmospheric pressure. The

centripetal force toward the major axis is about 300 ton and that toward the minor axis is over 1500 tons. The electromagnetic force produced by the interaction of the loop current (0.4 MA) with the poloidal field and by that of saddle current at the thick ring with the toroidal field are less than 0.5 kg/cm^2 and 5 kg/cm^2, respectively. The maximum stress caused by the above forces and thermal expansion is about 32 kg/mm^2 when the hight, pitch and thickness of the bellows are 80 mm, 20 mm and 2.0 mm, respectively.

Moreover, another stress is added to the above at the connection with the thick ring. This local stress is caused by the difference of radial deflection between the bellows and the thick ring. In order to decrease this deflection, the thick ring is vertically supported by supporting rods which restrict the deflection caused by the electromagnetic force due to saddle current and do not restrict the thermal expansion.

(2) Liner

Rectangular liners are attached to the inner surfaces of the vacuum vessel. Liner material is molybdenum. Molybdenum is considered a good material for a liner because of the high melting temperature and low sputtering yields. The baking temperature is 500°C and the outgassing rate is expected less than 10^{-11} torrℓ/sec·cm^2. The thickness, width and length of the liner are about 5 mm, 80 mm and less than 400 mm, respectively. The longest liners overhanging the bellows have slits to decrease the electromagnetic force. The temperature of the liners around the magnetic limiter rises up to about 700°C. The shape of the liner surface is flat.

(3) Fixed limiters

Axisymmetric fixed limiters are placed on the inner surfaces of the vacuum vessel as shown in Fig. VIII.3.2-1. Their material, baking temperature and outgassing-rate are the same as those of the liner. The maximum temperature of the fixed limiter will be about 2,200°C under the severest condition with heat load of 22 MW × 10 sec. The limiter has slots on its surface to decrease thermal stress. And the surface of the limiter is treated by electro-polishing.

(4) Magnetic limiter plates

Magnetic limiter plates are positioned on the outer side of the vessel. Fig. VIII.3.2-2 shows the schematic view of the magnetic limiter plates.

The material, baking temperature and outgassing-rate are the same as those of the liner. Cooling is done by N_2 gas. In normal operation, the heat load is about 500 W/cm^2 × 2 cm^2 width. The maximum surface temperature rise is 430°C. The maximum thermal stress is 5.6 kg/mm^2 (compression). The mechanical stresses due to the electromagnetic forces are small enough to disregard. The design effort is made to reducing the heat load of the magnetic limiter plate that the intersection of a separatrix line and the plate is fluctuated over the length 10 cm during a discharge by superposing the current of small amplitude and a frequency of 5 Hz on the quassisteady current of the magnetic limiter coil. The surface damage due to runaway electron bombardment is under consideration.

3.2.3 Toroidal field coils

The TF coil system consists of 18 coil blocks with an inner diameter of 3.88 m and an outer diameter of 5.64 m. The coil blocks shown in Fig. VIII.3.2-3 equally spaced at a major radius of 3.32 m maintain the field ripple to less than 0.3 % in the plasma region. This arrangement of the coil blocks provides access to the vacuum vessel required for neutral beam injection, diagnostic and vacuum pumping. The coils will operate in a pulsed mode in which the current is ramped up to the desired flat top value of 52 kA, held for 5 seconds at the value and then gradually decreased. Detailed specifications for the TF coil system are listed in Table VIII.3.2-3. Each coil block is composed of two 36-turn pancake windings which are connected in series and enclosed in a common metallic outer case. Each turn of the winding has two parallel water cooling circuits. Thickness of turn as seen in Fig. VIII.3.2-4 is determined to make the temperature distribution as uniform as possible in the wedge-shaped section of the coil block. Each turn is made of two kinds of copper materials. One for the high stress region near the center support is 0.2 %Ag-OFC of 40% cold working ratio and the other for the low stress region away from the center support is OFC of 20% cold working ratio.

They are connected by brazing at the top and the bottom of the coil block to make a full turn. Each turn is provided with 1 mm thick F-stage layer insulation. The pancake winding is also wrapped with 10 mm F-stage ground insulation. The TF coils are supported by the upper and the lower base structures against the torque due to interaction of the poloidal field and the coil current. Return winding is located in such a way to lessen

the error field produced by the block-to-block connecting leads.

Three different computer codes were used in order to estimate field distribution, field ripple and error field. The maximum field of 98 kG occurs at the innermost conductor in the horizontal symmetry plane. The ripple and the error field are expected to be less than 0.3 % and 30 G in the plasma region, respectively. The error field is produced by the leads and the return winding and also by the error in the manufacture and the positioning. A tolerance of manufacturing and positioning should be restrained within a few millimeters.

Magnetic force produced by the toroidal and poloidal fields consists of centripetal force of 100,000 tons, hoop force of 270,000 tons and torque of 26,000 ton-m. The stresses in the coils have been analysed by the finite element method taking into account the above forces and thermal expansion. The maximum stress intensity of 22 kg/mm^2 and 47 kg/mm^2 are observed in the conductor and the support structure at the wedge-shape section of coils.

A two dimensional code is used to calculate the temperature distribution. The maximum temperature rise of the conductor is up to 70°C in the wedge-shaped cross section. The maximum temperature difference between two adjacent turns is less than 5°C. Therefore thermal stress remains quite small.

3.2.4 Poloidal field coils

The Poloidal Field coils (PF coils) are composed of ohmic heating coils (OH coils), vertical field coils (V coils), quadrupole field coils (Q coils), horizontal field coils (H coils) and magnetic limiter coils (M coils). The first four coils are located in the space between the vacuum vessel and the toroidal field coils and the last inside the vacuum vessel. As a consequence, the PF coils have to be assembled in a very small space. The in-place assembling requires at least one demountable mechanical joint per turn, which poses the major design problem of the PF coils. Additional design requirements are imposed on the M coils which are placed inside the vacuum vessel.

Each PF coil is composed of many coil blocks connected in series as shown in Fig. VIII.3.2-5. This coil block arrangement not only provides access to the vacuum vessel for many ports but also satisfies the required field condition. Each coil block comprises several turns wrapped with a layer of about 5 mm thick mica-epoxy F-stage insulation. Each turn of the coil is to be provided with at least one mechanical joint suited for

assembling in a very narrow space. The insulation system is designed to withstand the maximum voltage of 25 kV. The coil conductors are cooled by water flowing through pipes soldered in the groove at one edge of the conductors. The PF coils outside the vacuum vessel are supported by eighteen stainless steel support structures placed between the toroidal field coil blocks.

The M coils are encased in non-magnetic steel cases, which are fixed to the thick ring of the vacuum vessel. The case is heated nearly up to about 500°C during the baking operation and the hot wall discharge operation. In order to reduce the thermal stress due to the differences of thermal expansion between the case and the coil, a sliding device with roller bearings and disk springs is attached, and a thermal insulator is provided to protect the coil against the heat transferred from the vacuum vessel. The inside of the case is kept at atmospheric pressure. The PF coil specifications are listed in Table VIII.3.2-4.

3.2.5 Support structure

Support structure consists of upper and lower support structures, a center column, support columns and support arms of vacuum vessel, support arms of toroidal field coils and poloidal field coils and connecting arms as shown in Fig. VIII.3.2-6. Support structure must have enough strength to endure the weight about 4,500 tons, several types of electromagnetic forces and earthquake etc.

Upper and lower support structures are separated into 10 parts to reduce the eddy current, respectively. Major-radial spring constants of the center column are distributed in the axial direction to decrease the stresses on the toroidal field coils. Connecting arms connect the upper support structure and the building, and support the twisting moment of the toroidal field coils. The detail of support structure is to be determined.

3.2.6 Primary cooling system

The primary cooling systems provided with circulation subsystems and heat exchangers capable of not only removing the field coil waste heat and plasma influx energy to the vacuum vessel within 600 seconds interval between shots but also cooling down the vacuum vessel baked 500°C to room temperature within 60 hr. The main requirements of the thermal load and the pressure drop in the main components of JT-60 are listed in Table VIII.3.2-5.

The circulation subsystems are devided into two separate groups — the field coil (TF coils and PF coils) cooling system and the vacuum vessel cooling system. The magnetic limiter coil located inside the vacuum vessel can be cooled by both cooling systems, that is, by the coil cooling system during a normal operation and by the vacuum vessel cooling system during a baking operation. The subsystems are composed of pumps, a storage tank, pipings, filters and valves. Four pumps in the coil cooling loop are capable of total flow rate of 2500 m^3/hr and outlet pressure of 16 kg/cm^2. On the other hand, hydrolic capability of two pumps in the vacuum vessel cooling loop is 130 m^3/hr flow rate and 12 kg/cm^2 outlet pressure. A spare pump backups the above pumps in each cooling loop. A heat exchanger in the vacuum vessel cooling system and five ones in the coil cooling system provide sufficient heat removal capability mentioned in Table VIII.3.2-5. In addition, the system is provided with purification subsystem capable of maintaining the extremely pure water with at least 10^5 Ω-cm electric resistivity as well as purifying the initial water charge and subsequent make up water. Instrumentation and controls for the cooling water circuits are located locally in the primary cooling system room and centralized in the process control room.

3.2.7 Movable limiter

A pair of the fast-acting movable limiters are to be installed in the vacuum vessel of JT-60 to suppress skin current in the plasma column. They should travel across the vacuum vessel over a stroke of about 1 m in 0.1 sec in the build-up phase of the plasma current. Each movable limiter system consists of the drive system, a vacuum seal, a bearing usable at high temperature in a vacuum, a molybdenum rail limiter head and its auxiliary members. For the drive is used a hydraulic mechanism with servo-valves to control the oil flow. For the vacuum seal are welded Inconel 718 bellows supported by pantographs. For the bearing is adopted a self-lubricant material. The limiter head strengthened by an Inconel 625 support is cooled by air flowing through the support during 10 min.

3.2.8 General layout and buildings

An overall view of a possible site layout is shown in Fig. VIII.3.2-7. This layout has developed from the different functions and inter-relationships of the various buildings, allowing for an in-built flexibility to

permit furture adaptations and extensions.

More detailed drawings of the experimental building are shown in Fig. VIII.3.2-8 and Fig. VIII,3.2-9. A space suitable for the torus hall will be 40 m wide × 40 m long × 28 m clear height to the lowest point of the crane bridge. These dimensions have been determined by the space requirements and maintenance of the machine.

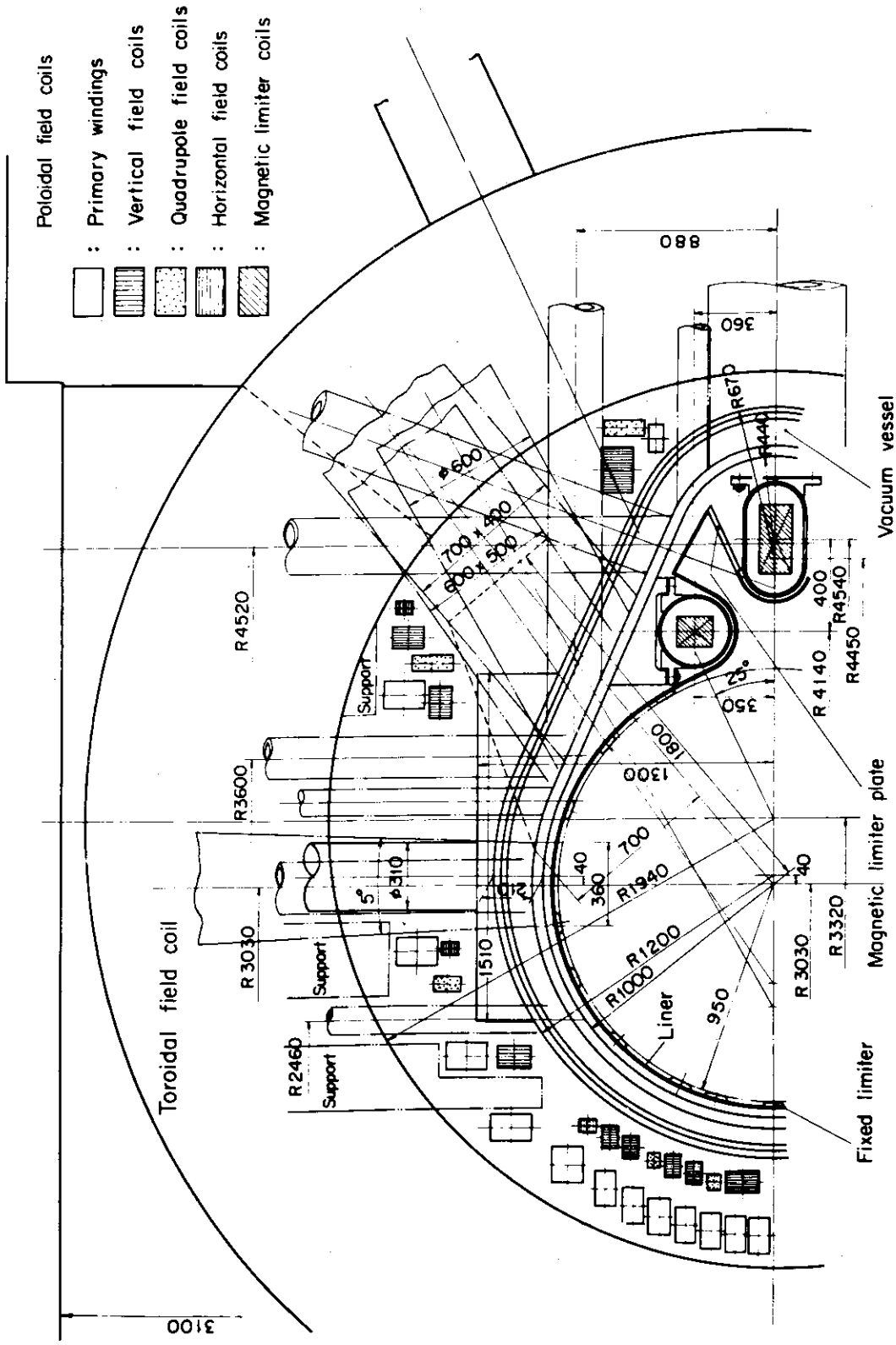

Fig.VIII.3.2-1 Cross sectional view of a vacuum vessel

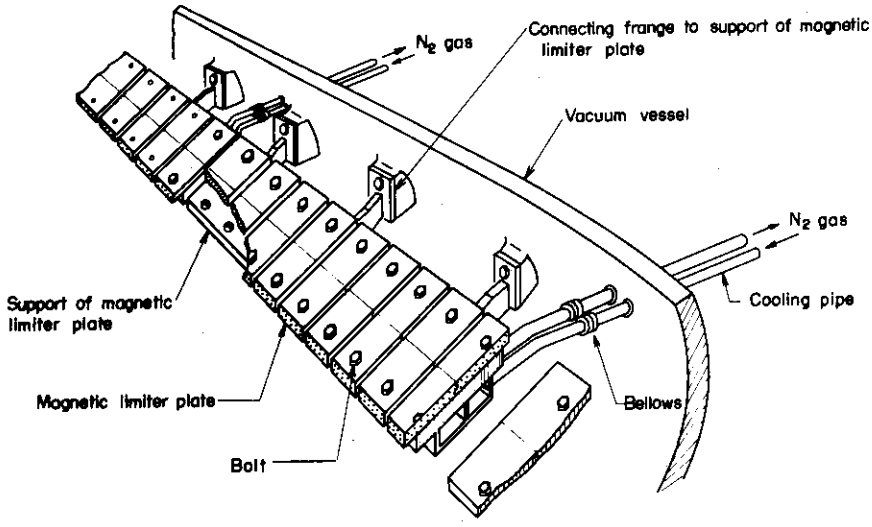

Fig.VIII.3.2-2 Components of magnetic limiter plates

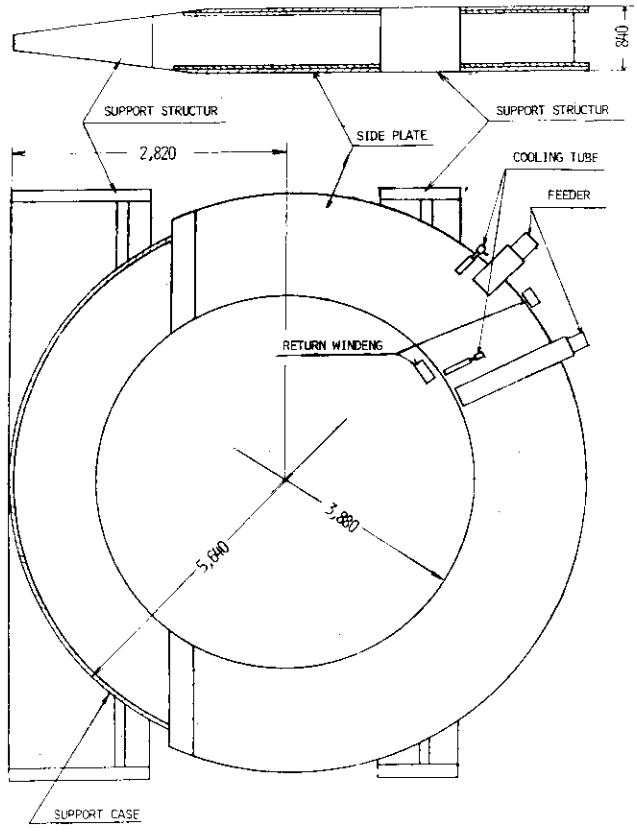

Fig.VIII.3.2-3 TF coil block

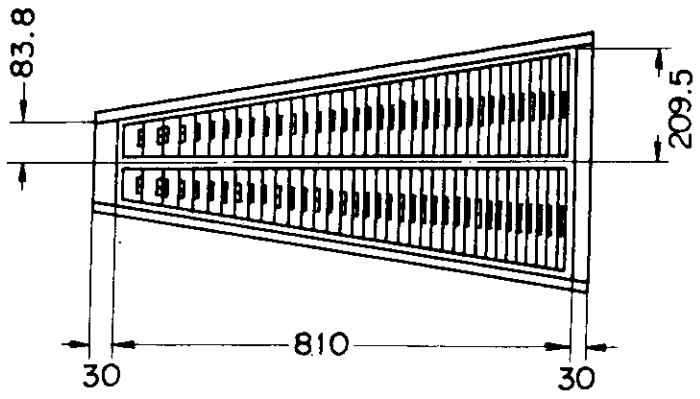

Fig.VIII.3.2-4 Wedge-shaped cross section of TF coils

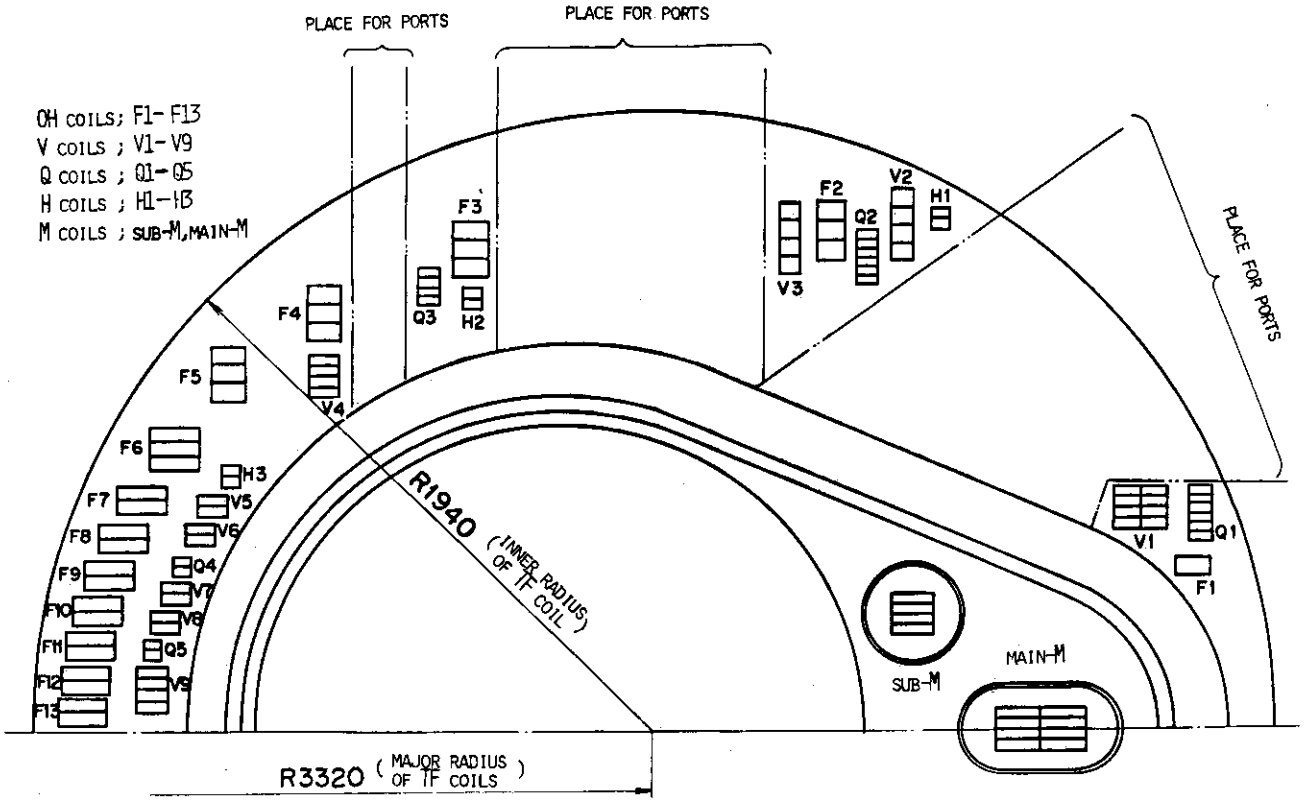

Fig.VIII.3.2-5 Arrangement of PF coils

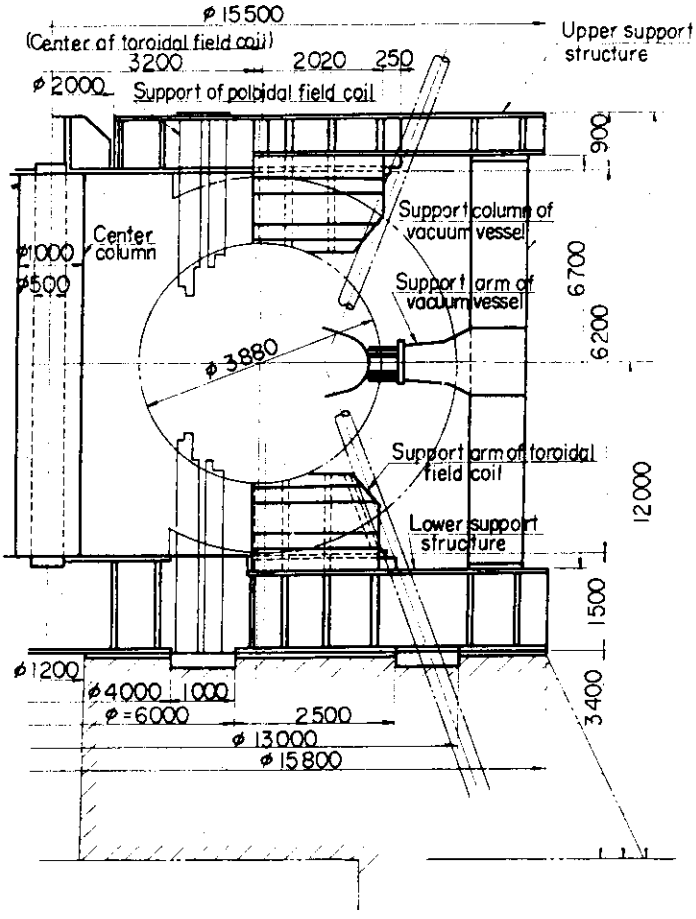

Fig.VIII.3.2-6 Support structure

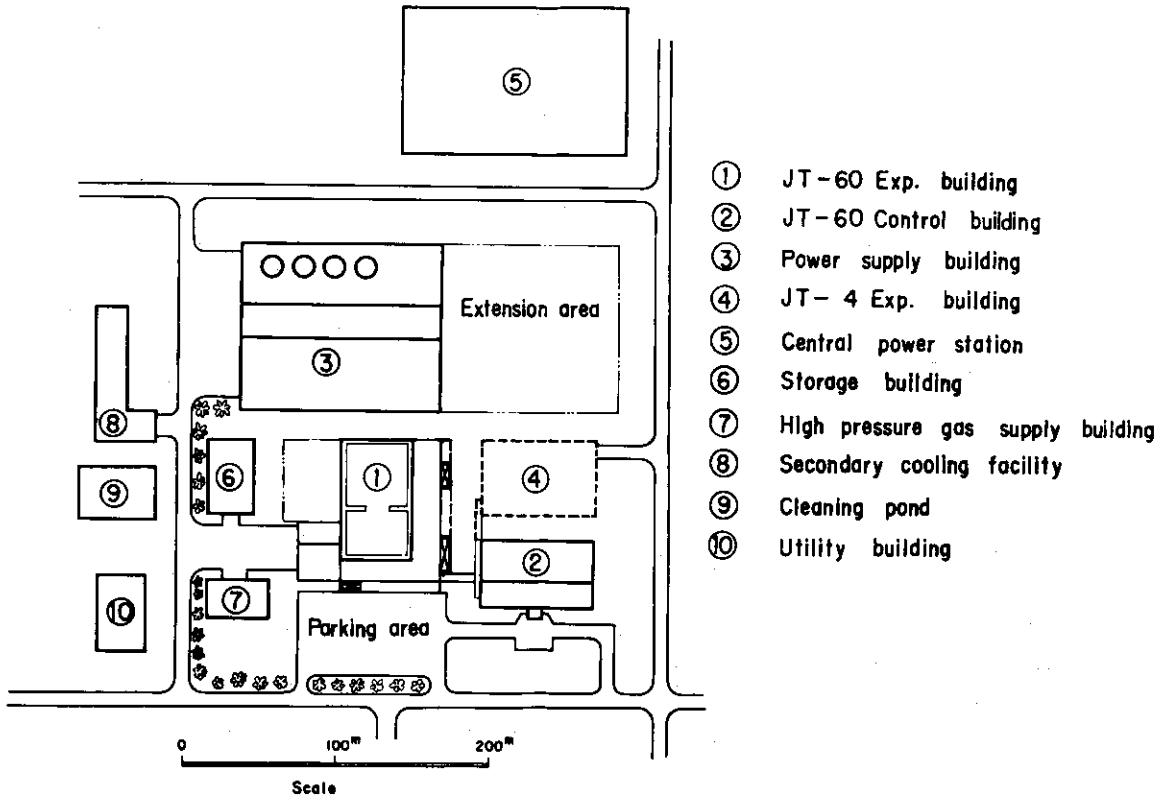

Fig.VIII.3.2-7 Site layout

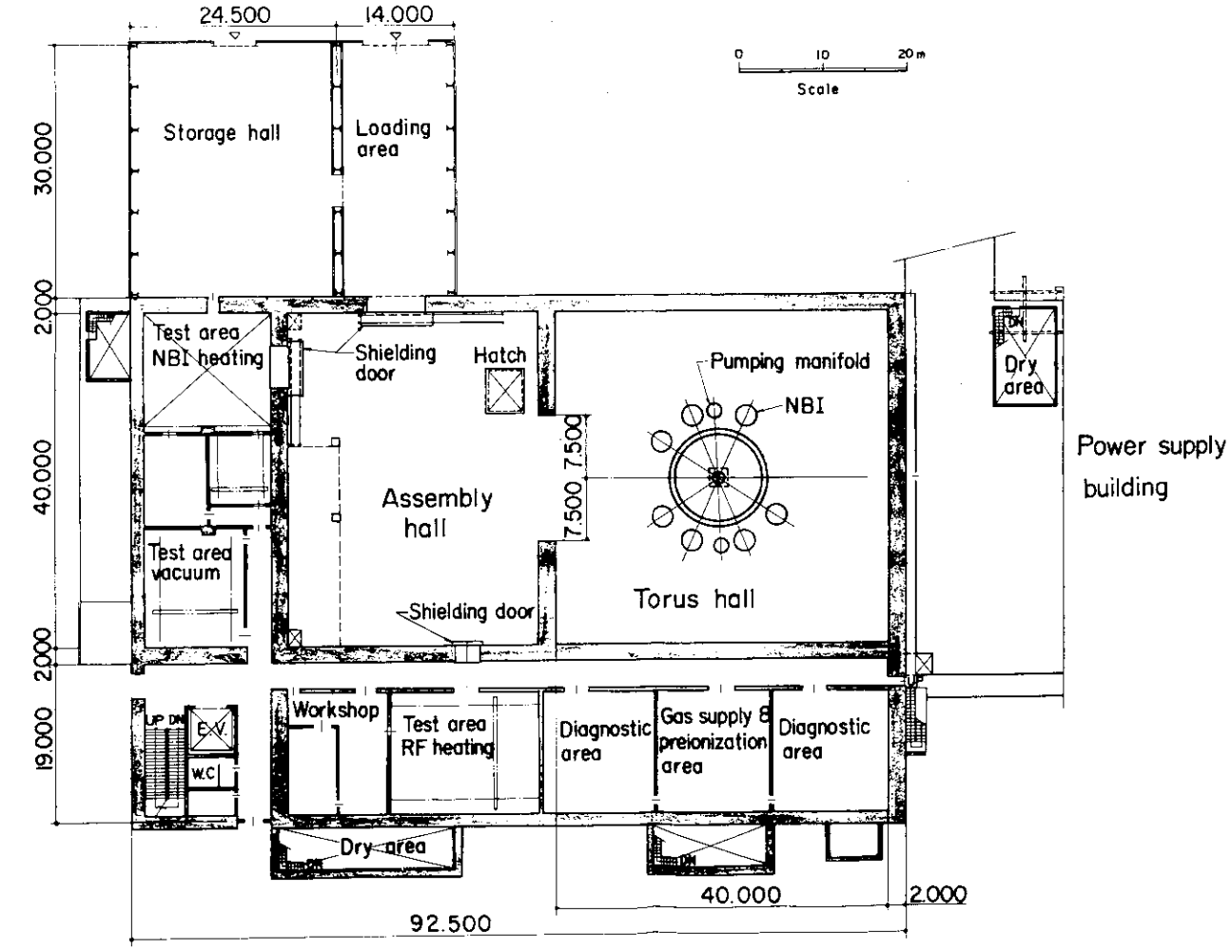

Fig.VIII.3.2-8 Experimental building of JT-60 (a)

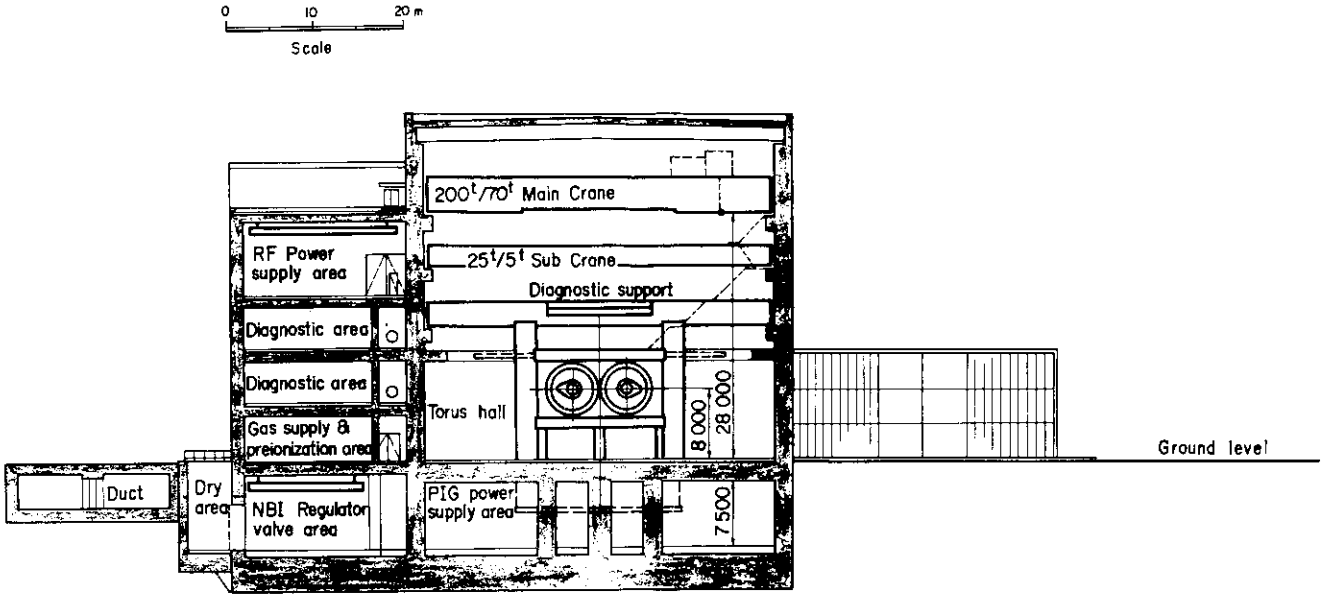

Fig.VIII.3.2-9 Experimental building of JT-60 (b)

Table VIII.3.2-1 Specifications of vacuum vessel

Structure	U-shaped bellows and thick rings
Cross section	Ref. Fig. VIII.3.1-1
Materials	Inconel 625
Magnetic permeability	<1.02
Electric resistance	>1.3 mΩ
Allowable He leak rate	$<5\times10^{-7}$ torrℓ/sec
Expected outgassing rate	$<1\times10^{-11}$ torrℓ/sec cm^2
Expected ultimate vacuum	$<10^{-8}$ torr
Baking temperature	
Vacuum chamber	500°C
Ports	250°C
Vacuum seal	
Vacuum chamber	Welding
Ports	Metal seal
Earthquake proof	0.3 G

Table VIII.3.2-2 Specifications of liner, fixed limiter and magnetic limiter plate

Material	Molybdenum
Cross section	Ref. Fig. VIII.3.1-1
Thickness	
Liner	5 mm
Collector plate	20 mm
Baking temperature	200~500°C
Expected outgassing rate	$<10^{-11}$ torrℓ/sec cm^2
Earthquake proof	0.3 G

Table VIII.3.2-3 TF coil specification

Number of coil	18	
Coil current	52.1	KA
Total turn	1296	turn
Coil major radius	3.32	m
Coil inside radius	1.94	m
Coil outside radius	2.86	m
Field at plasma center	45	KG
Maximum field in coil	98	KG
I^2R	390	MW
$1/2\ LI^2$	2.85	GJ
Equivalent square wave pulse length	38	sec
Total energy consumption per pulse	8.66	GJ
Coil inductance L	2.1	H
Coil resistance R	84	mΩ
Coil time constant L/R	25	sec
Maximum current density	26.8	A/mm^2
Forcing voltage	7.5	KV
Flat top voltage	4.4	KV

Table VIII.3.2-4 PF coil specification

Type of PF coils		OH	V	Q	H	M
Ampere turns	MAT	±5.5	±1.8	±0.5	±0.13	±0.75
Total turns		60	64	40	12	16
Max. current	kA	91.7	57.3	21.7	25	94.4
I^2R	MW	29.3	37.5	1.7	8.8	22.6
$1/2\ LI^2$	MJ	35.3	18.7	0.1	1.1	4.1
Time const.	sec	2.4	8.8	0.4	0.3	0.4
Max. current density	A/mm^2	18.9	27.5	16.4	20.0	27.7
Equivalent square wave pulse length	sec	7.3	5.8	6.8	7.0	5.6
Ground voltage	kV	<30	<25	<10	<5	<5
Turn to turn voltage	kV	<1.5	<1.5	<1.5	<1.5	<1.5

Table VIII.3.2-5 Cooling system specifications

		the field coil system	the vacuum vessel system
Total removal energy	MW	21	2
Total water flow rate	m^3/hr	2800	130
Maximum system pressure	kg/cm^2G	16	12
Number of pump		4	2
Number of heat exchanger		5	1
Max. outlet temperature from heat exchanger	°C	42	
Resistivity of coolant	Ω-cm	10^5	
pH of coolant		5∿9	

3.3 Safety analysis

3.3.1 Vacuum vessel

(1) Temperature rise of fixed limiter and magnetic limiter plate under runaway electron bombardment

Runaway electrons have been observed in many Tokamaks. Runaway electron bombardment gives rise to a surface melting of the fixed limiter (F.L) as seen, e.g., in JFT-2 and JFT-2a. In case of JT-60, these damages of the F.L and/or the magnetic limiter plate (M.L.P) are considered to be more severe because the plasma current is very large (2.7 MA). To estimate such surface melting, we calculated transient temperature analytically[1]. The calculation conditions are listed in Table VIII.3.3-1 and the results are shown in Fig. VIII.3.3-1. We assumed conservatively that runaway electrons carry the total plasma current and are generated steadily during the discharge. As seen from the figure, the surface temperatures of F.L and M.L.P exceed melting point within 0.03 sec and 0.3 sec, respectively, so that if runaway discharge occurs, the surface melting cannot be avoided. Therefore, it is necessary to check the surface damage beforehand and to exchange F.L and M.L.P before fatal damage. The operation in which runaway discharge hardly occurs is needed and this is one of the subject for reactor grade Tokamak plasma.

(2) Accident due to breaking of JT-60 vacuum vessel

Abrupt deterioration of vacuum is due to damages of the vacuum vessel and accessories such as windows and bellows of the diagnostic ports.

These damages are due to the following matters: (a) Earthquake, (b) Creep, (c) Buckling due to creep, (d) Fatigue, (e) Superposition of creep and fatigue, (f) Corrosion of external surface of the material of the vacuum vessel, (h) Missile (Flying of magnetic instruments, tool and so on in strong magnetic fields).

The influences of the abrupt deterioration of vacuum on the vacuum vessel are the internal pressure rise and oxidation of liners, fixed limiters and magnetic limiter plates in the vacuum vessel.

(2)-1 Internal pressure rise of the vacuum vessel

The vacuum vessel is replaced with straight tube as a model as shown in Fig. VIII.3.3-2.

The reflected shock pressure is calculated and is about fifty times larger than the initial.

The specified maximum pressure in the vacuum vessel is 3 torr at the oxidation and deoxidation surface treatment. Therefore, the resulting pressure is 150 torr and is the safety pressure for the design of the vacuum vessel.

(2)-2 Oxidation of the molybdenum

The air inflow into the vacuum vessel oxidises the molybdenum quickly at high temperature.

The thickness of the oxide films on the molybdenum is estimated on severe condition, that is, the abrupt deterioration of vacuum occurs during plasma discharge and at the same time, the air flows quickly into the vacuum vessel which is kept at a temperature of 400°C.

The maximum temperatures of the liner, the fixed limiter and the magnetic limiter plate during plasma discharge are 500°C, 1600°C and 500°C, respectively.

The thicknesses of the oxide films on the molybdenum are calculated in the temperature range from 300°C to 1370°C and time range from 0.1 hr to 10 hr.[2],[3],[4]

The results are shown in Fig. VIII.3.3-3 and Fig. VIII,3.3-4.

It is estimated that the fixed limiters are oxidised several thousands microns and the liners and the magnetic limiter plates several microns at each maximum temperature.

The following countermeasures for the accident are considered; the fixed limiters damaged intensely are exchanged and the other fixed limiters, the liners and the magnetic limiter plates are re-installed after the treatment of electrolytic polishing.

For this reason, the structures of the liners, the fixed limiters and the magnetic limiter plates are designed as exchangeable.

(3) Temperature rise of liner by the direct NBI when plasma does not build up

The analysis describes the estimation of the temperature rise for a liner when the plasma is not formed and at the same time the safety device of NBI, which is prepared to work immediately to stop the beam injection, does not work. 14 NBI units 1.4 MW each are used for the plasma heating of

20 MW. The center line of neutral beam path strikes an edge of the liner which is opposite to the injection port (Fig. VIII.3.3-5). In the case when this beam strikes the liner at an angle of 29.5 degrees to the toroidal direction and 7 degrees to the poloidal one, the peak value of heat flux of a gaussian distribution is 735 W/cm^2.

The transient temperature of the liner irradiated by the direct NBI is shown in Fig. VIII.3.3-6. Point A reaches melting temperature of molybdenum (T_m=2610°C) in the period of about 7 sec for the initial temperature of 20°C and about 6 sec for 400°C, and then this region begins to melt. The point B also reaches melting temperature in the period of about 9 sec for 20°C and 8 sec for 400°C. After the period of this time, the A-B part of the liner melts and is missing. The neutral beam strikes directly the rigid sector or the bellows if the A-B part of the liner is missing. If the neutral beam strikes the rigid sector, the temperature rise of the sector surface is about 1200°C after the period of 4 sec. If the beam strikes the bellows, this region begins to melt after about 4 sec because it is made of the thin material and consequently the vacuum vessel is broken.

In order to avoid these accidents, the following must be prepared.

a) A high reliability of the safety device for NBI.
b) The thicker material is used as the liner which is irradiated by the beam.
c) The secondary safety device, which functions by the signal from thermocouples embedded in the liner, is provided.

(4) Temperature rise of the bellows due to eddy current induced when plasma current does not build up

The induced current on the vacuum vessel when plasma current does not build up is shown in Fig. VIII.3.3-7.

Total amount of dissipated heat in the bellows with an electrical resistance of 1.3 mΩ is calculated as 11.8×10^6 joule.

Since total weight of the bellows is 2850 kg and specific heat of the bellows is 0.486 joule/g·°C, temperature rise ΔT of the bellow becomes

$$\Delta T = \frac{11.8 \times 10^6}{2.85 \times 0.486 \times 10^6} = 8.5°C.$$

Inconclusion, this temperature rise does not matter for the design of the vacuum vessel.

3.3.2 Coil system

The main purpose of this part is to describe the coil safety analysis.

(1) Short-circuits of toroidal field coils

In order to calculate the forces acting on the structure due to short circuits of the toroidal field coils, it is necessary to estimate the transient current. Assumptions for the analysis of the fault are as follows.

(1) Some coils develop a short-circuit across its connection.

(2) The nominal current, 52.1 kA, is chosen as the initial value.

(3) Arc resistance of the fault is 1.0 μΩ.

The equivalent circuit of the coil system is shown in Fig. VIII.3.3-8. The calculated value of current reduced factor $(I_o-I)/I_o$ is shown in Fig. VIII.3.3-9.

Where; I_o = Nominal current (52.1 kA)

I = Current of the fault coils

If the fault occurs, the lateral force acts on each of the neighbouring coils and the unbalanced centering force occurs due to the distorted toroidal field. Fig. VIII.3.3-10 shows results of the unbalanced centering force at 100 msec after the fault.

The maximum bending stress of the center column reaches more than 40 kg/mm^2. In order to avoid the failure of the center column, It is necessary to operate the protection system within 50 msec.

The power supply can be shut down safely without the damages of the center column even if the fault occurs, because the protection system has been able to be operated less than 50 msec.

(2) Short circuits of poloidal field coils

Considerations have been given to the short circuits of the ohmic heating (OH) coils, since the maximum voltage is developed across the OH coils. The short circuits may appear during the plasma initiation phase when the highest voltage of the coil is produced. The equivalent circuit of the coil system is shown in Fig. VIII.3.3-11.

Fig. VIII.3.3-12 shows the current waveform in case of the short circuit of half of the OH coils. After the fault occurs, the transient current through the shortcircuited coils increases gradually due to the interaction between the shortcircuited coils and the remaining OH coils. The induced current increases at a remakable rate if only a few coils are shortcircuited.

For example, the maximum induced current is about 770 kA in case of the short circuit of one OH coil (F13) which is the most inward coil near a torus axis.

The excessive current may cause damage to the shortcircuited coils and the surrounding parts by the arc energy and the magnetic force. Fig. VIII.3.3-13 shows the excessive magnetic force acting on the coil F13 in case of short circuit of one OH coil (F13). In order to minimize the damage, the very fast switch which is connected in parallel with the voltage adjusting resistor needs to be operation

(3) Temperature rise of the magnetic limiter coil when its cooling system is troubled during the baking process

If a trouble occurs in the cooling system of the magnetic limiter coil shown in Fig. VIII.3.3-14, during a high temperature baking operation, it is expected that the coil temperature rises gradually if any measure are not taken. In this case, a spreading phenomenon to be avoided at first from the view point of a coil safety is the thermal damage of the electrical insulation wrapped around each conductor. To prevent it, therefore, a re-starting of the cooling system is required before the insulation temperature reaches a limit, which is 155°C if the F-stage is used.

A time dependent temperature of the coil was calculated by setting the following assumptions:

(1) An initial temperature of the insulation is assumed to be 100°C.
(2) As a heat flux, 300 W/m^2 is used in a support section and assumed to be constant.
(3) Conduction heat transferred from the can is accumulated only in the copper.

The result is shown in Table VIII.3.3-2 and indicates that the insulation temperature reaches 155°C after 2 hr from the outbreak of the trouble, hence the insulation does not be damaged instantly. Moreover, an auxiliary pumping system and an emergency electric power supply are prepared in the JT-60 machine. As a conclusion, it is expected that the magnetic limiter coil does not suffer any fatal damages.

3.4 Miscellaneous

3.4.1 Runaway electron beam irradiation test of the fixed limiter and magnetic limiter plate

Runaway electron bombardment gives rise to a surface melting of fixed limiter (F.L) and/or magnetic limiter (M.L.P), which are made of molybdenum in JT-60. It is considered that these damages reduce the mechanical strength greatly due to the notch effect and after a number of bombardments proceed breaking accident. The electron beam irradiation tests with an electron beam welding machine were performed to obtain preliminary data about these damages and to estimate the reduction of the mechanical strength. The test conditions are as follows; 150 keV beam energy, 33 kW/cm^2 heat flux, and 2.5 cm × 0.05 cm beam irradiated region. The duration, cooling time and number of repetitions are shown in Table VIII.3.4-1. The sample numbers in Table VIII.3.4-1 correspond to the one in Photo. VIII.3.4-1. Before and after the tests, the bending strength and hardness were measured and the microstructure was examined. After the cyclic heat supply, surface damages were observed as shown in Photo VIII.3.4-1. The bending strength of these samples decreases by 34-68 % compared with the one before the irradiation. The results show that if runaway discharge occurs the surface melting of the limiter cannot be avoided. Therefore, it is needed to check the surface damage beforehand by a detector such as in-situ observation system and to exchange F.L and M.L.P against a fatal damage.

3.4.2 Recrystallization of molybdenum liners under the bombardment of fast neutral hydrogens[5]

In NBI heating phase, fast neutral hydrogens which penetrate into the plasma will bombard the molybdenum liner. This bombardment induces a problem about particle-wall interactions such as sputtering and blistering. On the other hand, the surface temperature increases locally and an engineering problem such as the reduction of the mechanical strength of the liner due to the recrystallization, might become a serious problem after a larger number of NBI experiments in the hot liner operation (base temperature ≃ 450°C). From the experimental data obtained as the isothermal one, the reduction of the molybdenum tensile strength becomes to be prominent at 10 % recrystallization. Therefore, we decide the allowable limit as 10 % recrystallization. However, the actual temperature of the

liner varies. To estimate the limited shot numbers of NBI that the recrystallization proceeds up to 10 %, we have made the computer code 'RECRYSTAL' which converts the recrystallization due to the transient temperature variation into the equivalent isothermal recrystallization which is characterized by the equivalent isothermal recrystallization time Δt_{eq} and the temperature $T(t_1)$.

$$\Delta t_{eq} = \frac{\int_0^{t_2} e^{-\frac{Q_R}{R \cdot T(t)}} dt}{e^{-\frac{Q_R}{R \cdot T(t)}}} \qquad (1)$$

Δt_{eq} ; equivalent isothermal recrystallization time
Q_R ; activation energy for recrystallization
R ; gas constant
$T(t)$; time dependent temperature function
t_2 ; period of a heat cycle
t_1 ; $0 < t_1 < t_2$

The heat flux of the beams on the plasma surface is about 1000 W/cm^2. However, this heat flux depends on the plasma parameters and decreases rapidly as the plasma density increases. The temperature rises of the liner surface at the end of 5 sec pulse are 190 ∿ 310°C, 80 ∿ 120°C and 50 ∿ 70°C in the case of $n_e = 1 + (4.5 \sim 2.5)t$ and $Z_{eff} = 1$, 2 and 3, respectively. (n_e; plasma density (10^{13} cm^{-3}), t; time (sec)).

The calculated results under these conditions show that the recrystallization is below 10 % after 10^4 - 10^5 shots and found to be not a serious problem. Further studies concerning sputtering and blistering must be made.

References

(1) Carslaw, H.S. and Jaeger, J.C.: "Conduction of Heat in Solid", Oxford University Press (1973).
(2) Gulbransen, E.A. and Wysong, W.S.: Metals Technology (Sep. 1947), 1-17.
(3) Lustman, B.: Metal Progress, 57, 629, (1950).
(4) Semmel, J. W. Jr.: "High Temperature Materials" April 16-17, (1957) pp 510.
(5) to be published.

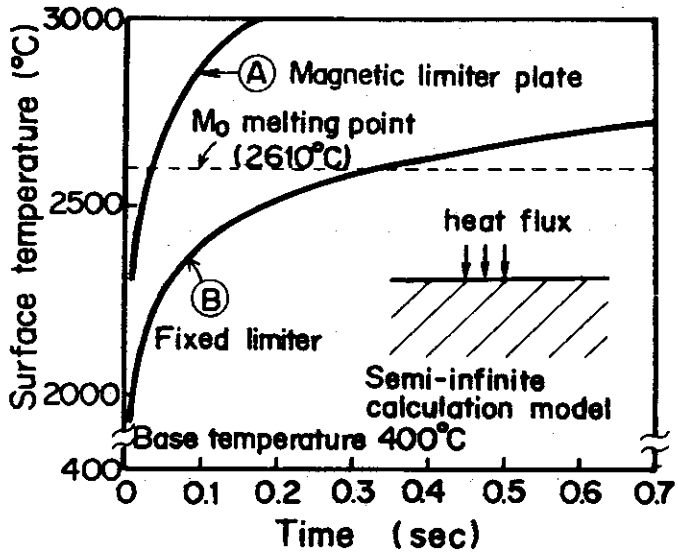

Fig.VIII.3.3-1 Surface temperature at the center of an irradiated region under runaway electron bombardment

	A	B
Heat flux (kW/cm^2)	140	200
Beam width (cm)	0.01	0.005
Irradiated area (cm^2)	28	18.8

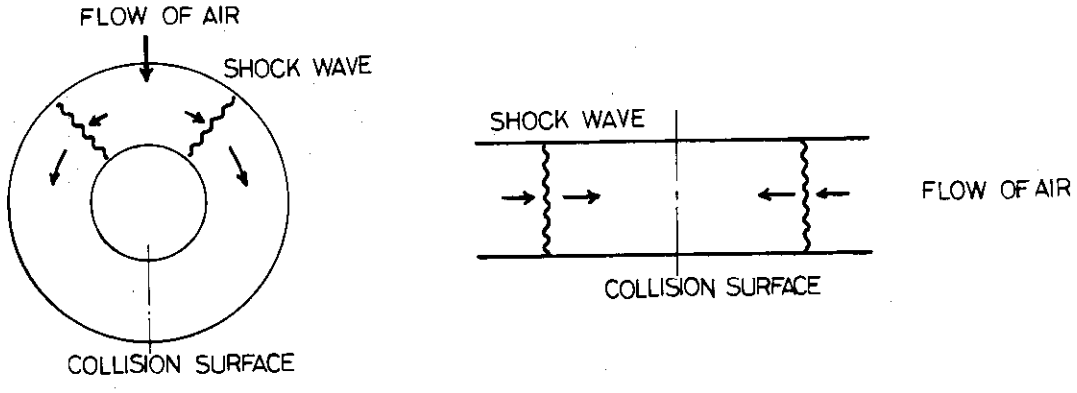

Fig.VIII.3.3-2 Ring model and straight tube model

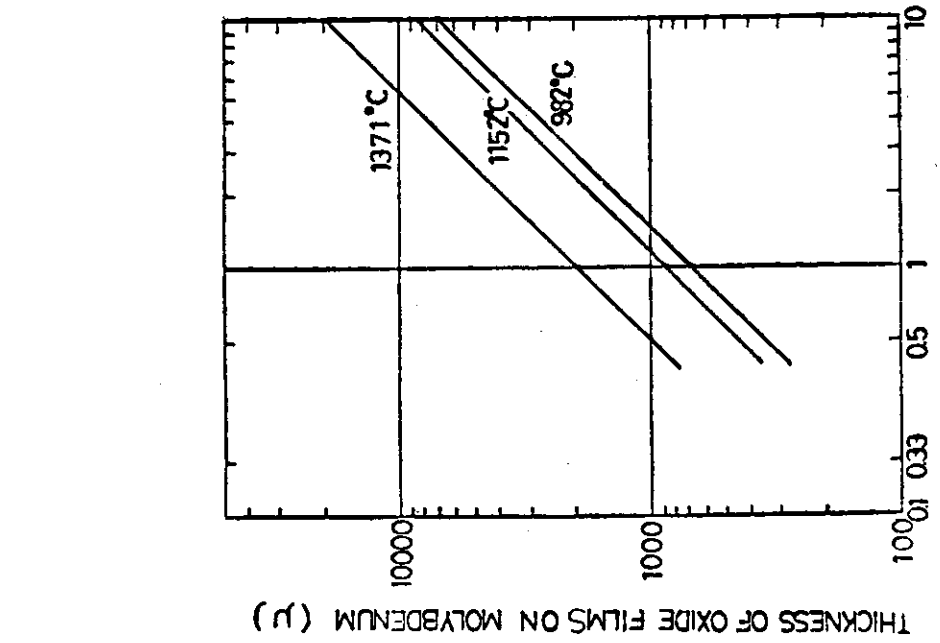

Fig.VIII.3.3-4 Thickness of oxide films on molybdenum in air

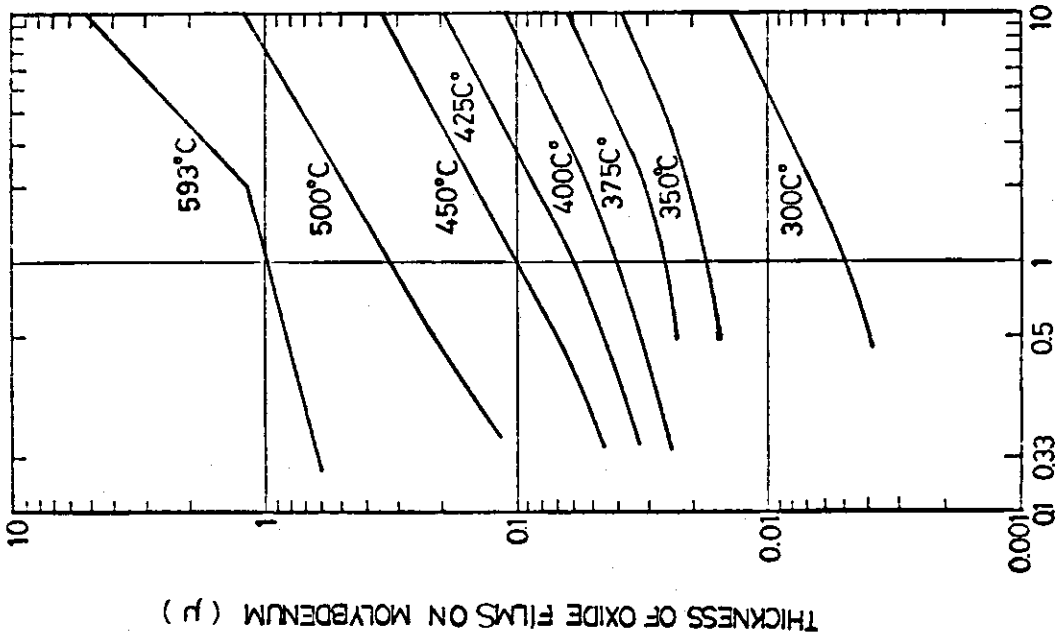

Fig.VIII.3.3-3 Thickness of oxide films on molybdenum in air

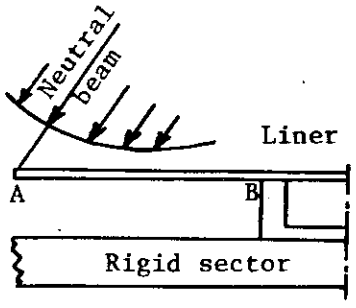

Fig.VIII.3.3-5 Calculation model

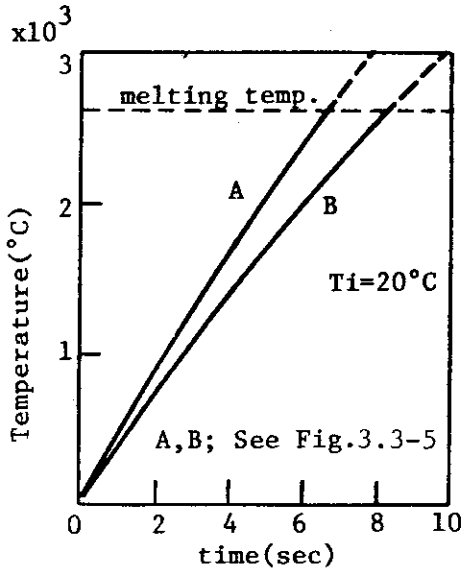

Fig.VIII.3.3-6 Temperature rise of a liner

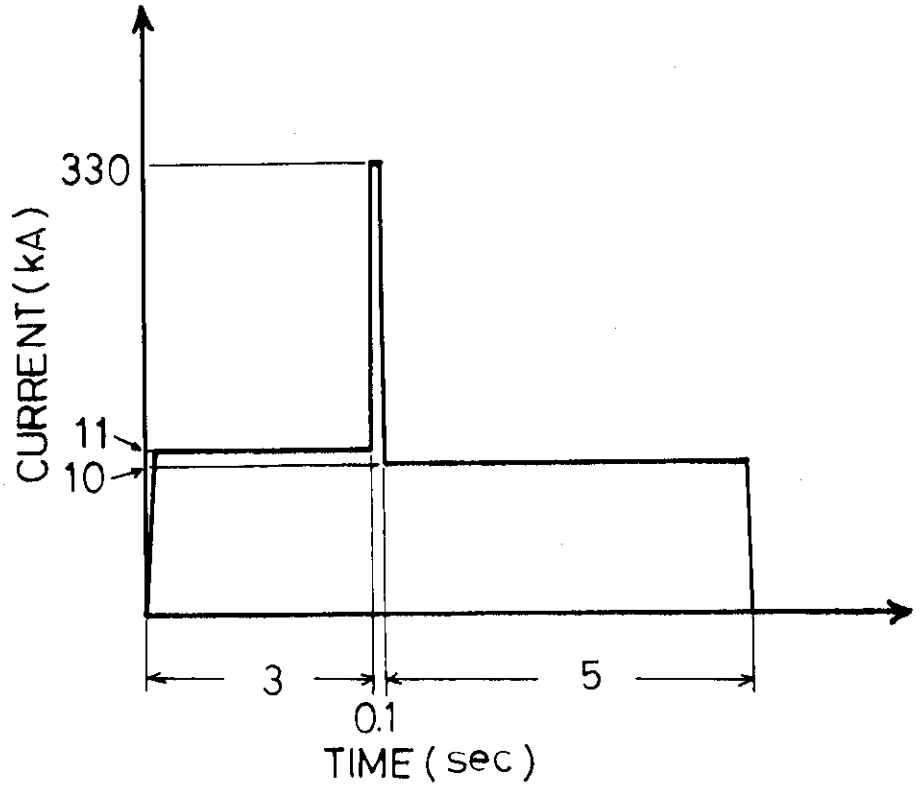

Fig.VIII.3.3-7 Induced current on the vacuum vessel

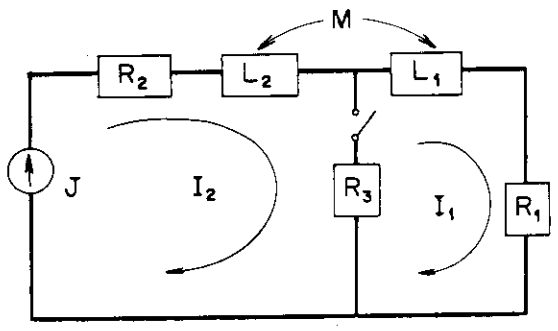

R_1=resistance of short coils
R_2=resistance of remaining coils
L_1=inductance of short coils
L_2=inductance of remaining coils
M =mutual inductance between short coils and remaining cc
R_3=arc resistance (assumed to 1.0$\mu\Omega$)
J = constant current source

Fig.VIII.3.3-8 Equivalent circuit for TF coil fault condition

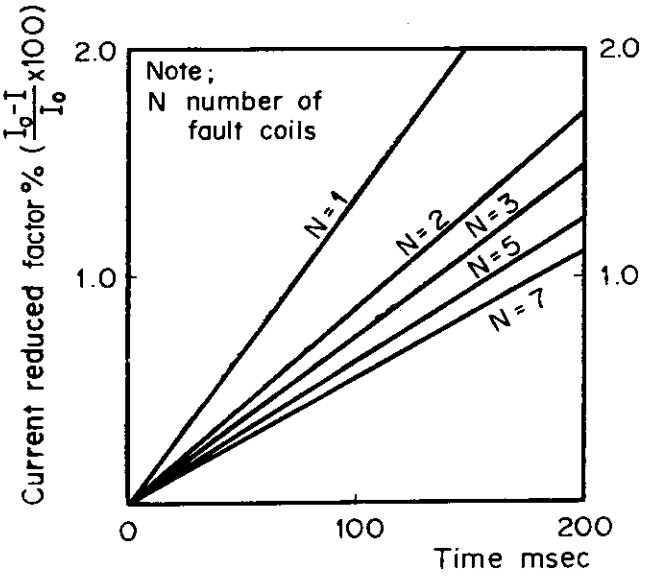

Fig.VIII.3.3-9 Current reduced factor for fault coils

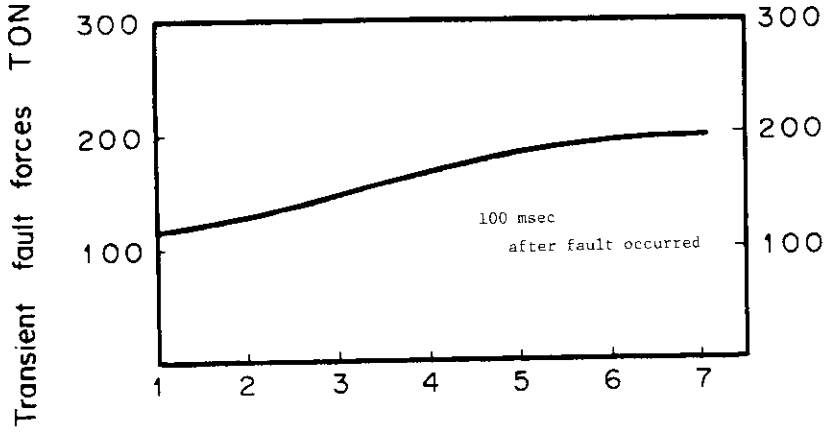

Fig.VIII.3.3-10 Unbalanced centering force

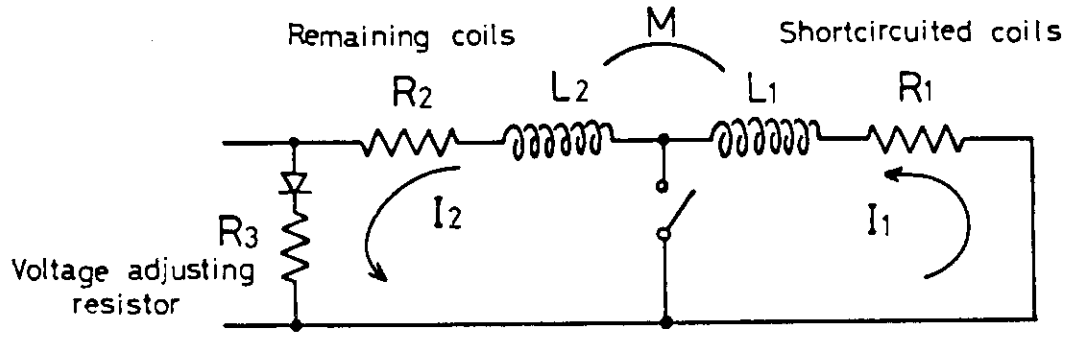

Fig.VIII.3.3-11 Equivalent circuit for a fault situation of OH coil

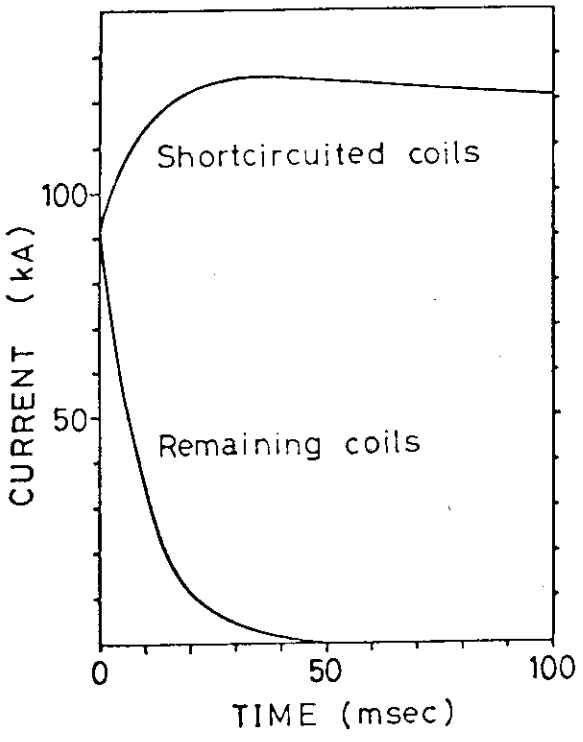

Fig.VIII.3.3-12 Current waveform in case of the short circuit of half of the OH coils

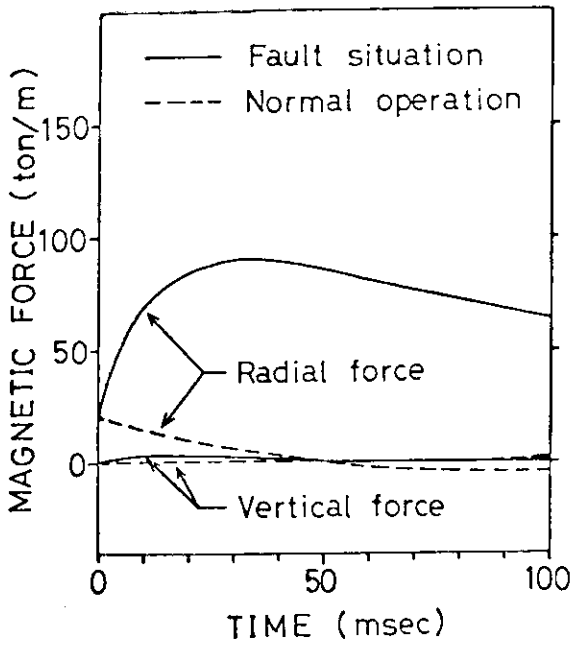

Fig.VIII.3.3-13 Magnetic force of coil F13 in case of the short circuit of one OH coil

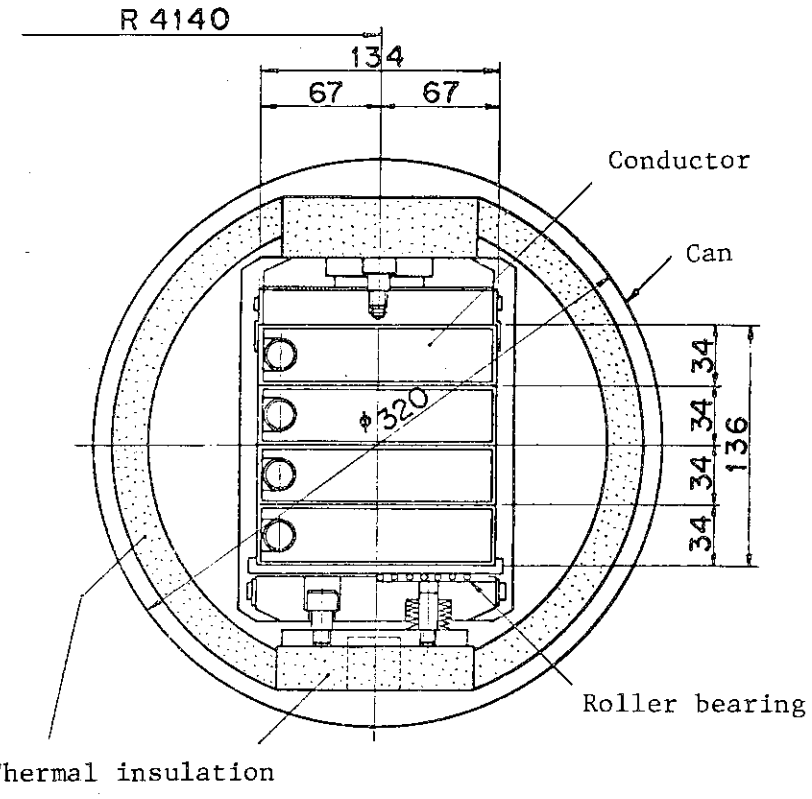

Fig.VIII.3.3-14 Cross section of sub-magnetic limiter coil

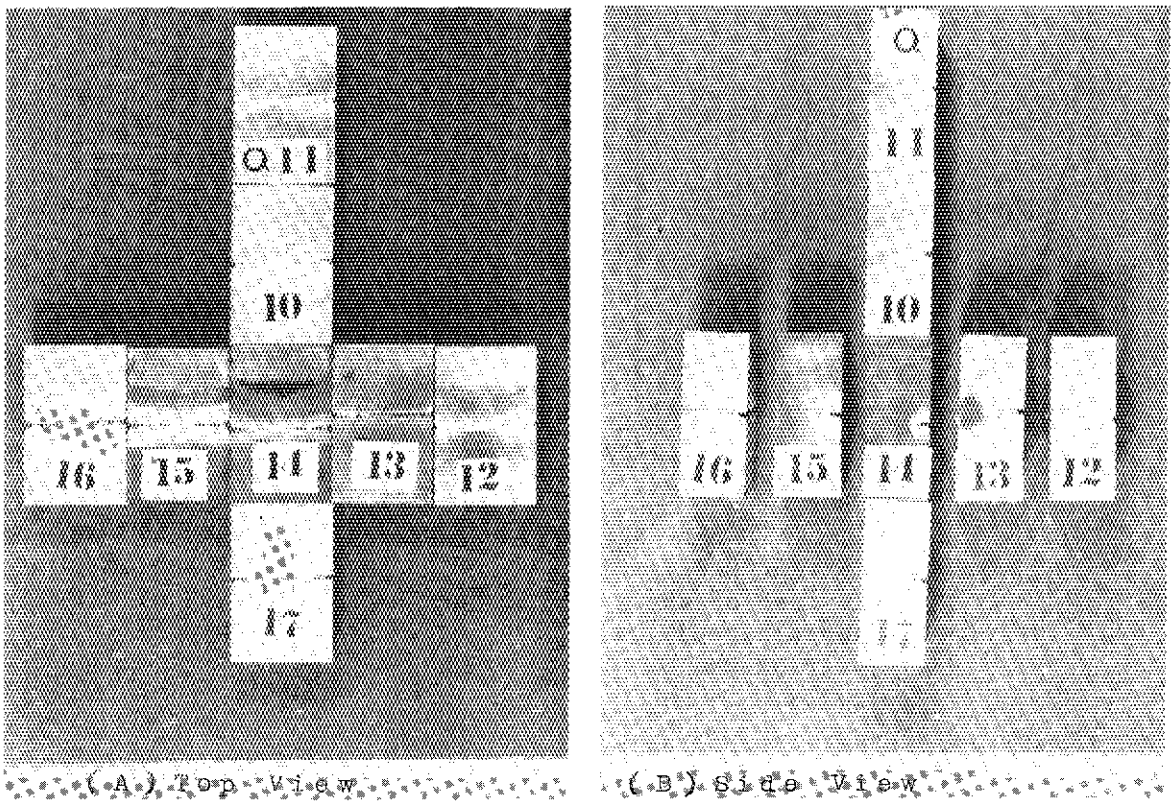

Photo. VIII.3.4-1 Samples after the electron beam irradiations

Table VIII.3.3-1 Calculation condition

Runaway Electron		
Energy	10	MeV
Number	1.35×10^{19}	n/shot
Plasma Parameters		
Plasma Current	2.7	MA
Duration	5	sec
Confinement Time	0.4	sec

Table VIII.3.3-2 Time variaton of insulation temperature

	Time (hr)				
Temperature (°C)	0.5	1	2	3	4
	113	126	152	179	205

Table VIII.3.4-1 Heating conditions spond Sample numbers corrected to the one in Photo VIII.3.4-1

Sample No.	Duration	Cooling time	Repetitions
Q-10	1 sec	60 sec	10
Q-11	3	60	10
Q-12	5	60	1
Q-13	5	60	3
Q-14	5	60	10
Q-15	5	60	20
Q-16	5	60	30
Q-17	10	60	10

4. Design of Power Supplies

4.1 Review of power supply design

4.1.1 Toroidal field power supply

The JT-60 toroidal field coil system requires a large electric power to generate a toroidal field of 45 kG at the major radius and to sustain it for 5 seconds. To supply this large power to the coil, the toroidal field power supply is designed to consist of two lines;

(1) the line which feeds the electric power directly from the utility power network (utility power line),

(2) the line which feeds the electric power generated by a motor generator with flywheel set (MG line).

The load pattern of both power lines is shown in Fig. VIII.4.1-1. The peak load of the power system becomes 328 MW and the total energy is 8.5 GJ.

The peak load of the utility line must be less than 160 MW at the interface to the utility network system to reduce the network frequency perturbation less than 0.05 Hz. Then the MG line has to share the power of 211MVA and the energy of 3.83 GJ if we take into account of power losses in the transformers, rectifiers, feeders and others. To satisfy the power requirements the motor-generator set becomes so large that the weight of the rotor including the flywheel is about 1,000 tons. The engineering problems lie in the designs of the thrust-bearing, the flywheel material strength and the high-speed rotor vibrations.

4.1.2 Poloidal field power supply

A check and review work on the design of the poloidal field power supply has been continued.

Figure VIII.4.1-2 shows a schematic diagram of the JT-60 poloidal field power supply. Each of the ploidal field coils is separately powered and controlled by independent thyristor converters to meet various operation requirements. A motor-generator supplies AC electric power for all these converters.

A vertical-shaft type generator with the peak apparent power of 500 MVA has been selected. The generator capacity was determined from the detailed analysis of power consumption during one cycle of operation.

The design of the ohmic heating system has been modified. In the

modified circuit (Fig. VIII.4.1-2), mechanical polar conversion switches have been removed to increase overall reliability and controllability of the circuit. Voltage control even in the plasma current build up phase becomes possible in this circuit and the voltage ripples which appear across the ohmic heating coil are also reduced.

A vacuum circuit breaker has been selected for the ohmic heating circuit. The selection was made on the basis of the technical evaluation of the results of the R & D made for D.C circuit breakers (1975 - 1976).

For excitation of the vertical field coil, a high power thyristor controlled D.C power supply has been selected. This selection was made to have a good performance of the plasma maintaining operation and experimental flexibility.

Specifications of thyristor converters are summarized in Table VIII.4.1-1.

4.2 Design of grounding system of JT-60

4.2.1 Purpose of JT-60 grounding system

JT-60 has a feature of large electric power plant, so that the grounding system is important in the safe and reliable operation of JT-60. Grounding systems are usually provided at electric power plants such as stations and substations for two purposes: (1) safety to operating personnel and to the public, and (2) provision of connections to earth for transformer and other power-equipment neutrals. The JT-60 grounding system is required furthermore to reduce the interferences among power lines and also the electrostatic or electromagnetic disturbances to noise-sensitive devices, namely, diagnostic instruments, control systems and computers.

4.2.2 Structure of grounding system

JT-60 has four main facilities which are placed separately in buildings; experimental buildings, power buildings, control building and high voltage (275 kV) substation. The layout of them is shown in Fig. VIII.4.2-1. The grounding system of JT-60 is illustrated schematically in Fig. VIII.4.2-2. Each building is constructed on an individual ground mat. These mats are connected electrically with each other by interbuilding ground buses. The buses are composed of underground metal ducts in which power feeders, signal cables and wires are laid. All of ground mats and ground buses are connected

to earth with low resistance by grounding rods. The grounding system does not make a close loop as a whole. Inner-building ground buses, which provides ground neutral systems of JT-60 equipments, are connected to the mats at sub-terminals. Lightning arresters of each building are grounded independently of the JT-60 ground mat system. The grounding system of the high-voltage substation is isolated from that of JT-60.

Ground Mat

The ground mats, made of mesh wires, in usual power plants are employed for reducing the ground resistance. In the JT-60 grounding system, however, the ground mats are rather used to flatten the distribution of electric potentials arisen on the mats when JT-60 is operated or some ground faults occur. Flattening the potentials by means of the mats is essentially important for satisfying the JT-60 electric safety requirements.

Ground Rod

The grounding resistance of the JT-60 grounding system is not so essential as that of prevailed power plant grounding systems. However, it is desirable to reduce the resistance as small as possible if we suppose a voltage rise of the whole grounding system due to some faults. The grounding resistance depends on the characteristics of the soil in the JT-60 area and the structure and number of the grounding rods. The grounding resistance in JT-60 may be chosen so small as that of the high voltage substation (0.03Ω).

Inter-Building Ground Bus

All of cables, wires and feeders are laid in ducts, whose metal walls constitute the inter-building ground buses. When some ground faults occur a heavy current up to hundreds of kiloamperes probably flows through the buses. To keep the voltage differences between the buildings under a level for personnel safety, the impedance of every bus must be less than one milli-ohm.

Inner-Building Ground Bus

Inner-building ground buses are classified into two groups; grounding feeders for JT-60 power equipment neutrals and grounding feeders for all exposed metal parts of switches, structures, covers, walkways, fences, steelwork of buildings, switchboards, etc.. These feeders maintain the voltages of the power equipment neutrals and non-current-carrying equipments

at the ground mat level, so that equipments and personnels near the equipments on the same ground mat are protected from dangerous rise in voltage under abnormal conditions.

Lightning Arrester

Lightning arresters are connected to earth by grounding plates with sufficiently low resistance. Each of lightning arrester systems are electrically independent of the JT-60 grounding system. Hence lightning shocks do not influence the JT-60 system.

Grounding System of High-Voltage Substation

The 275 kV high-voltage substation has its own ground mat which is isolated from the JT-60 grounding system. The grounding resistance of the substation is so small as 0.03 Ω. Then if the utility network is stuck by lightning or ground faults occur in the substation, dangerous effects do not extend directly to the JT-60 system.

4.2.3 Voltage distribution in JT-60 system and ground fault

To assure the usefulness of the JT-60 grounding system against deleterious effects of the voltage unbalance, simulation calculations have been made in case where a surge current (1 × 10 micro-seconds) rushes into the sub-terminal of the power building ground mat. The circuit model used in this simulation is shown in Fig. VIII.4.2-3. The simulation shows that the finite grounding resistance meshes are superior to the infinite ones. Thereby the best choice for the grounding mats is to employ bared mesh wires.

The ground fault analysis is made for six power supplies; toroidal field p.s., ohmic heating p.s., vertical field p.s., quadrupole field p.s., horizontal field p.s. and magnetic field p.s.. The most dangerous fault is the simultaneous shortenings of the D.C. feeders of all power supplies to the earth and the fault current is up to 340 kA by the concurrent ground faults of all the power supplies.

4.3 Design-related studies

4.3.1 Analysis of early phase phenomena in the plasma current build-up time

As far as the present-day tokamaks are concerned, the physical processes in the early time of the plasma current build-up seem to be well-understood. In case of a large tokamak, however, new problems which arise from the

larger size of the plasma, the larger leakage field, the limited operational regime of filling gas pressures and so forth have to be considered. It is also much more important for the large tokamak to have a good reproducibility of the initial plasma produced by the breakdown.

A computer model was developed 1) and compared with a JFT-2 breakdown experiment and the necessary improvements to describe the experiment have been made. This is a zero dimensional model solving a simplified particle balance equation and circuit equations coupled with plasmas first developed by Papoular 2).

We have applied this calculation to JT-60 to see the effect of error fields on the time evolution of the breakdown electric fields. The following parameters are used; R_0 = 300 cm, a = 95 cm, B_t = 45 kG, $p_0 = 10^{-4}$ torr H_2, initial ionization degree 2×10^{-9}, error field B_v = 60 G, non axial component of B_t 0.1 %, commutation capacitor 1 mF and charged voltage -12.5 kV.

Figure VIII.4.3-1 shows the time evolution of the OH coil voltage and the loop voltage on the vacuum vessel and of the plasma for different applied voltages. The breakdown occurs at 0.55 ms for the applied voltage of 25 kV, 0.6 ms for 15 kV and 0.8 ms for 5 kV. Here we define the breakdown occurs when the plasma loop voltages go down abruptly.

JT-60 has a low resistance welded structure vessel, and a large loop current is induced on it as shown in Fig. VIII.4.3-2. Figure VIII.4.3-3 is the time evolution of the electric field in the plasma. A positive voltage in the early time is due to numerical convenience made in this calculation. Figure VIII.4.3-4 shows the electron density and the resistance of the plasma. Based on this calculation, possible breakdown region of JT-60 is considered and shown in Fig. VIII.4.3-5 where the applied voltage which causes the breakdown is plotted against the filling gas pressure with breakdown time lags as parameters. These results show that reasonably wide breakdown region exists within the designed OH coil maximum voltage of 25 kV, even if an error field is as high as 60 G.

4.3.2 Operation of thyristor converter systems and the required power for the generator of the poloidal field power supply

The poloidal field power supply of JT-60 consists of thyristor converter systems for respective poloidal field coils and a single set of motor-generator which is common to all the converter systems.

A comparative study was made of three types of operation mode of

thyristor converters with particular emphasis on the required power for the generator and the controllability of the converter systems. The transient peak power (apparent) for the generator was calculated on the basis of a reference mode of operation of the poloidal field power supply. It is 550 MVA for the normal rectifier operation of the thyristor converters, 440 MVA for the rectifier-inverter operation and 220 MVA for the by-pass mode of operation. Among these operations, the rectifier-inverter operation seems to be appropriate for the JT-60 poloidal field power supply to meet both requirements of power-factor improvement and good controllability of the thyristor systems.

4.3.3 Interference with utility power network

The electric power for operation of JT-60 is supplied from the utility power network system at 275 kV, 50 Hz. The JT-60 pulsed load gives various perturbations to the network system. Therefore the JT-60 power system has to be carefully designed, taking account of the allowable perturbation levels.

The pulsed active load in the JT-60 power system causes the network frequency perturbation because the network system generators are decelerated and accelerated due to their loading unbalances. Then the allowable frequency variation defines the maximum pulse load. According to the utility network system analysis, the pulsed load of the JT-60 power system must be less than 180 MW in case of the lowest power demand (11,000 MW).

Step changes of the JT-60 power load, which occur after the termination of discharge, influence significantly the performance of the network system generators adjacent to JT-60. Such a sudden drop of the load brings about large fluctuations of the generator outputs. The fluctuation amplitude increases proportionally to the load power step. The step width allowed for the JT-60 power load is less than 70 MW.

Considerable amounts of reactive power are associated with the JT-60 active power pulse although the reactive power compensators are provided. A rapid change of the reactive power causes voltage fluctuations of the network system. The reactive power step load is therefore related to the amplitude of the network voltage.

Higher harmonics born in the AC-DC converter system penetrate into the power network system, resulting in disturbing the communication network system. Reduction of the higher harmonics needs the increase of the rectifier phase number as well as the adoption of the high frequency filters.

The perturbations to the power network system arising from the operation of the JT-60 power system are summarized in the following table. It is found that the operation of the JT-60 power supplies can be chosen so that the perturbations do not exceed the allowable limits except the higher harmonic current limitation.

4.3.4 Analysis of transient voltages induced in the JT-60 toroidal field coil system

Detailed analysis for transient voltages induced in the toroidal coil system when JT-60 is operated has been required to specify the insulators and also the protection system of the coils. Dangerous overvoltages are possibly induced by a plasma negative spike and/or a voltage change in the ohmic heating coil associated with the interruption of the OH circuit.

In the present analysis, a distributed constant circuit model is introduced for the related equipments; the toroidal field coils, the poloidal field coils, the vacuum vessel and the plasma. A universal computer code FNAP-2 is used for carrying out this analysis.

When a voltage impulse (amplitide 12,5 kV, rise-time 100 μS) is applied to the ohmic heating coil, a voltage surge induced in the toroidal coil has an amplitude of 0.67 V/layer and an oscillating period of 370 μS. This surge can be reduced furthermore if a surge absorber is connected in series to the toroidal coil system.

References

(1) Shimada, R., et al.: Internal memo (in Japanese).
(2) Papoular, R.: EUR-CEA-FC-769 (April, 1975).

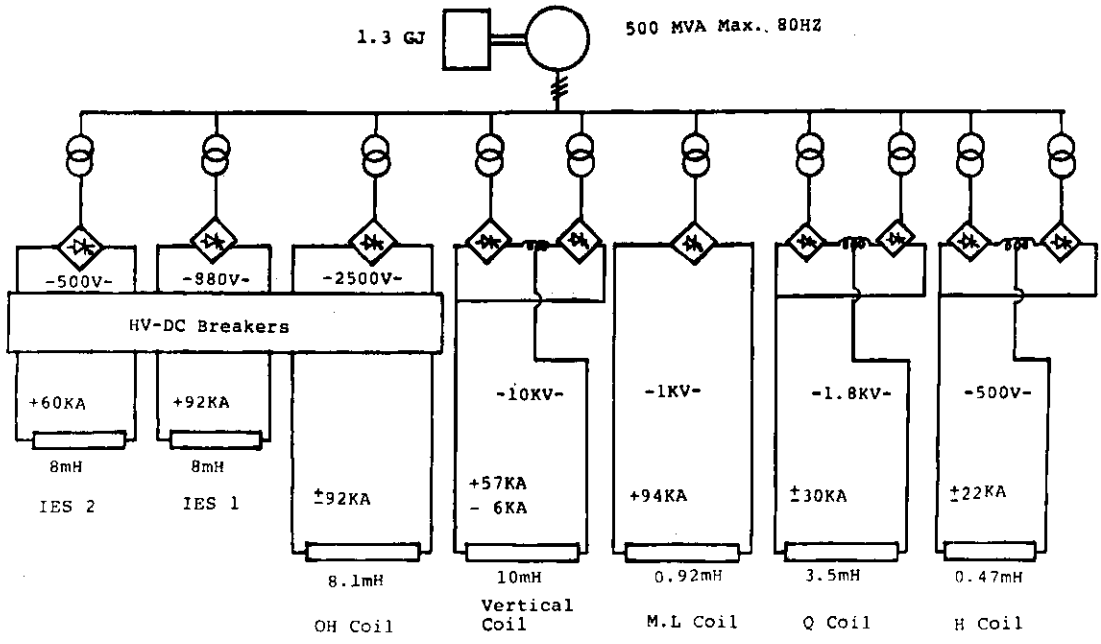

Fig.VIII.4.1-1 Load pattern of JT-60 toroidal field power supply

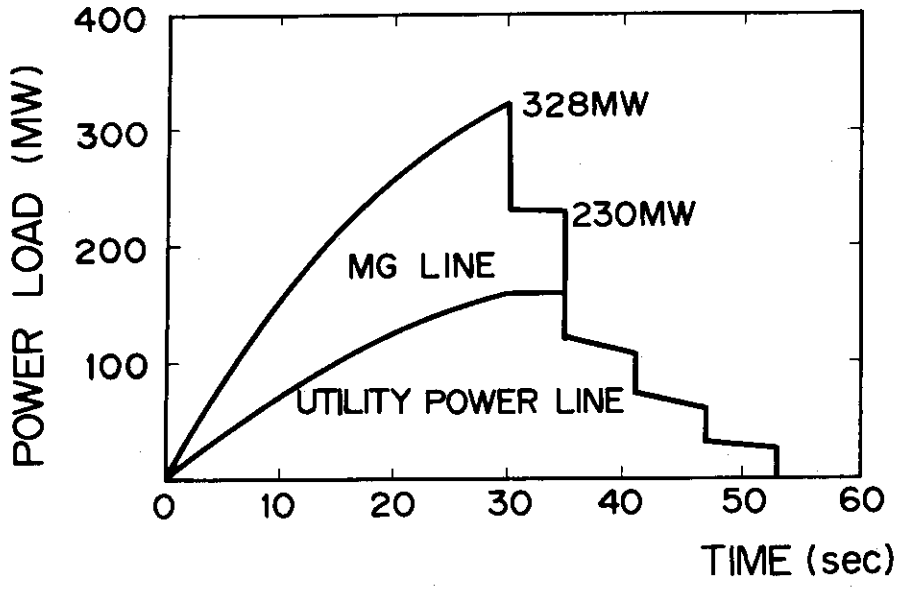

Fig.VIII.4.1-2 Poloidal field power supply of JT-60

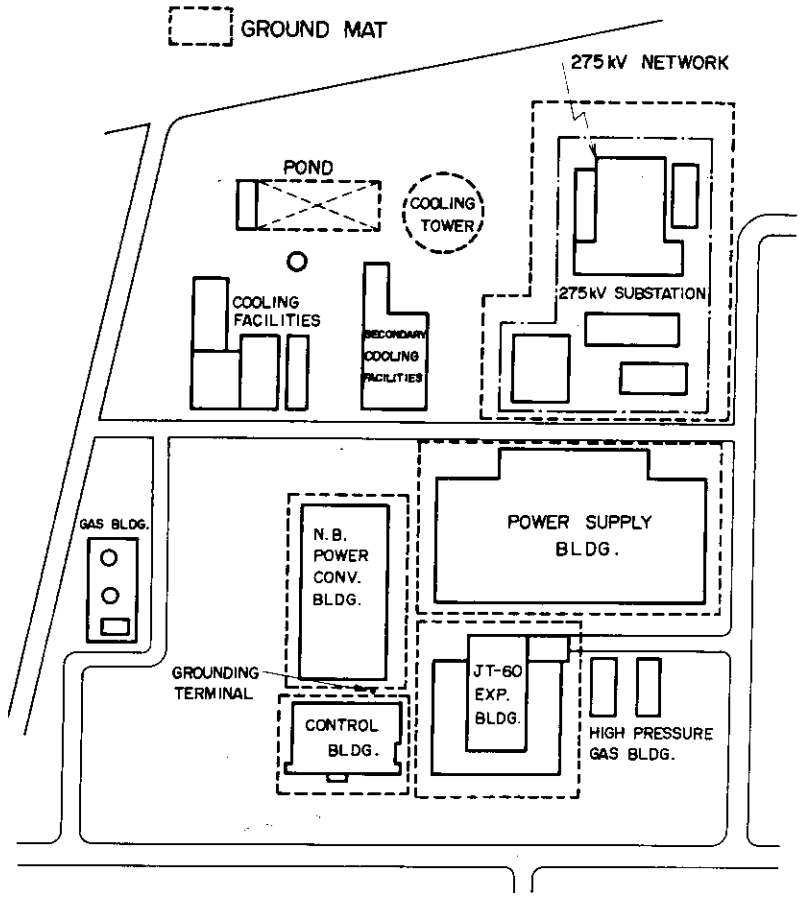

Fig.VIII.4.2-1 JT-60 site plan and ground mat location

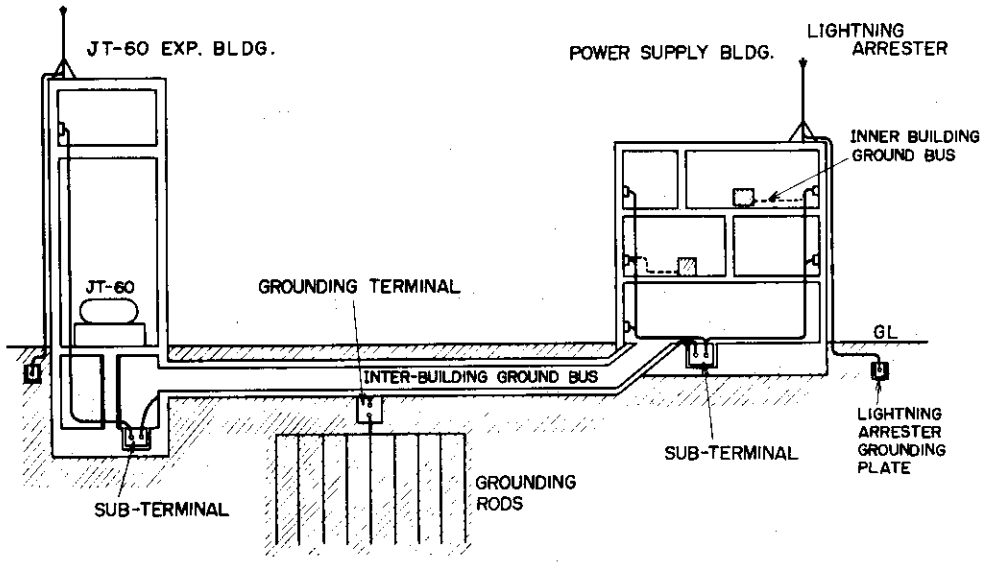

Fig.VIII.4.2-2 Schematic of grounding system

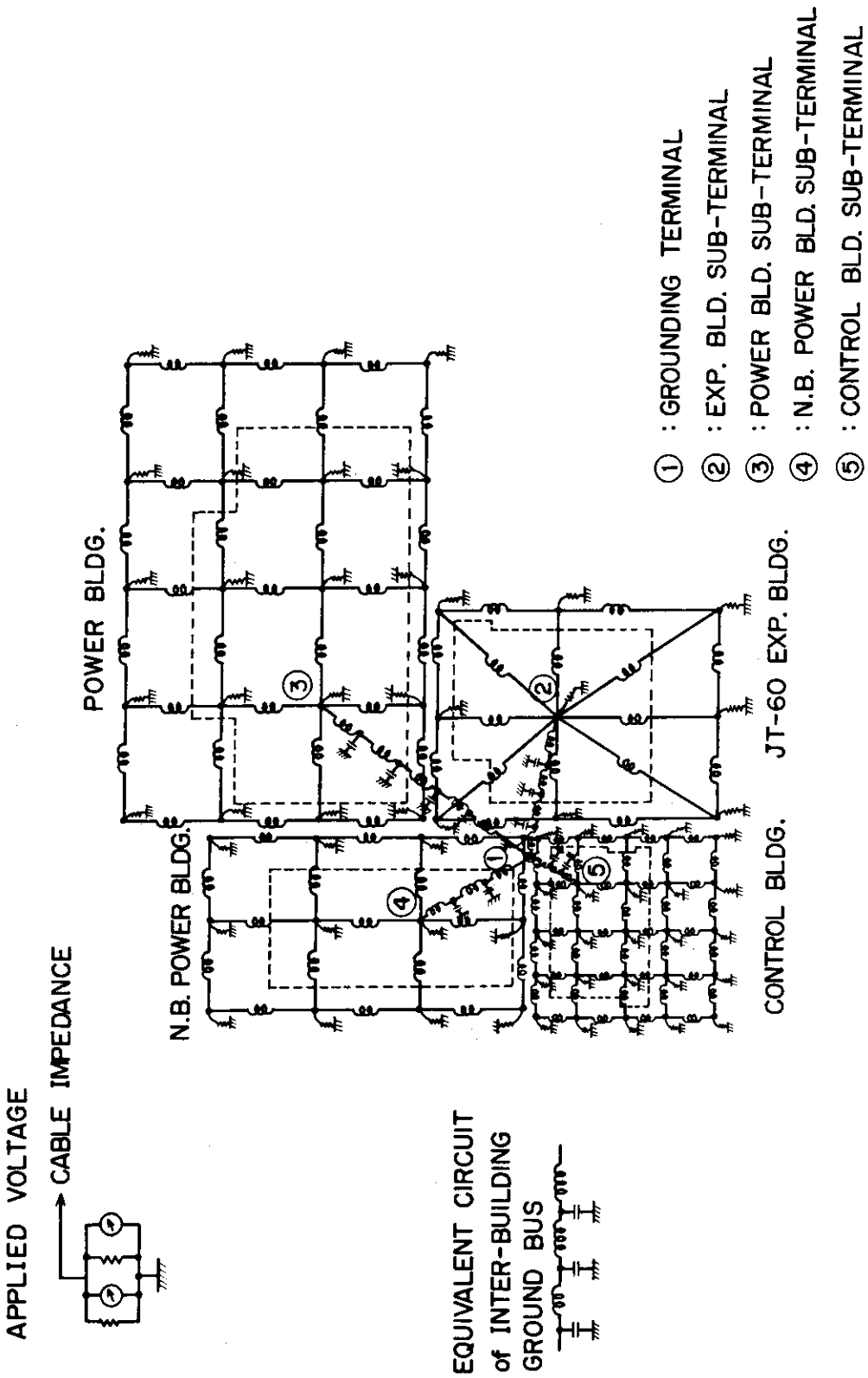

Fig.VIII.4.2-3 Simulation model of grounding system

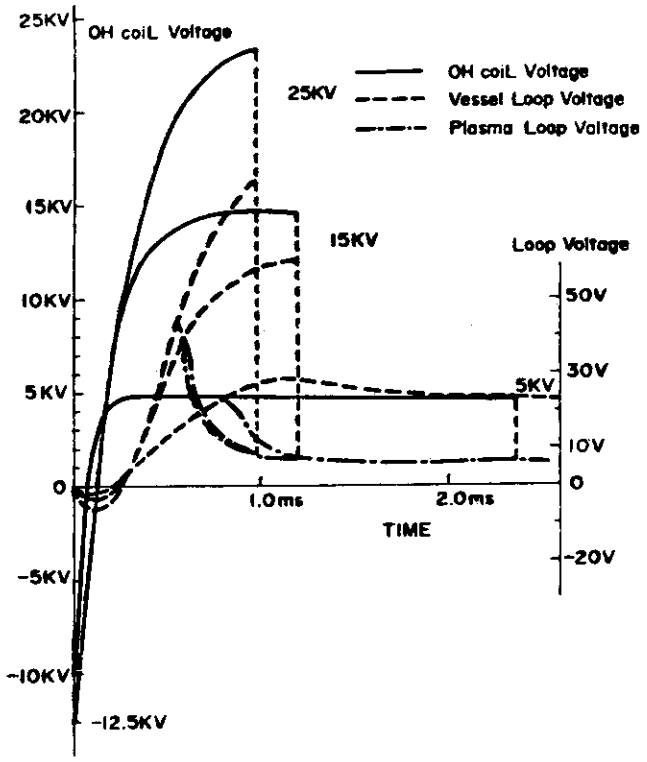

Fig.VIII.4.3-1 Time evolution of the OH coil voltage, the vessel loop voltage and the plasma voltage for $P_0=10^{-4}$ torr.

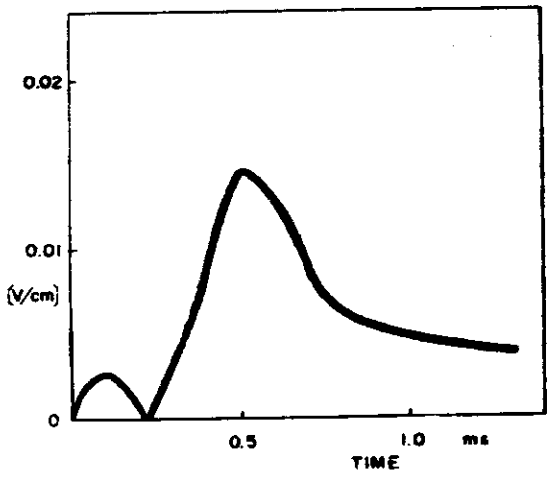

Fig.VIII.4.3-3 Time evolution of the electric field in the plasma for V_{OH}=15 kV.

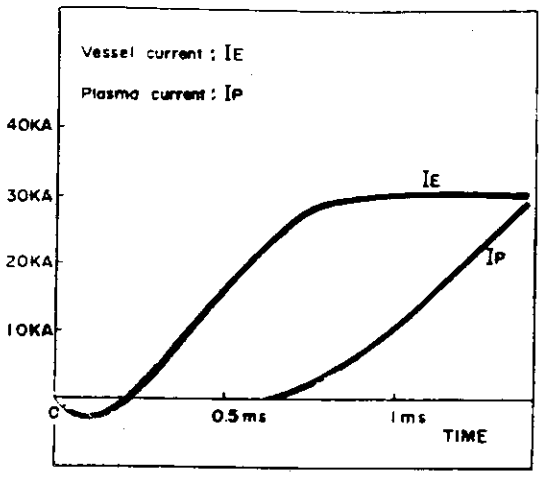

Fig.VIII.4.3-2 Time evolution of the vessel current I_E and the plasma current I_p for V_{OH}=15 kV.

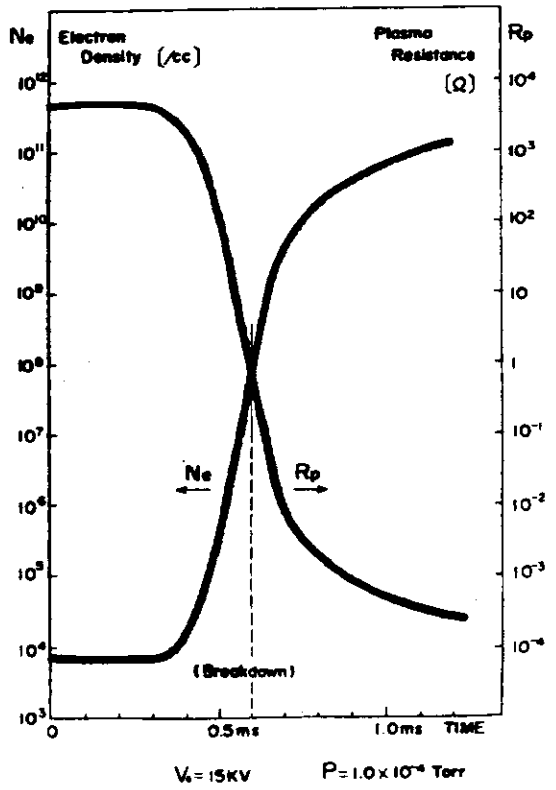

Fig.VIII.4.3-4 Time evolution of the electron density N_e and the plasma resistance R_p.

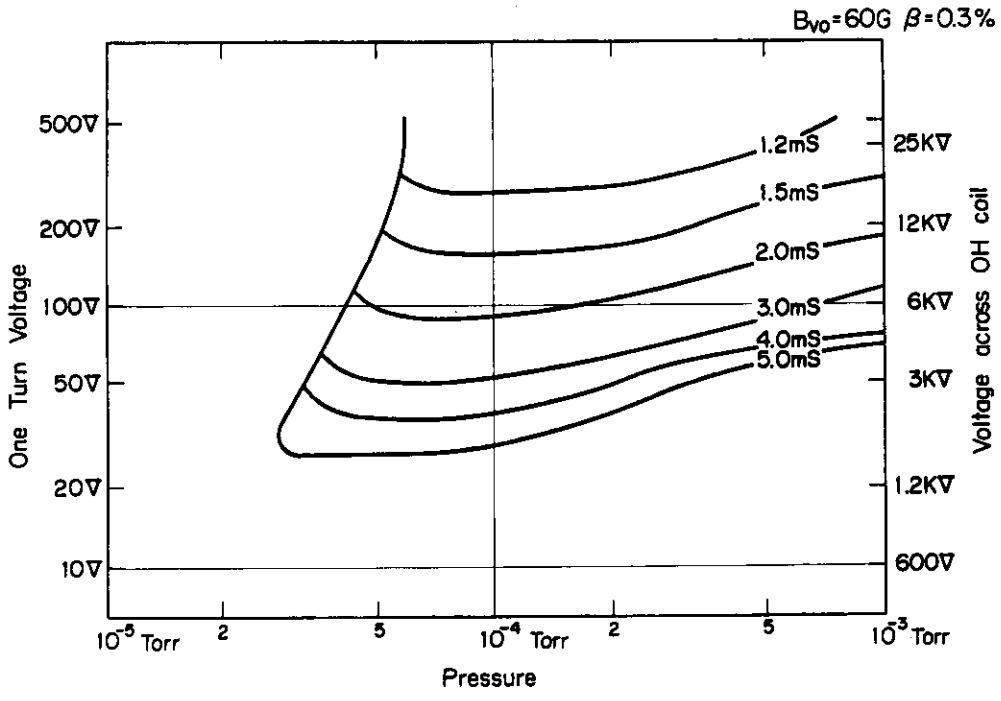

Fig.VIII.4.3-5 Possible breakdown region of JT-60.

Table VIII.4.1-1 Specifications of thyristor converters

OH coil P.S.	SCR 24 pulse	92 kA	2500 V
IES1 coil P.S.	SCR 12 pulse	92 kA	880 V
IES2 coil P.S.	SCR 12 pulse	60 kA	500 V
Vertical field coil P.S.	SCR 24 pulse*	+57 kA - 6 kA	10 kV
M. Limiter coil P.S.	SCR 12 pulse	94 kA	1000 V
Q. field coil P.S.	SCR 12 pulse*	±25 kA	1800 V
Horizontal field coil	SCR 12 pulse*	±22 kA	500 V

* bi-polar

Table VIII.4.3-1 Perturbations to utility power network by operation of JT-60 power supply system

	Allowable limit	Maximum perturbation level
Frequency variation	within ± 0.05Hz	-0.045Hz ∿ +0.015Hz
Fluctuation amplitude of network system generator output	within 4 %	2.4 %
Voltage fluctuation	within ±1 %	0.22 %
Voltage waveform distortion	within 1 %	0.3 %
equivalent disturbance current	within 1.9 A	3.3 A

5. Design of Control and Diagnostic System

5.1 Review of control system design

5.1.1 Design requirements and solutions

The control system has to ensure an efficient use of JT-60 device. To attain this role, some requirements are imposed on the control system and respective solutions are taken into design consideration.

The basic requirements for the design of control system in JT-60 device are as follows:

(a) Large data capacity.
The quantity of data to be handled becomes inevitably large. Because JT-60 is a big and developmental machine, a principle is established to extract the maximum amount of data.

(b) Plasma controllability.
Though in a conventional plasma device an intention to control the plasma characteristics has been weak, it is explicit in JT-60; the control objects include plasma position and shape, plasma current and its distribution, plasma density, etc.

(c) Flexibility and future expansibility.
These requirements must be also characteristic to an experimental device such as JT-60.

(d) Reliability, maintainability and easy handling by a small number of operators.
These are common in plant control system.

The solutions which are mostly multi-purposed are as follows:

(a) Computarization.
The operational flexibility as well as the ability to handle large amount of data can be easily achieved by making use of computers. The number of different models of the computers shall be minimized to ensure the maintainability. The control system is equipped with a large computer which is one of the means to enable the control of the physical characteristics of the plasma.

(b) Centralization of functions.
This ensures operatability by a small number of operaters. Data

including physical ones are centralized to enable the direct control of plasma characteristics. The physical data are also used in the protection of the machine triggering interlocks; for example, insufficient plasma current can tell the failure of the discharge to enable the control system to make counterplans.

(c) Redundancy.
The computers are backed up by hard-wired circuits in order to improve the reliability.

(d) Standardization.
To ensure the maintainability, standards, such as JIS (Japanese Industrial Standards), JEM (Standards of Japanese Electromachinery Manufactures Association), ISO, CAMAC, etc. shall be adopted.

5.1.2 Structure of the control system

The control system has a hierachical structure shown in Fig. VIII.5-1. It is constituted by two levels: a central controller and facility controllers. The control system can use the large computer in the data processing system to compute the control parameters such as time variations of coil currents during the time interval between two successive shots.

The computers in the control system are classified as shown in Fig. VIII.5-1. The computers I are for the total system of JT-60 device and the computers II are for individual control objects. The computers a and b are for plant control and for discharge control, respectively. On the other hand the computers c are for other purposes.

The central controller consists of central consoles and several minicomputer CPU's backed up by hard-wired circuits as shown in Fig. VIII.5-1. The consoles are equipped with CRT displays directly connected to the computers. The computer system Ia is for total plant control. Its function includes control for plant, monitoring and data logging and man-machine communication. The computer system Ib is for discharge control. Its function includes event-oriented sequential control. The computer system IIb is for real time feedback control of discharge. Its objects are the poloidal field coil power supplies and the gas injection system. The safety and protection system and the timing system are made of hard-wired circuitaries. However, the preshot check and failure diagnosis are carried out with the computer system Ic.

The facility controllers consist of eight sub-consoles, local consoles and the computer systems IIa. The controllers have their respective object facilities: coil power supplies, vacuum pumping system, gas injection system, movable limiter, neutral beam injection system, etc. The subconsoles consist of control desks and panels. The computer systems IIa, mini- or micro-computers, are connected with the computers of central controller throught CAMAC interfaces as shown in Fig. VIII.5-2. Control for local testing and maintenance can be accomplished in the facility controllers independently of the central controller.

The data from facilities are treated with the computer systems IIa. On the other hand, the plasma data are treated with the computer systems Ib, IIb and data processing system. The computer system Ib processes the data which are used for the event-oriented sequential control and protection and the system IIb for the feedback control. The data processing system treats the data from plasma diagnostic instruments. There are two ways for diagnostic data to flow into the control system as shown in Fig. VIII.5-2. Some diagnostics have their own crates, while others share the crates with data processing system. In both of the configuration, the control system can gather diagnostic data without any help of the data processing mini-computers in real time.

A brief description on the control room design is given in the following. The control building has two main rooms; one for consoles and panels and the other for computers. Each occupies about same area, $\sim$1000 m^2. The two rooms are shown in Fig. VIII.5-3.

The former room,control room, has master control console connected with the man-machine communication subsystem of the central controller, sub-consoles and display panels. Several CPU's of mini-computers of central controllers and a large computer for data processing are placed in the computer room.

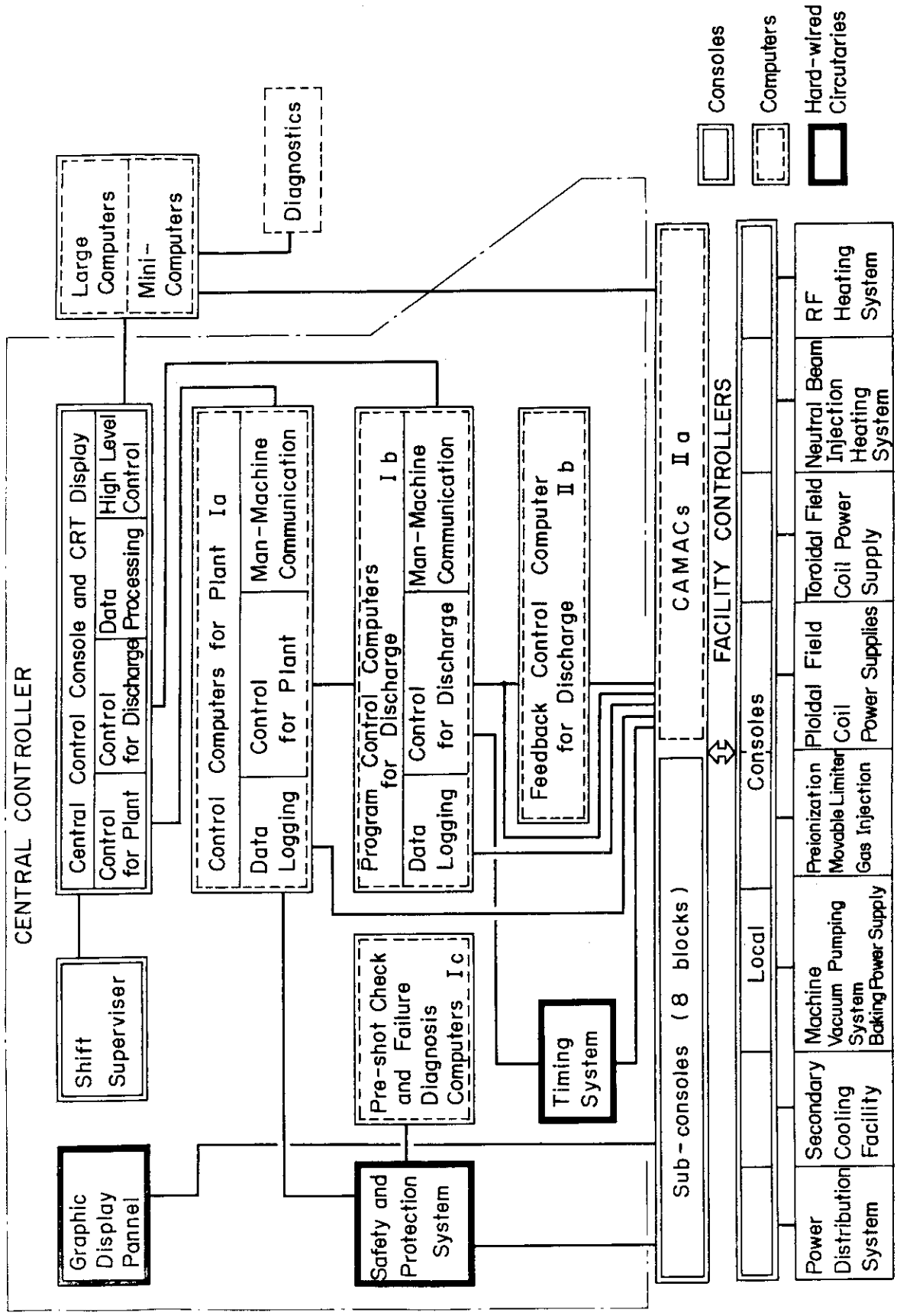

Fig.VIII.5-1 Functional block diagram of the control system in JT-60 device.

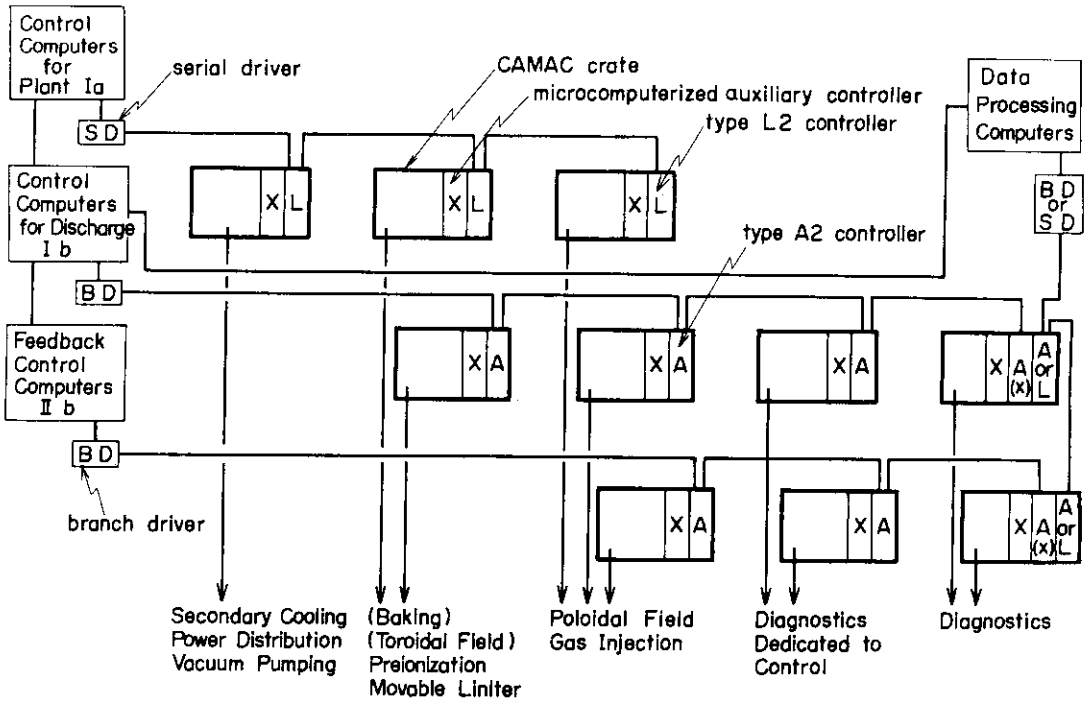

Fig.VIII.5-2 CAMAC organization in the control system.

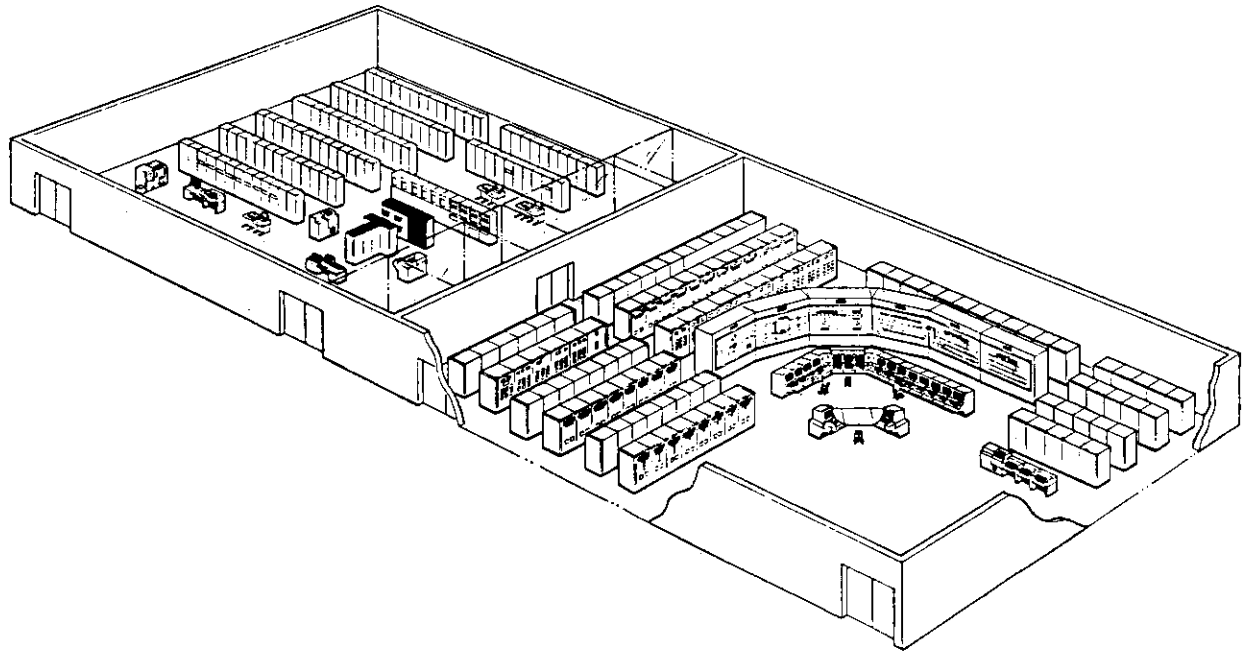

Fig.VIII.5-3 Control room.

5.2 Plasma current, position and shape control

JT-60 will have four feedback-controllable coils; air-core transformer, vertical, horizontal and quadrupole field coils to control current, horizontal position, vertical position and ellipticity of plasma, respectively[1].

5.2.1 Tokamak circuit analysis[2]

The plasma position and shape control requires the description of a tokamak system in terms of electrical circuit theory or automatic control theory. The concept of tokamak circuit is developed for this purpose. In principle, a tokamak is nothing but a transformer with a secondary circuit of a plasma so that the interactions among the plasma and tokamak components are readily described by equivalent circuit equations according to the tokamak circuit concept. In the equations, magnetic interactions are expressed by inductances, which are derived from flux functions based on the MHD theory.

A computer code to solve the equations is developed which can simulate the time variations of plasma position, cross section, and currents in the plasma column and tokamak components taking account of the performance of the feedback control system.

5.2.2 Optimal feedback control of plasma current, position and shape[3]

JT-60 will have at least five feedback control loops; in addition to four loops for plasma current, positions and shape, the feedback control loop for plasma density control will be also equipped. It is known that difficulties arise in such a multiple-loop feedback control system from interactive effects; the action of one feedback loop affects the action of the others. The interaction is normally such that the stability margins of system operation are reduced, and it is desirable to design multiple-loop systems in such a way to avoid interactive effects which are prejudicial to system stability.

One solution for the interaction problem is use of the optimal control theory. The physical requirements and constraints of the plasma current and position are formalized in the standard description of the optimal theory; state equations, output equations and cost function. The state equations, which are a set of linear ordinary differential equations, are derived from circuit equations and the equation of plasma motion. The output equations are derived from the magnetic probe signals which are functions of plasma

current, position and magnetic field. The cost function penalized both the departure of the plasma current, position and shape from desired values, and use of input energy by quadratic forms. Once the standard description is given, the optimal theory readily afford the details of the control system design.

References

(1) Suzuki, Y., Ogata, A., Ninomiya, H., Nakagawa, S., Tsuzuki, N. and Yamagishi,T.: Proc. Symp. Engng. Problems Fusion Research (Oak Ridge, Tenn., 1977) vol.1, 112.

(2) Suzuki, Y., Ninomiya, H., Ogata, A., Kameari, A. and Aikawa, H.: Jap. J. Appl. Phys. 16 (1977) 2237.

(3) Ogata, A., Ninomiya, H. and Suzuki, Y.: JAERI-M 7126 (1977).

5.3 Eddy current analysis

Eddy currents induced in tokamak components due to plasma motion and change of poloidal field coil currents play an important role in control of the plasma position and shape. The field due to these eddy currents modifies the original magnetic field distribution and affects the plasma equilibrium especially in the current build-up and shut-down phases. The eddy current flowing in the vacuum vessel along the toroidal direction reduces the ohmic heating voltage applied on the plasma. Furthermore, the interaction between the eddy current and the magnetic field exerts large stress on the vacuum vessel. Thus, the accurate estimation of eddy currents is important in the design study of large scale tokamak devices.

5.3.1 Finite element circuit method analysis

As the eddy current density is divergence-free, we can introduce the current potential to solve the eddy current problem on a thin conductor of any shape. We have adopted two methods to obtain the equation which govern the time variation of the current potential.

In the first method, the equation of the current potential is obtained from Maxwell's equation and Ohm's law[1]. Using the difference method, we obtain a matrix equation among the coefficients which can be solved with the Lunge-Kutta method.

The second method extends the first method applicable to a more general case. A thin conductor of any shape is subdivided into finite elements on

each of which a current potential is defined[2],[3]. Each element is regarded to compose a electric circuit and is coupled each other through mutual inductance and resistance matrices. These matrices can be obtained from the integral calculations of the magnetic energy and Joule loss. A set of circuit equations which govern the time variation of the eddy current is formulated with these matrices and solved by the eigenvalue analysis.

Eddy currents in the vacuum vessel and upper and lower supports are calculated in current build-up and shut-down phases and during the spike phenomenon of discharge. The error fields by the eddy current are evaluated in the domain occupied by the plasma.

5.3.2 Three-dimensional finite element method analysis[4],[5]

We can solve the eddy current problem in an isolated component of a tokamak using the finite element circuit method in so far as the thin plate approximation is applicable. However, actual tokamak has many components of thick conductors such as toroidal field coils. Furthermore, eddy currents induced in components interact each other. To treat the eddy currents in many thick components simultaneously, three-dimensional finite element method is developed.

To solve electromagnetic equations, its energy functional is derived. The solutions of electromagnetic equations are obtained by the functional minimization. The pentahedron element is selected as the finite element and the vector and scalar potentials in it are assumed as linear functions of the local cylindrical coordinates of vertices.

Vector and scalar potentials, vertical magnetic fields and induced eddy currents are calculated using the method, where coils, vacuum vessel and plasma are taken into account and shapes of some components are simplified to make the analysis easy. In spite of these simplication, dimension and half width of the global matrix are 8000 $\sim$ 10000 and 400 $\sim$ 600, respectively, which we believe are one of the largest ever treated by digital computers.

The solutions obtained from the method are compared with the experimental data of the model apparatus of JT-60. Size of the model is 1/13 of JT-60. The structure of the model apparatus is simplified but reflects the structure of JT-60 well. The results obtained from the three-dimensional finite element method are in good agreement with those obtained from the experiment.

References

(1) Takahashi, T., Takahashi, G., Kazawa, Y. and Suzuki, Y.: Proc. 7th Symp. Engng. Problems Fusion Research (Oak Ridge, Tenn., 1977) vol.2, 1393.
(2) Kameari, A. and Suzuki, Y.: JAERI-M 7120 (1977).
(3) Kameari, A. and Suzuki, Y.: Proc. 7th Symp. Engng. Problems Fusion Research (Oak Ridge, Tenn,, 1977) vol.2, 1386.
(4) Ninomiya, H., Ogata, A., Tanabe, Y., Sawada, Y., Yamamoto, K. and Yamaguchi, M.: to be submitted in the 10th Symposium on Fusion Technology.
(5) Takano, I. and Suzuki, Y.: JAERI-M 7062 (1977).

5.4 Planning of diagnostic system

The diagnostics plans of JT-60 project were made along with the design of the main machine[1]. In order to obtain the optimum performance of the whole diagnostic system in JT-60, a conceptual design of an interface between the data processing system and the each measuring apparatus was firstly studied. CAMAC interface will be used for the standard interface of diagnostic system. Some conceptual designs of measuring apparatus have also been studied in this period.

5.4.1 Interferometric and scattering measurements

Interferometric diagnostic system is composed of microwave interferometers and submillimeter wave interferometers. Some results obtained from the conceptual designs of the 4 mm and the 2 mm microwave interferometers are as follows:

(1) A block diagram of microwave interferometer is shown in Fig. VIII.5.4-1. The modulation unit is set at the intermediate frequency (IF) stage, in order to obtain high resolution power.
(2) The wave guide should be inserted into the observing port to minimize the transmission loss.
(3) A microwave reflector, which will be set on the magnetic limiter plate, is designed for the measurement of the electron density in the magnetic limiter region by the reflecting method.

Submillimeter wave interferometer is planned to measure electron density in the central region[2]. Considering a bending effect of the probing beam and a vibration of the measuring apparatus, we have selected

the cyanogen (HCN) laser and the methyl alcohol (CH_3OH) laser, of which the oscillating wavelengths are 337 μm and 119 μm, respectively. The sub-millimeter interferometer must be taken on the adoption of the modulation method for real time measurement. The modulation frequency is expected to be 1 MHz and more.

Thomson scattering apparatus can be used to measure electron temperature, electron density, ion temperature and effective ionic charge. The measuring apparatus for tomporal and radial behavior of electron temperature and density should be composed of a multi-pulse visible laser, a optical fiber array and a 2-dimensional photo-electric detector. The multi-pulse visible lasers have been studied with ruby laser (6943 Å), YAG-glass laser (10600 Å) and second harmonic YAG-glass laser (5300 Å). The laser system may emit more than 10 light pulses in series. We have planned to adopt intensified charge coupled device (ICCD) or photo detector array as the 2-dimensional photo-electric detector. The special merit to adopt the above detectors is that they have the performances of high speed readout and quantum detection limit.

The scattering apparatus for ion temperature and effective ionic charge is planned to be composed of a high power far-infrared (FIR) laser and a heterodyne detector[3]. These components are vigorously developed at MIT[4] and UCLA[5]. The most probable type of the FIR laser or the detector is to be chosen according to the situations of the developments.

5.4.3 Spectroscopic measurement

Spectroscopic measuring systems are planned to obtain informations of neutral atoms and low-Z and high-Z impulities in the JT-60 plasma. The spectroscopic systems designed conceptually are as follows:

(1) The visible spectroscopic systems are used to diagnose the plasma with the aid of measuring the electron temperature T_e of less than 100 eV in the peripheral and the magnetic limiter regions.

(2) The vacuum ultra-violet (VUV) spectroscopic systems are used to diagnose the plasma of 100 eV$<T_e<$1 keV in the intermediate region.

(3) The ultra soft X-ray (USX) spectroscopic systems are used to diagnose the plasma of $T_e>$1 keV in the central hot-core region.

The physical quantities measured with these spectroscopic systems are summarized in Table VIII.5.4-1.

The conceptual constitution of these systems is shown in Fig. VIII.5.4-2. The system is composed of the spectrometer part, the detector part and the operating part (remote control and data acquisition). Spectroscopic measurements are mainly made on the vertical access port or the oblique access port. In order to obtain intensities of many spectral lines during a single discharge, we have to employ a 2-dimensional detector such as the multi-channel plate or the image dissector tube. Furthermore, the time-resolved doppler profiles for one spectral line can be obtained by using the same detector.

In the present conceptual designs of the spectroscopic systems, there are some problems as follows:

(1) The multi-channel plate and the image dissector tube are not yet use as the detector of the VUV or the USX spectrometer. Therefore, the reliability tests should be intensely made here after.

(2) Spatial distribution of the intensities of the spectral lines in the VUV and the USX range can not be measured with the planned systems during a single discharge.

(3) Crystal spectrometers must be developed to measure radiation intensities and doppler profiles of metal impurities with a good signal to noise ratio.

5.4.3 X-ray and particle measurements

(A) X-ray measurement

The measurement of X-rays radiated from hot plasmas, in which electron temperatures are above about one kiloelectronvolt, is one of the most important methods for obtaining the basic parameters of plasmas. Conceptual designs of some measuring systems obtained up to now are as follows:

(1) Soft X-ray pulse height analysis

Measurements on the continuum and line spectra of soft X-ray enable us to obtain electron temperatures and metal impurity concentrations, respectively. Two systems are prepared for soft X-ray pulse height analysis. One is for vertical access ports and the other for oblique access ports, through which radial distributions of electron temperatures can be measured as shown in Fig. VIII.5.4-3.

Intrinsic germanium (Ge(I)) detectors cooled by liquid N_2 are used in the both systems covering a wide energy region from 1 to 200 keV.

Their energy and time resolutions required are about 200 eV FWHM (at 5.9 keV) and 20 nsec or less, respectively.

A high counting rate pulse height analysing (PHA) system whose average counting rate is above 100 fold for the conventional one is planned to be adopted, and then the following advantages are expected:

a) As the statistical errors would become small, complete X-ray spectra can be obtained in one shot of discharge.
b) Time resolution of measurements is high.
c) The dead time can be practically neglected.
d) Though X-ray fluxes emitted from JT-60 plasmas may be very high, the design of collimators can become easy.

Figure VIII.5.4-4 shows a block diagram of the high counting rate PHA system, which is a multi-discrimination type with 100 channel scalers according to CAMAC standard. The accuracy of discriminators required is less than 0.1 %.

(2) Soft X-ray detectors

A hot column and internal modes of fluctuations of plasmas should be obtained from the measurement of the spatial distribution of soft X-ray fluxes. An array of soft X-ray detectors, such as SSD (silicon surface-barrier detectors) or PIN diodes, is installed in an oblique access port as shown in Fig. VIII.5.4-3. The detectable energy range of X-rays is from 0.5 to 20 keV and absorber foils can be used to adjust the energy range.

(3) Hard X-ray detectors

Measurements on the hard X-ray spectra enable us to get some informations on runaway electrons. Two systems are prepared for measurements in the region of main plasma and in the region of magnetic limiter. Plastic scintillators or liquid scintillators may be used covering the required energy region from 0.1 to 20 MeV. The time resolution required would be less than 10 nsec. The high counting rate PHA system can also be used in the spectrum analysis.

(B) Neutron measurement

The measurement of thermonuclear neutrons is one of the most useful methods for obtaining ion temperatures of JT-60 plasmas. The separation of thermonuclear neutrons from those produced by the γ-n reaction is required for obtaining ion temperatures exactly.

The use of He^3 spectrometers and liquid scintillators is being investigated for the measurement on neutron spectra ranging from 1 to 15 MeV emitted from JT-60 plasmas. The energy and time resolutions required are 0.1 MeV FWHM or less (at 3.2 MeV) and 50 nsec or less, respectively.

Neutron counters are prepared for the measurement of the amount of neutrons. B^{10} counters and U^{235} fission chambers may be used for the total neutron monitoring. LiF scintillation counters may be used for 14.1 MeV (D-T) neutrons. In order to monitor the amount of 2.45 MeV (D-D) neutrons, however, it is necessary to use the results from the neutron spectrometer.

(C) Neutral particle measurement

The energy distribution analysis of neutrals emitted from JT-60 plasmas is important for measuring charge exchange losses in order to understand particle and energy balances of plasma. Moreover, it can be used for studying the slowing down process of high energy neutrals in case of neutral beam injection heating. Some measuring systems classified into two groups are as follows:

(1) Charge exchange neutral particle analysers

Two types of analysers may be prepared; one is for energy analysis of neutrals and the other for their mass and energy analysis.

The neutral particle energy analyser is composed of a charge stripping cell and 45° parallel-plate electrostatic analyser with 10 channel ion detectors (as an example, Ceratron). The analysing energy range of protons and the energy resolution required are from 0.1 to 75 keV and from 5 % (at channel 10) to 25 % (at channel 1), respectively.

The neutral particle mass and energy analyser is composed of a charge stripping cell, a magnetic momentum analyser, 6 channel cylindrical electrostatic analysers and ion detectors. In order to obtain complete mass and energy spectra of protons and deutrons with energy from 0.1 to 75 keV in a single discharge, the coil current in the analysing magnet and the applied voltage in the electrostatic analyser must be swept.

(2) High energy neutral particle detectors

Silicon surface-barrier detectors (SSD) may be used for detecting high energy neutral particles. Energy spectra of neutrals may be obtained by means of pulse height analysis. The detectable energy range and energy resolution of SSD's required are from 5 to 75 keV and 10 %, respectively.

The array of SSD's installed in an oblique access port as shown in Fig. VIII.5.4-3 are planned to be used for measuring the spatial distribution of fluxes and energy spectra of hydrogen atoms. As X-rays are also emitted from plasmas, it is important to separate neutral signals from X-ray ones. A mass and energy analysing system with SSD's is also prepared for the measurement in case of D^0 beam injection.

5.4.4 Boundary layer and wall surface analyses

In the plasma monitoring and boundary layer diagnostic systems, electromagnetic sensors, bolometers, infrared TV, visible TV, gas sensors, a movable probe, and a compact visible spectromator are planned to be prepared to obtain the basic plasma parameters, and to observe the behavior of the boundary plasma.

As electromagnetic sensors, there are two kinds of magnetic probes (one is named T-probe for measuring the tangential poloidal field, the other is named N-probe for measuring the normal one, Rogowski coil for measuring a plasma current, one-turn loops for measuring one turn voltage, diamagnetic loops for measuring plasma pressure, and thermocouples for measuring the temperature at fixed limiters, liners, and magnetic limiter plates. In our apparatus, it is indispensable to set them inside the vacuum chamber to suppress the time delay of the signals from the sensors due to the induced currents on the vacuum chamber. So, we consider to set them in the space between the vacuum chamber and the liners. Then, we must take into account the effect of the high temperature of the vacuum chamber ($\leq$650°C), the high vacuum conditions, and the high electric voltage insulation. Moreover, it is necessary to make the thickness of the metal surface of the probes as thin as possible, to obtain fast responses from the sensors.

In order to overcome these severe conditions, we have performed the research and development by manufacturing the electromagnetic sensors for trial. The investigations of the other sensors (bolometers, TV, gas sensors, etc.) are now under way, and the design of these sensors are roughly determined at the present. As a result of the above investigation the movable proble is found to be expected to serve for a wide and flexible use by exchanging a sensor head of the probe.

A conceptual design of the surface monitoring system, which can contribute to study plasma-wall interaction, to monitor vacuum condition and to inspect surface erosion, was also made in this period.

Basic feature of the system is similar to conventional system (e.g. QWASS in IPP, SAS in PPPL); a sample/substrate is exposed to plasma at the surface of the first wall and then carried to an analyzing chamber. A schematic diagram is shown in Fig. VIII.5.4-5. The chamber will be equipped with mainly AES, SIMS and SEM. A carrier system is under consideration at present, in order to transfer the sample/substrate. The carrier has a motor drive mechanism, and can move along the guide rails. It would also have a capability of the measurement of the temporal variation.

In addition to the method mentioned above, two other diagnostic methods are recommended. The one is a more direct way to monitor the wall surface condition; the analyzing head (AES, SEM) is inserted into the observing port by using manipulator during the plasma interval and observe the actual wall surface. Another is a method using electromagnetic wave; atomic fluorescence spectroscopy, resonant scattering (like KFA), change of reflection coefficient, infrared absorption spectroscopy, etc.. Consideration of these methods is under way, at present.

5.4.5 Data processing system

Because JT-60 is an expensive machine, we have to derive experimental information as much as possible from a single shot, and store and value it. A suitable data processing system has to be chosen for this purpose. Some design requirements are as follows:

(1) The data processing system has to process and display the experimental results immediately after a shot, and enable the operators to feed them back to the control of the next shot. For this purpose, the system has to be able to perform the calculations which have been carried out by an off-line large computer for the tokamak experiments at present.

(2) The system has to store all the data and display them occasionally according to the operator's request. In some sense, it has to be able to reproduce a shot by itself.

(3) It is a matter of course that every portion of the system has to function organically with each other. In addition, it is also required that the portions which directly interface the diagnostic devices can be separated from the main system in the stages of development and test of the diagnostic devices.

(4) There are also requirements which are not characteristic to our system; i.e., future expansibility, maintainability, reliability, flexibility, etc.

The system has a hierarchical structure of large-, mini- and micro-computers as shown in Fig. VIII.5.4-6. The micro-computers are housed in the auxiliary controller modules of CAMAC crates. They control the diagnostic devices and gather data from them during a shot. Only the micro-computers have active functions during a shot for data acquisition, while the mini- and the large-computers function during the interval between two successive shots.

The mini-computers control CAMAC crates via either serial or parallel highways. Self-consistent calculations for the data reduction are also carried out in the mini-computers, while the process data from different mini-computers are carried out in the large-computer.

The performances of the large computer under consideration is comparable with that of IBM 3031. It will be used besides processing experimental data, to carry out calculations to specify control parameters using the modern control theory. It is equipped with data memory of large capacity (10 GB) and small access time (1 min) so that the operator can compare the fresh experimental data with the old ones occasionally.

The CAMAC standardization is made at the lowest, micro-computer level as shown in Fig. VIII.5.4-6. Each diagnostic device has a least a pair of CAMAC crates: one for the diagnostic room and the other for the torus hall. The crate at the diagnostic room interfaces operators, while the one at the torus room interfaces the diagnostic device. Though the pair is a part of the whole system, it can constitute a stand-alone system to develop and test the diagnostic device. In the stand-alone configuration, the micro-computer controls the crate pair. Peripheral devices of a minimum requirement can be connected via a GPIB interface module to the crate at the diagnostic room for this configuration.

There are two routes connecting the data processing system and the control system. One route connects the large-computer and the program control computers. This route is used in the shot interval. The other connects CAMACs and the feedback control computer. This is used during the shot.

The data processing system will take care of all the data produced by the diagnostic devices, but the present design is offered mainly for the

standard diagnostics, excluding some new diagnostics such as heavy ion beam method, CO_2 laser scattering, Zeeman splitting, etc.. A rough estimation of data amount is given in Table VIII.5.4-2.

Figure VIII.5.4-7 gives the logical sequences to derive the plasma parameters. The "AND" symbol shows that the parameter is derived as a function of plural primary parameters, while the "OR" symbol shows the parameter is obtainable independently from one of the preceding parameters. This diagram is useful to specify job scheduling of computers and to estimate error transfer.

References

(1) Matoba, T., Suzuki, Y., Funahashi, A. and Itagaki, T.: JAERI-M 7220 (1977).

(2) Itagaki, T., Matoba, T., Funahashi, A. and Suzuki, Y.: JAERI-M 7121 (1977) (in Japanese).

(3) Itagaki, T., Matoba, T., Funahashi, A. and Suzuki, Y.: JAERI-M 7295 (1977) (in Japanese).

(4) Woskoboinibow, P., Mulligan, W. and Cohn, D.R.: Bulletin Am. Phys. Soc. 22 (1977) 1175.

(5) Semet, A. and Luhmann, N.C. Jr.: Appl. Phys. Lett. 28 (1976) 659.

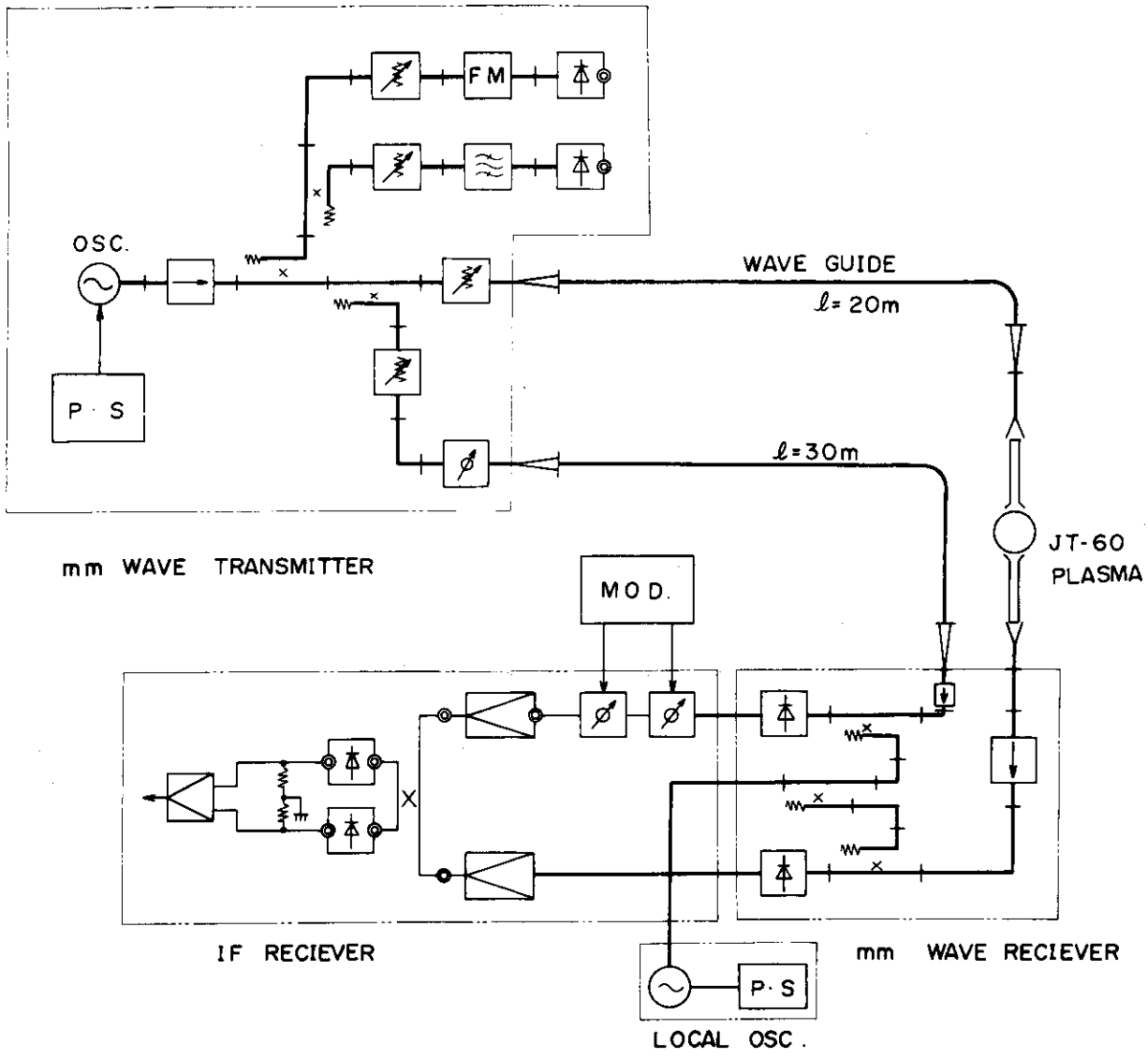

Fig.VIII.5.4-1 Conceptual block diagram of mm microwave interferometer.

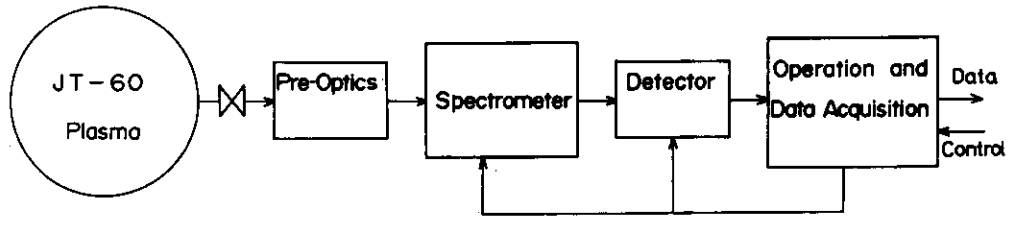

Fig.VIII.5.4-2 Basic block diagram of measuring apparatus in spectroscopy.

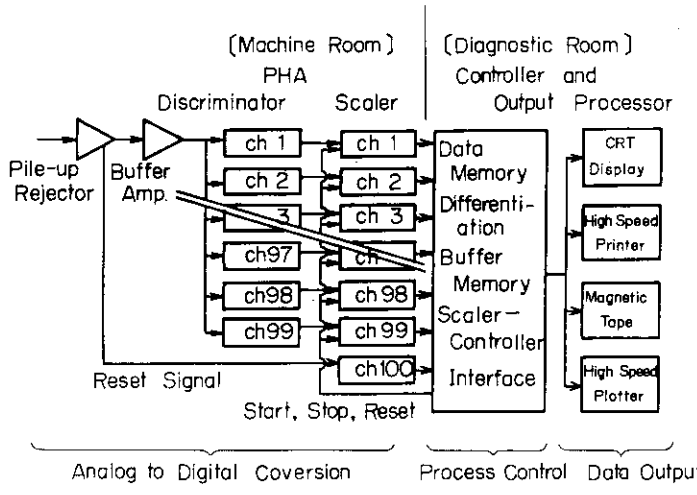

Fig.VIII.5.4-3 Schematic drawing of multi director system in soft X-ray and neutral particle measurements.

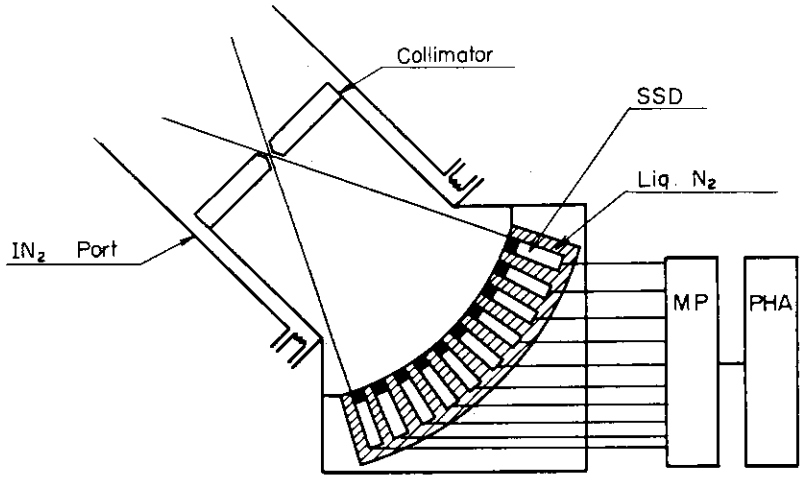

Fig.VIII.5.4-4 Conceptual block diagram of high counting rate pulse hight analyzer.

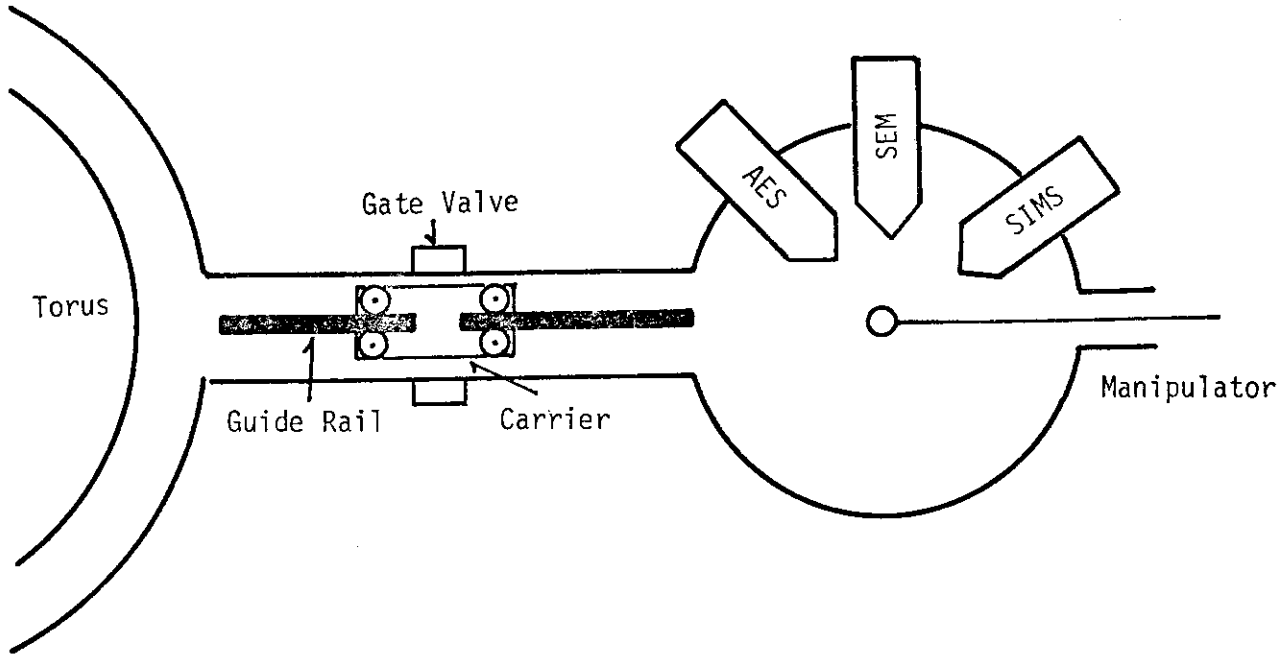

Fig.VIII.5.4-5 Schematic diagram of surface monitoring system of JT-60.

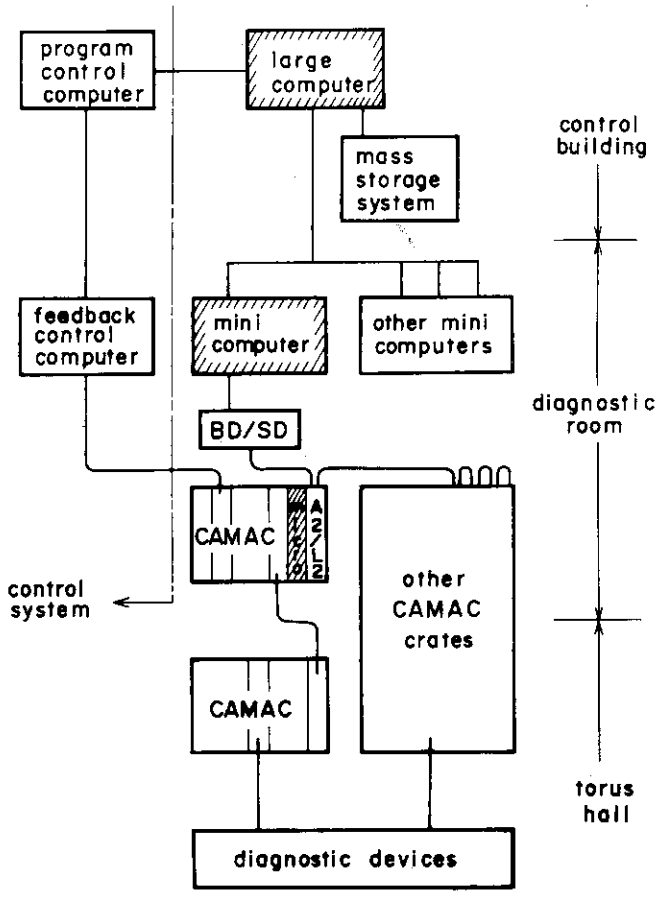

Fig.VIII.5.4-6 Constituting of data processing system. Connections between control system is also shown. The computers are hatched. The areas where the data processing devices are placed are given at the right hand side.

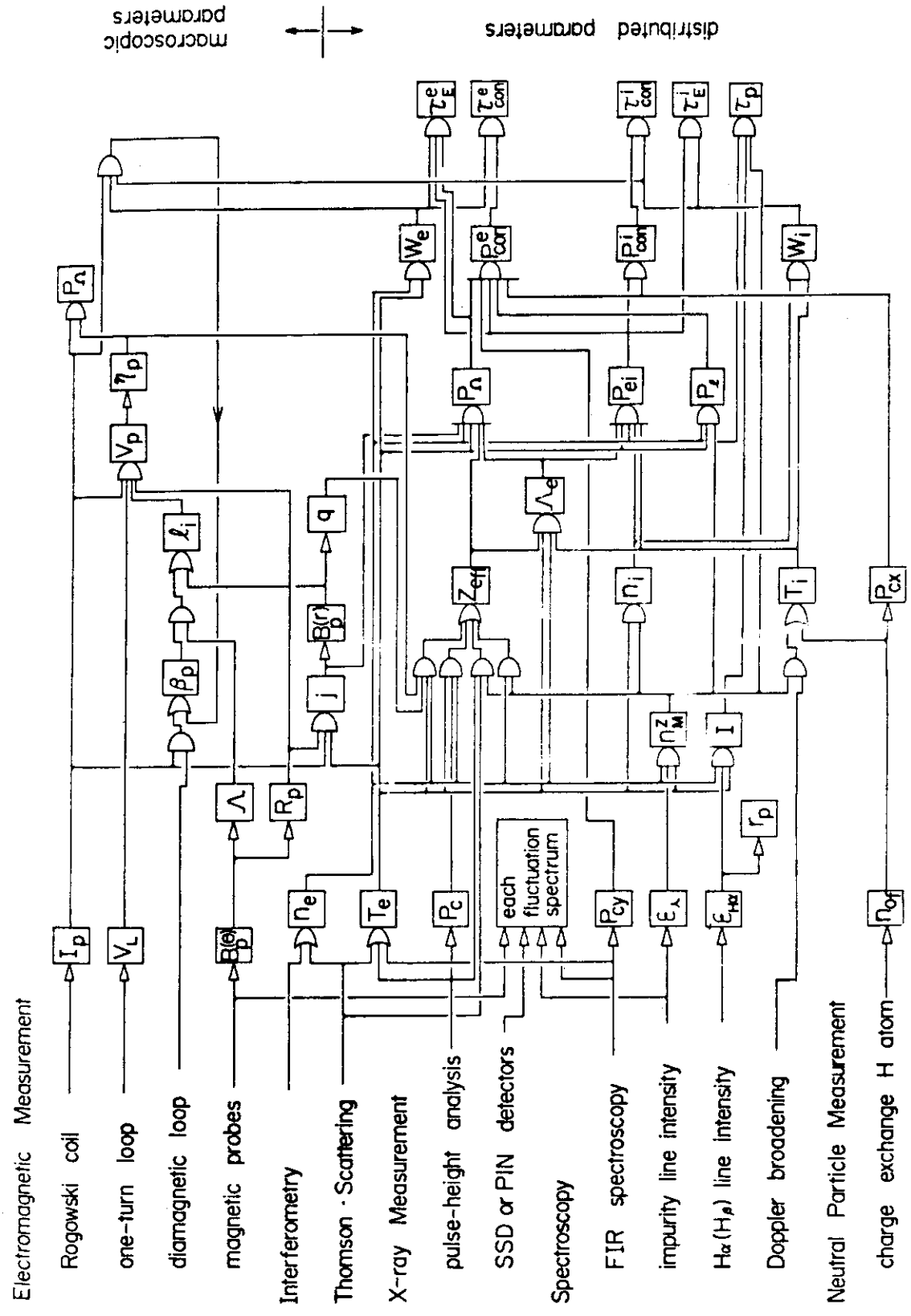

Fig.VIII.5.4-7 Logical sequence diagram for plasma parameter derivations.

Table VIII.5.4-1 Physical quantities to be measured by spectroscopic method

	Measured Physical Quantities
Visible Spectroscopic System	I) Neutral Atom Density of a Working Gas II) Content of Low-Z Impurities in a Peripheral and Magnetic Divertor Regions III) Doppler Temperature of Low-Z Impurity Ions or Neutral Atoms
VUV Spectroscopic System	IV) Content of Low-Z Impurities V) Radiation Loss from Low-Z Impurities VI) Doppler Temperature of Low-Z Impurity Ions VII) Monitor of Metal (High-Z) Impurities
USX Spectroscopic System	VIII) Content of Metal (High-Z) Impurities IX) Radiation Loss from Metal (High-Z) Impurities X) Doppler Temperature of Metal (High-Z) Impurity Ions

Table VIII.5.4-2 Data amount

interferometory	196	kw/shot
Thomson scattering	3.6	
spectroscopy	850	
X-ray, neutron, particle measurement	324	
electromagnetic measurement	359	
total	1723.6	kw/shot

6. Design of Auxiliary Systems

6.1 Review of auxiliary system design

In the fiscal year 1975-7 the design of vacuum pumping system, secondary cooling system, and power distribution system were made by industry as part of the detailed design of JT-60. The design studies of gas supply and preionization systems were also made. During the past year the design was reexamined and some modifications were incorporated into the design.

6.1.1 Vacuum pumping system

The vacuum pumping system of JT-60 is to provide ultrahigh vacuum in the vacuum vessel and help produce clean surfaces at the first wall (limiters and liners). It also should have a pumping capability large enough to evacuate the vacuum vessel in an interval between discharges.

The system consists of the following major subsystems:

Pump subsystem (main pumps, auxiliary pumps, roughing pumps, and maintenance pumps),
Compressor subsystem,
Cooling subsystem,
Liquid nitrogen supply subsystem,
Nitrogen gas inlet subsystem, and
Control and measurement subsystems.

The main pumps are turbomolecular pumps and have a net total pumping speed of 14,000 ℓ/sec (N_2). The vacuum pumping system consists of two identical sets each connected to a pumping port of vacuum vessel.

6.1.2 Secondary cooling system

The secondary cooling system is to remove and dissipate heat generated in each system of JT-60 transferred through its heat exchanger. Major components of the system are a cooling tower, water pumps and pipes, and water processing units.

The design was made under the following conditions; maximum wet thermometer temperature 26.5°C, maximum temperature of supply water 30°C, and maximum allowable water supply 150 m^3/hr. Some of the characteristic values of the system is summarized below:

Total circulation of water	8,800 m^3/hr
Inlet temperature at exchanger	33°C
Outlet temperature at exchanger	39°C
Cycle number	4
Total water supply	110 m^3/hr
Average heat removed	5.2×10^7 kcal/hr

6.1.3 Power distribution system

The power distribution system receives electric power from the central power station and distributes the power directly to the toroidal and the poloidal field coil power supply and through power distribution subsystems to the vacuum pumping, secondary cooling, and other systems and to the buildings. The distributed power is as follows:

1. Toroidal field coil power supply:
   - to motor-generator 25 MVA
   - to the coil directly 180 MVA
2. Poloidal field coil power supply:
   - to motor-generator 20 MVA
3. Supplementary heating power supply:
   - to motor-generator 20 MVA
4. Operation distribution subsystem: 25 MVA
5. Buklding distribution subsystem: 30 MVA

6.1.4 Gas supply system

The system serves for the purpose of injecting gases (H_2, D_2, He, Ne, O_2 and Ar) into the vacuum vessel. It can be classified into five supply subsystems, one continuous and four pulsed. The latter four are used respectively for initial filling of the vessel, for density control, for terminating discharges and for impurity injection.

Specifications of the system are summarized below:

1. Continuous gas supply subsystem
   - Vacuum vessel pressure for discharges 1×10^{-5}-1×10^{-2} torr
   - Vacuum vessel pressure for the oxidation-deoxidation process 0.1-2.75 torr, for H_2 and O_2

2. Pulsed gas supply subsystem for initial filling

Vacuum vessel pressure for discharges	5×10^{-5}-5×10^{-4} torr
Supply duration	10 msec

3. Pulsed gas supply subsystem for density control

Supply rate	0.5-500 torr.l/sec
Control response duration	10 msec

4. Pulsed gas supply subsystem for terminating discharges

Supply	50-350 torr.l
Supply duration	0.1-0.5 sec

5. Pulsed gas supply subsystem for impurity injection

Supply rate	0.5-10 torr.l/sec
Supply duration	10 msec-10 sec

6.1.5 Preionization system

The system aims at producing a weakly-ionized plasma in a gas filled in the vacuum vessel before the initiation of a discharge.

Four type of preionization methods are considered. They are those using an electron gun, a J×B plasma gun, a radio frequency power supply, and a power supply at electron cyclotron resonance frequency.

Specifications of system is summarized below:

1. An electron gun

Filaments current		45 A
Emission current		0.5 A

2. A J × B plasma gun

Power supply	capacitor	100 μF
	charge voltage	10 KV

3. A radio frequency power supply

Frequency		1 MHz
Power	continuous	300 KW
	pulse (20 msec)	1.2 MW

4. A power supply at electron cyclotron resonance frequency

Frequency	maximum	35 GHz*
Power	pulse (5 msec)	10 KW

* A power supply at 130 GHz is also considered depending on its availability.

7. Studies on Plasma Physics and Elementary Processes Relevant to JT-60 Program

7.1 Studies related to particle and energy balances

7.1.1 Simulation by a fixed distribution code

One-dimensional tokamak code has been developed for recent several years, and simulated results of JT-60 plasmas were reported[1],[2]. On the otherhand a fixed distribution code is more suitable to make priliminary estimation of JT-60 plasmas by various scaling laws. This code calculates the time development of the space-averaged plasma parameters such as density and temperature, fixing their spatial profiles (in the calculations, parabolic distribution is assumed). Assuming a cylindrical hydrogen plasma, basic equations are

$$\frac{d\bar{n}}{dt} = \frac{1}{V}\left(-\Gamma^* + S + S_B\right) \tag{1}$$

$$\frac{3}{2}\frac{d\bar{n}\kappa\bar{T}_e}{dt} = \frac{1}{V}\left(-\Gamma^*_{xi} - \Gamma^*_{ce} + P_{Be} - P_{ei} + P_j - P_i\right) \tag{2}$$

$$= -\frac{\frac{3}{2}n\kappa\bar{T}_e}{(\tau_E)_e} + \frac{1}{V}\left(P_{Be} - P_{ei} + P_j\right) \tag{2}$$

$$\frac{3}{2}\frac{d\bar{n}\kappa\bar{T}_i}{dt} = \frac{1}{V}\left(-\Gamma^*_{xi} - \Gamma^*_{ci} + P_{Bi} + P_{ei} - P_{cx}\right) \tag{3}$$

where electron and ion densities are the same when the impurity content is low enough, i.e. $n_e = n_i = n$. T_e and T_i are electron and ion temperatures, respectively. Each term on the right hand side of Eq. (1) represents particle flow due to diffusion, particle sources by ionization of recycling neutrals and injected energetic neutrals. First to fourth terms on the right hand sides of Eqs. (2) and (3) represent energy losses due to conduction and convection, additional heating input by NBI (energetic neutral beam injection), collisional energy transfer between ions and electrons. P_j: joule input power, and P_{cx}: charge exchange loss. We consider molybdenum impurities and the energy loss per unit volume due to those is given approximately[3] as $P_i = 3.2 \times 10^{-36}\, C_{Mo}\bar{n}^{\,2}M^2$ (W/m^3), where C_{Mo} and M are impurity content in percent and atomic mass number, respectively.

The asterisk represents that we estimate particle or energy flow on a certain magnetic flux surface at $r^* = \frac{2}{3}a$. Where V and a are plasma volume and minor radius, respectively. Abovementioned particle and energy sources,

and losses are the ones integrating their calculated spatial distribution over the plasma volume.

Following three scaling laws are considered in the calculation

Case 1) trapped particle instability scaling[4]

Case 2) ALCATOR scaling which has been improved in JFT-2[5] and 2a[6] by reducing the impurity content; $(\tau_E)_e = 5 \times 10^{-21} \sqrt{q}\bar{n}a^2$

Case 3) empirical anomalous coefficients of diffusion and electron thermal conductivity; $D = 400(D)_{classical}$, $\chi_e = 1000(\chi_e)_{classical}$.

Figure VIII.7.1-1 shows the results of Case 1). The mean ion temperature rises to only 3 keV even in the case of no impurity content, and after 1.2 s temperature is saturated and $n\tau_E$ increases according to density increase by NBI. The results of Case 2) have same tendency except the maximum mean ion temperature of 6.5 keV as shown in Fig. VIII.7.1-2. On the other-hand in Case 3), temperature and $n\tau_E$ become sufficiently large (Fig. VIII.7.1-2).

These scaling laws give quite different results, but this explicitly implies uncertainty what will happen in a higher temperature. In either case, it will be made clear in comming a few years by the devices with large NBI heating such as ISX-B, PLT or DOUBLET III. At least, above-mentioned ALCATOR scaling should be improved by twice in order to achieve a break-even plasma, even if we can expect that this scaling law will be applicable in a multi-keV range.

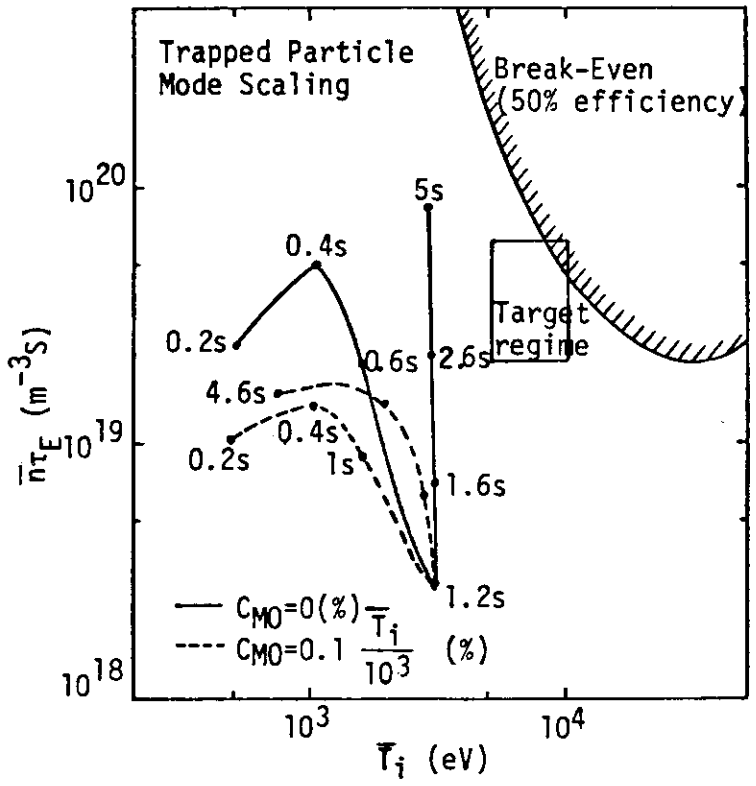

Fig.VIII.7.1-1 $\bar{n}_i\tau_E$-$\bar{T}_i$ diagram of JT-60 by trapped particle instability scaling.

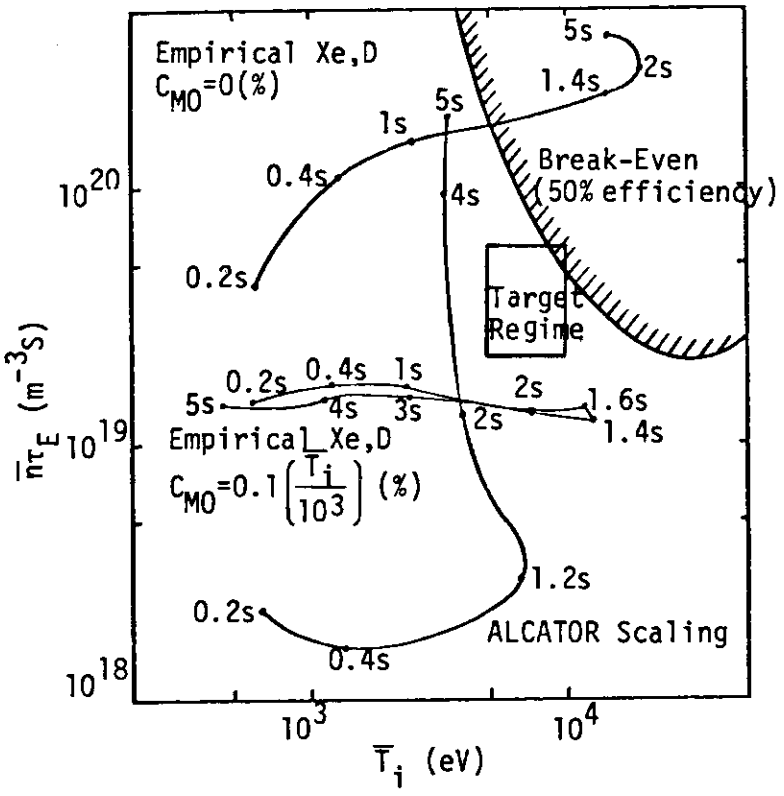

Fig.VIII.7.1-2 $\bar{n}_i\tau_E$-$\bar{T}_i$ diagram of JT-60 by empirical anomalous transport and ALCATOR scaling.

7.2 Experimental studies of surface-related problems

7.2.1 In-situ coating of molybdenum by coaxial magnetron sputter method

The major production mechanisms of light impurities are the particle-induced desorption and/or the thermal desorption of water and methane, etc., which are formed by the chemical reaction with incident hydrogen and surface impurities. Hence, attaining a clean surface of the first wall is a simple and useful countermeasure. In-situ coating is one of the most powerful method to attain a clean surface.

Vacuum deposition using a molybdenum filament has been investigated[7]. The weakpoint of this method is that the coating layer will exfoliate when its thickness becomes over than 10 μm. In order to form more fine grained layer, in-situ coating by sputter method[8],[9] is suitable because of its energetic sputtered atoms.

Figure VIII.7.2-1 shows a schematic drawing of the sputter device for molybdenum coating. Water-cooled magnetic coils, which produce mirror field to trapp argon plasma, are installed inside a target of a molybdenum pipe. These coils are motor-drived to avoid localized damages of the target by sputtering. Since a low pressure atmosphere is necessary to form a fine grained layer, RF discharge is more suitable than DC discharge as shown in Figs. VIII.7.2-2 and 3. Deposition rate is sufficiently large as shown in Fig. VIII.7.2-4, which is 600 Å/min near the target. Since the distance between the first wall surface and the target is 1-5 m, it will takes about 10 minutes so coat the first wall surface by 100 μm thickness.

The characteristics of the coating layer such as dependence of coating structure on substrate temperature and argon pressure, mechanical strength, resistance against evaporation and repeating heat load, etc., will be investigated in 1978-1979.

7.2.2 Surface damages due to intense hydrogen ion bombardment

Neutral beam injection is one of the useful methods for the supplemental heating of the joule heated tokamak plasma in JT-60. But, it will give rise to serious problems such as the impurity contamination and surface erosion due to sputtering, blistering and grain ejection.

Experimental investigations were performed with intense H^+ and H_2^+ ion beam about the surface damage of various materials such as polycrystalline molybdenum, singlecrystalline molybdenum, polycrystalline niobium, copper,

SUS 316 stainless steel, inconel 625 and Mo-coated hasteloy-X. Our experimental conditions are different from similar experiments by many authors compearing with their beam current densities. A pulsed ion beam was used at 25 keV energy with a dose rate of 30 60 mA/cm^2 for 100 ms. with a duty cycle of 6.7 $\sim$ 9.0 %. Experiments were performed with doses from 1 C/cm^2 to 20 C/cm^2. Experimental apparatus are shown in Ref. 10. The surface damages were mainly observed by scanning electron microscope (SEM) and photomicrographs showed the large scale surface damage greater than a grain size of about several tens of micrometers (Figs. VIII.7.2-5, 6 and 7). These surface damages are quite different from blistering or sputtering at the point of the formation mechanism, i.e. these large scale surface damages are considered as the strong hydrogen embrittlement due to the implantation by the bombarment with intense hydrogen ion beam. These surface damages will be harm to vacuum conditions because of its chapped structure. These surface damages except for Fig. VIII.7.2-5 are quite different from blistering or sputtering at the point of the formation mechanism, i.e. these large scale surface damages are considered as the strong hydrogen embrittlement due to the implantation by the bombarment with intense hydrogen ion beam. These surface damages will be harm to vacuum conditions because of its chapped structure.

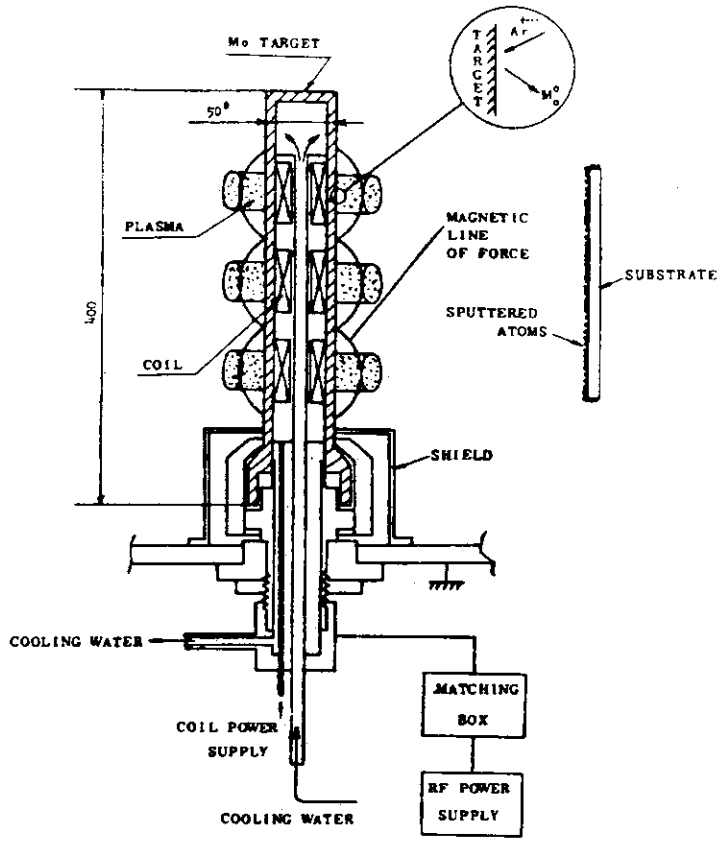

Fig.VIII.7.2-1 Schematic drawing of the sputter device for molybdenum plating.

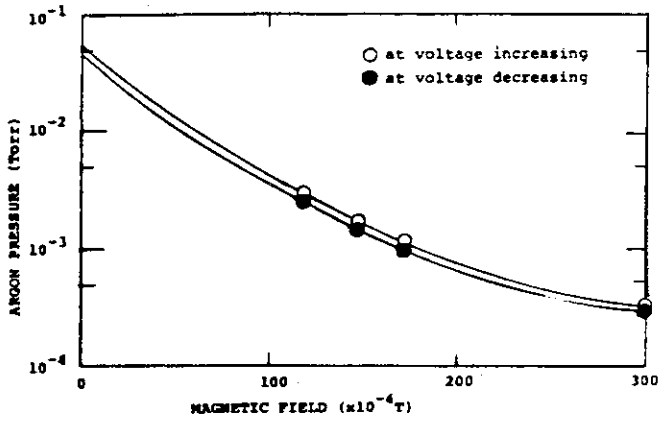

Fig.VIII.7.2-2 Arc burning relation between gas pressure and magnetic field at DC turget voltage of 500 V.

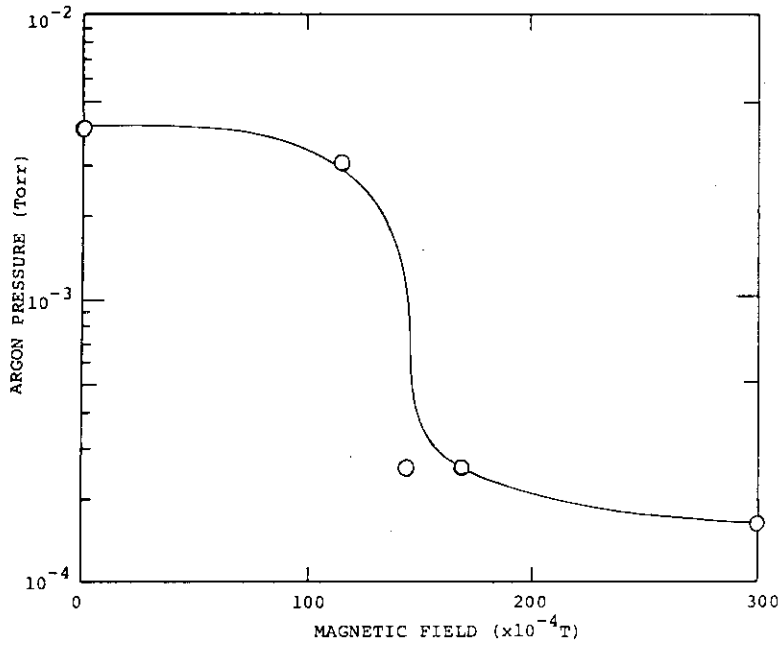

Fig.VIII.7.2-3 Arc burning relation between gas pressure and magnetic field with RF power of 4 kW (13.56 MHz).

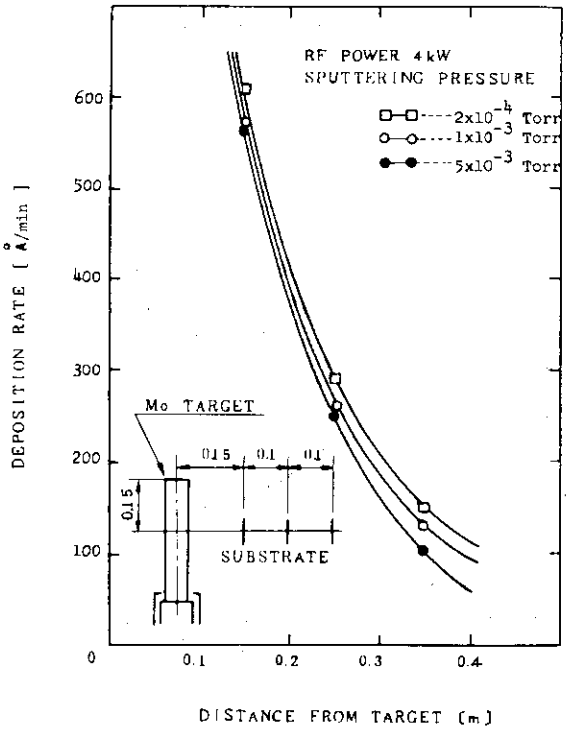

Fig.VIII.7.2-4 Deposition rate by RF sputtering (13.56 MHz) as function of distance from target.

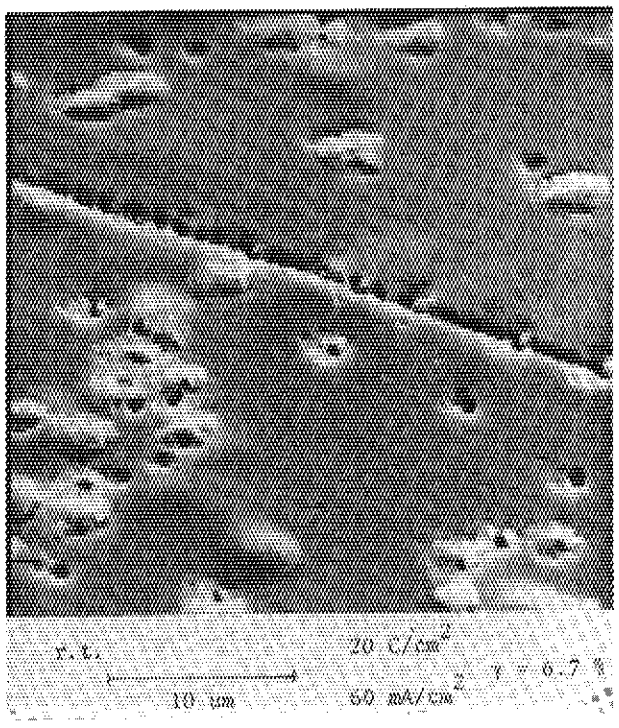

Fiv.VIII.7.2-5 Blister formation on copper surface.

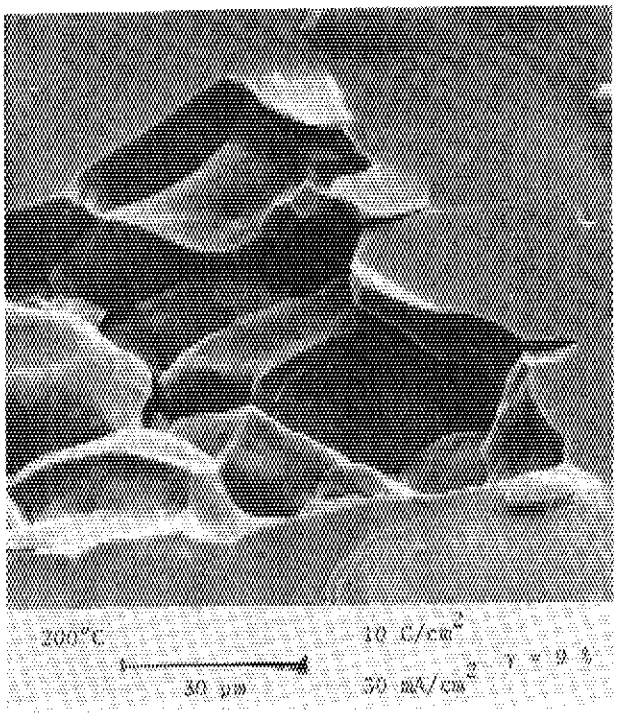

Fig.VIII.7.2-6 Grain ejection on polycrystalline molybdenum.

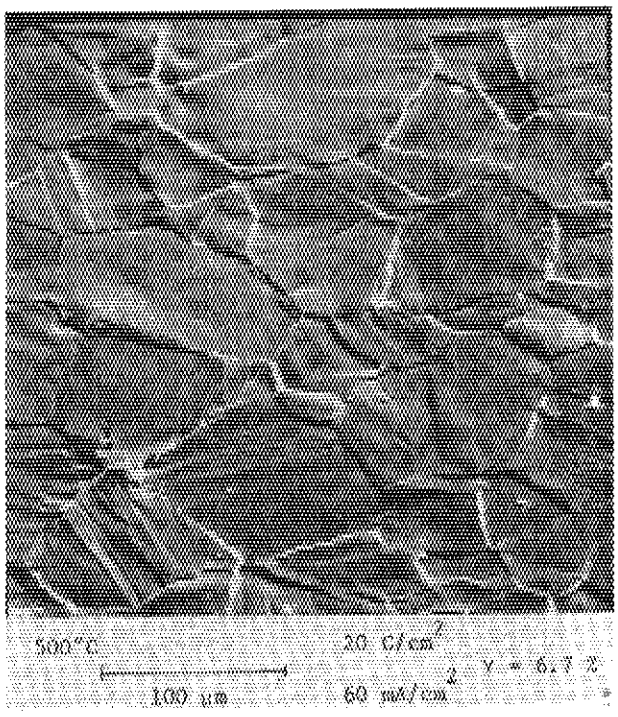

Fig.VIII.7.2-7 The chapped structure on inconel 625.

7.3 Studies of supplementary plasma heating in JT-60

7.3.1 Studies of neutral beam injection heating

To attain effective plasma heating by neutral beam injection, it is important to reduce sufficiently the loss of the injected power and also the impurity influx associated with the beam injection.

A simulation code we have developed to analyze the fast ion slowing-down process includes Monte-Carlo techniques which can precisely describe the behaviours of the fast ions and charge exchange fast neutrals. By adopting this code to JT-60, we have studied extensively the fast ion loss process and furthermore the impurity influx arising from the sputtering of the first wall by high energy particle fluxes.

The energy spectrum of escaping fast neutrals produced by charge-exchange reaction df_{cx}/dE and that of escaping fast ions due to drift motion df_{ob}/dE are shown in Fig. VIII.7.3-1. The major amount of the escaping ions have energies greater than 30 keV. Therefore the sputtering yield by these particles is expected to be small. On the other hand, the fast neutrals which bombard the wall have large population around the energy of 5 keV. In this energy region the molybdenum, the JT-60 first wall, exhibits the peak of the sputtering yield. This fact indicates that the charge-exchange neutrals bring about not only the beam energy loss but also the influx of impurities. The amount of molybdenum atoms sputtered by charge exchange neutrals was able to be calculated with aids of the experimental data on the sputtering yield of molybdenum.

The density dependences of the outflux of the fast neutrals I_{cx}^{f} and the influx of molybdenum atoms emitted by the fast neutrals Y_{cx}^{f} are shown in Fig. VIII.7.3-2 in case of $T_e(0) = 5$ keV, $n_o(a) = 8 \times 10^{14}$ m^{-3} and the injected beam power $P_b = 20$ MW. The outflux of charge exchange hot neutrals I_{cx}^{b} and the influx of molybdenum atoms sputtered by the hot neutrals were also calculated by an one-dimensional integral equation method. The density dependences of I_{cx}^{b} and Y_{cx}^{b} are also given in Fig. VIII.7.3-2. It can be seen in this figure that both the outflux of fast neutrals and the influx of molybdenum atoms do not change significantly with increase of the plasma density under a condition that the background neutral density at the plasma periphery and Z_{eff} are fixed at 8×10^{14} m^{-3} and 3.0 respectively. Molybdenum atom influx caused by the fast neutrals becomes greater than that by the hot neutrals for $n_e(0) \gtrsim 3 \times 10^{19}$ m^{-3}, $T_e(0) = 5$ keV and $P_b = 20$ MW.

7.3.2 Studies of lower hybrid heating

Lower Hybrid Heating (L.H.H.) is planned to provide supplementary heating for the JT-60 plasma, using a phased waveguide array. To heat the core of the plasma (expected plasma parameters; $\bar{n}_e$ = 3 to 8 × 10^{19} m^{-3}, B_o = 3.5 to 4.5 Tesla, $\bar{T}_i$ = 2 to 5 keV, Z_{eff} = 1 to 3), the applied frequency is required to be between 1.3 GHz and 2.45 GHz. L.H.H. experiments in JT-60 will be made in two steps. In the first phase, the net power transmitted into the plasma is 1.25 MW. It will be increased up to 10 MW in the second phase, aiming at the heating of higher density plasmas.

According to the linear theory, incident electromagnetic waves have to satisfy the accessibility condition to penetrate deeply into a plasma. Furthermore, especially for efficient ion heating, it is important to know the location of the turning point where cold plasma wave is converted into hot plasma wave, because the turning point corresponds roughly to the linear absorption region. The location of the turning point can be determined by using the warm plasma theory. One of the advantages of using a phased waveguide array is to be able to control N_z, the refractive index parallel to the external magnetic field. The value of N_z, which is required for both satisfying the accessibility condition and travelling of waves up to the turning point, depends on the applied frequency and the plasma parameters. Figure VIII.7.3-3 shows the dependence of N_z on the applied frequencies within the range of 1.3 GHz to 2.45 GHz in the case of the expected JT-60 plasma parameters shown in Table VIII.7.3-1.

Although the absorption region can be roughly estimated by using the linear theory, it is much more difficult to predict the dominant damping mechanism. The linear theory predicts effective ion heating due to ion cyclotron harmonic damping and ion Landau damping perpendicular to the external magnetic field. On the other hand, non-linear effects, including parametric decay instability and stochastic heating, may also paly a competitive role, as they could have a bearing on the choice of the frequency.

References

(1) JAERI-M 6359 (Annual Report, 1976) p.104.
(2) Kobayashi, T., et al.: JAERI-M 7014 (1977) (in Japanese).
(3) JAERI-M 7479 (Annual Report, 1978) p.289.
(4) WASH-1295 (1974).

(5) Konoshima, S.: to be presented at 3rd. Int. Conf. Plasma Surface Interactions in Controlled Fusion Devices (Culhum, 1978) paper 18.

(6) Shimomura, Y.: to be presented at 3rd. Int. Conf. Plasma Surface Interactions in Controlled Fusion Devices (Culhum, 1978) paper R5.

(7) Matsuda, T., et al.: to be presented at 3rd. Int. Conf. Plasma Surface Interactions in Controlled Fusion Devices (Culhum, 1978) paper p.18.

(8) Tazima, T.: to be presented at 3rd. Int. Conf. Plasma Surface Interactions in Controlled Fusion Devices (Culhum, 1978) paper 20.

(9) Tazima, T.: to be reported in JAERI-M 7717 (1978) (in Japanese).

(10) Nakamura, Y., et al.: J. of Nucl. Mats. 68 (1977) p.253.

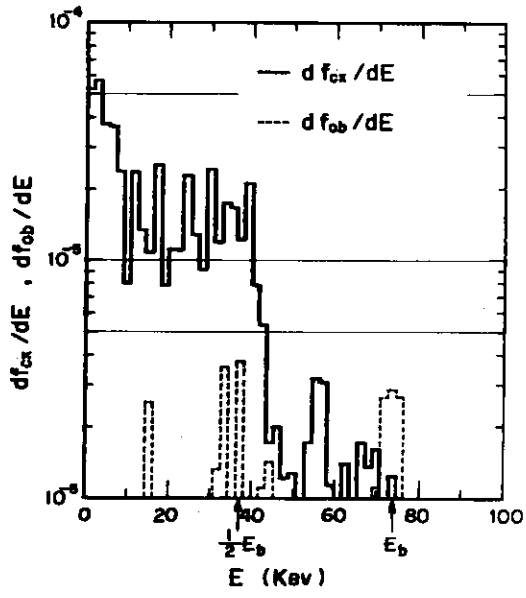

Fig.VIII.7.3-1 Energy spectra of escaping fast neutrals f_{cx}/E and escaping fast ions f_{ob}/E, where E is the injected beam energy.

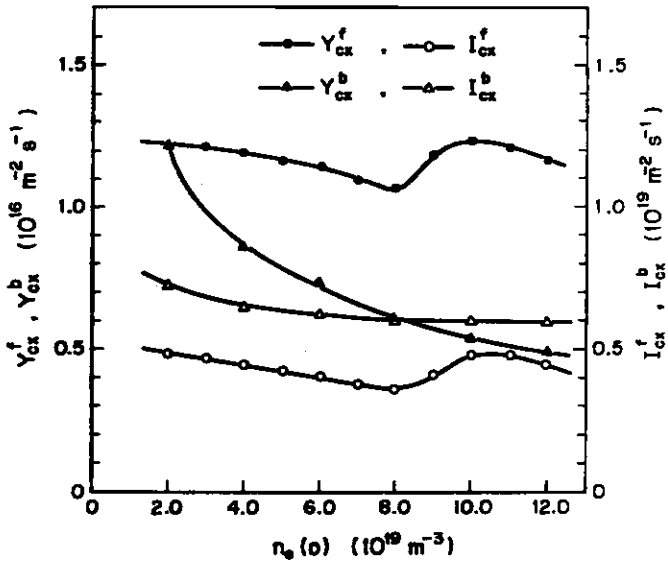

Fig.VIII.7.3-2 Density dependences of the outflux of fast neutrals I^f_{cx}, outflux of hot neutrals I^b_{cx}, influx of molybdenum atoms sputtered by fast neutrals Y^f_{cx} and influx of molybdenum atoms supttered by hot neutrals Y^b_{cx}. It is assumed here that $n_0(a) = 8\times10^{14}$ m^{-3}, $T_e(0) = 5$ keV and $P_b = 20$ MW.

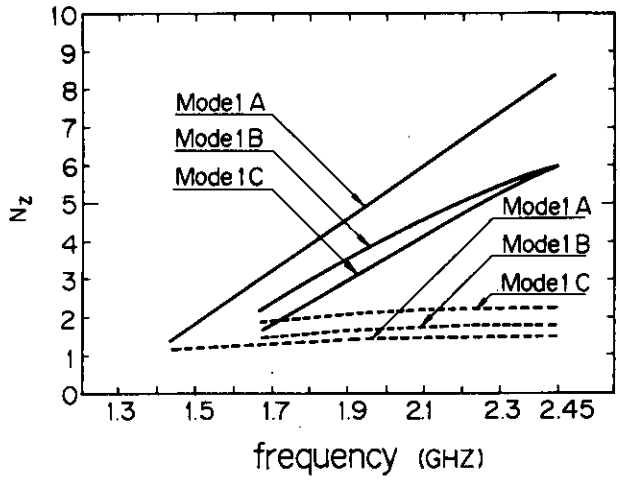

Fig.VIII.7.3-3 Dependence of N_z on frequency. Dashed curves indicate N_z required to satisfy the accessibility condition. Full curves indicate N_z necessary for waves travelling up to the turning point. Models used in this figure are shown in Table VIII.7.3-1.

Table VIII.7.3-1 Expected JT-60 plasma parameters and location of turning point (r_t) normalized by minor radius (a). Each model is used for calculating N_z.

	$\bar{n}_e$ (m^{-3})	B_0 (T)	$\bar{T}_i$ (keV)	Z_{eff}	r_t/a
Model A	3×10^{19}	4.5	2	2	0.3
Model B	5×10^{19}	4.0	2	1	0.5
Model C	7×10^{19}	3.5	3	3	0.7

IX. DEVELOPMENT OF A NONCIRCULAR TOKAMAK --- JT-4

1. Introduction

JT-4 is a tokamak device under design with a plasma column of noncircular cross section and axisymmetric divertors. The basic purpose of JT-4 is to obtain experimental informations about the improvement of efficiency of future large tokamaks or reactors. There are two main objectives in JT-4 program; experimental investigation of 1) the effect of noncircular plasma cross section on attaining higher beta values and 2) the effect of divertor on reducing impurity contents and on controlling plasma density.

The experimental results on above objectives are essential to design efficient and low cost tokamak devices or reactors. To make these studies extrapolatable to larger devices, high temperature plasmas are required for JT-4. Plasma temperature of more than 1 keV is set as one of the requirements. The secondary heating by neutral beam injection with 50 keV and 6 MW will be applied to get plasma beta value of 0.05.

The main parameters of JT-4 are shown in Table IX.1-1. The bird's eye view of JT-4 and one of the equilibrium calculation results are shown in Figs. IX.1-1 and IX.1-2.

The purposes and design of JT-4 were examined at an official committee (The Nuclear Fusion Council) in 1977. And a special subcommittee of JT-4 began its work on cooperative study with some universities.

Following the preliminary design of JT-4[1],[2] in FY 1975, the engineering studies and the test of critical components were carried out in FY 1976, and the design adjustment was finished in FY 1977. The final design which is almost the first stage of the construction is planned in FY 1978, and the construction is expected to start in FY 1979. The device is expected to be operational at the biginning of 1983, the same time as JT-60.

The outline of the results of the design adjustment done in FY 1977 is described in the following sections.

2. System Design

The JT-4 system consists of the machine, the power supplies to the toroidal and the poloidal field coils, and the auxiliary systems as the vacuum pumping system, the cooling system, the control system, etc.

The cross section of the main part of JT-4 machine is shown in Fig. IX.2-1. The details of the vacuum vessel is described in 3.1. The poloidal field coils are set around the vacuum vessel. There are 18 D-shaped toroidal field coils surrounding the poloidal field coils and the vacuum vessel. The splittable toroidal field coils were taken as the basic design concept of JT-4 in order to avoid the splittable poloidal field coils. It is because the available work space for the poloidal coils between the TF coils and the vacuum vessel is narrow and deep, and there are about 260 turns of PF coils which would have to be jointed if the TF coils were not splittable. The insulation voltage of TF coils is much smaller than that of PF coils, and the insulation problem in the coil joints can be avoided. The difficulties of the machine are concentrated on the splittable toroidal field coils and on the support structure. The design of them are described in 3.3.

The electric power for the coils are supplied by larger motor generators of JT-60. The time interval between discharge at the full power operation is 10 minutes when both JT-4 and JT-60 are operating alternately.

The secondary cooling water, the emergency power supply and the secondary heating power (NBI and RF) are supplied by the systems of JT-60. There are close relations between JT-4 and JT-60, and care was taken to adjust the design of both machines, especially in design of the control systems.

The basic specifications of the machine design are: 1) high vacuum conditions in the vacuum vessel, i.e. up to 5×10^{-9} Torr of vacuum pressure, 2) 30 kG at R = 1.4 m, 3) plasma current of up to 1 MA, 4) discharge duration of 2 sec and 5) number of operation of 100,000 at full power of 30 kG and additional 100,000 times for low pressure operations.

3. Design of Machine

3.1 Vacuum vessel and its auxiliary components

The vacuum vessel and its auxiliary components are composed of 1) vacuum vessel, ii) liner plates, iii) limiters, iv) divertor plates, v) N-coils (coils set inside the vacuum vessel), vi) installed detectors, vii) pumping system, viii) baking system and cooling system.

Parameters of the vacuum vessel and its auxiliary components are given in Table IX.3.1-1.

i) Vacuum vessel

The basic design requirements for the vacuum vessel are to (1) maintain a base pressure of 5×10^{-9} Torr or less, and support a continuous 1 atmosphere pressure load, (2) be bakable to a temperature of 250°C, (3) have a resistance of 2 milliohms or more, and (4) withstand electromagnetic force.

Figs. IX.3.1-1 and IX.3.1-2 show a cross-sectional view and a development of the vacuum vessel, respectively. The vessel is composed of two thick plate sections and two bellows sections. The bellows section has a double vacuum structure with a thick outer wall. It is designed on the basis of the engineering study and the test of critical components made in FY 1976[3]. The cross section of the bellows section are shown in Fig. IX.3.1-3.

The thick wall outside the bellows is required to (1) maintain a pressure of 76 Torr or less in the outer vacuum region, (2) be bakable, (3) have electrical insulation in the toroidal direction and (4) withstand various mechanical loads, especially an electromagnetic force produced by saddle currents in thick plate sections. The outer wall is separated by a vacuum-tight insulator with a key structure. The shear stress due to the electromagnetic force is 1.6 kg/mm^2 at the key.

The thick plate sections are made of 30 mm thick plate of SUS316L. There are 241 port appendages; 104 diagnostics ports, 6 neutral beam injection ports, 2 vacuum pumping ports, 40 divertor pumping ports, 7 gas injection ports, 2 movable limiter ports, etc.

The vessel is supported at the midplane by toroidal field coils. 7 support structures are connected to ports and thick plate sections. They have a slide mechanism to prevent the stress due to the thermal expansion of the vessel. The primary stress intensity on the vessel at the support structure is 5.8 kg/mm^2 and the primary and secondary stress intensity is 21 kg/mm^2.

ii) Liner plates

Liner plates are attached to the inner surface of the vacuum vessel to protect the vessel wall, bellows and installed detectors. Liner material is SUS316L except bellows liners of Mo. Stainless steel liners are 5 mm thick square plates of 100 mm × 100 mm. The maximum allowable thermal input from the plasma is 50 W/cm^2 × 1 sec at an interval of 10 min and a

temperature rise is 64°C. The stress due to a electromagnetic force and the thermal stress are 6.9 kg/mm^2 and 14.2 kg/mm^2, respectively.

iii) Limiters

Two types of limiters are used, fixed limiters and movable limiters. Fixed limiters are placed on the inner surface of the vacuum vessel in the toroidal direction, as shown in Fig. IX.3.1-1. Curved Mo plate of 10 mm thick is used as limiter head. The allowable thermal input is 2 MW × 1 sec and the maximum temperature is 798°C, which is lower than the recrystallization temperature of Mo. The thermal stress is 21 kg/mm^2.

To movable limiters are inserted into the vessel. They are manually operated and the stroke is 400 mm. The heads of the movable limiter are insulated from the vessel. The torelable input is 0.6 MW × 1 sec. Limiter heads are cooled by oil cooling boxes behind them.

iv) Divertor plates

In the divertor room, there are divertor plates which neutralize the diverted plasma particles and absorb the heat flux. The divertor plates are made of curved Mo plates of 10 mm thick and insulated from the vessel. The torelable heat flux is 1.2 kW/cm^2 and the maximum temperature is 996°C. They are cooled by oil channels.

v) N-coils

N-coils consist of N1-coils N2-coils and N3-coils, as shown in Fig. IX.3.1-1. Their casing has several bellows sections to avoid the thermal stress and to give an electrical resistance of 20 milliohms or more. Each N-coil is supported by 8 support structures which are slidable in the radial direction.

vi) Installed detectors

Several types of detectors are installed in the vacuum vessel. For the measurement of the electromagnetic properties of the plasma, one-turn coils, Rogowski coils and magnetic probes are placed behind liner plates. For monitoring mechanical conditions of the vessel and inner components, thermocouples and strain gauges are used.

vii) Pumping system

The vacuum vessel is pumped through 2 pumping ports. The main pumps are turbomolecular pumps and the effective pumping speed at vessel pumping apertures is 2000 l/s (N_2). This system is insulated from the vessel and bakable at a temperature of 160°C. In addition, the divertor room is pumped by the divertor pumping system.

viii) Baking system and primary cooling system

To heat the vessel and inner components up to 250°C in 20 hr, oil piping is placed on them. Oil piping also removes the heat deposited in the vessel, limiters, divertor plates and N-coil liners. The heating power is 370 kW and the cooling power is 225.5 kW. The total flow rate is 30 m^3/hr.

There are thermal insulation layers on the heating oil pipes and water cooling pipings in them. The vacuum vessel cooling system, the toroidal field coil cooling system and the poloidal field coil cooling system compose the primary cooling system. The total flow rate is 333 m^3/hr.

3.2 Poloidal field coils

The poloidal field coil (PF coil) system consists of two independent coil systems, the primary coil of a current transformer (OH-coil) and the equilibrium field coils (EF-coils). The latter is composed of six species of poloidal coil:

i)	divertor coil	(D-coil)
ii)	shaping coil	(S-coil)
iii)	vertical field coil	(V-coil)
iv)	quadrupole field coil	(Q-coil)
v)	position control coil	(C-coil)
vi)	horizontal field coil	(H-coil)

The OH-, S-, V-, H-, and a part of Q-coil are located between the toroidal field coil bore and the vacuum vessel, while the rest inside the vacuum vessel (these coils are named N-coil) for the purpose of controlling the plasma position and shape rapidly.

In FY 1977, a design adjustment of PF coil system was made on the basis of the detailed engineering design made in 1976. As a result, a partial change of coil configuration was made. The general view of the

coil positions and the specifications of PF coils are shown in Fig. IX.3.2-1 and Table IX.3.2-1, respectively.

Each turn of the PF coils is made of water cooled rectangular hollow-copper conductors. The copper alloy is 0.2 % silver bearing copper. To insulate the turns from each other and to provide for structural integrity of the PF coils, the turns are wrapped with fiberglass reinforced plastics (FRP) and impregnated with epoxy. The insulation scheme is two levels of protection. First, a 10 mm thick layer of FRP is placed between turns and structure, and between the OH-coil and the EF-coils. This gives the turns the capability to withstand a turn-to-ground potential. Second, each turn is wrapped with a 3 mm thick layer of FRP tape, which gives a turn-to-turn withstand capability. To support the PF coils, they are divided to eleven blocks. Each block have a stainless steel can, which is supported by the vacuum vessel.

The maximum hoop stress due to the electromagnetic force is approximately 3.9 kg/mm^2 in the OH-coil, 3.8 kg/mm^2 in the EF-coils outside the vacuum vessel, and 1.29 kg/mm^2 in the N-coil. The maximum axial compressive force in the double-winding solenoid of the OH-coil is about 43 ton, resulting in a maximum compressive stress of 0.35 kg/mm^2. The maximum thermal stress in the conductor is less than 4.5 kg/mm^2.

The maximum error field produced by feeder lines and return windings is less than 50 gauss in the plasma region.

3.3 Toroidal field coils

The design of the splittable TF coils is one of the key points in the JT-4 design, and a great deal of efforts have been made on the TF coil design. The points of the design are; 1) the strong electromagnetic force, 2) the thermal stress, 3) the cooling and 4) the assembly and disassembly.

In the preliminary design of FY 1975, many ideas are proposed and investigated analytically. In FY 1976, a joint structure was selected which is strong enough to support the whole electromagnetic force without any other support structure as casing, but the length of the joint section is too long. And there left problems to be solved in the structure of cooling pipes of the joint section and in the assembling procedure.

In FY 1977, another design was investigated in which the assembly problem is solved. The electromagnetic force is supported with both the copper conductors and the casing. In this design, the conductors push the

outer conductors or the casing, and attension was paid on the stress of the insulator between copper conductors or casing.

The present design of TF coils is shown in Fig. IX.3.3-1 and Table IX.3.3-1, and the picture of the joint structure is shown in Fig. IX.3.3-2.

The joint structure is made of Cr-Cu and most of the coil is made of Ag-Cu. The main part of the coil and the joint structure are connected by either teeth structure or welding.

About 1/3 of the electromagnetic tensile force at the straight section of the torus center is supported by the stainless steel casing and the average tensile stress of the copper is only 2.5 kg/mm^2. The maximum value is 2.7 kg/mm^2 of the outermost turn. The local maximum tensile stress is high because of the stress concentration at the joint structure, and the maximum stress is 15.8 kg/mm^2, while the tensile strength of Cr-Cu is more than 40 kg/mm^2. The maximum stress of the casing is 8.4 kg/mm^2 which is the value limited by total tensile stretch of 0.5 mm. The maximum compression stress of the insulator is 5.3 kg/mm^2 by the inward centripetal force and 4.9 kg/mm^2 by thermal expansion.

The thermal analysis are also carried out and the maximum temperature is 96°C at the joint structure. The contact resistance of the joint is about 1.3 μΩ for a joint.

3.4 Layouts

The floor plan of the JT-4 main building is shown in Fig. IX.3.4-1. The machine of JT-4 locates at the center of the experiment room. The machine body stands on a support pillar. There are four floors in the experiment room; basement, second basement, ground floor and upper floor. Most of the main devices are placed on the ground floor. The north half is used for the neutral beam injectors and the south half for the diagnostic devices. On the upper floor, the power supplies of the NBI and one of the vacuum pumping devices are placed. The basement and the second basement are used mainly for auxiliary devices as cooling, electric power feeder lines, etc. The upper floor is removable to use the 100 ton crane.

3.5 Diagnostic ports

There are 241 ports on the vacuum vessel and 104 of them are for diagnostic use. The details of the diagnostic ports are shown in Table

IX.3.5-1. The 'A' ports are used to observe vertically the inner and outer periphery of the plasma cross section at four different major radius. Through 'M_1' and 'M_2' ports, the main plasma near Z = 0 can be observed horizontally. 'M_3' and 'K' ports are used for measurement of the outer plasma near the 'null point' of the separatrix surfaces, 'D_1' ports can be used as divertor room access ports.

The cross sections of the vacuum vessel at the ports are shown in Fig. IX.3.5-1. The layouts of the ports are shown in Fig. IX.3.1-2, 'L', 'P' and 'B' denote ports for movable limiters, vacuum pumping systems and neutral beam injectors, respectively.

4. Design of Power Supplies

4.1 Toroidal field coil power supply

The electric power for the toroidal field coils is supplied by motor generator of the JT-60. The coil current of JT-4 is about twice larger than that of JT-60. The power from the motor generator is supplied as high voltage ($\sim$10 kV) ac, and the power supply of JT-4 consists of power transformers with variable voltage taps and rectifier diodes. The value and waveform of the current during pulse are controlled by the motor generator (i.e. the current control of the field winding). Although the time constants of the toroidal field coils of JT-4 and JT-60 are different (4.4 sec and 25 sec, respectively), current waveform can be controlled without changing any hardware of the motor generator system.

There is an additional small SCR power supply for continuous operation at 3 kG for the cleaning discharge. The SCR supply is connected to the power network.

4.2 Poloidal field coil power supply

The JT-4 poloidal field coil power supply provides electric power for the following constituents or subsystems; (i) the ohmic heating system which induces a plasma current of up to 1.0 MA and maintains it for about 2 seconds, (ii) the plasma maintaining field system which controls the plasma equilibrium position and shape. The system consists of six poloidal field coils shown in §IX.3.2.

In FY 1977, the detailed engineering design of the poloidal field coil power supply was made. The basic design concept is to constitute the

poloidal field coil power supply by a single set of motor generator for the JT-60 which is followed by thyristor controlled rectifier stages for respective coil. The design purposes are to determine the detailed electric circuits and to settle the performance and specifications of the major components of the poloidal field power supply to meet the required operation sequences and conditions. The specifications of the poloidal field power supply are given in Table IX.4.2-1 and the peak working output dc power is about 140 MW.

4.2.1 Ohmic heating power supply[9]

The basic design requirements for the ohmic heating power supply under I_p = 1 MA operation are; (i) a total magnetic flux variation of 5 volt-sec., and (ii) a minimum one-turn voltage of 100 volts at the beginning of the plasma discharge.

The high peak voltage and power required to initiate the plasma discharge in JT-4 will be obtained with an inductive energy storage. In this system, the OH-coil functions as an inductive energy storage coil. Prior to the discharge, an external power supply is used to establish a dc bias current, $I_{OH} \simeq 45$ kA, in the OH-coil. At the desired instant, an interrupter switch is used to transfer the OH-coil current from the power supply to a high impedance RC network. The resulting RLC oscillation generates an initial peak voltage of up to 10 kV across the OH-coil, inducing a rapid build up of plasma current. Eventually, the capacitance in the RC network reverses the OH-coil current, and auxiliary switching is used to reconnect the power supply with reversed polarity to further increase the reversed current up to -50 kA to sustain the plasma current flattop ($I_p \simeq 1$ MA) during 2 seconds.

A candidate for the interrupter switch in JT-4 is a solid state (Thyristor) circuit breaker which interrupts a current of 45 kA with recovering voltage of 12 kV. The capacitor bank has a nominal capacitance of 0.6 F with a peak working voltage of 1.6 kV.

4.2.2 Power supplies for equilibrium field coils

In JT-4, the external magnetic field required for the toroidal equilibrium, (B_v, n), is applied by six EF-coils shown in §IX.3.2. S-coil induces the dominant portion of the equilibrium field by controlling of its current and/or changing its connection. V- and Q-coil produce the

small field, (δV_v, δn), to adjust the major radius and shape of an equilibrium plasma. By varing the flux values of these three coils and the D-coil, either circular, elliptical, or D-shaped configuration with the magnetic limiter can be achieved. For $q_{limiter} = 3$, typical plasma current is about 0.55 MA for a circular discharge, 1.0 MA for a 1.7 : 1 ellipse at $B_t = 3.0$ T. C- and H-coil produce the horizontal magnetic field to control the vertical position of an equilibrium plasma.

Each of these EF-coils is connected to a thyristor controlled rectifier system, and, prior to the discharge, each current is programmed to sustain the plasma equilibrium position and shape. Additionally the V-, Q- and C-coil current are controlled by feedback method. The specification of the EF-coil power supply is given in Table IX.4.2-1.

4.2 Plasma position and shape control

In JT-4, the plasma position and shape are controlled by feedback system of V-, Q- and C-coil currents. Axisymmetric mode involving overall vertical displacement of plasma column of an elliptic discharge is the most troublesome problem in JT-4. C-coil and its feedback loop are set in order to suppress this mode.

In FY 1977, the soft- and the hard-ware analysis on feedback system were separately made. The former is a transient response analysis of feedback loop to survey some optimal coefficients of the control device by using a simulation code developed in JT-60 project. The latter is a design of the thyristor rectifier system of which specifications are shown in Table IX.4.2-1. The results through these analyses are given in Table IX.4.2-2.

4.4 Power distribution system

The continuous electric power for relatively small power devices are distributed to each device through the power distribution system.

The total power for the distribution system is 9 MVA, which is divided into 2.4 MVA for the toroidal field coil continuous operation, 2.5 MVA for the secondary heating system and 4 MVA for the other small devices as control, cooling pumps, vacuum pumps, etc. The power for the diagnostic systems is over estimated to be 1.7 MVA, which may be reduced to 0.7 MVA.

The large pulsive power for the toroidal and the poloidal field coils

and for the secondary heating system is not included in the power distribution system. They are supplied by motor generators of JT-60 as described before.

5. Control system

The problems encountered in the design of the control system are surveyed. The details of the design are left for future because the details of the actual design of the whole system are necessary to the design of the control system. The signals and the informations which should be interchanged between JT-4 and JT-60 are listed up. The main factors in the design of the control system are the adjustment between JT-4 and JT-60, the timing system and the man-machine communications.

6. Diagnostics and Data Aquisition System

The diagnostic system will have to yield as much experimental information as possible during a discharge. The data aquisition system must be consistent with the requirement and be able to handle up to 700 thousand words per discharge.

The proposed diagnostics are listed in Table IX.6-1. Most of these diagnostics are in operation for JFT-2, DIVA or under development for JT-60 project.

Magnetic probes are designed to be compact cartridge type because it is needed to set up as many probes as possible in vacuum vessel for measuring magnetic flux of JT-4 plasma with non-circular cross section.

All diagnostic signals will be conditioned to conform to the levels established for the CAMAC interface of the aquisition system. CAMAC equipments will be located in the room next to the experimental areas. Approximately 50 crates will be used for JT-4 diagnostics.

All data will be processed in the diagnostic computers which are placed in the control room. The diagnostic computer system is shown in Fig. IX.6-1. It is possible to store one shot data in each CAMAC crate and one day data in the diagnostic computer and permanently in magnetic tapes.

All data of diagnostics will be presented in the graphic display on the consoles. Experimentalists can set up diagnostic parameters and monitor every experimental devices from the central and local consoles in the control room.

7. Auxiliary System Design

7.1 Gas supply system

There are 6 fast acting gas valves and a slow valve in JT-4. The fast valves are divided into two groups; 4 valves for initial gas supply just before the discharge and 2 valves for additional gas injection during discharge. The piezo-electric valves are used as the fast acting valves. The slow valve is used for continuous gas supply or nitrogen gas filling before opening of vessel. The waveforms of the gas pulse of each fast acting valve can be controlled independently by a gas supply control computer. The gas species of the three groups of the valves are either of 8 gas species; hydrogen, deuterium, helium, nitrogen, carbon dioxide, methane, oxygen, and argon. The pressure of the supplied gas or that of the gas reservoir is automatically controlled.

7.2 Preionization system

The J × B gun is designed as a preionization system in the JT-4 design adjustment. The gun itself is same as that used in JFT-2a. The objectives of the design are to know whether there is any problem in the control, power supply or space for the device.

References

(1) JT-4 Group: JT-4 Program, JAERI-M 6666, (August, 1976), 265 pp, (in Japanese).

(2) Kitsunezaki, A., Seki, S., Saito, R., Matsuda, T., Yokomizo, H. and Yoshikawa, M.: JT-4 Program, Proc. of International Symposium on Plasma Wall Interaction, (Permagon Press, 1977).

(3) Matsuda, T., Kitsunezaki, A., Seki, S., Yokomizo, H. and Saito, R.: Design of Noncircular Welded Bellows, JAERI internal report, (November, 1977), 127 pp, (in Japanese).

(4) Matsuda, T., Kitsunezaki, A., Yokomizo, H., Saito, R. and Seki, S.: Experiments on in-situ coating of Molybdenum, internal report, (August, 1977), 18 pp, (in Japanese).

(5) Matsuda, T., Kitsunezaki, A., Yokomizo, H., Saito, R. and Seki, S.: Experimental study on in-situ coating of molybdenum, International Conference on Plasma-Surface Interactions in Controlled Fusion Device, (Culham, 1978).

(6) Yokomizo, H., Kitsunezaki, A., Matsuda, T., Saito, R. and Seki, S.: Experiment of Ti sublimation pump for JT-4 divertor, internal report, 22 pp, (in Japanese).

(7) Kitsunezaki, A., Seki, S., Yokomizo, H., Matsuda, T. and Saito, R.: Design of splittable noncircular toroidal field coils, internal report, 47 pp, (in Japanese).

(8) Kitsunezaki, A., Seki, S., Yokomizo, H., Matsuda, T. and Saito, R.: Design of axisymmetric divertors in JT-4 tokamak, internal report, 13 pp.

(9) Saito, R., Seki, S., Yokomizo, H., Matsuda, T. and Kitsunezaki, A.: Conceptual Design of a Current Transformer in a Tokamak Device, JAERI-M 7810, (July, 1978), (in Japanese).

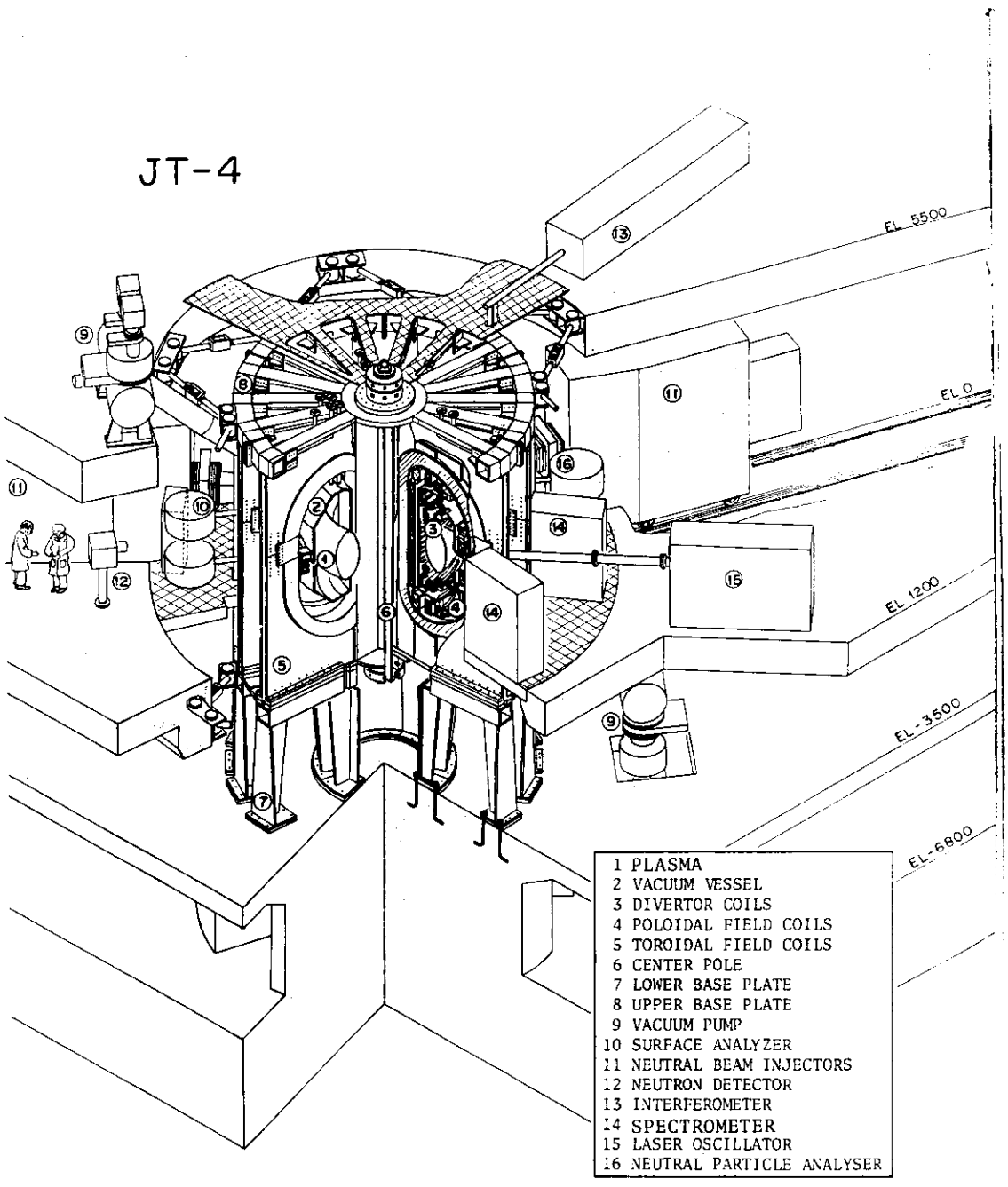

Fig.IX.1-1 Bird's eye view of JT-4

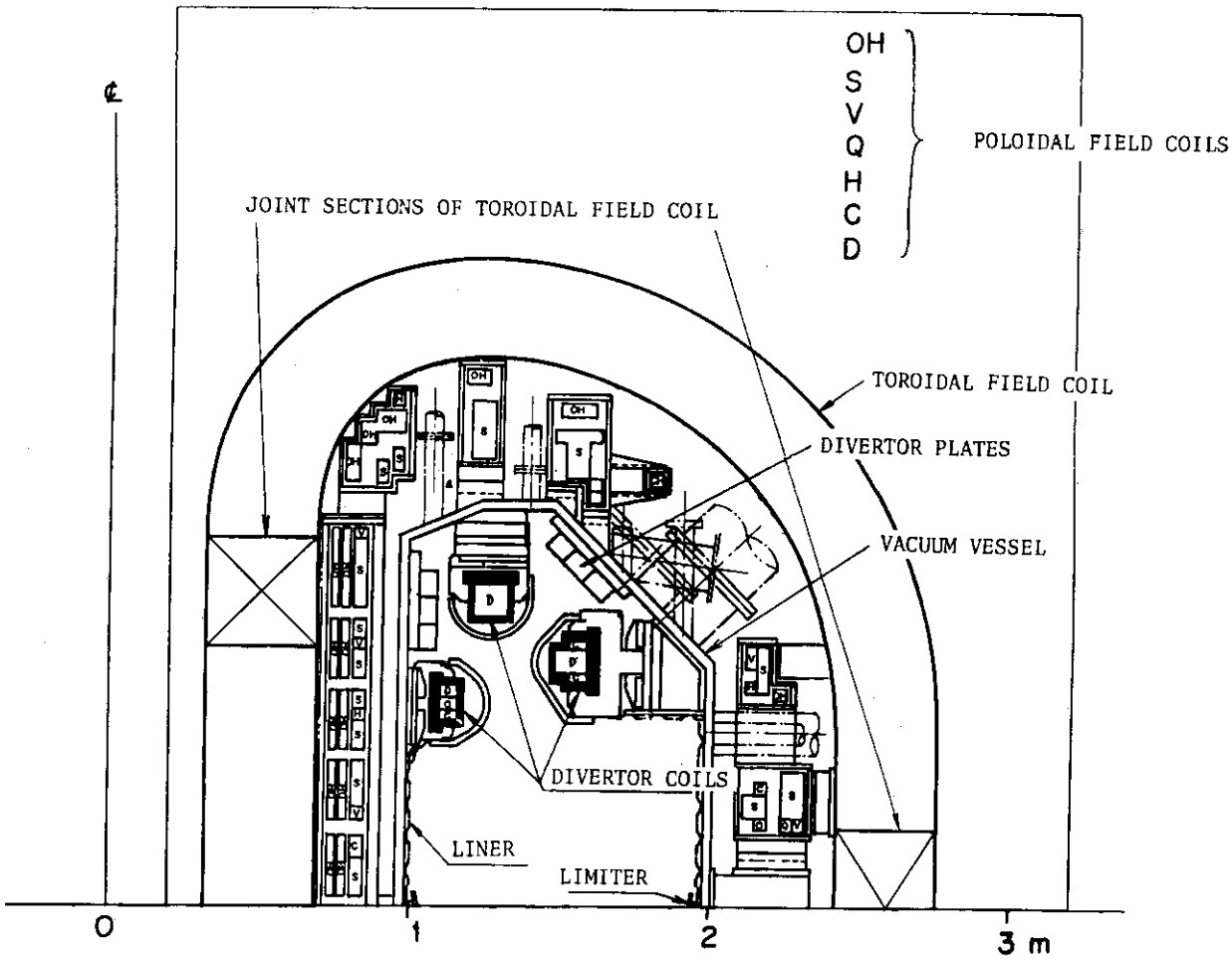

Fig.IX.2-1 Cross section of JT-4 machine

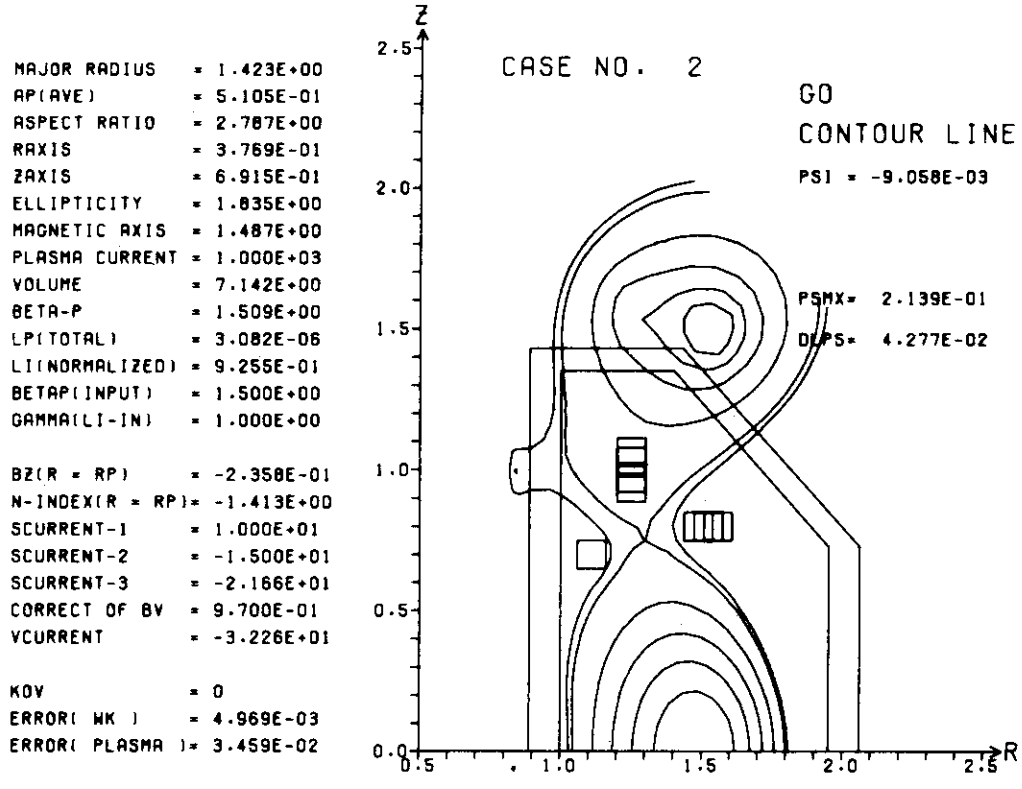

Fig.IX.1-2 Plasma equilibrium configuration of JT-4

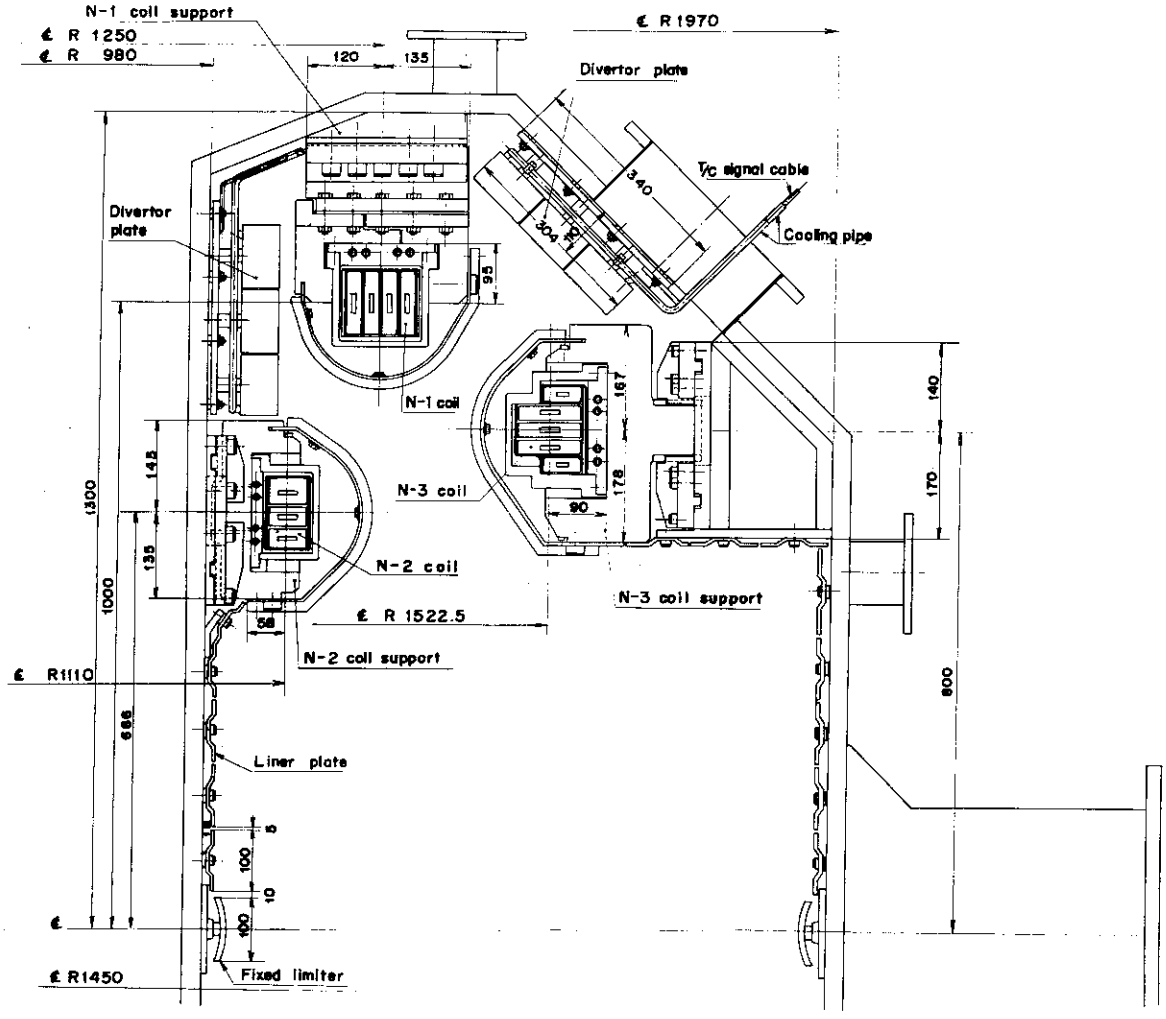

Fig.IX.3.1-1 Cross section of vacuum vessel

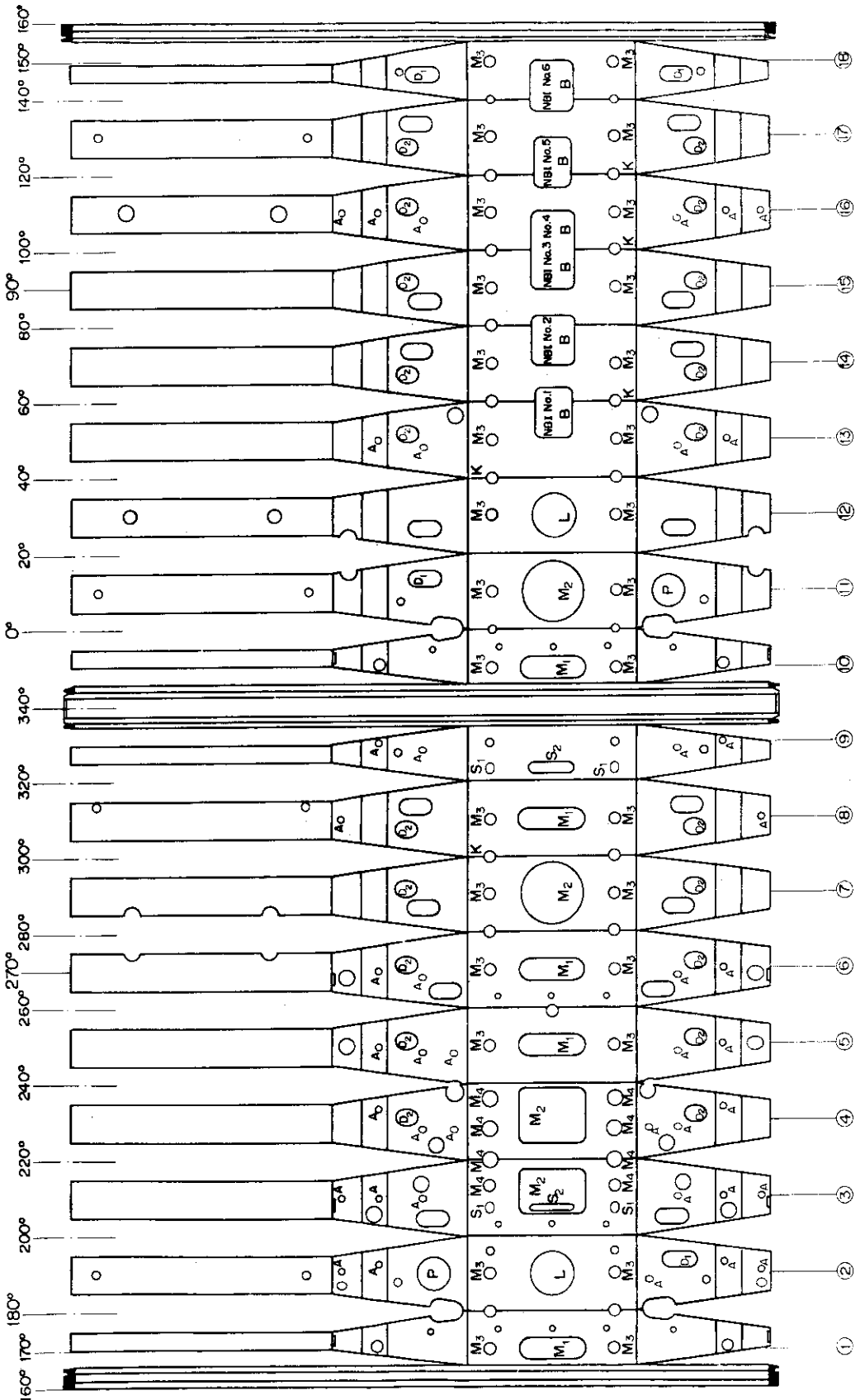

Fig.IX.3.1-2 Development of vacuum vessel

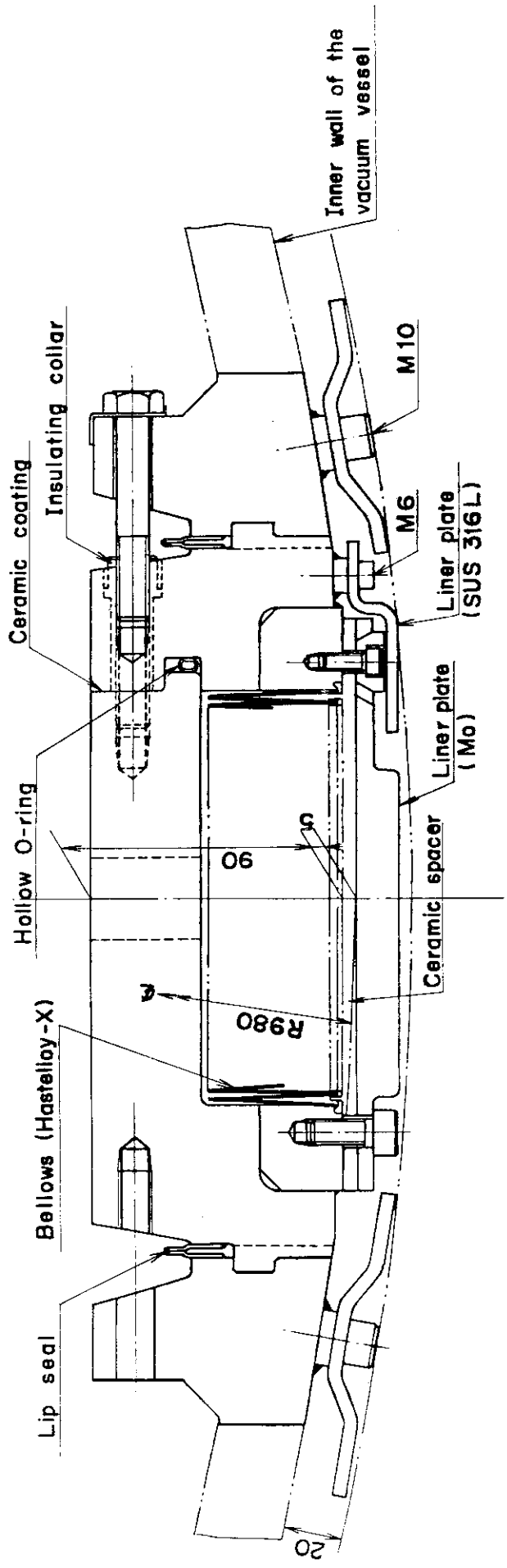

Fig.IX.3.1-3 Cross section of bellows section

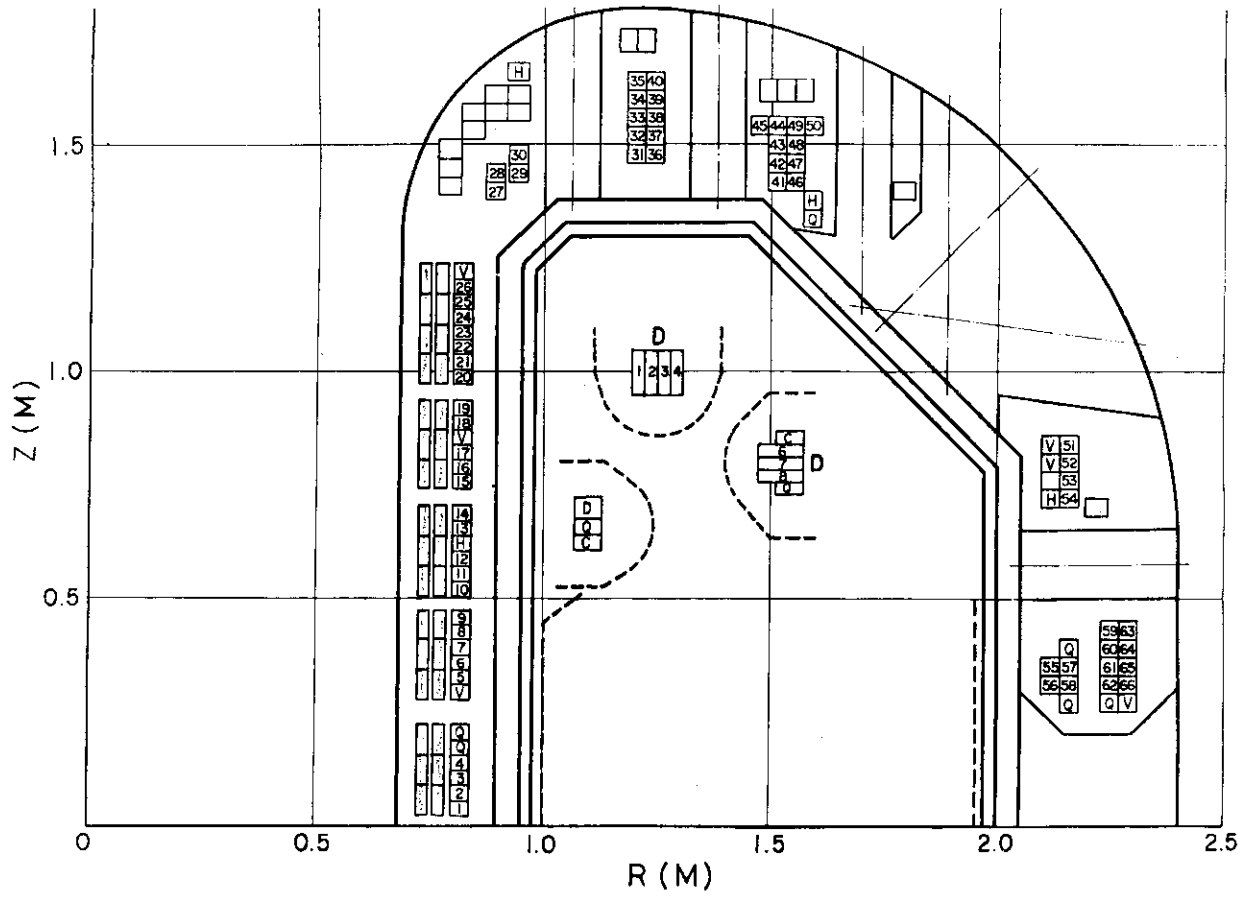

Fig.IX.3.2-1 Positions of poloidal field coils

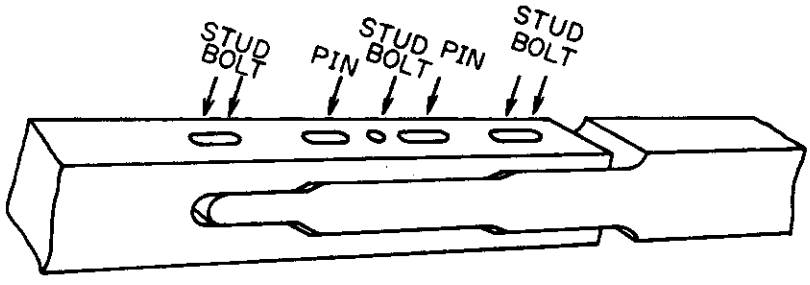

Fig.IX.3.3-2 Picture of toroidal field coil joint structure

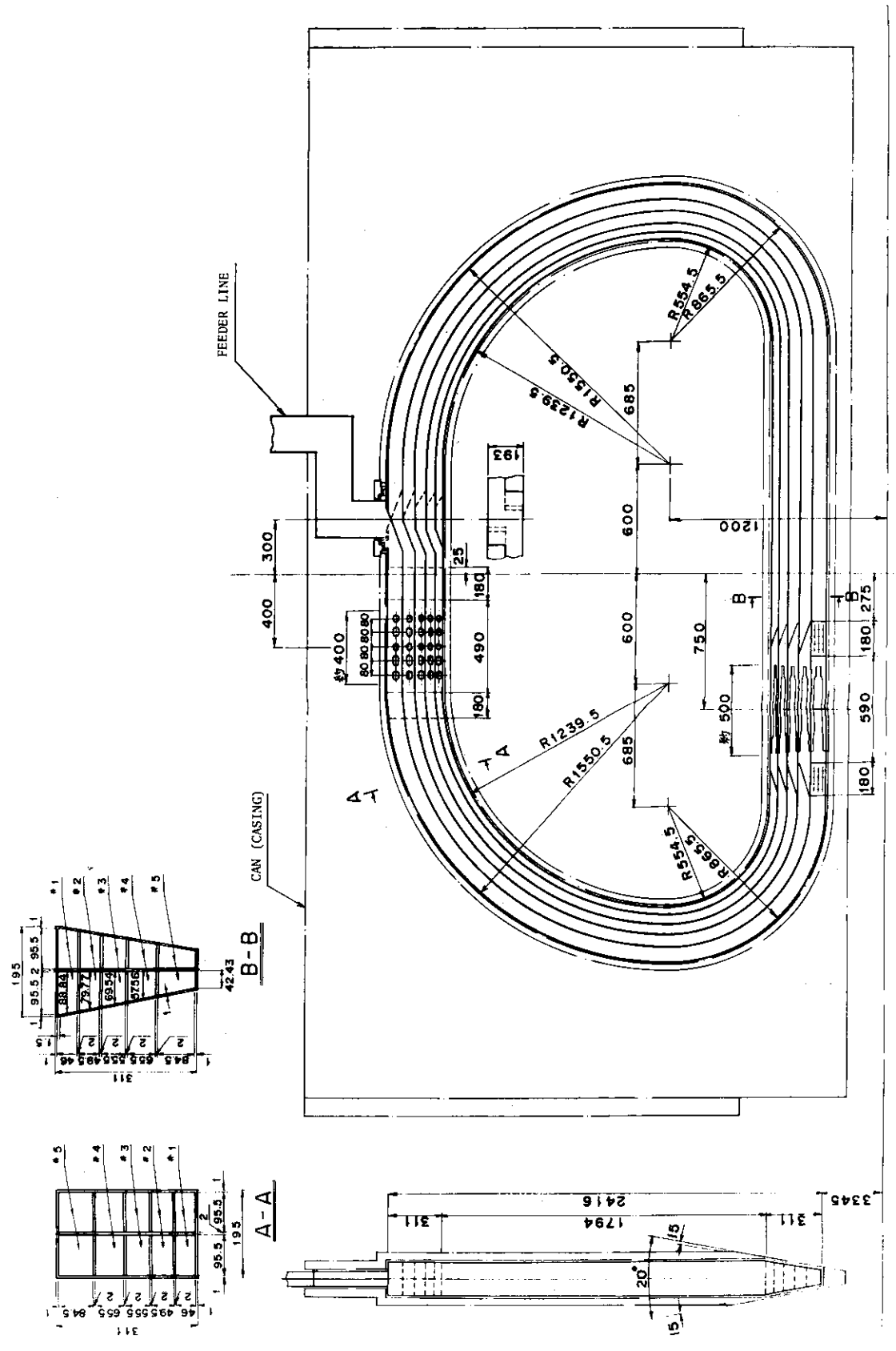

Fig.IX.3.3-1 Splittable toroidal field coil

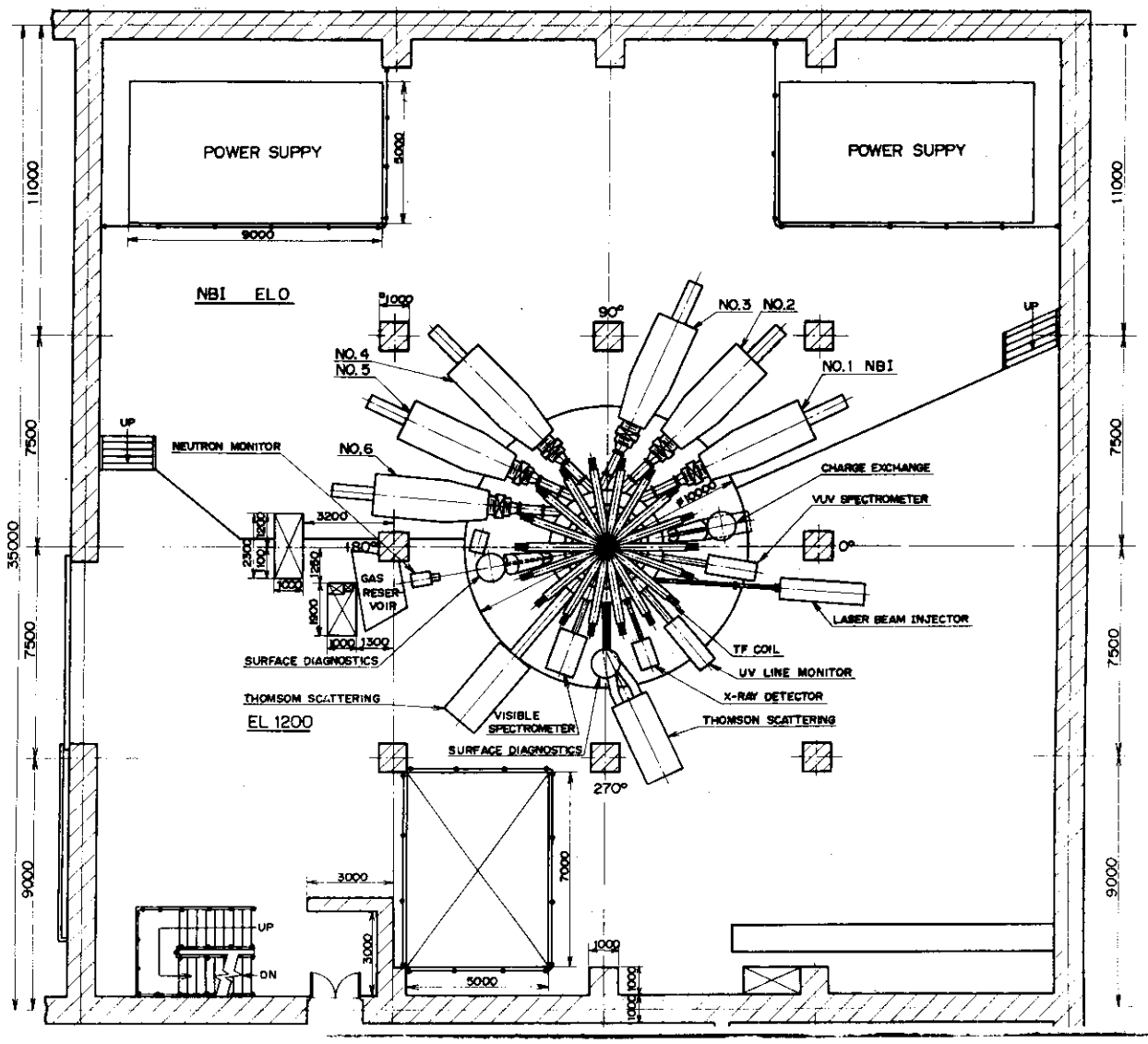

Fig.IX.3.4-1 Floor plan of ground floor

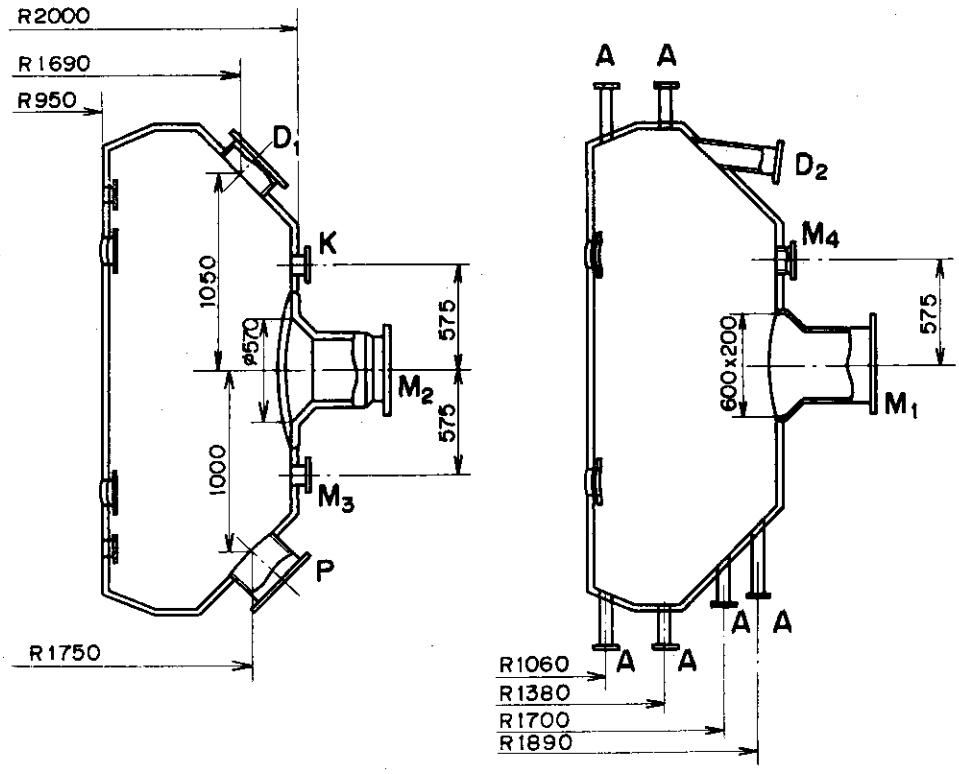

Fig.IX.3.5-1 Cross section of ports

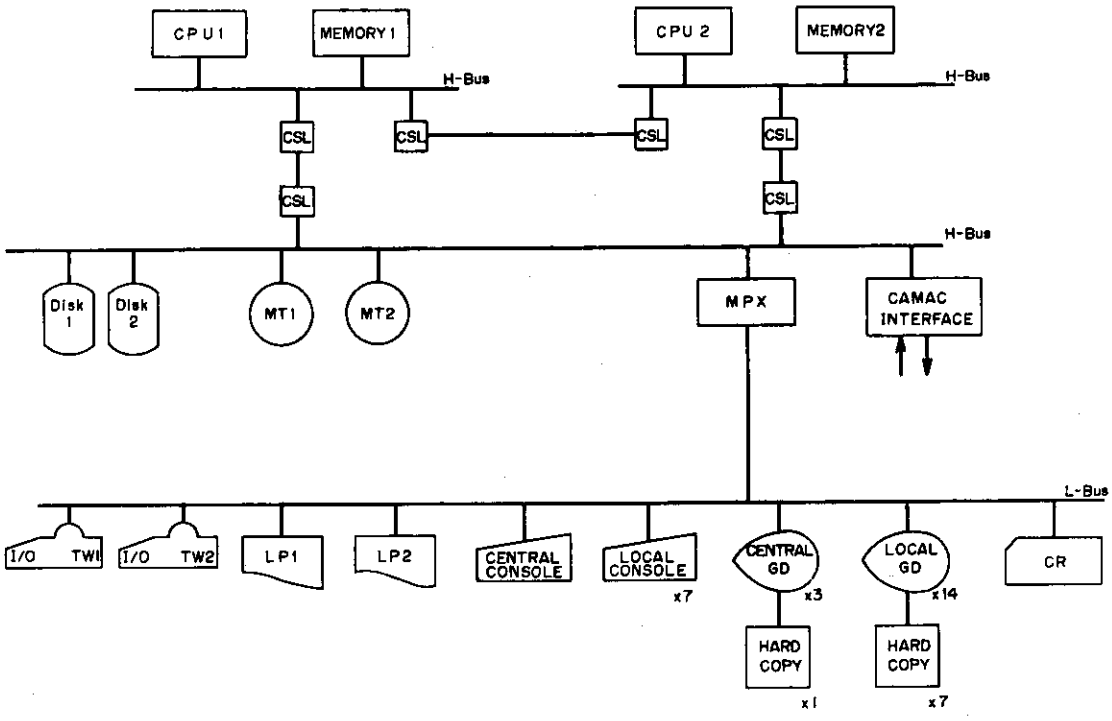

Fig.IX.6-1 Diagnostic computer system

Table IX.1-1 JT-4 main parameters

Major radius	1.45 m
Minor cross section half width	
Vertical (b)	0.68 m
Horizontal (a)	0.4 - 0.45 m
Ellipticity (b/a)	1.0 - 1.7
Toroidal field	30 kG
Flattop	2 sec
Maximum plasma current	1.0 MA
NBI heating power	6 MW

Table IX.3.1-1 Parameters of the vacuum vessel and its auxiliary components

Vessel shape	Ref. Fig. IX.3.2-1
Vessel material	SUS 316 L
	Hastelloy-X (bellows)
Maximum radius	2010 mm
Minimum radius	950 mm
Height	2665 mm
Width	1060 mm
Thickness	30 mm
	0.6 mm (bellows)
Vessel weight	35 ton
Electrical resistance	$\geq$2 mΩ
Baking temperature	250°C
	160°C (ports)
Vessel volume	24 m^3
Vessel surface area	553 m^2
Internal pressure	$\leq 5 \times 10^{-9}$ Torr
Maximum He leak rate	5×10^{-8} Torr.ℓ/s
Outgassing rate	$\leq 5 \times 10^{-12}$ Torr.ℓ/s$\cdot cm^2$
Pumping speed (N_2)	2000 ℓ/s
Heating medium	oil
Heating medium flow rate	29.6 m^3/hr
Cooling medium	water
Cooling medium flow rate	87×10^3 kg/hr

Table IX.3.2-1 Poloidal field coils specifications

Parameter	OH	D	S	V	Q	C	H
Ampere turns (MA)	± 4.8	± 0.4	± 1.98	± 0.27	± 0.36	± 0.06	± 0.12
Total turns	96	16	132	12	16	4	8
Max. current (KA)	50	50	30	45	45	30	30
RI^2 (MW)	27.75	7.88	23.85	7.47	10.83	2.18	3.82
$1/2\ LI^2$ (MJ)	6.43	0.47	3.87	0.31	0.38	0.09	0.12
Time const. (msec)	580	134	400	93	82	87	74
Max. current density (A/mm^2)	37.3	22.5	31.0	46.5	46.5	22.5	31.0
Max. permissible square wave pulse length (sec)	3.0	3.0	3.0	3.0	3.0	3.0	3.0
Max. temperature rise (°C)	26	10	18	41	41	10	18
Working ground voltage	29	4.8	34	3.6	4.8	1.2	2.4
(KV) turn-to-turn	0.3	0.3	0.3	0.3	0.3	0.3	0.3
Others	$\Delta\phi \sim 5.0$ V·s		$B_z \sim 3000$ G $n=-2.1 \sim 1.0$	$\delta B_z \sim 725$ G	$\delta n \cdot B_z$ ~ 0.194 T	$B_R \sim 215$ G	$B_R \sim 200$ G

Table IX.3.3-1 Toroidal field coil parameters

Toroidal field (R = 1.4 m)	30	kG
Ampere turns	21	MAT
Number of coils	18	
Turns per coil	10	
Length of turn	∿10	m
Area of cross section at center	11700	cm^2
Average current density at center (with space factor : 0.75)	24	A/mm^2
Resistance (75°C without feeder bars)	9.1	mΩ
Inductance	40	mH
Time constant	4.4	sec
Stored energy	274	MJ
Flattop current	117	kA
Flattop voltage	1065	V
Flattop power	125	MW
Voltage between turns	5.8	V
Rise time (Forcing 130%)	4.8	sec
Equivalent square wave width	6.8	sec

Table IX.3.5-1 JT-4 diagnostic ports

kind	number	shape and dimension	comment
A	42	φ60	vertical access
D_1	4	ℓ=150, R=75 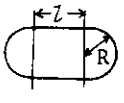	diverter room
K	5	φ100	outer plasma
M_1	5	ℓ = 400, R = 100	main plasma
M_2	2	φ360	main plasma
M_3	30	φ100	null point investigation
M_2'	2	600 × 500, 600 × 400	Thomson scattering
M_4	8	φ140, φ100 (one)	Thomson scattering
S_1, S_2	6		laser beam injection, damping
Total	104		

Table IX.3.6-1 Proposed JT-4 diagnostic systems

Diagnostic Name	Brief Description of Purpose
Voltage Loops	one-turn voltage around toroidal direction
Rogowski Loops	plasma current
Magnetic Probe Coils	plasma position and shape, gross fluctuation
4 mm μ-wave Interferometers	electron density of initial breakdown
2 mm μ-wave Interferometers	electron density
Submillimeter-wave Interferometers	electron density
Thomson scattering	electron temperature and density
FIR Spectrometers	cyclotron radiations
Visible Spectrometers	hydrogen and impurity content
V.U.V Spectrometers	impurity content
Ultra-soft X-ray Spectrometers	impurity, power radiated, ion temperature
X-ray Pulse Height Analysis	electron temperature, electron velocity distribution, impurity concentration
Soft X-ray Detectors	internal plasma fluctuation
Hard X-ray Detectors	runaway electron effects
Neutral Particle Detectors	ion temperature
Neutron Counters	neutron flux
Boundary Layer Analysis[1)]	total power loss to limiter or wall, etc.
Wall Surface Analysis[2)]	examine wall surface effects
TV and Camera System	view inside vacuum vessel during pulse

1) Bolometers, thermocouples, ion gauges, mass analyser, etc.
2) Auger electron spectroscopy, secondary ion mass analyser, etc.

Table IX.4.2-1 Rectifier system specifications

		OH	D	S	V	Q	C	H
coil	inductance (μH)	5145	373	8357	301	376	195	273
	resistance at 75° (mΩ)	10.3	3.15	26.5	3.67	5.35	2.42	4.24
	max. voltage & current (V-KA)	800 - 50	344 - 50	3020 - 30	620 - 40	920 - 45	462 - 30	178 - 30
	peak power (MW)	40	14	35	18	32	8	4
rectifier	phase	12-phase in all rectifiers						
	connection	3φ bridge	double 3φ star	3φ bridge				double 3φ star
	rating (V-KA)	945 - 50	380 - 50	3260 - 50	690 - 40	1210 - 45	700 - 30	200 - 30
transformer capacity (MVA)		29 × 2	10.6 × 2	54 × 2	15.3 × 2	31 × 2	12 × 4	3.12 × 2
others (Method of control)		PR (+FB)	PR	PR	PR + FB	PR + FB	anti-parallel rectifier set PR + FB	PR

PR : preprogram control
FB : feedback control

Table IX.4.2-2 Feedback control specifications

	V	Q	C
Object of control	$\lvert\delta R_p\rvert \leq 5$ cm	$\lvert\delta\kappa\rvert \lesssim 0.05$	$\lvert\delta Z_p\rvert \lesssim 3$ cm
Control field	$\delta B_V \sim \pm 300$ G	$\delta n \sim \pm 0.8/B_V(T)$	$B_R \sim \pm 215$ G
Control current	$\sim \pm 17$ KA	$\sim \pm 22.5$ KA	$\sim \pm 30$ KA
Current response time 0 - 10 KA	10 msec	8.3 msec	5 msec

X. DEVELOPMENT OF THE NEXT LARGE TOKAMAK MACHINE

The study of the concept of the next large tokamak machine to JT-60 was initiated from April by Planning and Coordination Group of Division of Large Tokamak Development. Since D-T burning is out of the scope for JT-60, the next large tokamak aims the fully D-T burning machine. However, it is not simple to define the role of the next machine as there are many different opinions about the scope of the next generation machine around the world.

To make the scope as clear as possible, the study started from physical survey for plasma engineering especially about ignition approach within the technical extension which might be expected in next five years. With NbTi toroidal field coils, the minor radius larger than two meters will be required to ignite plasmas if the most severe scaling law of trapped ion mode is directly applied. If the empirical law by Daughney or one-tenthly suppressed trapped ion mode scaling is applied, it is possible to reach ignition with minor radius of 1.4 meter with very careful impurity control as shown in Fig. X-1.

On the other hand, the essential technology for the tokamak reactor such as superconducting magnet technology, tritium production and handling technology, shielding or remote maintenance engineering are inevitable to be integrated in single machine. Successing JT-60 which is purely a physics-oriented machine, the next large tokamak should play the role of go-between from physics to engineering. Thus the role of the next large tokamak machine, hitherto called Mock-up Test Facility, is defined as one step to realize the tokamak reactor to integrate the essential reactor plasma technology with possibility to reach self-ignition conditions.

The scope of the next machine is quite dependent on the development of superconducting magnet. Design parameters of Mock-up Test Facility are summarized in Table X-1 assuming the application of NbTi coils and they were presented at IAEA Conference and Workshop on Fusion Reactor Design held at Madison, U.S.A. in October[1]. Mock-up Test Facility has relatively large aspect ratio of 4.5 to use effectively the toroidal field and to make machine structure easier for design and maintenance. The plasma has non-circular cross section with elongation of 1.5. Burning period is limited to 30 seconds with small duty cycle due to common use of power supply with JT-60. Wall loading is suppressed under 1.0 MW/m^2.

Essential choice for machine structure is whether divertors should be employed or not. We do not have the definite answer for impurity control. Therefore, the design concept study has to run with two options of divertors or gas blanket concept.

At the present time, the perspectives of physics at high plasma temperature is too vague to determine the required magnetic field and the plasma size. Therefore, the design concept study in the next year will shift to more engineering phase assuming the certain size of plasma which can reach ignition with the scaling laws mentioned in the above.

References

(1) Hiraoka, T., Sugihara, M., Kasai, M. and Mori, S.: A Concept of JAERI's D-T Burning Test Facility, IAEA Conf. and Workshop on Fusion Reactor Design, Madison, Wis. U.S.A., Oct. 1977.

Table X-1 Main design parameters of mock-up test facility

Operation Mode	Fusion power (MW)	230∿400
	Operation period (s)	1200
	Burn time (s)	30∿60
	No. of pulse/line ($\times 10^6$)	0.025
Dimensions	Major radius (m)	6.3
	Plasma radius (m)	1.4/2.1
	Plasma volume (m^3)	367
	Reactor radius (m)	9.8
	Reactor height (m)	10.5
Plasma	Ion temperature (keV)	6∿10
	Ion density ($\times 10^{20}$ m ^{3})	1.2
	Effective charge	
	Confinement time 9s)	4
	B_T on axis (T)	4.7
	Safety factor	≥2.5
	Poloidal β	2.7∿3.4
	Toroildal β(%)	3.8∿4.9
	Plasma current (MA)	4.8
TF Coil	No. of coils	
	Conductor	NbTi
	Bore (height/width) (m)	
	Max. field (T)	8
PF Coil	Conductor (EFC/OHC)	Cu/Cu
	Position	
NBI	Beam energy (keV)	120∿150
	Injection power (MW)	∿60
	Injection time (s)	
Vac. Vessel	Position	First Wall
	Material	Inconel 625
First Wall	Type and material	Inconel 625
	n wall loading (MW/m^2)	0.54∿0.96
	Wall life (effective Y_r)	
Inner Shield (Blanket)	Structure material	none
	Coolant	-
	Breeding material	-
	Thickness (m)	-
Bulk Shield	Material	
	Thickness (m)	0.6
	Coolant	
Tritium	Flow rate (g/h)	
	Plant inventory (kg)	∿0.2
	Annual consump. (kg/y)	

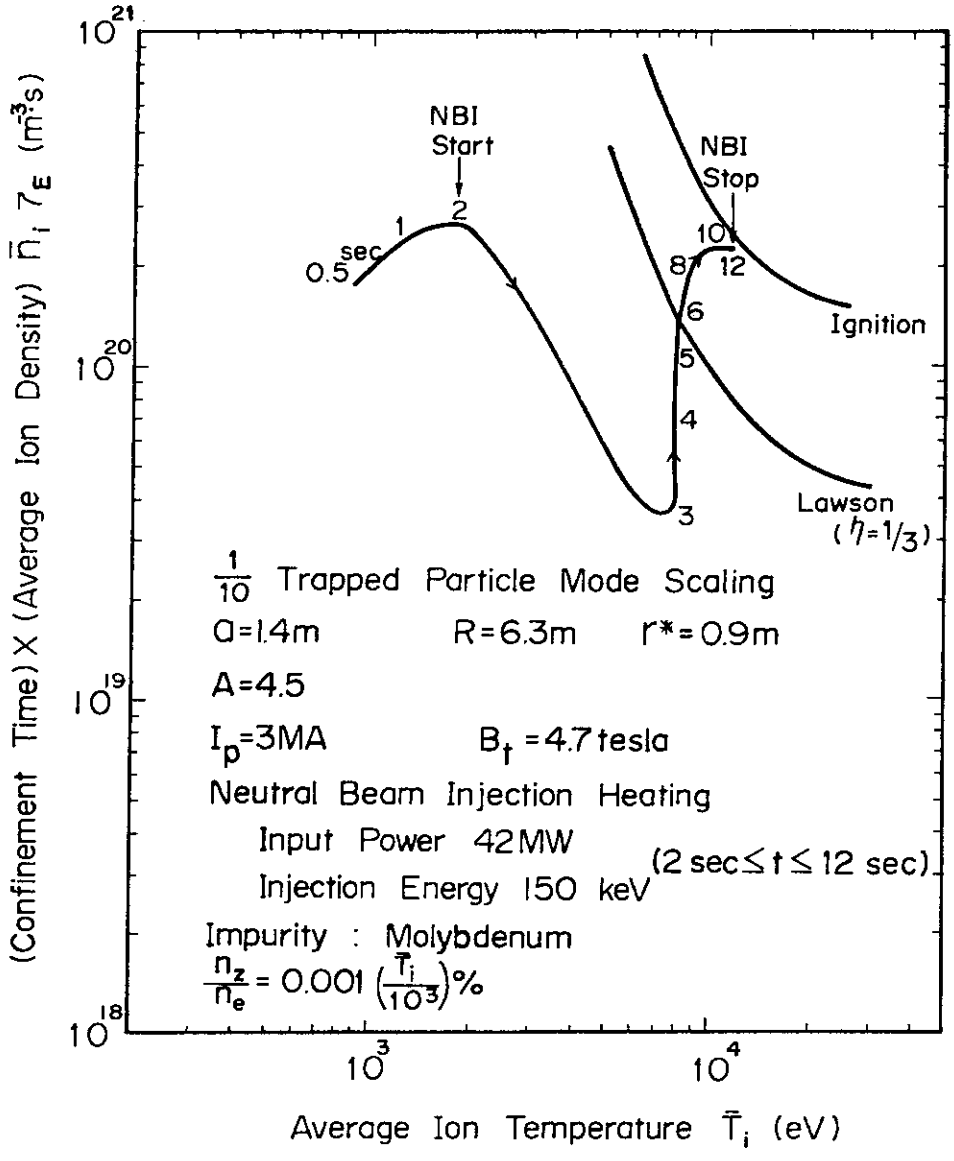

Fig.X-1 Ignition approach

APPENDIXES

A1. Publication List

A1.1 List of JAERI-M Report

1) Sugawara, T.*1, Akiba, M.*2, Arakawa, Y.*3, Fujisawa, N., Funahashi, A., Hirayama, T., Horiike, H.*4, Itoh, T., Kondoh, U.*5, Konoshima, S., Maeno, M., Matsuda, S., Ohara, Y., Ohga, T., Shibata, T., Shimada, M., Shirakata, H., Suzuki, N., Takahashi, K., Takeuchi, H., Tanaka, S. and Yamamoto, T.*6: "JFT-2 tokamak neutral injector and preliminary results of additional heating experiment ", JAERI-M 7043 (April 1977).
   *1 On leave from Tokyo Shibaura Electric Co., Ltd.
   *2 On leave from Tokyo Institute of Technology
   *3 On leave from University of Tokyo
   *4 On leave from Osaka University
   *5 On leave from Nissin Electric Co., Ltd.
   *6 On leave from Nagoya University.
2) Takano, I.* and Suzuki, Y.: "Three-Dimensional Analysis of Eddy Current with the Finite Element Method", JAERI-M 7062 (April 1977) (in Japanese).
   (* On leave from Tokyo Shibaura Electric Co., Ltd.)
3) Matsuda, S.: "Influence of error field on the plasma confining field and the plasma confinement in tokamak", JAERI-M 7103 (May 1977).
4) Kameari, A.* and Suzuki, Y.: "Eddy Current Analysis by the Finite Element Circuit Method", JAERI-M 7120 (May 1977) (in Japanese).
   (* On leave from Mitsubishi Atomic Power Industries Inc.)
5) Itagaki, T., Matoba, T., Funahashi, A. and Suzuki, Y.: "FIR-Interferometer for JT-60", JAERI-M 7121 (May 1977) (in Japanese).
6) Ogata, A., Ninomiya, H. and Suzuki, Y.: "Formalization for Optimal Feedback Control of Plasma Current and Position in a Tokamak", JAERI-M 7126 (June 1977).
7) Takashima, T. and Okamura, H.: "Simulation of drive characteristics of JT-60 movable limiter", JAERI-M 7130 (May 1977).
8) Tsunematsu, T., Kurita, G., Ninomiya, H. and Takeda, T.: "Application of REDUCE-2 to the Computation in CTR", JAERI-M 7179 (June 1977) (in Japanese).
9) Saidoh, M., Sone, K., Yamada, R., Ohtsuka, H. and Murakami, Y.: "Surface Roughness Effects on Blister Formation in Polycrystalline

Molybdenum", JAERI-M 7182 (July 1977).

10) Matoba, T., Kumagai, K., Funahashi, A. and Kawakami, T.: "Evaluation of Radiation Cross Sections of K X-rays and Application to Measurement of Metal Impurity Densities in High-Temperature Plasma", JAERI-M 7196 (July 1977) (in Japanese).

11) Obara, K., Abe, T. and Nakamura, H.: "Sputtering Yield and Surface Observation of Molybdenum Honeycomb Walls", JAERI-M 7216 (July 1977) (in Japanese).

12) Sugie, T., Shiho, M., Kasai, S., Odajima, K., Nagami, M., Maeda, H. and Shimomura, Y.: "Intensity calibration of a vacuum monochromator in a wavelength region of 1000-2000 Å and spectroscopic measurement in DIVA", JAERI-M 7217 (August 1977) (in Japanese).

13) Matoba, T., Suzuki, Y., Funahashi, A. and Itagaki, T.: "Diagnostic Planning in JT-60 Project", JAERI-M 7220 (August 1977).

14) Okamoto, M., Takeda, T., Tanaka, M., Asai, K.*, Nakano, K.** and Kawakami, I.***: "Implementation of the OLYMPUS system and a pre-processor for it",JAERI-M 7228 (July 1977) (in Japanese).
(* Computing Center, JAERI, ** CRC Corp., *** Guest staff, JAERI, Nihon University)

15) Obara, K., Ohtsuka, H., Yamada, R., Abe, T. and Sone, K.: "Construction of Ion Accelerator for Ion-Surface Interaction Research", JAERI-M 7250 (September 1977) (in Japanese).

16) Kimura, H., Ueda, N., Maeda, H., Yamamoto, S., Shimomura, Y., et al.: "Heat Flux in the Divertor Region of DIVA", JAERI-M 7287, (September 1977).

17) Itagaki, T., Matoba, T. Funahashi, A. and Suzuki, Y.: "FIR-Laser Scattering in JT-60", JAERI-M 7295 (August 1977) (in Japanese).

18) Yabuno, K.*, Tani, K., Shimada, R., Kishimoto, H., Yoshida, H. and Tamura, S.: "Design Study of the vertical field power supply for JT-60", JAERI-M 7296 (September 1977) (in Japanese).
(* Hitachi, Ltd.)

19) Yamamoto, S., Sengoku, S., Kimura, H., Shimomura, Y., Maeda, H., et al.: "Loss Mechanism of the Superthermal Electrons Across the Separatrix into the Scrape-off Layer in DIVA", JAERI-M 7309 (September 1977).

20) Yamanaka, K.: "Heat transport due to collisionless drift tearing turbulence", JAERI-M 7314 (October 1977) (in Japanese).

21) Okamoto, M.: "Simulation of lower hybrid wave propagation", JAERI-M 7313 (October 1977) (in Japanese).

22) Okamoto, M., Takizuka, T., Wada, Y.* and Okada, T.*: "An I/O routine based on the BSAM level", JAERI-M 7337 (October 1977) (in Japanese). (* Fujitsu Ltd.)

23) Shiho, M., Odajima, T., Sugie, T., Maeda, H., Kasai, S., Takeuchi, H., Azumi, M., Kimura, H., Nagami, M., Sengoku, S., Yamamoto, S. and Shimomura, Y.: "Spectroscopic and bolometric measurements of radiation loss in DIVA", JAERI-M 7397 (November 1977).

24) Gomay, Y.*, Tazima, T., Satake, T.**, Mizuno, M.**: "Surface cleaning of molybdenum by chemical reaction with oxygen and hydrogen gases", JAERI-M 7405 (1977) (in Japanese).
(* On leave from Research and Development Center, Tokyo Shibaura Electric Company, Ltd., ** ULVAC Corporation)

25) Ide, T.*, Seki, Y. and Iida, H.: "Three-dimensional Analysis of the Effects of Penetrations on Radiation Shielding of a Tokamak Fusion Reactor", JAERI-M 7420 (December 1977) (in Japanese).
(* On leave from Sumitomo Heavy Industries, Ltd.)

26) Shoji, T., Kawakami, T., Funahashi, A. and Shimada, M.: "Data processing system for tokamak experiments", JAERI-M 7456 (January 1978) (in Japanese).

27) Shimomura, Y., Maeda, H., Kimura, H., Azumi, M., Odajima, K., et al.: "Scaling for Scrape-off Layer Plasma in Tokamak", JAERI-M 7457 (December 1977).

28) Yoshida, K. Ando, T. and Shimamoto, S.: "Magnetic Field and Stress Analysis for ORNL-LCT", JAERI-M 7543 (in Japanese).

29) Hosoda, Y. and Shimamoto, S.: "Study of Thermal Problem in ORNL-Large Coil Task", JAERI-M 7546 (in Japanese).

30) Ohtsuka, M.*, Tani, K., Kishimoto, H., Shimada, R., Yoshida, H., Hoshino, K. and Tamura, S.: "Fast ion spatial distribution in neutral beam injection into a tokamak", JAERI-M 7551 (January 1978) (in Japanese).
(* Hitachi Ltd.)

31) Tsunematsu, T. and Takeda, T.: "A subroutine package ATLAS for large scale matrix computation", JAERI-M 7573 (March 1978) (in Japanese).

32) Iida, H. and Seki, Y.: "Induced Activities of Fusion Reactor Structural Materials", JAERI-M 7582 (March 1978) (in Japanese).

33) Ohga, T., Kondoh, U.*, Matsuda, S., Ohara, Y., Shibata, T., Shirakata, H. Sugawara, T.** and Tanaka, S.: "Injector test stand ITS-2 for two-stage ion source development" JAERI-M 7604 (March 1978) (in Japanese).
(* On leave from Nissin Electric Co. Ltd., ** On leave from Tokyo

Shibaura Electric Co., Ltd.)

34) Shimomura, Y., Maeda, H., Odajima, K., Kimura, H., Nagami, M., et al.: Recent Results in the DIVA Experiment", JAERI-M 7610 (March 1978).

35) Kondoh, U.*1, Horiike, H.*2, Morita, H.*3, Sugawara, T.*4 and Tanaka, S.: "Preliminary experiments of cooled extraction grids in ion source for neutral beam injector", JAERI-M 7612 (March 1978) (in Japanese).
*1 On leave from Nissin Electric Co., Ltd.
*2 On leave from Osaka University
*3 On leave from Mitsubishi Heavy Industries, Ltd.
*4 On leave from Tokyo Shibaura Electric Co., Ltd.

36) Sakuraba, J.* and Shibata, T.: "Calculation of heat input to cryopumps by Monte Carlo method", JAERI-M 7611 (March 1978) (in Japanese).
(* On leave from Sumitomo Heavy Industries, Ltd.)

37) Maki, K.*, Tone, T. and Yamato, H.**: "Studies on Plasma Shutdown of JAERI Experimental Fusion Reactor", JAERI-M 7635 (April 1978) (in Japanese).
(* On leave from Energy Research Laboratory, Hitachi, Ltd., ** On leave from Research and Development Center, Tokyo Shibaura Electric Co., Ltd.)

38) Maki, K.*, Tone, T. and Yamato, H.**: "Studies on Plasma Ignition of JAERI Demonstration Fusion Reactor", JAERI-M 7676 (May 1978) (in Japanese).
(* On leave from Energy Research Laboratory, Hitachi, Ltd., ** On leave from Research and Development Center, Tokyo Shibaura Electric Co., Ltd.)

39) Hosoda, Y. and Shimamoto, S.: "Thermal Stress Analysis of Superconducting Magnet by SAP-4", JAERI-M 7675 (in Japanese).

A1.2 List of Papers Published in Journals

1) Kumagai, K., Matoba, T., Funahashi, A. and Kawakami, T.: "An intrinsic germanium Ge(I) detector for measurements of soft X-ray spectra radiated from high temperature tokamak plasmas", Japan. J. Appl. Phys. 16 (1977) 871.

2) Takeuchi, H., Takahashi, K., Funahashi, A. and Yoshida, H.: "The local counting efficiency of a ceratron multiplier for plasma diagnoses", Japan. J. Appl. Phys. 16 (1977) 873.

3) Takeuchi, H., Funahashi, A. and Takahashi, K.: "Ion temperature scaling on JAERI tokamaks", Japan J. Appl. Phys. 16 (1977) 1227.

4) Sometani, T., Fujisawa, N. and Hasebe, K.: "Shell current and vertical field due to it in a tokamak model shell", Japan. J. Appl. Phys. 16 (1977) 1343.

5) Suzuki, Y., Ninomiya, H., Ogata, A., Kameari, A.* and Aikawa, H.: "Tokamak Circuit", Japan. J. Appl. Phys. 16 (1977) 2237.
(* On leave from Mitsubishi Atomic Power Industries Inc)

6) Tanaka, S., Murakami, Y. and Shibata, T.: "Measurement of Energy Reflection from Metals Bombarded by 10-30 keV Hydrogen Ion Beam", Japan. J. Appl. Phys. 17 (1978) 183.

7) Ohara, Y., Matsuda, S., Shirakata, H. and Tanaka, S.: "Hole geometry optimization of the extraction electrode in a duoPIGatron ion source", Japan. J. Appl. Phys., 17 (1978) 423.

8) Kasai, S., Azumi, M., Funahashi, A., Sugie, T. and Takizuka, T.: "Doppler temperature and particle confinement time determined from measurements of H_α-line on a tokamak plasma in the JFT-2a device". Japn. J. Appl. Phys. 17 (1978) 903.

9) Nagashima, A.*, Funahashi, A., Kawakami, T., Shoji, T. and Takahashi, K.: "A 2-mm wave digital interferometer for tokamak discharges in the upgraded DIVA", Japan. J. Appl. Phys. 17 (1978) 1263.
(* On leave from Tokyo Institute of Technology)

10) Kasai, S., Funahashi, A., Konoshima, S., Nagami, M., Sugie, T. and Mori, K.: "Absolute calibration of a grazing-incidence vacuum monochromator by means of tokamak discharges", Japan. J. Appl. Phys. 17 (1978) 1625.

11) Takeda, T. and Tsunematsu, T.: "Application of the finite element method to the spectrum analysis of mhd oscillations",Butsuri 33 (1978) 196.

12) Takizuka, T. and Abe, H.*: "A binary collision model for plasma simulation with a particle code", J. Comp. Phys. 25 (1977) 205. (* Kyoto University)

13) Takizuka, T.: "Numerical calculation on the breakdown of the tokamak discharge", Hoden-Kenkyu 69 (1977) 31.

14) Matsuda, S.: "Problems of discharge in neutral beam injector", Hoden-Kenkyu 69 (1977) 43 (in Japanese).

15) Nagashima, T.: "Problems of discharge in radiofrequency heating", Hoden-Kenkyu 69 (1977) 48 (in Japanese).

16) Tazima, T.: "Physical requirements and its design considerations for the first wall of JT-60", Hoden-Kenkyu 69 (1977) 50 (in Japanese).

17) Nagashima, T.: "Radiofrequency heating", Kakuyogo-Kenkuy 37 (1977) Appendix No.3, p.29.

18) Nakamura, Y.*, Shibata, T. and Tanaka, M.: "Grain ejection from surface of the polycrystalline molybdenum irradiated by intense H^+ and H_2^+ ion beams", J. Nuclear Materials 68 (1977) 253. (* On leave from Sumitomo Heavy Industries Co., Ltd.)

19) Sone, K., Abe, T., Obara, K., Yamada, R. and Ohtsuka, H.: "Graphite Surface Erosion by 100 keV Helium and Hydrogen Bombardment", J. Nucl. Materials 71 (1977) 82.

20) Tazima, T., Nakamura, Y., Inoue, K.: "Density distributions of impurities and related energy losses in tokamak plasmas", Nuclear Fusion 17 (1977) 419.

21) Shimomura, Y.: "Possibility of Heavy-Impurity Control by Light-Impurity Radiation in a Large Tokamak", Nuclear Fusion 17 (1977) 626.

22) Shimomura, Y.: "A Model for Heavy-Impurity Recycling at a Limiter and Power-Loss Limitation to a Limiter in Tokamak", Nuclear Fusion 17 (1977) 1377.

23) Yamamoto, S., Sengoku, S., Kimura, H., Shimomura, Y., et al.: "Behavior of Superthermal Electrons in the Scrape-off Layer Plasma of DIVA", Nuclear Fusion 18 (1978) 205.

24) Nagami, M., Shimomura, Y., Maeda, H., Ohtsuka, H., Shiho, M., et al.: "Formation of a Light-Impurity Free Plasma in DIVA", Nuclear Fusion 18 (1978) 529.

25) Seki, Y. and Maekawa, H.: "Cross-Section Sensitivity Analysis of U-235 and U-238 Fission Rates Measured in a Graphite-Reflected Lithium Assembly", Nucl. Sci. and Eng. 66 (1978) 243.

26) Iida, H., Seki, Y. and Ide, T.*: "Induced Activity and Dose Rate in a Fusion Reactor with Molybdenum Blanket Structure", J. Nucl. Sci. Tech. 14 (1977) 68.
(* On leave from Sumitomo Heavy Industries Co., Ltd.)

27) Okamoto, M.: "Effect of finite wavelength of the pump on the parametric threshold of lower hybrid wave", J. Phys. Soc. Japan 43 (1977) 1105.

28) Tuda, T. and Tanaka, T.: "Impurity drift instability of dissipative type", J. Phys. Soc. Japan 43 (1977) 1407.

29) Takeuchi, H., Shoji, T., Funahashi, A. and Takahashi, K.: "Study on proton behavior in the JFT-2 tokamak from analyses of charge-exchanged fast atoms", J. Phys. Soc. Japan 44 (1978) 1363.

30) Sugie, T., Takeuchi, H., Kasai, S., Funahashi, A., Takahashi, K. and Kimura, H.: "Ion temperature characteristics of upgraded DIVA", J. Phys. Soc. Japan 44 (1978) 1960.

31) Fukuyama, A.*, Momota, H.*, Itatani, R.* and Takizuka, T.: "Stochastic acceleration by an electromagnetic waves near ion cyclotron harmonics", Phys. Rev. Lett. 38 (1977) 701.
(* Kyoto University)

32) Takahashi, H.*, Daughney, C.C.*, Ellis, C.A.*, Goldston, R.J.*, Hsuan, H.*, Nagashima, T., Paolon, F.J.*, Sivoands, A.J.* and Suckewer*: "Ion heating in ATC tokamak in the ion cyclotron range of frequencies", Phys. Rev. Lett. 39 (1977) 31.
(* Princeton Plasma Physics Laboratory)

33) Takashima, T., Ohta, M. and Shimizu, M.: "Drive characteristics of a fast movable limiter in the JT-60 tokamak", Rev. Sci. Instrum. 49(2) (1978) 194.

34) Takeda, T. and Tsunematsu, T.: "Two-dimensional code for tokamak transport", Report on the numerical analysis of MHD equations (1976) p.48 (in Japanese).

35) Tsunematsu, T. and Takeda, T.: "MHD stability analysis by the finite element method", Report on the numerical analysis of MHD equations (1976) p.98 (in Japanese).

36) Gomay, Y.*, Tazima, T. and Fujisawa, N.: "Discharge cleaning experiment in the JFT-2 tokamak with surface observation by AES", J. Vacuum Science Technology 15 (1978) 103.
(* On leave from Research and Development Center, Tokyo Shibaura Electric Company, Ltd.)

37) Sone, K., Ohtsuka, H., Abe, T., Yamada, R., Obara, K., Narusawa, T.*, Tsukakoshi, O.*, Satake, T.* and Komiya, S.*: "Sputtering Yield Measurement on First Wall Materials of Thermonuclear Fusion Devices", J. Vacuum Soc. Japan 20 (1977) 136.
(* ULVAC Corporation)

38) Obara, K., Abe, T., Sone, K., Yamada, R. and Ohtsuka, H.: "Observation on Surface Deformation of Pyrolytic Graphite Bombarded by 100 keV He^+, H^+ Ions", J. Vacuum Soc. Japan 20 (1977) 176.

A1.3 List of Papers Published in Conference Proceedings

1) Toyama, H.*, Inoue, S.*, Itoh, K.*, Iwahashi, A.*, Kaneko, H.*, Makishima, K.*, Ochiai, I.*, Shinohara, S.*, Suzuki, Y. and Yoshikawa, S.**: "Experiments on Non-Circular Tokamak and Related Topics", Proceeding of 6-th International Conf. of Plasma Phys. and Controlled Nuclear Fusion Research, Berchtesgaden 1976 vol.I, 323.
(* Tokyo University, ** Princeton University)

2) Tuda, T.: "Temperature gradient effect on the impurity ion transport in a tokamak", Third International Conference on Plasma Theory (Trieste, Italy, 1977).

3) Suzuki, Y., Ogata, A., Ninomiya, H., Nakagawa, T.*, Tsuzuki, N.* and Yamagishi, T.*: "Control System of Plasma Position and Cross Sectional Shape in Large Tokamak", Proceeding of the 7th Symposium on Engineering Problems of Fusion Research, Knoxville, 1977, Vol.I, 112.
(* Tokyo Shibaura Electric Co.,Ltd.)

4) Ohara, Y., Arakawa, Y.*, Horiike, H.**, Kondoh, U.***, Matsuda, S., Ohga, T., Okumura, Y. and Shirakata, H.: "Ion source development for JT-60 neutral beam injector", Proc. 7th Symp. on Engineering Problems of Fusion Research, (IEEE, New York, 1977) p.273.
(* On leave from University of Tokyo, ** On leave from Osaka University, *** On leave from Nissin Electric Co.,Ltd.)

5) Shibata, T., Itoh, T., Kawai, M., Morita, H.*, Matsuda, S., Nakamura, Y.**, Sakuraba, J.** and Tanaka, S.: "Beam line studies of the JT-60 neutral beam injector", ibid., p.544.
(* On leave from Mitsubishi Heavy Industries, Ltd., ** On leave from Sumitomo Heavy Industries, Ltd.)

6) Yamato, H.*, Shinya, K.*, Morimiya, O.*, Miura, A.*, Murakami, Y., Matsuda, S. and Sako, K.: "Design study of a neutral injection system for the JAERI experimental fusion reactor (JXFR)", ibid., p.560.
(* Tokyo Shibaura Electric Co.,Ltd.)

7) Kameari, A.* and Suzuki, Y.: "Eddy Current Analysis by the Finite Element Circuit Method", idib., Vol. II, 1386.
(* Mitsubishi Atomic Power Industries Inc.)

8) Takahashi, T.*, Takahashi, G.*, Kazawa, A.* and Suzuki, Y.: "Numerical and Experimental Analysis of Eddy Currents Induced in Tokamak Machines", ibid. Vol, II, 1393.

9) Sako, K. and Minato, A.*: "Blanket structure design for JAERI

experimental fusion reactor", Proc. of the 7th Symposium on Engineering Problems of Fusion Research, Knoxville, 1977, Vol.II, 1490.
(* On leave from Kawasaki Heavy Industries, Ltd.)

10) Iida, H., Ide, T.* and Seki, Y.: "Nuclear Heat Deposition in Cryosorption Pumps of a Fusion Reactor", Proc. of the 7th Symposium on Engineering Problems of Fusion Research, Knoxville, 1977, Vol.II, 1658.
(* On leave from Sumitomo Heavy Industries, Ltd.)

11) Shimada, R., Tamura, S., Ohta, M., Ohsaki, O.* and Sawada, Y.*: "Voltage oscillations in the poloidal field coils of JT-60", Proc. of the 8th Symp. on Engineering Problems of Fusion Research (Knoxville, USA, 1977).
(* Tokyo Shibaura Electric Co., Ltd.)

12) Nakamura, H., Shimizu, M., Ohta, M., Aizawa, T.*, Naito, T.* and Kasai, M.*: "Electron beam bombardment test in JT-60 mangetic limiter plate", Proc. 7th Symposium on Engineering Problems of Fusion Research, Knoxville, 1977.
(* Mitsubishi At. Power Ind. Ltd.)

13) Takatsu, H., Yamamoto, M., Shimizu, M., Ohta, M., Saigo, T.*, Miyata, H.**, Sato, H.** and Itoh, Y.**: "Stress analysis of vacuum vessel in JT-60", Proc. 7th Symposium on Engineering Problems of Fusion Research, Knoxiville, 1977.
(* Staff on leave from Hitachi, Ltd., ** Hitachi, Ltd.)

14) Suzuki, Y.: "Review of the Work on Plasma Wall Interaction in Tokamak Plasma Confinement at JAERI", Proceeding of the International Symposium on Plasma Wall Interaction.

15) Yamamoto, S., Maeda, H., Shimomura, Y., Odajima, K., et al.: "Reduction of Power Loss Due to Heavy Impurities in DIVA", Proc. 8th Europ. Conf. on Controlled Fusion and Plasma Physics (Prague 1977) 1, 33 and 2, 123.

16) Yoshikawa, H.**, Gomay, Y.*, Sugiyama, Y.**, Mizuno, M.**, Komiya, S.**, and Tazima, T.: "Outgassing rates before, during and after bake-out for various vacuum and first wall candiate materials of a large tokamak device", Proc. 7th Int. Vacuum Congr. & 3rd Int. Conf. Solid Surfaces (1977) 367.
(* On leave from Research and Development Center, Tokyo Shibaura Electric Company, Ltd., ** ULVAC Corporation)

17) Narusawa, T.*, Tsukakoshi, O.*, Satake, T.*, Mizuno, M.*, Ohtsuka, H., Sone, K. and Komiya, S.*: "An Experimental UHV Apparatus to Investigate

Interactions of Low Energy Light Ions with Solid Surfaces", ibid., p.371.
(* ULVAC Corporation)

18) Sone, K., Saidoh, M., Abe, T., Yamada, R., Obara, K., Ohtsuka, H. and Murakami, Y.: "Surface Erosions by Energetic Helium and Hydrogen Bombardment of Molybdenum and Pyrolytic Graphite", Proc. 7th Int. Vacuun Congr. & 3rd Int. Conf. Solid Surfaces (Vienna 1977) p.375.

19) Kawasaki, K., Nishio, S., Ohkubo, M., Ando, T., Ohta, M., Matsui, M.*, Kitazawa, H.* and Saito, R.*: "THE TOROIDAL FIELD COIL FOR JT-60", Proc.6th International Conference on Magnet Technology, Bratislava, 1977.
(* Hitachi, Ltd.)

20) Ohkubo, M., Ando, T., Miki, N.*, Kawasaki, K., Nishio, S., Ohta, M., Ishimura, M.** and Takano, H.**: "THE POLOIDAL FIELD COIL FOR JT-60", Proc. 6th International Conference on Magnet Technology, Bratislava, 1977.
(* On leave from Tokyo Shibaura Electric Co., Ltd., ** Tokyo Shibaura Electric Co., Ltd.)

A2. Personnel of the Division

A2.1 Number of the staff of the Division

	FY 1976	FY 1977	FY 1978
Regular staff*1	102	121	140
Staff on loan	24	22	27*2
Guest scientist	4	6	7*3
Scholarship fellow	20	30	30

*1 Including scientists, technicians, and secretaries.

*2 Seven from Tokyo Shibaura Electric Co., Ltd.
Five from Hitachi, Ltd.
Two from Mitsubishi Atomic Power Industries Inc.
Two from Sumitomo Heavy Industries, Ltd.
Two from Mitsubishi Electric Co.
Two from Mitsubishi Heavy Industries, Ltd.
Two from Oki Electric Industry Co., Ltd.
One from Fuji Electric Co., Ltd.
One from Sumitomo Electric Industries, Ltd.
One from Nissin Electric Co., Ltd.
One from Kawasaki Heavy Industries, Ltd.
One from Hitachi Wire and Cable, Ltd.

*3 Four from the University of Tokyo
Two from Nihon University
One from Ochanomizu University

A2.2 List of Scientific Staffs and Officers during FY 1977

MORI, Sigeru (Senior Supervisor in Fusion Research)

(A) Division of Thermonuclear Fusion Research

MORI, Sigeru (Head)
OBATA, Yukio (Deputy Head)
AKAMA, Kouzou (Administrative Manager)

Plasma Theory Laboratory

AZUMI, Masafumi
KURITA, Gen'ichi
OKAMOTO, Masao***
TAKEDA, Tatsuoki
TAKIZUKA, Tomonori
TANAKA, Masatoshi (Chief)
TSUNEMATSU, Toshihide
TUDA, Takashi
YAMANAKA, Kaoru**1

Experimental Plasma Physics Laboratory

TANAKA, Yuji (Chief)

* JFT-2

FUJISAWA, Noboru
HIRAYAMA, Toshio
KONOSHIMA, Shigeru
MAENO, Masaki
SHIMADA, Michiya
SUZUKI, Norio
UEHARA, Kazuya**2
YAMAMOTO, Takumi

* JFT-2a/DIVA

KIMURA, Haruyuki
MAEDA, Hikosuke
NAGAMI, Masayuki

ODAJIMA, Kazuo
OHASA, Kazumi**1
SENGOKU, Seio
SHIMOMURA, Yasuo
YAMAMOTO, Shin

* Diagnostics

FUNAHASHI, Akimasa
KASAI, Satoshi
KAWAKAMI, Tomohide
KUMAGAI, Katsuaki
NAGASHIMA, Akira**3
SHOJI, Teruaki
SUGIE, Tatsuo
TAKAHASHI, Koki
TAKEUCHI, Hiroshi
YAMAUCHI, Toshihiko

Facility Operation and Engineering Section

ANNO, Katsuto
ARAI, Takashi
HASEGAWA, Kouichi
HIRATSUKA, Hajime
ISAKA, Masayoshi
KAZAWA, Minoru
KIKUCHI, Kazuo
KUNIEDA, Shunsuke (Deputy Chief)
MATSUZAKI, Yoshimi
SHIBATA, Takatoshi
SHIINA, Tomio
SUNAOSHI, Hidenori
SUZUKI, Kihachiro
TANI, Takashi
TOYOSHIMA, Noboru
YOKOKURA, Kenji

Plasma Heating Laboratory

SHIRAKATA, Hirofumi (Chief)

* Neutral Beam Injection Heating

ARAKAWA, Yoshihiro**4
HORIIKE, Hiroshi**5
ITOH, Takao
KAWAI, Mikito
KONDOH, Umeo*1
MATSUDA, Shinzaburo
MORITA, Hiroaki*2
OHARA, Yoshihiro
OKUMURA, Yoshikazu
SAKURABA, Junji*3
SHIBATA, Takemasa
TANAKA, Shigeru

* Radiofrequency Heating

IMAI, Tsuyoshi
NAGASHIMA, Takashi

Plasma Engineering Laboratory

ABE, Tetsuya
MURAKAMI, Yoshio (Chief)
OBARA, Kenziro
OHTSUKA, Hidewo
SAIDOH, Masahiro
SHIRAISHI, Kensuke
SONE, Kazuho
YAMADA, Rayji

Superconducting Magnet Laboratory

ANDO, Toshinari
HOSODA, Yoshikado*4
NISHI, Masataka
OHKUMA, Hirotsugu*5

SATOW, Takashi*6

SHIMAMOTO, Susumu (Chief)

TADA, Eisuke

YOSHIDA, Kiyoshi

Fusion Reactor System Laboratory

IDE, Takahiro*3

IIDA, Hiromasa

IOKI, Kimihiro*7

MAKI, Koichi*8

MINATO, Akio*9

SAKO, Kiyoshi (Chief)

SEKI, Yasushi

TONE, Tatsuzo

YAMAMOTO, Takashi*10

YAMATO, Harumi*11

YAMAUCHI, Michinori*11

(B) Division of Large Tokamak Development

ISO, Yasuhiko (Head)
SAITO, Jo (Administrative Manager)
SHIRAISHI, Kensuke (Principal Engineer)

JT-60 Project Office I

YOSHIKAWA, Masaji (Chief)

* Planning and Coordination Group

GOMAY, Yoshio*11
HIRAOKA, Toru
KASAI, Masao*7
NAKAMURA, Yukiharu*3
SUGIHARA, Masayoshi
TAZIMA, Teruhiko
TOKUTAKE, Toshikuni

* Power Supplies Group

ARAKAWA Kiyotsugu**6
HOSHINO Katsumichi
KISHIMOTO, Hiroshi
OHTSUKA, Michio*8
SHIMADA, Ryuichi
TAMURA, Sanae
TANI, Keiji
YABUNO, Kohei*8
YOSHIDA, Hidetoshi

* Control Group

AIKAWA, Hiroshi
ITAGAKI, Tokiyoshi
KIMURA, Toyoaki
MATOBA, Tohru
NINOMIYA, Hiromasa
OGATA, Atsushi
SUZUKI, Yasuo

TSUKADA, Masahiro*12
TSUZUKI, Naohisa*11

* JT-4 Group
KITSUNEZAKI, Akio
SEKI, Shogo
YOKOMIZO, Hideaki
MATSUDA, Toshiaki
SAITO, Ryuta*6

JT-60 Project Office II

IIJIMA, Tsutomu (Chief)

* Mahcine Group
ANDO, Toshiro
KAWASAKI, Kozou
KURIYAMA, Masaaki
MIKI, Nobuharu*11
NAKAMURA, Hiroo
NISHIO, Satoshi
OHKUBO, Minoru
OHTA, Mitsuru
SAIGO, Tsugumoto*8
SHIMIZU, Masatsugu
TAKASHIMA, Tetsuo
TAKATSU, Hideyuki
YAMAMOTO, Masahiro

* Auxiliary Facilities Group
HIRUTA, Kazuharu
KODAMA, Kozou

(C)

Office of Fusion Program

OHKUBO, Yoshiharu (Administrative Manager)
INOUE, Kenji
TAKEDA, Takashi
KUROIWA, Katsuhiko

Guest Scientists

IWATA, Giichi (Ochanomizu University)
KAWAKAMI, Ichiro (Nihon University)
TUZI, Yutaka (The University of Tokyo)

KANEKO, Kumetaro (The University of Tokyo)
MIYAMOTO, Goro (Ibaraki University)
YASUKOCHI, Ko (Nihon University)

On leave from

*1 Nissin Electric Co., Ltd.
*2 Mitsubishi Heavy Industries Ltd.
*3 Sumitomo Heavy Industries Ltd.
*4 Sumitomo Electric Co., Ltd.
*5 Tokyo Shibaura Electric Co., Ltd.
*6 Mitsubishi Electric Co.
*7 Mitsubishi Atomic Power Industries Inc.
*8 Hitachi, Ltd.
*9 Kawasaki Heavy Industries Ltd.
*10 Fuji Electric Co., Ltd.
*11 Tokyo Shibaura Electric Co., Ltd.
*12 Oki Electric Industry Co., Ltd.

Scholarship fellows

**1 Nagoya University
**2 University of Tsukuba
**3 Tokyo Institute of Technology

**4 The University of Tokyo

**5 Osaka University

**6 Tokai University

*** Now at the Institute of Plasma Physics, Nagoya University

A3. Budget of the Division

(unit: million yen)

	FY*1 1976	FY*1 1977	FY*1 1978
Scientific program	3,531.4	6,925.0	9,391.8*2
(excluding staff & administrative cost)	(11,491.6)	(16,516.2)	(14,335.7*3)
Building	345.6	410.8	1,155.5

*1 From April to March

*2 Including cashing of the financial obligation in FY 1978.

*3 The total financial obligation from FY 1978 to FY 1981 for the construction of part of the components of JT-60 and for the development of plasma heating systems and super conductig magnet.